Department of
Industry and Resources

RECORD
2005/4

GSWA LANCER 1 WELL COMPLETION REPORT (INTERPRETIVE PAPERS) OFFICER AND GUNBARREL BASINS WESTERN AUSTRALIA

edited by A. J. Mory and P. W. Haines

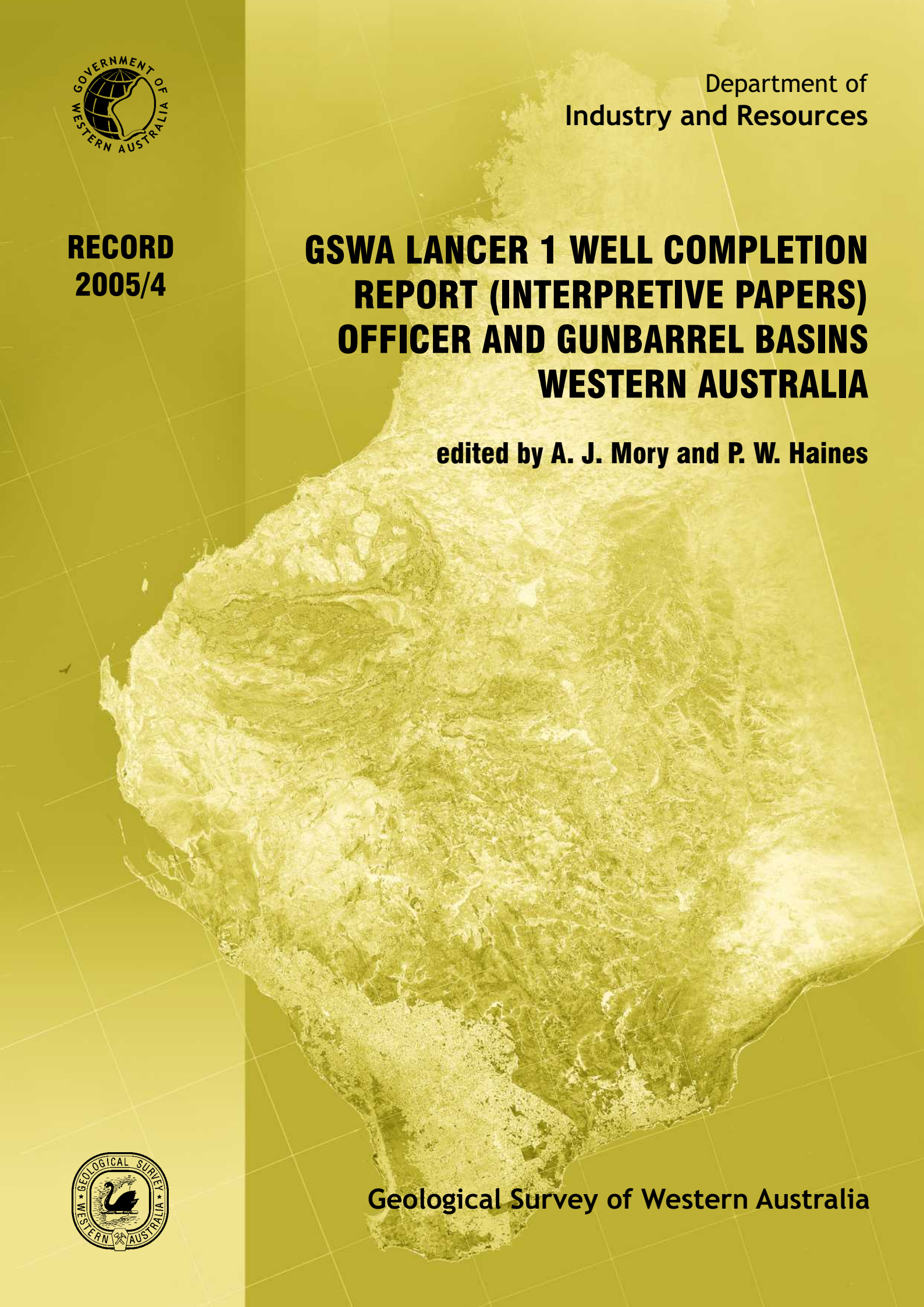

Geological Survey of Western Australia

GEOLOGICAL SURVEY OF WESTERN AUSTRALIA

Record 2005/4

GSWA LANCER 1 WELL COMPLETION REPORT (INTERPRETIVE PAPERS), OFFICER AND GUNBARREL BASINS, WESTERN AUSTRALIA

edited by
A. J. Mory and P. W. Haines

with contributions by
J. Backhouse[1], D. Dawson[2], D. N. Dewhurst[3], K. Grey, K. Grice[2], P. J. Hamilton[4], A. C. Hill[5], G. Koch[6], F. Pirajno, S. Pisarevsky[7], M. D. Raven[8], M. K. Stevens, and M. T. D. Wingate[7]

1 Backhouse Biostrat Pty Ltd
2 ARC/Stable Isotope and Biogeochemistry Group, Centre for Applied Organic Geochemistry, Curtin University of Technology
3 CSIRO Petroleum
4 Department for Applied Geology, Curtin University of Technology
5 Bar Point, N.S.W.
6 Geoscience Associates Australia, Adelaide
7 School of Earth and Geographical Sciences, The University of Western Australia
8 CSIRO Land and Water

Perth 2005

MINISTER FOR STATE DEVELOPMENT
Hon. Alan Carpenter MLA

DIRECTOR GENERAL, DEPARTMENT OF INDUSTRY AND RESOURCES
Jim Limerick

DIRECTOR, GEOLOGICAL SURVEY OF WESTERN AUSTRALIA
Tim Griffin

REFERENCE
The recommended reference for this publication is:
MORY, A. J., and HAINES, P. W., (editors), 2005, GSWA Lancer 1 well completion report (interpretive papers), Officer and Gunbarrel Basins, Western Australia: Western Australia Geological Survey, Record 2005/4, 81p.

National Library of Australia Card Number and ISBN 0 7307 8996 9

Grid references in this publication refer to the Geocentric Datum of Australia 1994 (GDA94). Locations mentioned in the text are referenced using Map Grid Australia (MGA) coordinates, Zone 51. All locations are quoted to at least the nearest 100 m.

Cover image modified from Landsat data, courtesy of ACRES

Published 2005 by Geological Survey of Western Australia
This Record is published in digital format (PDF), and is available online at www.doir.wa.gov.au/gswa/onlinepublications.
Laser-printed copies can be ordered from the Information Centre for the cost of printing and binding.

Further details of geological publications and maps produced by the Geological Survey of Western Australia are available from:
Information Centre
Department of Industry and Resources
100 Plain Street
EAST PERTH, WESTERN AUSTRALIA 6004
Telephone: +61 8 9222 3459 Facsimile: +61 8 9222 3444
www.doir.wa.gov.au/gswa/onlinepublications

Contents

Appendix

Plate

Preface

Lancer 1 (latitude 25°02'44.5"S, longitude 123°45'20.1"E) is a stratigraphic corehole that was drilled in the northwestern Officer Basin and overlying Gunbarrel Basin by the Geological Survey of Western Australia in October–November 2003 to increase knowledge of the stratigraphic succession and petroleum potential in that area. An initial well completion report, containing basic data and some early interpretive results, was compiled by Haines et al. (2004), and further stratigraphic analysis of the well is included in Grey et al. (2005).

The papers in this Record follow the initial well completion report and present the results available to date of the interpretations of various aspects of the geology of the corehole. They include isotope chemostratigraphy (Hill), biostratigraphy (Grey; Backhouse), magnetostratigraphy (Pisarevsky and Wingate), igneous petrology (Pirajno), and aspects directly related to petroleum geology (Hamilton; Grice and Dawson; Raven and Dewhurst). Also included is a discussion of amendments to the long-spaced density calibration coefficient (Stevens and Koch). The revised well index sheet and composite well log (Plate 1) reflect minor amendments to well location, stratigraphy, and wireline log data since the release of Haines et al. (2004).

P. W. Haines
A. J. Mory

References

HAINES, P. W., MORY, A. J., STEVENS, M. K., and GHORI, K. A. R., 2004, GSWA Lancer 1 well completion report (basic data), Officer and Gunbarrel Basins, Western Australia: Western Australia Geological Survey, Record 2004/10, 39p.

GREY, K., HOCKING, R. M., STEVENS, M. K., BAGAS, L, CARLSEN, G. M, IRIMIES, F., PIRAJNO, F., HAINES, P. W., and APAK, S. N., 2005, Lithostratigraphic nomenclature of the Officer Basin and correlative parts of the Paterson Orogen, Western Australia: Western Australia Geological Survey, Report 93, 89p.

Stable isotope stratigraphy, GSWA Lancer 1, Officer Basin, Western Australia

by

A. C. Hill

Bar Point, NSW

Abstract

Carbon-isotope data from mid-Neoproterozoic (Cryogenian) strata of the Buldya Group in GSWA Lancer 1 and GSWA Empress 1A within the western Officer Basin show a good correlation, although the sections are 264 km apart. There is a close agreement between formation boundaries and informal $\delta^{13}C$ correlation units in these drillholes. This correlation is supported by the presence of the two dominant stromatolite assemblages — *Acaciella australica* and *Baicalia burra*. Together with the acritarch *Cerebrosphaera buickii*, these confirm the correlation of this succession with the Bitter Springs Formation in the Amadeus Basin, and the Callanna and Burra Groups in the Adelaide Rift Complex.

The 53 carbon-isotope ratios measured in GSWA Lancer 1 vary between -4 and +8.5‰, and are consistent with the large perturbations in the carbon cycle during the mid-Neoproterozoic. The heaviest carbon-isotope ratios imply periods of massive organic-carbon burial, but only low total-organic-carbon values have been measured in Lancer 1. These carbon-isotope ratios are interpreted to be close to their primary values based on their oxygen-isotope ratios and the preservation of carbonate fabric in thin sections. The five strontium-isotope ratios measured are too heavy to be useful for correlation.

Introduction

Carbon ($\delta^{13}C$) and strontium ($^{87}Sr/^{86}Sr$) isotope stratigraphy underpins regional and global correlation in the late Neoproterozoic (Walter et al., 2000; Hoffman and Schrag, 2002). Without it, recognition of the Ediacaran — the first geological period to be named in more than a century — would not have been possible (Knoll et al., 2004). Now that the Ediacaran has been defined, attention is switching to earlier Neoproterozoic successions, for which the thick Cryogenian (Supersequence 1) sections in GSWA Lancer 1 and GSWA Empress 1A will play a significant role. Whereas the utility of stable carbon and strontium isotopes as correlation tools for late Neoproterozoic successions is well established, their utility in older Neoproterozoic rocks is poorly known.

Hill and Walter (2000, fig. 10) showed that it is possible to correlate Supersequence 1 across the Centralian Superbasin to the Adelaide Rift Complex using a combination of isotope stratigraphy, stromatolite biostratigraphy, and palynology. In the Adelaide Rift Complex, Supersequence 1 is equivalent to the Willouran and Torrensian series (Preiss, 2000). Two major correlation points are possible with these series: 1) at ~830 Ma, between the Browne Formation (western Officer Basin), Bitter Springs Formation (Amadeus Basin), and the Coominaree Dolomite/Younghusband Conglomerate (northern Adelaide Rift Complex); and 2) at ~760 Ma, between the Kanpa Formation (western Officer Basin) and upper Burra Group (northern Adelaide Rift Complex).

New isotope data from GSWA Lancer 1 closely matches that from GSWA Empress 1A. A revised and more accurate correlation of Supersequence 1 is made here based on new strontium-isotope ratios from the upper Loves Creek Member of the Bitter Springs Formation (Gore et al., 2004) and the recent discovery of the acritarch *Cerebrosphaera buickii* in the 'Finke beds' (uppermost Supersequence 1 in Wallara 1; Sirgo Exploration Inc, 1990).

Carbon isotopes

Well-preserved carbonate carbon isotope ratios ($\delta^{13}C_{carb}$) are common in carbonate rocks, thereby allowing $\delta^{13}C$ stratigraphy to be used as correlation tools especially in poorly or unfossiliferous marine successions. Organic carbon isotope ratios ($\delta^{13}C_{org}$) are more susceptible to alteration, and $\delta^{13}C$ stratigraphy based on $\delta^{13}C_{org}$ values alone, will generally be unsuccessful. An exception to this rule was provided by Calver and Lindsay (1998) and

Calver (2000), who showed a consistent mostly $\delta^{13}C_{org}$ stratigraphy for Australian Ediacaran successions across several basins.

In this study, $\delta^{13}C_{org}$ values are important for assessing how well the carbon-isotope record is preserved, and for maintaining the continuity of the $\delta^{13}C$ stratigraphy where carbonate is absent or not well preserved. When organisms convert carbon dioxide (CO_2), mostly in the form of dissolved carbonate, to biomass they preferentially incorporate ^{12}C over ^{13}C. This produces organic matter that is 25–30‰ lighter compared to the Vienna Pee Dee Belemnite (VPDB) standard, than the precursor carbonate, depending on the type of carbon-assimilation pathway an organism uses. The isotopic difference between $\delta^{13}C_{carb}$ and $\delta^{13}C_{org}$ ($\Delta\delta^{13}C$) is remarkably constant throughout the Proterozoic and Phanerozoic (Des Marais, 2001), and its average value in a particular succession can be used to estimate $\delta^{13}C_{carb}$ from $\delta^{13}C_{org}$ values. If $\Delta\delta^{13}C$ values are outside the range of 25–30‰, then the organic-carbon signal is probably too altered for use in isotope stratigraphy. Such changes in $\delta^{13}C_{org}$ values are probably due to consumption by heterotrophic bacteria or thermal decomposition during burial, or both.

Strontium isotopes

The $^{87}Sr/^{86}Sr$ ratio of strontium (Sr) in marine carbonate and sulfate records large-scale crustal processes over geological time, and reflects the balance between Sr entering the oceans from mid-ocean-ridge volcanism ($^{87}Sr/^{86}Sr$ ~ 0.703) and continental weathering ($^{87}Sr/^{86}Sr$ ~ 0.710). There is a well-defined global $^{87}Sr/^{86}Sr$ seawater curve for the Neoproterozoic (Shields and Veizer, 2002) that shows that ratios at this time, if unaltered, should fall within the range 0.7057 – 0.7063.

Strontium-isotope ratios are highly susceptible to diagenetic alteration during which carbonates and sulfates inevitably recrystallize in the presence of detrital silicates, particularly clay minerals. Detrital silicates are high in ^{87}Rb, which decays to ^{87}Sr and produces higher $^{87}Sr/^{86}Sr$ ratios. Fortunately, this means that $^{87}Sr/^{86}Sr$ ratios always become heavier through diagenesis. Most carbonate facies contain clay minerals, thereby yielding few isotopic ratios (~15–20%) that can be used for stratigraphy.

Australian Supersequence 1 rocks have mostly yielded $^{87}Sr/^{86}Sr$ ratios greater than 0.7069, because the ubiquitous presence of dolomite rarely preserves pristine ratios. The exceptions are bedded sulfates in the Gillen Member of the Bitter Springs Formation (0.7057 – 0.7063, Fanning, 1986; reproduced in Hill et al., 2000a) and molar-tooth limestone in Unit 3 of the Loves Creek Member of the Bitter Springs Formation (0.7063 – 0.7065, Gore et al., 2004).

Lancer 1 has relatively abundant anhydrite as thin beds and nodules. Five of these nodules were analyzed for their $^{87}Sr/^{86}Sr$ ratios. Five $^{87}Sr/^{86}Sr$ ratios were determined on sulfate nodules in Empress 1A, the lowest ratio being 0.7069, which is too high to be used for correlation.

Oxygen isotopes

In Proterozoic isotope stratigraphy $\delta^{18}O_{carb}$ values, which are simultaneously acquired with $\delta^{13}C_{carb}$ values at no extra cost, are used as indicators of post-depositional alteration of $\delta^{13}C_{carb}$ values. During burial, carbonates can mix with meteoric water ($\delta^{18}O < -5‰$) during recrystallization, thereby depleting primary $\delta^{18}O_{carb}$ values, which are usually close to 0‰ in modern carbonates. A positively co-varying trend is common in Proterozoic carbonates and indicates some, albeit minimal, alteration of primary $\delta^{13}C_{carb}$ values during diagenesis and burial. There is, however, evidence that near primary $\delta^{18}O_{carb}$ values are retained in Proterozoic carbonates, for example, in parts of the Bitter Springs Formation (Hill et al., 2000a). Heavy $\delta^{18}O_{carb}$ values in Supersequence 1 of Empress 1A (-5 to +5‰) suggest good retention of primary values in what was an evaporative or saline setting as indicated by the abundance of halite.

Methods

The analytical strategy for Lancer 1 is comparable to that for Empress 1A — 53 carbon-isotope ratios were determined for Lancer 1 versus 52 for Empress 1A over similar stratigraphic thicknesses (998 m in Lancer 1, and 986 m in Empress 1A), with an average sampling interval of 19 m. Five $^{87}Sr/^{86}Sr$ ratios were determined from nodular anhydrite for each drillhole. Twelve thin sections were prepared from a representative selection of carbonates in Lancer 1 to determine how well fabrics are preserved, and in turn whether isotopic ratios are altered.

Carbon and oxygen isotope analyses were completed in the laboratories of Environmental Isotopes Pty Ltd, Sydney. For carbonate-isotope analyses, 10–25 mg of powder was drilled from carbonate facies, which have not been significantly altered by recrystallization or veins. The powders were reacted in individual evacuated carbonate reaction vessels with 103‰ phosphoric acid at 25ºC for at least 4 hours. After reaction was complete the CO_2 produced was analyzed using a Finnigan MAT 252 mass spectrometer in dual inlet mode against an internal gas standard. The gas standard has been calibrated against a carbonate standard (NBS19: $\delta^{13}C$ = -1.95‰ VPDB and $\delta^{18}O$ = -2.2‰ VPDB). Samples were demineralized and the residues subjected to $\delta^{13}C_{org}$ analysis using an elemental analyzer – isotope ratio mass spectrometer (Europa Roboprep on a Finnigan MAT 252). All carbon- and oxygen-isotope ratios have a precision of ± 0.2‰.

The $^{87}Sr/^{86}Sr$ ratios were completed in the CSIRO Division of Exploration and Mining, North Ryde, Sydney. The sulfate powders were dissolved in 0.5 M acetic acid, the Sr separated on cation exchange columns, and the $^{87}Sr/^{86}Sr$ ratios determined on a VG354E thermal ionization mass spectrometer against a NBS987 standard ratio of 0.710279.

Results

All isotopic results for Lancer 1 are shown in Table 1. Ten carbon-isotope ratios were measured in the Browne

Table 1. Lancer 1 isotopic data

GSWA #	Depth (m)	Formation	$\delta^{13}C_{carb}$ ‰ (VDPB)	$\delta^{18}O_{carb}$ ‰ (VDPB)	$\delta^{13}C_{org}$ ‰ (VDPB)	$\Delta\delta^{13}C$ ‰ (VDPB)	$^{87}Sr/^{86}Sr$
193624	468.78	Kanpa	0.30	0.49	-30.79	31.09	–
193627	487.11	Kanpa	8.38	2.39	–	–	–
193632	505.73	Kanpa	5.73	2.78	–	–	–
193635	509.02	Kanpa	5.72	1.89	–	–	–
193638	526.40	Kanpa	5.86	0.62	-26.27	32.13	–
193652	576.98	Kanpa	4.79	1.19	-24.92	29.71	–
193654	589.59	Kanpa	5.26	0.58	–	–	–
193657	609.44	Kanpa	**3.39**	–	-25.32	–	–
193660	621.80	Kanpa	**5.49**	–	-23.22	–	–
193640	644.32	Kanpa	**3.99**	–	-24.72	–	–
193643	665.32	Kanpa	**0.08**	–	-28.63	–	–
193647	681.10	Kanpa	**3.37**	–	-25.34	–	–
193651	707.41	Kanpa	**4.67**	–	-24.04	–	–
193662	762.75	Hussar	4.06	1.14	–	–	–
193664	767.21	Hussar	4.27	-0.01	–	–	–
193665	796.63	Hussar	4.67	0.92	–	–	–
193669	809.19	Hussar	4.58	0.61	–	–	–
193670	859.58	Hussar	**4.4**	–	-24.31	–	–
193671	865.50	Hussar	**4.6**	–	-24.11	–	–
193672	877.28	Hussar	-0.11	-6.82	–	–	–
193673	891.04	Hussar	**4.64**	–	-24.07	–	–
193675	903.81	Hussar	-2.77	-2.22	–	–	0.707671 ± 0.0012
193680	922.74	Hussar	-2.34	-3.63	-28.03	25.69	–
193683	931.44	Hussar	-3.04	-2.81	-32.57	29.53	–
193689	943.93	Hussar	-2.57	-3.60	-31.56	28.99	–
193694	958.81	Hussar	-2.05	-3.86	-26.62	24.57	0.709245 ± 0.0015
193696	965.82	Hussar	-1.06	-3.08	-28.03	26.97	0.709336 ± 0.0014
193698	972.26	Hussar	**-0.63**	–	-29.34	–	–
193699	988.54	Hussar	**3.03**	–	-25.68	–	–
181801	1 001.08	Hussar	5.23	1.02	–	–	–
181804	1 010.07	Hussar	6.15	-3.17	–	–	–
181806	1 030.62	Hussar	4.08	-2.66	–	–	–
181809	1 044.92	Hussar	2.48	-1.83	-25.73	28.21	–
181812	1 059.40	Hussar	**4.07**	–	-24.64	–	–
181814	1 065.00	Hussar	3.64	-2.42	–	–	–
181816	1 073.76	Hussar	3.04	-2.03	–	–	–
181822	1 095.69	Hussar	3.86	-0.72	-24.13	27.99	–
181824	1 103.09	Hussar	–	–	–	–	0.710079 ± 0.0015
181827	1 113.03	Hussar	4.59	-1.33	–	–	–
181833	1 135.29	Hussar	4.77	-3.70	-24.89	29.66	–
181835	1 155.08	Hussar	6.25	-3.01	-24.67	30.92	–
181836	1 166.71	Hussar	6.18	1.13	–	–	–
181837	1 175.30	Hussar	6.27	-1.32	–	–	–
181838	1 195.03	Hussar	6.29	-0.99	–	–	–
181841	1 323.50	Browne	-1.33	-1.48	–	–	–
181844	1 335.07	Browne	-3.60	-3.72	–	–	–
181848	1 348.35	Browne	-1.92	-3.63	–	–	–
181850	1 356.77	Browne	6.49	-2.12	–	–	–
181852	1 369.84	Browne	5.20	-3.68	–	–	–
181854	1 394.48	Browne	-1.44	-3.99	–	–	–
181858	1 414.87	Browne	-3.27	-4.10	–	–	–
181864	1 456.80	Browne	-0.56	-3.64	–	–	–
181866	1 466.49	Browne	0.70	--3.29	-27.08	27.78	–
181869	1 477.99	Browne	1.95	--0.48	–	–	–
181870	1 478.84	Browne	–	–	–	–	0.707039 ± 0.0007

NOTES: $\delta^{13}C_{carb}$ ratios in bold are predicted from $\delta^{13}C_{org}$ ratios (see text for details)
VDPB: Vienna Peedee belemnite standard

Table 2. Empress 1A isotopic data

GSWA #	*Depth (m)*	*Formation*	$\delta^{13}C_{carb}$ ‰ (VDPB)	$\delta^{18}O_{carb}$ ‰ (VDPB)	$\delta^{13}C_{org}$ ‰ (VDPB)	$\Delta\delta^{13}C$ ‰ (VDPB)
E7	527.50	Kanpa	4.93	3.52	-26.67	31.6
E9	540.50	Kanpa	5.33	3.53	–	–
E10	554.90	Kanpa	**3.92**	–	-26.68	–
E12	579.80	Kanpa	5.01	4.90	–	–
E13	589.80	Kanpa	0.25	3.64	-32.58	32.83
E14	608.80	Kanpa	**-0.58**	–	-31.38	–
E15	619.40	Kanpa	1.38	-0.84	–	–
E17	629.30	Kanpa	3.83	4.29	-29.95	33.78
E19	644.90	Kanpa	3.32	3.89	–	–
E20	651.20	Kanpa	4.35	3.61	-27.29	31.64
E21	665.80	Kanpa	0.14	1.57	–	–
E22	685.60	Kanpa	6.82	1.83	–	–
E23	690.40	Kanpa	7.15	1.54	-25.36	32.51
E24	703.20	Kanpa	**0.85**	–	-29.95	–
E26	718.20	Kanpa	7.25	2.82	–	–
E27	734.40	Kanpa	7.72	1.76	-26.62	34.34
E30	753.80	Kanpa	8.09	1.23	-23.86	31.95
E32	762.40	Kanpa	8.01	1.85	–	–
E35	773.20	Kanpa	5.45	3.52	-24.25	29.7
E36	782.50	Kanpa	5.21	1.15	–	–
E37	800.10	Kanpa	**3.86**	–	-26.94	–
E38	815.50	Kanpa	**5.71**	–	-25.09	–
E39	830.10	Kanpa	**7.21**	–	-23.59	–
E41	843.70	Kanpa	**2.83**	–	-27.97	–
E42	880.00	Hussar	**7.81**	–	-22.99	–
E43	888.65	Hussar	**6.05**	–	-24.75	–
E44	941.20	Hussar	4.47	-1.33	–	–
E45	953.20	Hussar	4.31	-1.07	–	–
E46	965.50	Hussar	4.62	-0.05	–	–
E47	979.90	Hussar	**4.84**	–	-25.96	–
E48	985.50	Hussar	**2.23**	–	-28.57	–
E49	1037.50	Hussar	**0.99**	–	-29.81	–
E50	1067.1	Hussar	-0.05	-6.42	–	–
E55	1077.50	Hussar	0.29	-3.86	-30.02	30.31
E58	1109.50	Hussar	6.11	-1.22	–	–
E60	1137.30	Hussar	3.25	-2.67	–	–
E61	1146.40	Hussar	2.59	-1.19	–	–
E63	1165.80	Hussar	3.60	-2.36	-29.74	33.34
E65	1180.60	Hussar	4.19	-3.62	–	–
E66	1203.60	Hussar	4.67	-3.55	-29.23	33.9
E68	1226.35	Hussar	**1.41**	–	-29.39	–
E69	1236.90	Hussar	**0.21**	–	-30.59	–
E70	1247.20	Hussar	5.26	-3.92	–	–
E71	1297.70	Browne	6.35	-3.05	–	–
E74	1369.40	Browne	-2.33	-2.60	-25.77	23.44
E76	1380.90	Browne	-0.76	-3.80	–	–
E77	1383.00	Browne	-0.46	-3.67	–	–
E78	1395.05	Browne	**7.03**	–	-23.77	–
E80	1402.50	Browne	6.10	-1.46	–	–
E81	1492.20	Browne	-0.06	-6.04	-27.52	27.46
E82	1504.00	Browne	1.53	-4.59	–	–
E84	1513.40	Browne	2.51	0.10	-21.82	24.33

NOTES: $\delta^{13}C_{carb}$ ratios in bold are predicted from $\delta^{13}C_{org}$ ratios (see text for details)
VDPB: Vienna Peedee belemnite standard

Formation, 30 in the Hussar Formation, and 13 in the Kanpa Formation. These three formations are included within the Buldya Group (Haines et al., 2004 and Grey et al., 2005). Also included are isotopic results from the Buldya Group in Empress 1A (Table 2), which have been updated to include predicted $\delta^{13}C_{carb}$ values based on $\delta^{13}C_{org}$ ratios. Predicted $\delta^{13}C_{carb}$ values in both tables are shown in bold. In Lancer 1, the average $\Delta\delta^{13}C$ (n=11, excluding outliers of 32.13 and 24.57) is 28.78 ± 1.64‰ (= standard deviation). These results indicate $\delta^{13}C$ values are well preserved. This is consistent with the organic geochemistry results, which indicate that the Neoproterozoic section in Lancer 1 is within the oil-generative window (Haines et al., 2004). In Empress 1A, the average $\Delta\delta^{13}C$ (n=15) is 30.80 ± 3.46‰. Total organic carbon (TOC) values were not measured in this study, but 20 mudstones from the Browne, Hussar, and Kanpa Formations in Lancer 1 had an average TOC of 0.16% and a maximum value of 0.70% (Haines et al., 2004). Therefore TOC values are expected to be low (<1%) in the samples reported herein.

Lancer 1 $^{87}Sr/^{86}Sr$ ratios are too high to be used for correlative purposes, as is the case with Empress 1A for which the lowest $^{87}Sr/^{86}Sr$ ratio is 0.7069. Oxygen-isotope ratios ($\delta^{18}O_{carb}$) show apparent correlation with $\delta^{13}C_{carb}$ ratios (Fig. 1), but the weak correlation coefficient (R^2=0.375) indicates that $\delta^{13}C_{carb}$ ratios are not altered significantly. All dolomites in Lancer 1 are highly enriched in ^{18}O ($\delta^{18}O_{carb}$ range = -4.10 to +2.78‰), as they are in Empress 1A (-6.10 to +4.90‰). These results suggest that depositional conditions were probably evaporitic, and that meteoric waters remained evaporitic during dolomite recrystallization. Dolomites from the Kanpa Formation are more ^{18}O-enriched than for the Hussar or Browne Formations, which is reflected in the greater degree of fabric preservation including the small size of dolomite crystals (1–15 μm).

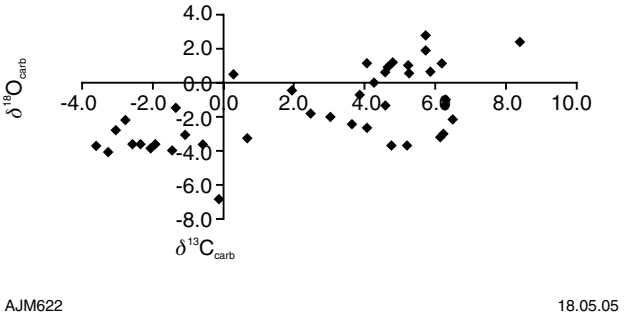

Figure 1. Plot of $\delta^{13}C_{carb}$ vs $\delta^{18}O_{carb}$ (in ‰VPDB)

Cryogenian (Supersequence 1) correlations of the western Officer Basin, Centralian Superbasin, and Adelaide Rift Complex

Drillhole and outcrop section locations in the Centralian Superbasin and Adelaide Rift Complex are shown in Figure 2. Lithostratigraphy, biostratigraphy, and isotope stratigraphy allow Cryogenian (Supersequence 1) correlations between the western Officer, Amadeus, and eastern Officer Basins, and the Adelaide Rift Complex (Fig. 3). Willouran age (Fig. 4) correlations incorporate the Browne Formation (western Officer Basin), Bitter Springs Formation (Amadeus Basin), Coominaree Dolomite (Peake and Denison Ranges, northern Adelaide Rift Complex), and Coominaree Dolomite correlative (eastern Officer Basin). Significant to this study is a close correlation between Lancer 1 and Empress 1A, which are 264 km apart in the western Officer Basin. The isotopic correlation is virtually identical to the lithological correlation between the drillholes, but is limited by the availability of suitable carbonate facies.

Torrensian age correlations are indicated for the Hussar, Kanpa, and Steptoe Formations (western Officer Basin), with the Bitter Springs Formation and 'Finke beds' (Amadeus Basin), and Kalachalpa Formation and 'unnamed transitional unit' (Peake and Denison Ranges, northern Adelaide Rift Complex). Torrensian successions in the central Adelaide Rift Complex (Hill and Walter, 2000, fig. 10) have been excluded because of renewed uncertainty in their stratigraphic position relative to the Sturtian glacial deposits. Sturtian glacial deposits unconformably overlie Supersequence 1 in the Amadeus Basin and Adelaide Rift Complex, but only the unconformity is seen in the western Officer Basin.

Ten correlation intervals (A–K, not including I) are identified from Lancer 1, Empress 1A, and other sections in the Centralian Superbasin and Adelaide Rift Complex:

A: In the western Officer Basin only, there is a close correlation based on $\delta^{13}C_{carb}$ values of ~2‰ in both Lancer 1 and Empress 1A, in well-preserved dolomitic facies just above the base of the unconformity separating basement rocks from Supersequence 1. Between point A and B in Lancer 1, $\delta^{13}C_{carb}$ values decrease to -3.27‰, but at this stratigraphic level in Empress 1A there is a 90 m thick mudstone- and halite-bearing interval without suitable carbonate lithologies. Over this gap, $\delta^{13}C_{carb}$ values change from -6.04‰ at 1492 m and +6.10‰ at 1402 m, hindering correlation of this part of the Browne Formation.

B: This is a strong correlation point between the mid-Browne Formation in the western Officer Basin and the Bitter Springs Formation in the Amadeus Basin, at the contact between the Loves Creek Member and Gillen Member. $\delta^{13}C_{carb}$ values approximate +6‰ and immediately precede the appearance of the *Acaciella australica* Stromatolite Assemblage. In Lancer 1 and Empress 1A the lithology and $\delta^{13}C$ values are very similar.

C: The co-occurrence of $\delta^{13}C_{carb}$ values between -4‰ and -1‰ and the *Acaciella australica* Stromatolite

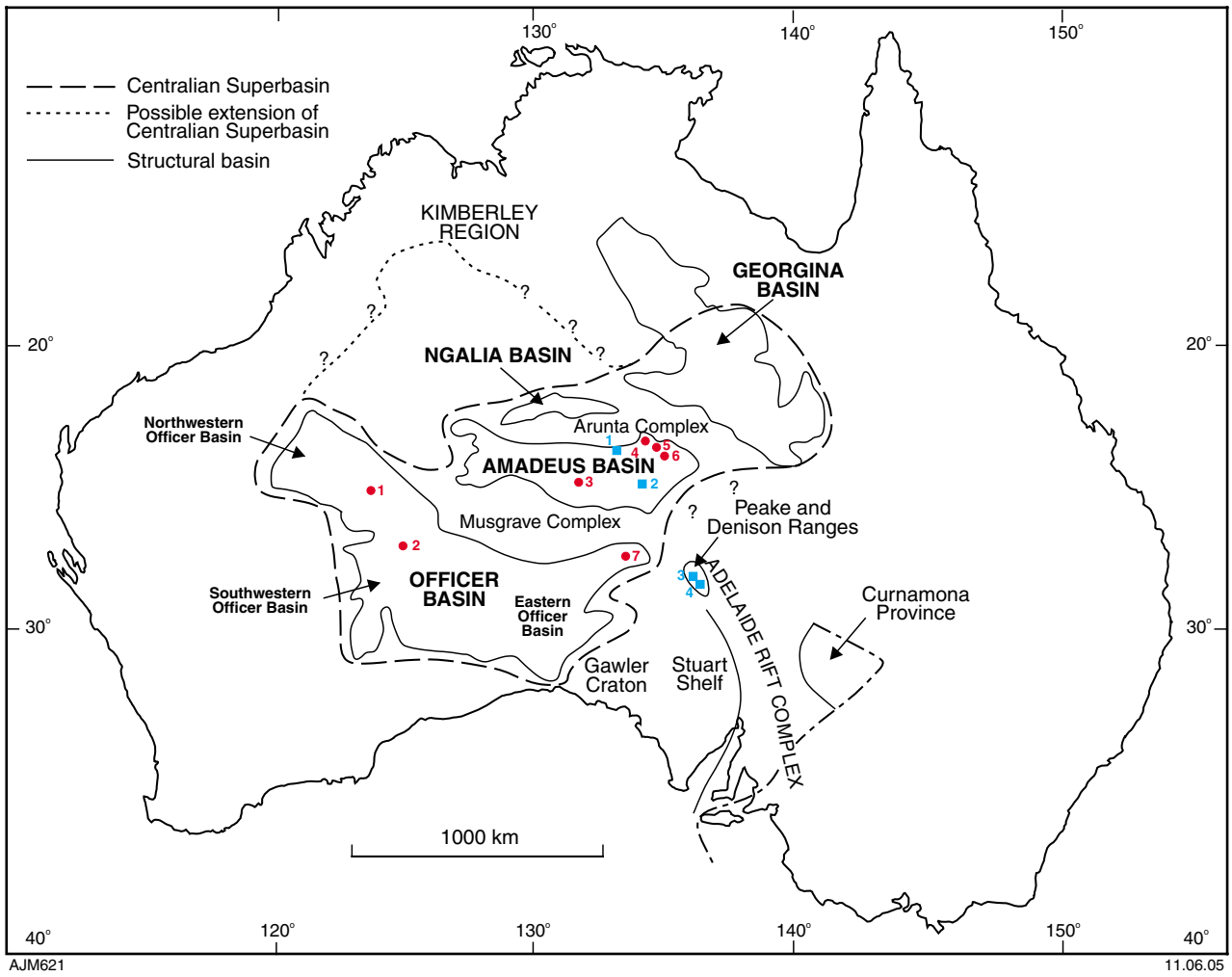

Figure 2. Drillhole and outcrop section locations in the Neoproterozoic Centralian Superbasin and Adelaide Rift Complex

Assemblage forms a strong correlation point between the Officer and Amadeus Basins, and the northern Adelaide Rift Complex. This is supported by a similar dolomite lithology in the Woolnough Member of the Browne Formation (western Officer Basin), Loves Creek Member (Units 2 and 3) of the Bitter Springs Formation (Amadeus Basin), Coominaree Dolomite (northern Adelaide Rift Complex), and Coominaree Dolomite correlative in Manya 5 (eastern Officer Basin). Preiss (1993) identified stromatolites in the Coominaree Dolomite and Coominaree Dolomite correlative as *Acaciella* form indeterminate (f. indet.). He also indicated that both formations are overlain by volcanic units, which are probable correlatives. Further details of the correlation of the eastern Officer Basin and Adelaide Rift Complex are presented in Hill and Walter (2000).

Within the *Acaciella australica* Stromatolite Assemblage there is a large positive $\delta^{13}C_{carb}$ excursion in the lower part of Unit 2 of the Loves Creek Member (Bitter Springs Formation, Amadeus Basin) in Wallara 1 and in outcrop near Bluebush Dam (Fig. 3). There is a possible correlation with the eastern Officer Basin (Hill and Walter, 2000, fig. 10) but not the western Officer Basin. The co-occurrence of similar $\delta^{13}C_{carb}$ values with the non-marine 'redbed' facies suggests this part of the succession cannot be included in basin-wide correlations as discussed in Hill and Walter (2000).

D: In the western Officer Basin there is a close lithological and isotopic correlation between the lower Hussar Formation in Lancer 1 and Empress 1A. There are, however, two anomalous $\delta^{13}C_{org}$ values in Empress 1A,

corrected to $\delta^{13}C_{carb}$ values of +0.21‰ and +1.41‰. If these two $\delta^{13}C_{carb}$ values were from well-preserved dolomite, it would be pertinent to alter this correlation tie point, but there are clear $\delta^{13}C_{carb}$ trends in both Lancer 1 (starting at +6.29‰, decreasing to +2.48‰, then increasing to +6.15‰) and Empress 1A (starting at +6.35‰, decreasing to +2.59‰, then increasing to +6.11‰) that strongly suggest the $\delta^{13}C_{org}$ values in Empress 1A are anomalous.

E: In Lancer 1 there is a cluster of $\delta^{13}C_{carb}$ values between -3 and -1‰, between 950 and 900 m, not seen in Empress 1A where the lowest $\delta^{13}C_{carb}$ value is -0.05‰. This represents a weak correlation. If carbonate was present at this stratigraphic level in Empress 1A it may have been possible to argue a strong correlation. A single $\delta^{13}C_{org}$ value of 0.99 ± 3.46‰ in Empress 1A cannot be relied upon to strengthen correlation. In contrast, dolomitic fabrics at this stratigraphic position in Lancer 1 are well-preserved, indicating near-primary carbon-isotope abundances and that the negative $\delta^{13}C_{carb}$ excursion is real. For the above reasons a correlation can only be made at $\delta^{13}C$ values of about 0‰.

F: There is a strong correlation between Lancer 1 and Empress 1A, and a weak correlation with the lower part of Unit 3 of the Loves Creek Member, Bitter Springs Formation, Amadeus Basin. In both drillholes of the western Officer Basin, a return to $\delta^{13}C$ values of about 4‰ at the base of the *Baicalia burra* Stromatolite Assemblage form the basis of correlation in the mid- to upper Hussar Formation. A $\delta^{13}C_{carb}$ value of -0.11‰ at 877 m in Lancer 1 is from grain-supported quartz sandstone with dolomite cement. The recrystallized nature of the dolospar (60–150 μm) matrix cement suggests the $\delta^{13}C_{carb}$ value is of diagenetic origin, and therefore cannot be used for $\delta^{13}C$ stratigraphy. The absence of carbonate in the upper Hussar and lower Kanpa Formations makes correlation difficult. Within the error bars of the corrected $\delta^{13}C_{org}$ values in both drillholes it is possible to make a weak correlation. A feature of the lower to mid-Kanpa Formation in both drillholes is an increase in $\delta^{13}C_{carb}$ values of about 5‰ prior to a positive excursion to a Supersequence 1 maximum of about 8‰.

Southgate (1991) and Hill et al. (2000a) identified sedimentary facies of Unit 3 in the Loves Creek Member as non-marine. However, $^{87}Sr/^{86}Sr$ ratios of 0.7063 – 0.7065 in molar-tooth limestone of Unit 3 indicate a marine origin for the carbonate facies, but not necessarily the 'redbed' facies (Gore et al., 2004). On this basis, $\delta^{13}C_{carb}$ values between +3 and +6‰ in Unit 3 correlate with similar values in the lower Kanpa Formation, just prior to the highest Supersequence 1 values of about +8‰ in the western Officer and Amadeus Basins and the northern Adelaide Rift Complex. Correlation with the Bitter Springs Formation is weakened by the absence of the *Baicalia burra* Stromatolite Assemblage and acritarch *Cerebrosphaera buickii*, which could be a function of the facies in Wallara 1. If, however, the correlation is correct, there is a hiatus in the Bitter Springs Formation between Units 2 and 3 of the Loves Creek Member spanning the deposition of the upper Browne Formation and lower Hussar Formation (i.e. the hiatus spans correlation intervals D and E).

G: A revision of the depositional environment of carbonate facies in Unit 3 of the Loves Creek Member (Gore et al., 2004) allows a correlation with the mid-Kanpa Formation of the western Officer Basin, and the 'unnamed transitional unit' of the northern Adelaide Rift Complex. It is based on the highest $\delta^{13}C_{carb}$ values in Supersequence 1 successions in Australia (+7 to +8.2‰) and other equivalent global successions, stromatolites, and palynology (Hill and Walter, 2000; Hill et al., 2000b). The stromatolite form *Baicalia burra* is widespread in the Burra Group of the Adelaide Rift Complex, and the distinctive Cryogenian index fossil *Cerebrosphaera buickii* is present in the Skillogalee Dolomite, which based on lithostratigraphy, is slightly older than the Kalachalpa Formation and 'unnamed transitional unit' of the northern Adelaide Rift Complex. Biostratigraphic correlation with the Amadeus Basin is weakened because no stromatolites of the *Baicalia burra* Stromatolite Assemblage are known, and *Cerebrosphaera buickii* first appears in the 'Finke beds', immediately below the Sturtian diamictite (Areyonga Formation) in Wallara 1 (Fig. 3).

H: Only in the western Officer Basin is there a large negative spike in $\delta^{13}C_{carb}$ values to about 0‰. In Lancer 1 this lies just below the unconformity at the top of Supersequence 1. In Empress 1A it is not possible to be certain whether the corrected $\delta^{13}C_{org}$ value of +0.85‰ at 703 m or the $\delta^{13}C_{carb}$ value of +0.14‰ at 666 m represents the $\delta^{13}C$ nadir. Taking into consideration the close agreement between formation boundaries and $\delta^{13}C$ stratigraphy in both Lancer 1 and Empress 1A, the latter interpretation is favoured. It is also consistent with Supersequence 1 being about 100 m thicker in Empress 1A, in which $\delta^{13}C_{carb}$ values return to about +4‰ in the Steptoe Formation.

J: A common feature of $\delta^{13}C_{carb}$ profiles in the western Officer and Amadeus Basins and the northern Adelaide Rift Complex is a large decrease in values from about +4‰ to between -2‰ and 0‰.

K: A return to $\delta^{13}C_{carb}$ values of between +4‰ and +5‰ just prior to the end of Supersequence 1 sedimentation is seen in all Australian Neoproterozoic basins, including the Black River Dolomite of the Togari Group in Tasmania (Calver, 1998). Within the Sturtian glacial deposits, $\delta^{13}C_{carb}$ values decrease to between -5‰ and -2‰ (Hill and Walter, 2000; Hoffman and Schrag, 2002).

Geochronology

The above correlations, which are only slightly different to those presented in Hill and Walter (2000), are summarized in Figure 4. These correlations imply that the Browne Formation was deposited before about 830 Ma, based on a U–Pb baddeleyite and zircon age of 827 ± 6 Ma for the Gairdner Dyke Swarm (Wingate et al., 1998).

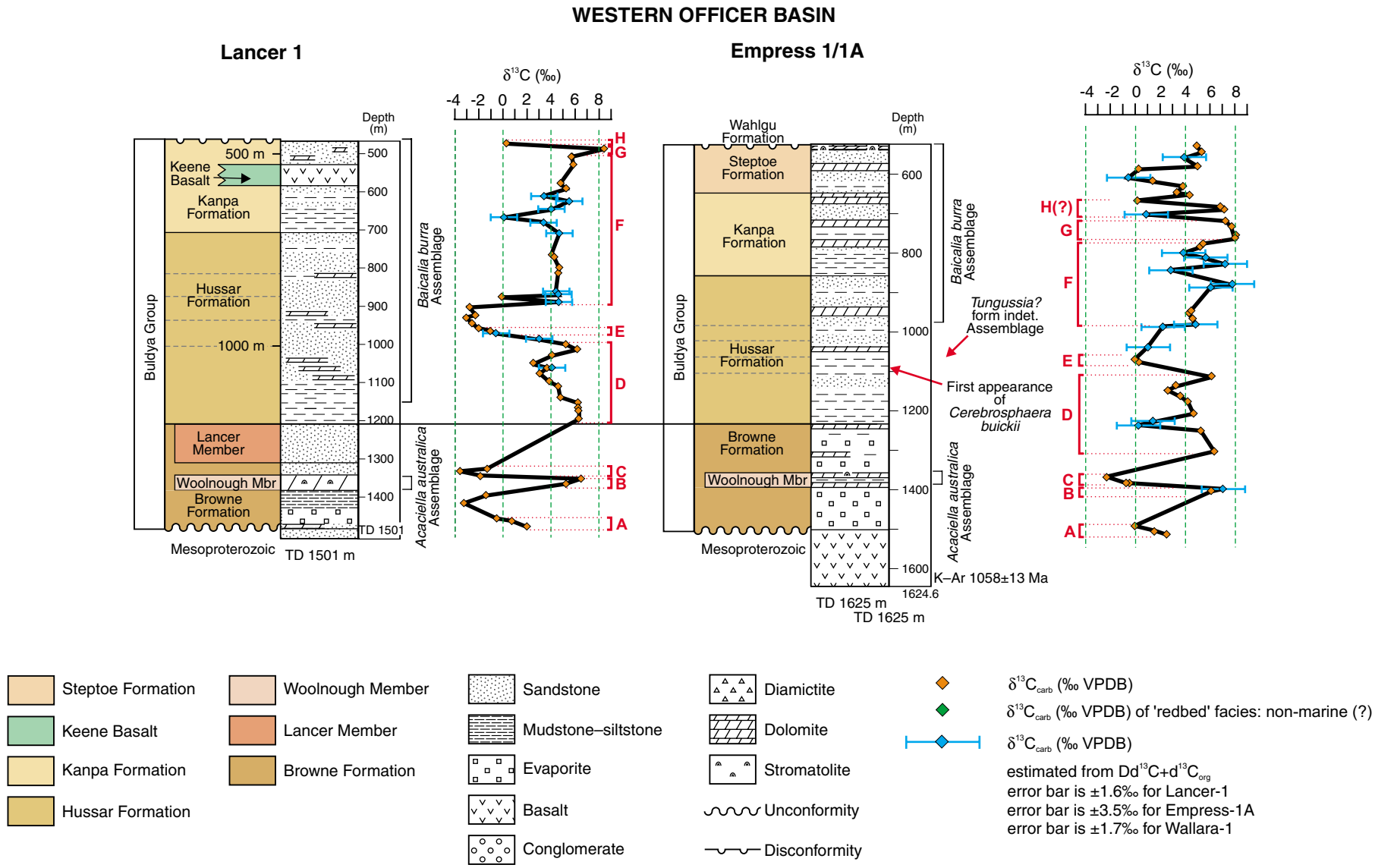

AJM623

18.05.05

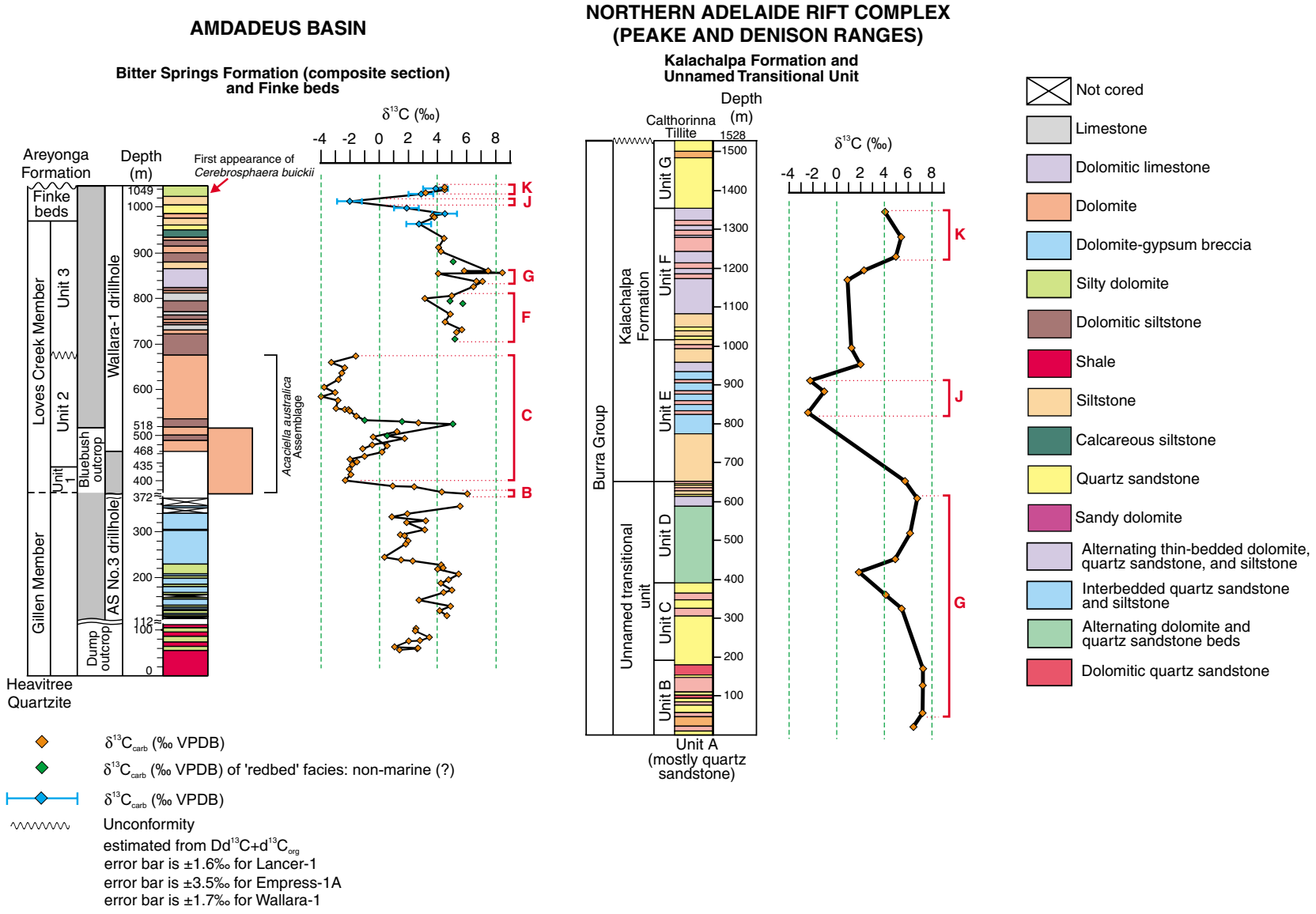

Figure 3. Carbon-isotope stratigraphy of Australian Cryogenian (Supersequence 1) successions, and correlations. Lancer 1 stratigraphy after Haines et al. (2004), Empress 1A stratigraphy after Stevens and Apak (1999), Bitter Springs Formation composite section after Hill et al. (2000), and Kalachalpa Formation and 'unnamed transitional unit' stratigraphy after Fairchild (1975)

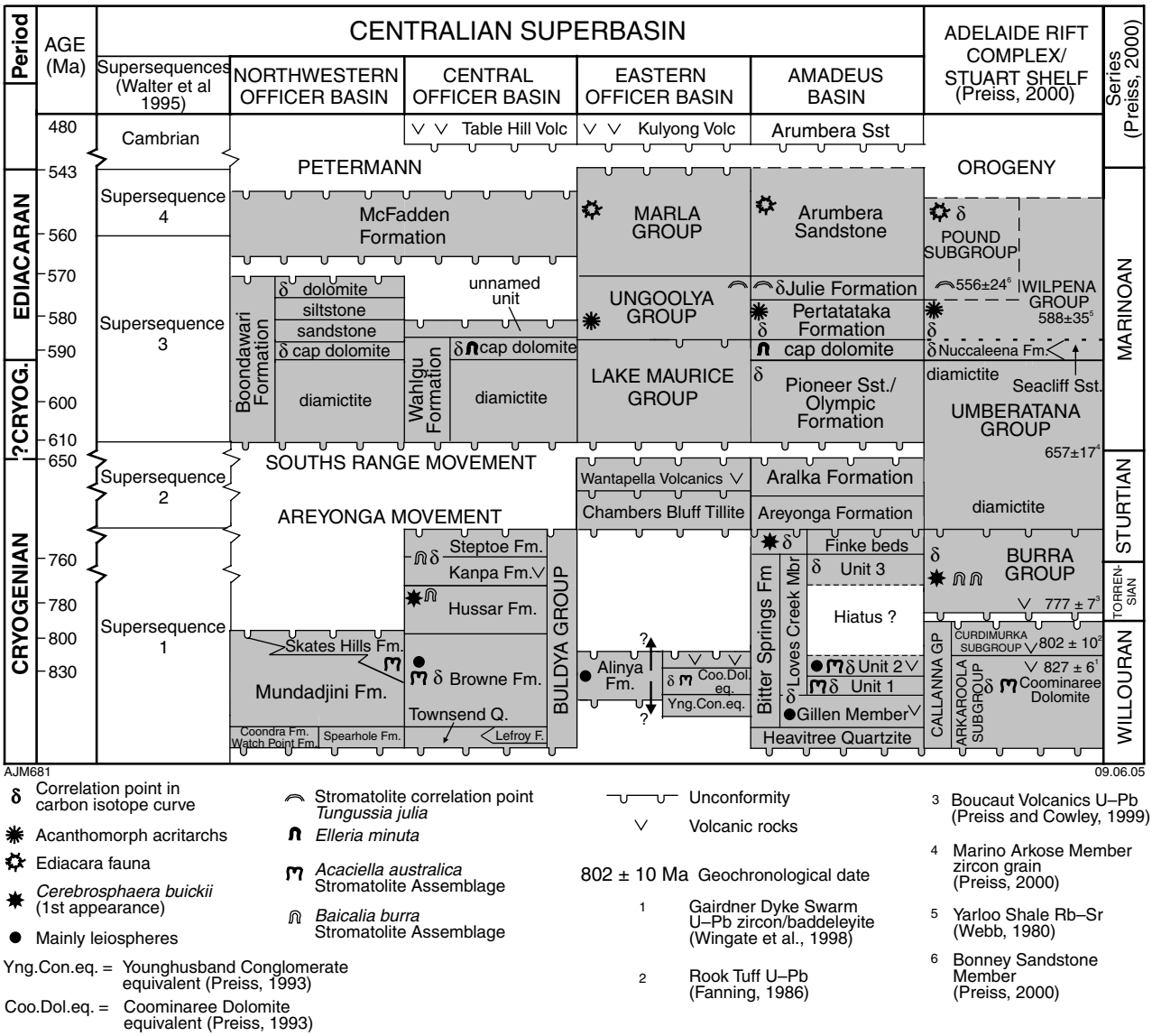

Figure 4. A revised Australian Neoproterozoic stratigraphy

The Gairdner Dyke Swarm was probably a feeder for the Wooltana Volcanics — a possible correlative of the Cadlareena Volcanics in the eastern Officer Basin (Preiss, 1993) — and volcanic rocks within the Bitter Springs Formation, based on strong similarities in geochemical and isotopic data (Wingate et al., 1998).

The global Cryogenian correlation scheme proposed by Hill and Walter (2000) is not changed by the new data from Lancer 1 and the ensuing re-interpretation of Australian correlations briefly mentioned above. A U–Pb zircon date of 777 ± 7 Ma from the Boucaut Volcanics (lowermost Burra Group) is consistent with a U–Pb zircon date of 758.5 ± 3.5 Ma from an ash bed in the Ombombo Subgroup of Namibia at the stratigraphic level of the Cryogenian $\delta^{13}C_{carb}$ high of about +8‰. Assuming regional and global correlations are correct, it is possible to postulate that the mid-Hussar and Kanpa Formations were deposited between about 780 Ma and 760 Ma.

Conclusions

On the basis of $\delta^{13}C$ stratigraphy, lithostratigraphy, stromatolite biostratigraphy, and acritarch palynology, it is possible to closely correlate the Buldya Group in Lancer 1 and Empress 1A, which lie 264 km apart in the western Officer Basin. The same techniques also allow correlation with the Amadeus Basin and Adelaide Rift Complex. Prior to about 830 Ma, a combination of $\delta^{13}C_{carb}$ values between -4‰ and -1‰ within the *Acaciella australica* Stromatolite Assemblage form the basis of correlation between the Browne Formation (western Officer Basin), mid-Bitter Springs Formation (Amadeus Basin), and the Coominaree Dolomite (Adelaide Rift Complex). In the Amadeus and western Officer Basins, the depleted $\delta^{13}C_{carb}$ values are immediately preceded by $\delta^{13}C_{carb}$ values of +6‰. Between approximately 780 Ma and 760 Ma, correlations can be made between the upper Hussar, Kanpa, and Steptoe Formations (western Officer Basin), with the upper Bitter Springs Formation and 'Finke beds' (Amadeus Basin),

and Kalachalpa Formation and 'unnamed transitional unit' (northern Adelaide Rift Complex), based on $\delta^{13}C_{carb}$ values, the *Baicalia burra* Stromatolite Assemblage, and the acritarch *Cerebrosphaera buickii*.

References

CALVER, C. R., 1998, Isotope stratigraphy of the Neoproterozoic Togari Group, Tasmania: Australian Journal of Earth Sciences, v. 45, p. 865–874.

CALVER, C. R., 2000, Isotope stratigraphy of the Ediacarian (Neoproterozoic III) of the Adelaide Rift Complex, South Australia, and the overprint of water column stratification: Precambrian Research, v. 100, p. 121–150.

CALVER, C. R., and LINDSAY, J. F., 1998, Ediacarian sequence and isotope stratigraphy of the Officer Basin, South Australia: Australian Journal of Earth Sciences, v. 45, p. 513–532.

DES MARAIS, D. J., 2001, Chapter 10: Isotopic evolution of the biogeochemical carbon cycle during the Precambrian, *in* Stable Isotope Geochemistry *edited by* J. W. VALLEY and D. R. COLE: Reviews in Mineralogy and Geochemistry, v. 43, Mineralogical Society of America, p. 555–578.

FAIRCHILD, T. R., 1975, The geological setting and palaeobiology of a late Precambrian stromatolitic microflora from South Australia: University of California, PhD thesis (unpublished).

FANNING, C. M., 1986, $^{87}Sr/^{86}Sr$ of gypsum/anhydrite and carbonate samples: Australian Mineral Development Laboratories Report G 6696/86 (unpublished).

FANNING, C. M., LUDWIG, K. R., FORBES, B. G., and PREISS, W. V., 1986, Single and multiple grain U–Pb zircon analyses for the early Adelaidean Rook Tuff, Willouran Ranges, South Australia: Geological Society of Australia, Abstracts, no. 15, p. 255–304.

GORE, A. P. K., SHIELDS, G. A., and HILL, A. C., 2004, A re-interpretation of marine versus non-marine environments in the Bitter Springs Formation of central Australia utilising the geochemistry of 'molar-tooth' structures: 17th Australian Geological Convention, 8–13 February 2004, Hobart, Tasmania, p. 232 (abstracts).

GREY, K., HOCKING, R. M., STEVENS, M. K., CARLSEN, G. M., BAGAS, L., IRIMIES, F., HAINES, P. W., and APAK, S. N., 2005, Lithostratigraphic nomenclature of the Officer Basin and correlative parts of the Paterson Orogen, Western Australia: Western Australia Geological Survey, Report 93.

HAINES, P. W., MORY, A. J., STEVENS, M. K., and GHORI, K. A. R., 2004, GSWA Lancer 1 well completion report (basic data), Officer and Gunbarrel Basins, Western Australia: Western Australia Geological Survey, Record 2004/10, 39p.

HILL, A. C., AROURI, K., GORJAN, P., and WALTER, M. R., 2000a, Geochemistry of marine and nonmarine environments of a Neoproterozoic cratonic carbonate/evaporite: the Bitter Springs Formation, Central Australia, *in* Carbonate Sedimentation and Diagenesis in the Evolving Precambrian World *edited by* J. P. GROTZINGER and N. P. JAMES: SEPM Special Publication no. 67, p. 327–344.

HILL, A. C., COTTER, K. L., and GREY, K., 2000b, Mid-Neoproterozoic biostratigraphy and isotope stratigraphy in Australia: Precambrian Research, v. 100, p. 281–298.

HILL, A. C., and WALTER, M. R., 2000, Mid-Neoproterozoic (~830–750 Ma isotope stratigraphy of Australia and global correlation: Precambrian Research, v. 100, p. 181–211.

HOFFMAN, P. F., and SCHRAG, D. P., 2002, The snowball Earth hypothesis: testing the limits of global change: Terra Nova, v. 14, p. 129–155.

KNOLL, A. H., WALTER, M. R., NARBONNE, G. M., and CHRISTIE-BLICK, N., 2004, A new period for the geologic time scale: Science, v. 305, p. 621–622.

PREISS, W. V., 1993, Neoproterozoic, *in* The Geology of South Australia, Volume 1, The Precambrian *edited by* J. F. DREXEL, W. V. PREISS, and A. J. PARKER: South Australian Geological Survey, Bulletin 54, p. 171–203.

PREISS, W. V., 2000, The Adelaide geosyncline of South Australia and its significance in Neoproterozoic continental reconstruction: Precambrian Research, v. 100, p. 21–63.

PREISS, W. V., and COWLEY, W. M., 1999, Genetic stratigraphy and revised lithostratigraphic classification of the Burra Group in the Adelaide Geosyncline: MESA Journal, v. 14, p. 30–40.

SHIELDS, G. A., and VEIZER, J., 2002, The Precambrian marine carbonate isotope database: version 1.1: Geochemistry, Geophysics, Geosystems, v. 3(6), DOI:10.1029/2001GC000266.

SIRGO EXPLORATION INC., 1990, Wallara No. 1 Well Completion Report: Northern Territory Geological Survey, Petroleum Report PR90/101B (unpublished).

SOUTHGATE, P. N., 1991, A sedimentological model for the Loves Creek Member of the Bitter Springs Formation, northern Amadeus Basin, *in* Geological and Geophysical Studies in the Amadeus Basin, central Australia *edited by* R. J. KORSCH and J. M. KENNARD: Australian Bureau of Mineral Resources, Geology and Geophysics, Bulletin 236, p. 113–126.

STEVENS, M. K., and APAK, S. N., (compilers), 1999, GSWA Empress 1 and 1A Well Completion Report, Yowalga Sub-basin, Officer Basin, Western Australia: Western Australia Geological Survey, Record 1999/4, 110p.

WALTER, M. R., VEEVERS, J. J., CALVER, C. R., GORJAN, P., and HILL, A. C., 2000, Dating the 830–544 Ma Neoproterozoic interval by isotopes of strontium, carbon (carbonate & organic), and sulfur (sulfate) in seawater: Precambrian Research, v. 100, p. 371–433.

WEBB, A. W., 1980, Geochronology of stratigraphically significant rocks from South Australia — Amdel Progress Report 30: South Australian Department of Mines and Energy, Report Book 80/6 (unpublished).

WINGATE, M. T. D., CAMPBELL, I. H., COMPSTON, W., and GIBSON, G. M., 1998, Ion microprobe U–Pb ages for Neoproterozoic basaltic magmatism in south-central Australia and implications for the breakup of Rodinia: Precambrian Research, v. 87, p. 135–159.

Preliminary palaeomagnetic results from GSWA Lancer 1, Officer Basin, Western Australia

by

S. A. Pisarevsky[1] and M. T. D. Wingate[1]
[1]School of Earth and Geographical Sciences, The University of Western Australia

Abstract

A total of 89 samples were analysed from 28 oriented intervals in the Neoproterozoic section of Lancer 1. The identical pole positions for the Browne Formation and the Mundine Well dykes on the Yilgarn Craton indicates no significant motion of Australia between deposition of the basal Browne Formation and intrusion of the Mundine Well dykes at 755 Ma. All inclination data indicate that Australia occupied low to moderate latitudes during the late Neoproterozoic to Cambrian.

Introduction

Samples from Lancer 1 for palaeomagnetic study were collected from intervals (called 'oriented intervals', or OI hereafter) for which azimuthal orientation could be determined using the Acoustic Scanner Composite Log (ASCL). The acoustic signatures of numerous fractures, pebbles, stromatolites, and cross-beds were matched with those features in the core to enable continuous intervals of core to be oriented. Once a piece of core was oriented, the core segments above and below it were pieced together until uncertainty arose as to a segment's orientation (due to core loss or a badly fractured section). A total of 89 samples were analysed from 28 OI. The magnetic properties and palaeomagnetic signatures varied strongly between different OI, and the results from each OI are described separately below (in descending order). Sampled intervals for each formation are listed in Table 1.

Palaeomagnetic results

Wahlgu Formation

Thirteen samples of red-brown diamictite and mudstone from five OI were studied. Thermal demagnetization isolated a highly dispersed, low-temperature, highly scattered component and a medium- to high-temperature component directed shallowly to the southwest. An example of thermal demagnetization is shown in Figure 1a. The high-temperature component is also dispersed (Fig. 2a) both within core and between cores, which is typical of diamictite. There is no apparent correlation between OI and palaeomagnetic direction (Fig. 2a). However, the mean direction is likely to represent an approximation of the palaeomagnetic field direction at the time of deposition (Table 1).

Keene Basalt

This part of the core contains numerous fractures in different orientations, making their signatures difficult to identify in the ASCL. Twelve samples were measured from four OI, although the palaeomagnetic results suggest that at least three (possibly all four) OI are incorrectly oriented in azimuth. All samples yield identical single-component stable magnetizations that have high coercivities and unblocking temperatures distributed between 570 and 700ºC (Fig. 1b). Thermal and alternating field (AF) demagnetization yielded similar results. Remanence declinations are similar within each OI, but vary between OI (Fig. 2b); the inclinations of all OI, however, are identical (~32º, which corresponds to a palaeolatitude of ~18°). Only a single magnetic polarity is present. Analysis of Curie temperatures (Fig. 3) indicates the dominance of almost pure magnetite, although thermal demagnetization curves (Fig. 1b) show that hematite is also present. A portion of the magnetite is oxidized to hematite during demagnetization at temperatures above 500ºC (Figs 3 and 4b).

Table 1. First palaeomagnetic data from Lancer 1

Formation	*Sampled depth interval (m)*	*N*	*n*	*D (º)*	*I (º)*	*k*	α_{95} *(º)*	*Plat (º)*	*Plong (º)*	*Dp (º)*	*Dm (º)*	*Polarity[(a)]*
Wahlgu	428.99 – 461.49	13	40	216.0	-14.5	2.7	31.5	42.3	175.7	16.5	32.3	Mixed
Keene	530.44 – 574.94	12	30	–	32.4	–	–	–	–	–	–	Reverse
Kanpa	702.41 – 705.85	5	9	176.9	28.7	20.0	17.5	79.8	106.6	10.6	19.2	Mixed
Hussar, group 1	811.92 – 885.20	6	6	168.8	4.9	4.9	33.6	65.0	96.5	16.9	33.7	Mixed
Hussar, group 2	836.12 – 836.78	3	3	–	36.2	–	–	–	–	–	–	Reverse
Browne	1 342.25 – 1 474.64	14	27	193.4	-33.8	26.5	7.9	44.5	141.7	5.1	9	Reverse
?Cornelia	1 494.48 – 1 495.25	2	6	219.6	45.5	41.6	10.5	54.5	225.7	8.5	13.4	Reverse

NOTES: N: number of samples
n: number of specimens studied
D, I: declination and inclination of stable remanence
k: Fisher's precision parameter
α_{95}(º): the semi-angle of the 95% cone of confidence
Plat: latitude of the palaeopole
Plong: longitude of the palaeopole
Dp, Dm: the semi-axes of the cone of confidence about the pole at the 95% probability level
(a) north declination is assumed to be north polarity

Kanpa Formation, bottom

Six samples of red mudstone and sandstone were collected from a single continuous OI, the orientation of which was verified by independent features at both ends. Four samples yielded internally consistent, stable remanence directions with unblocking temperatures between 500 and 630ºC (Fig. 1c). A sample from the middle of the OI exhibits north-northwest-up directions, whereas samples from above and below yield south-down directions (Fig. 2c), indicating that at least two polarity reversals occurred during deposition of this interval. Magnetic susceptibility did not change significantly during thermal treatment, except for a brief increase between 500 and 600ºC (Fig. 4a, red curve) that was not associated with any change in remanence direction (Fig. 1c). This part of the drillcore appears very suitable for palaeomagnetic study, and data from additional samples will improve the reliability of the result (Table 1).

Hussar Formation

Forty-two samples of pink and red sandstone and mudstone were collected from 15 OI. Unfortunately, most of the sandstone samples are magnetically unstable, and only a few samples (mostly mudstone) yielded stable remanences carried mainly by hematite (Fig. 1d). Well-grouped palaeomagnetic directions were isolated from 836.12 – 836.78 m (green symbols in Fig. 2d, group 2 in Table 1). However, this sample may be incorrectly oriented, and hence only the inclination of 36º (which corresponds to a palaeolatitude of 20°) is useful. The remaining directions from this OI (group 1 in Table 1) are highly dispersed and bipolar (north-up and south-down). Data from additional samples of the red mudstones are necessary to verify this result.

Browne Formation

Fourteen samples of red mudstone, siltstone, and sandstone were collected from two OI. Thermal demagnetization revealed a stable, high-temperature, unipolar remanence component in all samples (Fig. 1e). The remanence directions are highly consistent within and between samples, and between OI (Fig. 2e). The palaeomagnetic (Fig. 1e) and rock-magnetic (Fig. 4a, blue curve) characteristics of these rocks are very similar to those reported for Browne Formation samples from the Empress 1A drillcore (Pisarevsky et al., 2001). The corresponding palaeomagnetic pole (Table 1) is considered to be reliable and to have been acquired during deposition.

?Cornelia Formation

Two samples of grey quartzite were collected from a single OI. These rocks yielded a stable remanence that was isolated by thermal demagnetization between 200 and 500ºC. The remanence direction differs significantly from that observed in samples of Browne Formation. Heating above 500ºC causes changes in magnetic minerals, including production of magnetite (from ?siderite) and associated random directions (Fig. 1f). Because only two samples were measured, the statistics are calculated at specimen level (Fig. 2f, Table 1).

Comparison with previous palaeomagnetic results

Palaeopoles from this study are illustrated in Figure 5, together with late Neoproterozoic to Cambrian palaeopoles for Australia extracted from the Global Palaeomagnetic Database (Pisarevsky and McElhinny, 2003). The previous data include a high-quality pole for the 755 Ma Mundine Well dykes (Wingate and Giddings, 2000) and a revised Apparent Polar Wander (APW) path for Australia (Pisarevsky et al., 2003) that incorporates poles for the 1075 Ma Warakurna Large Igneous Province (Wingate, 2002, 2003; Wingate et al., 2002, 2004) and the 1212 Ma Fraser dykes (Pisarevsky et al., 2003). The large ovals of 95% confidence (which can be improved by additional sampling) and the lack of Australian palaeopoles between 1070 and 755 Ma make it difficult to use palaeomagnetic pole positions to date the studied rocks precisely. However, two important conclusions can be made at this stage:

a) Wahlgu Formation, 181791-2
(451.05 – 451.23 m)

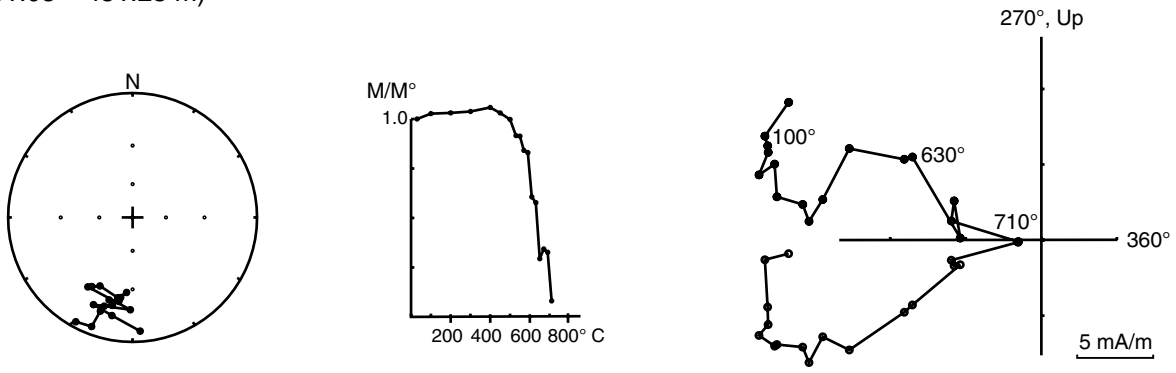

b) Keene Basalt, 193549-1
(530.44 – 530.55 m)

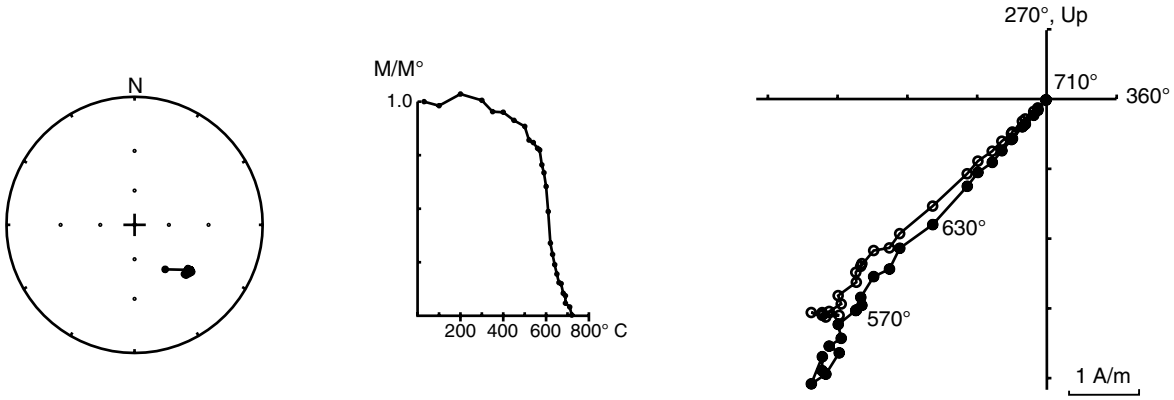

c) Kanpa Formation, 155426-1
(705.74 – 705.85 m)

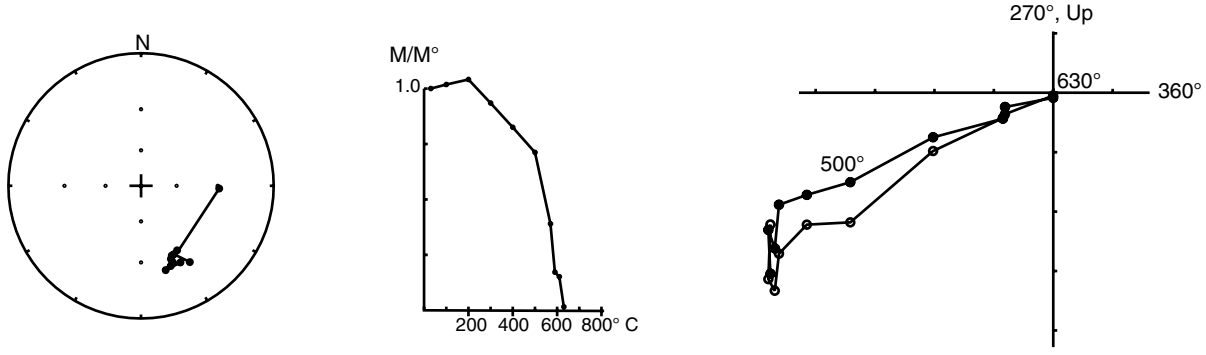

AJM612 18.05.05

Figure 1. Examples of thermal demagnetization of samples from Lancer 1. Orthogonal plots show trajectories of magnetization vector endpoints during demagnetization; open and closed symbols refer to the vertical and horizontal plane respectively. Curves show changes in remanence intensity during demagnetization. Stereoplots show upward- and downward-pointing palaeomagnetic directions with open and closed symbols respectively

d) Hussar Formation, 181896-1
(836.21 – 836.12 m)

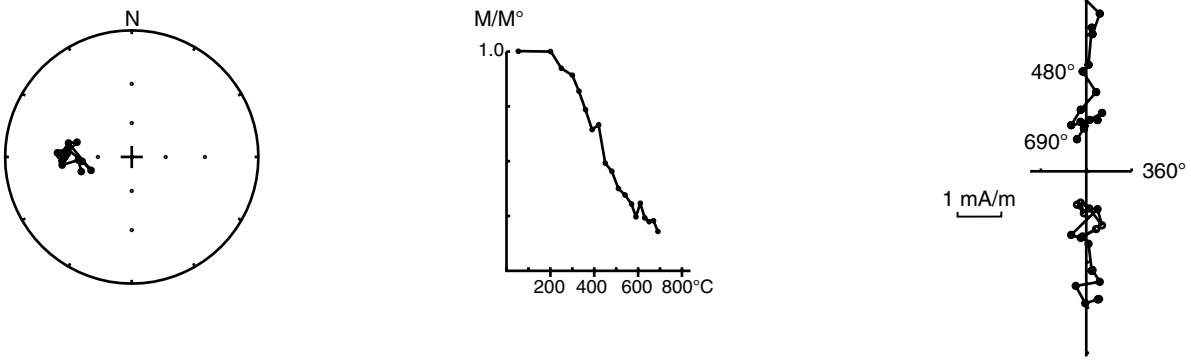

e) Browne Formation, 193539-2
(1356.48 – 1356.58 m)

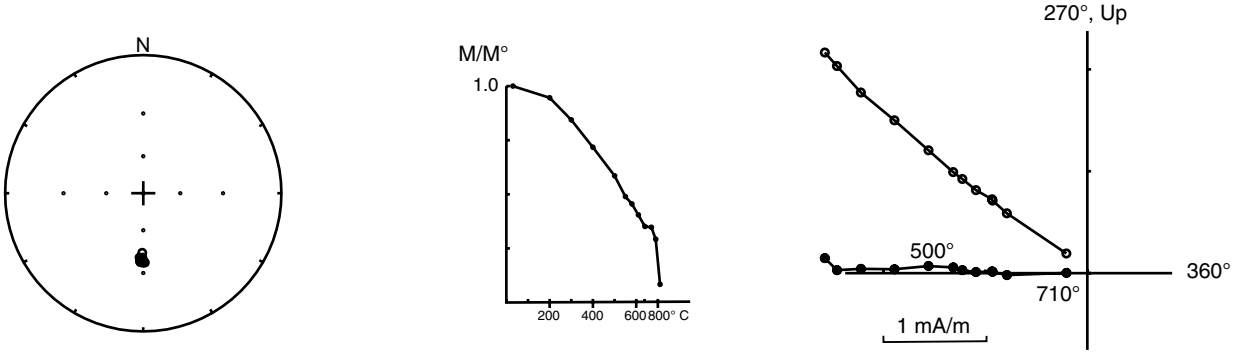

f) ?Cornelia Sandstone, 193531-1
(1495.06 – 1495.25 m)

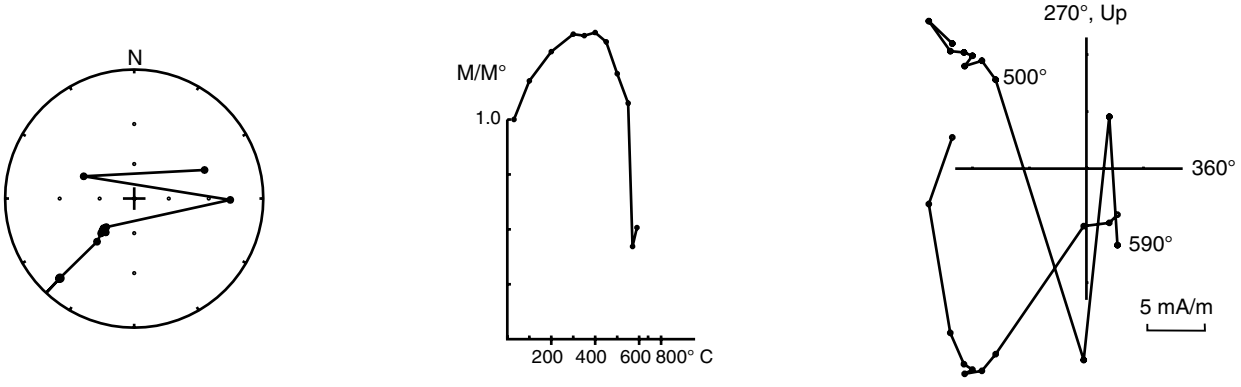

AJM613 18.05.05

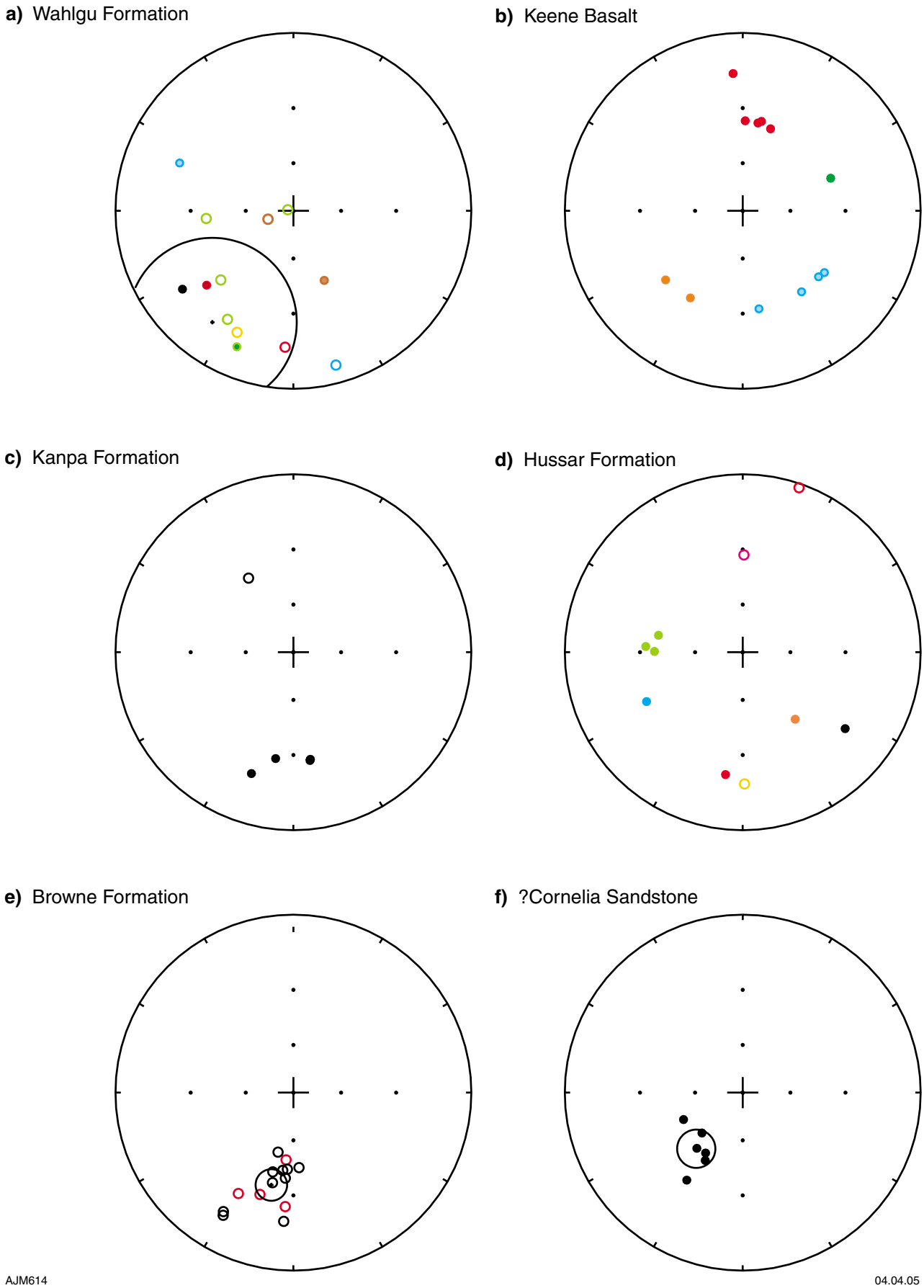

Figure 2. Stereoplots for parts of Lancer 1 core. Results from different oriented intervals are shown with different colours. Upward- and downward-pointing palaeomagnetic directions are shown with open and closed symbols respectively

a) Keene Basalt

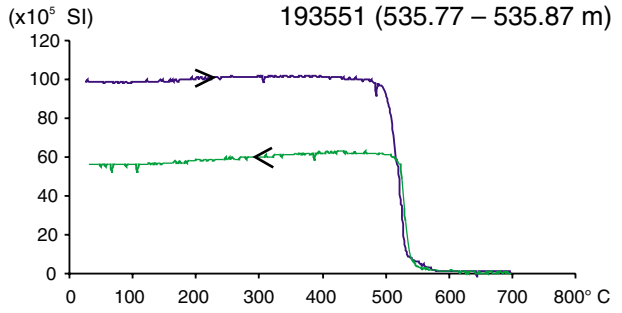

b) Keene Basalt

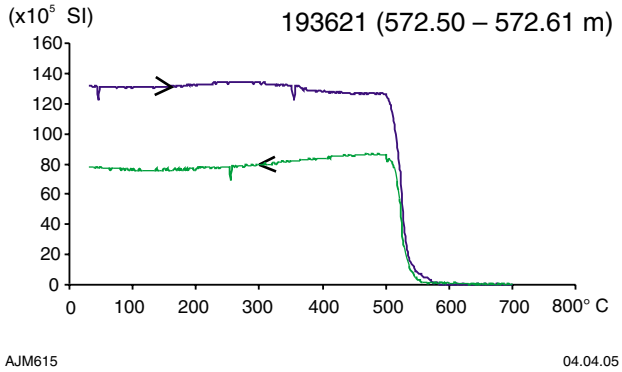

Figure 3. Analysis of Curie points using magnetic susceptibility versus temperature curves for samples of Keene Basalt. Measurements of susceptibility were made at the corresponding temperature

a) Kanpa and Browne Formations

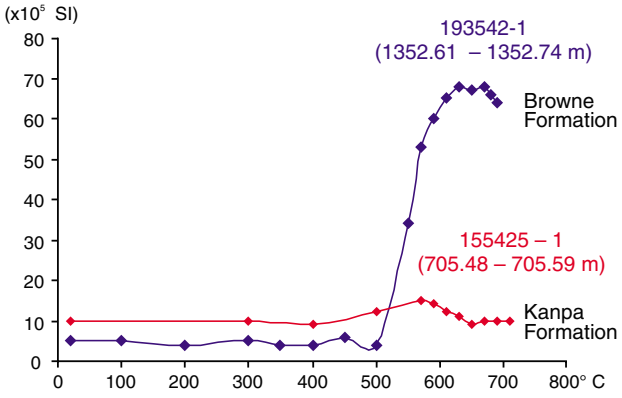

b) Keene Basalt

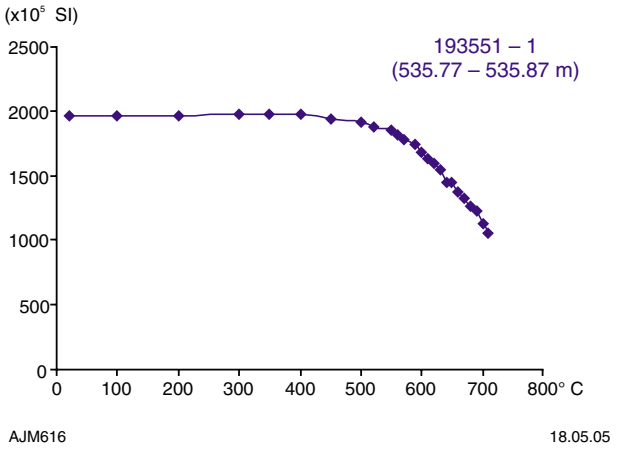

Figure 4. Magnetic susceptibility versus temperature curves for a) the Kanpa and Browne Formations; and b) the Keene Basalt. Measurements of susceptibility were made after cooling to room temperature

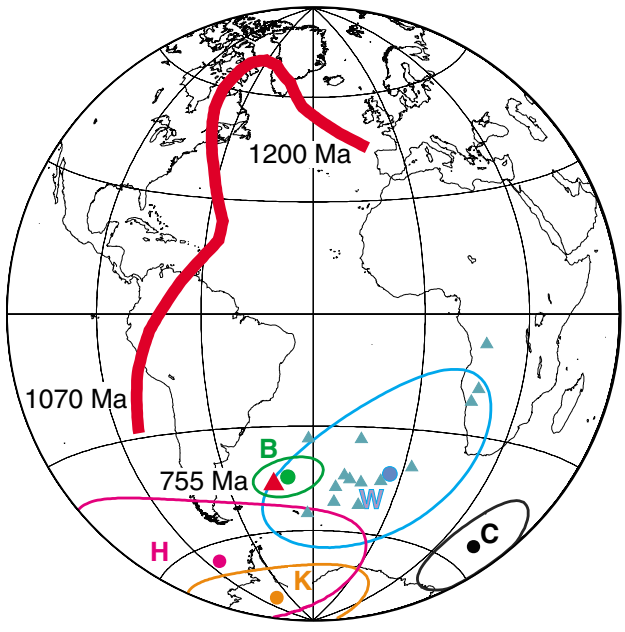

Figure 5. Australian palaeomagnetic poles. Circular symbols with 95% confidence ovals indicate poles from this study: W – Wahlgu, K – Kanpa, H – Hussar, B – Browne, C – ?Cornelia (Table 1). Triangular symbols represent other Australian poles between 755 and 530 Ma; the large red triangle represents the 755 Ma Mundine Well pole of Wingate and Giddings (2000). The red curve is a revised Apparent Polar Wander (APW) path for Australia between 1200 and 1070 Ma (Pisarevsky et al., 2003)

1. Identical pole positions for the Browne Formation and the Mundine Well dykes indicates that no significant motion of Australia occurred between the time of deposition of the basal Browne Formation and intrusion of the Mundine Well dykes at 755 Ma.

2. All inclination data obtained from Lancer 1 indicate that Australia occupied low to moderate latitudes during the late Neoproterozoic to Cambrian. This confirms similar conclusions from palaeomagnetic studies of the Empress 1A (Pisarevsky et al., 2001) and Vines 1 (Pisarevsky, 2001) drillholes.

References

PISAREVSKY, S. A., 2001, Appendix 4: Palaeomagnetic study of Vines 1, *in* GSWA Vines 1 well completion report, Waigen area, Officer Basin, Western Australia *compiled by* S. N. APAK, H. T. MOORS, and M. K. STEVENS: Western Australia Geological Survey, Record 2001/18.

PISAREVSKY, S. A., LI, Z. X., GREY, K., and STEVENS, M. K., 2001, A palaeomagnetic study of the Empress 1A corehole in the Officer Basin: no evidence for a high-latitude position for Australia in the Neoproterozoic: Precambrian Research, v. 110, p. 93–108.

PISAREVSKY, S. A., and McELHINNY, M. W., 2003, Global Paleomagnetic Data Base developed into its visual form: Eos transactions, American Geophysical Union, v. 84, p. 192.

PISAREVSKY, S. A., WINGATE, M. T. D., and HARRIS, L. B., 2003, Late Mesoproterozoic (ca 1.2 Ga) palaeomagnetism of the Albany–Fraser orogen: no pre-Rodinia Australia–Laurentia connection: Geophysical Journal International, v. 155, p. F6–F11.

WINGATE, M. T. D., 2002, Age and palaeomagnetism of Mesoproterozoic dolerite sills of the western Bangemall Basin, Western Australia: Western Australia Geological Survey, Record 2002/4, 48p.

WINGATE, M. T. D., 2003, Age and palaeomagnetism of dolerite intrusions of the southeastern Collier Basin, and the Earaheedy and Yerrida Basins, Western Australia: Western Australia Geological Survey, Record 2003/3, 34p.

WINGATE, M. T. D., and GIDDINGS, J. W., 2000, Age and palaeomagnetism of the Mundine Well dyke swarm, Western Australia: implications for an Australia–Laurentia connection at 755 Ma: Precambrian Research, v. 100, p. 335–357.

WINGATE, M. T. D., PIRAJNO, F., and MORRIS, P. A., 2004, The Warakurna large igneous province: a new Mesoproterozoic large igneous province in west-central Australia: Geology, v. 32, p. 105–108.

WINGATE, M. T. D., PISAREVSKY, S. A., and EVANS, D. A. D., 2002, Rodinia connections between Australia and Laurentia: no SWEAT, no AUSWUS?: Terra Nova, v. 14, p. 121–128.

Preliminary report on the Proterozoic biostratigraphy, GSWA Lancer 1, Officer Basin, Western Australia

by

K. Grey
Geological Survey of Western Australia

Abstract

In Lancer 1, a continuously cored Neoproterozoic section consisting of the ?Ediacaran (Supersequence 3 or 4) Lungkarta Formation, the ?Cryogenian (Supersequence 3) Wahlgu Formation, and part of the Cryogenian (Supersequence 1) Buldya Group (Kanpa, Hussar, and Browne Formations) was intersected from 169–1479 m, and a probable Mesoproterozoic section from 1479 m to total depth at 1501 m. Biostratigraphic studies of stromatolitic horizons and palynological preparations from the finer grained siliciclastic rocks allow correlation with a similar succession in GSWA Empress 1A, and with other drillholes and outcrop in the Officer Basin, as well as with other sections such as the Burra Group in the Adelaide Rift Complex and the Bitter Springs Formation in the Amadeus Basin.

Introduction

Preliminary results of biostratigraphic studies from GSWA Lancer 1 (Haines et al., 2004) indicate a very similar succession to that present in Empress 1A (Grey 1999a,b). Although several samples, particularly from the Browne Formation, are barren, the drillcore contains moderately well preserved palynomorphs and penetrates numerous stromatolitic horizons. Results allow correlation with other drillholes and outcrop in the western Officer Basin, and successions of the Adelaide Rift Complex and Amadeus and eastern Officer Basin (Figs 1–3). Both the palynology and stromatolite biostratigraphy are consistent with results from the isotope chemostratigraphy (Hill et al., 2000; Hill, 2005).

Palynological results from Lancer 1 are currently based on 20 conventional-core samples. Laola Pty Ltd processed the samples using a modified preparation technique for Proterozoic rocks, which eliminates harsh and vigorous treatments that might fragment large or delicate specimens (Grey, 1999c). Nine of 11 samples between 427.7 and 690.35 m yielded palynomorphs, but only four of nine samples between 937.44 and 1498 m contained palynomorphs, and these were sometimes poorly preserved. The uppermost Neoproterozoic interval (169.0 – 466.5 m), which comprises the ?Durba Sandstone, Lungkarta Formation, and diamictite of the Wahlgu Formation (Haines et al., 2004; Grey et al., 2005), consists of lithologies that are too coarse grained for palynological sampling to be worthwhile. Another unsampled interval coincides with the Keene Basalt (527.4 – 576.2 m; Haines et al., 2004), and an interval from the top of the Hussar Formation at 707.5 m to the middle of the formation at 937.44 m consists predominantly of sandstone-dominated lithologies with few horizons suitable for palynological sampling. Two assemblages have been identified and are similar to those observed in other drillholes in the basin (Zang, 1995; Grey, 1995, 1999a; Grey and Cotter, 1996; Grey and Stevens, 1997; Cotter, 1997, 1999; Hill et al., 2000). The younger assemblage is characterized by the presence of the distinctive acritarch species *Cerebrosphaera buickii* Butterfield 1994 in Butterfield et al. (1994). Detailed studies of both assemblages are in progress, and some further sampling of thin mudstone beds will be undertaken in an attempt to determine more closely the position of the first appearance of this key species, which is probably in a sandstone interval in the Hussar Formation. The slides are registered in the Geological Survey of Western Australia (GSWA) relinquishment collection.

Stromatolites were examined directly in the core. Fortunately, most Cryogenian stromatolite taxa are sufficiently distinctive and well documented for them to be identified from cut surfaces. Many specimens were easily identified, but others will require more-detailed studies. As in Empress 1A (Grey, 1999b), the Kanpa Formation and upper Hussar Formation contain the *Baicalia burra* Stromatolite Assemblage, and the Woolnough Member of

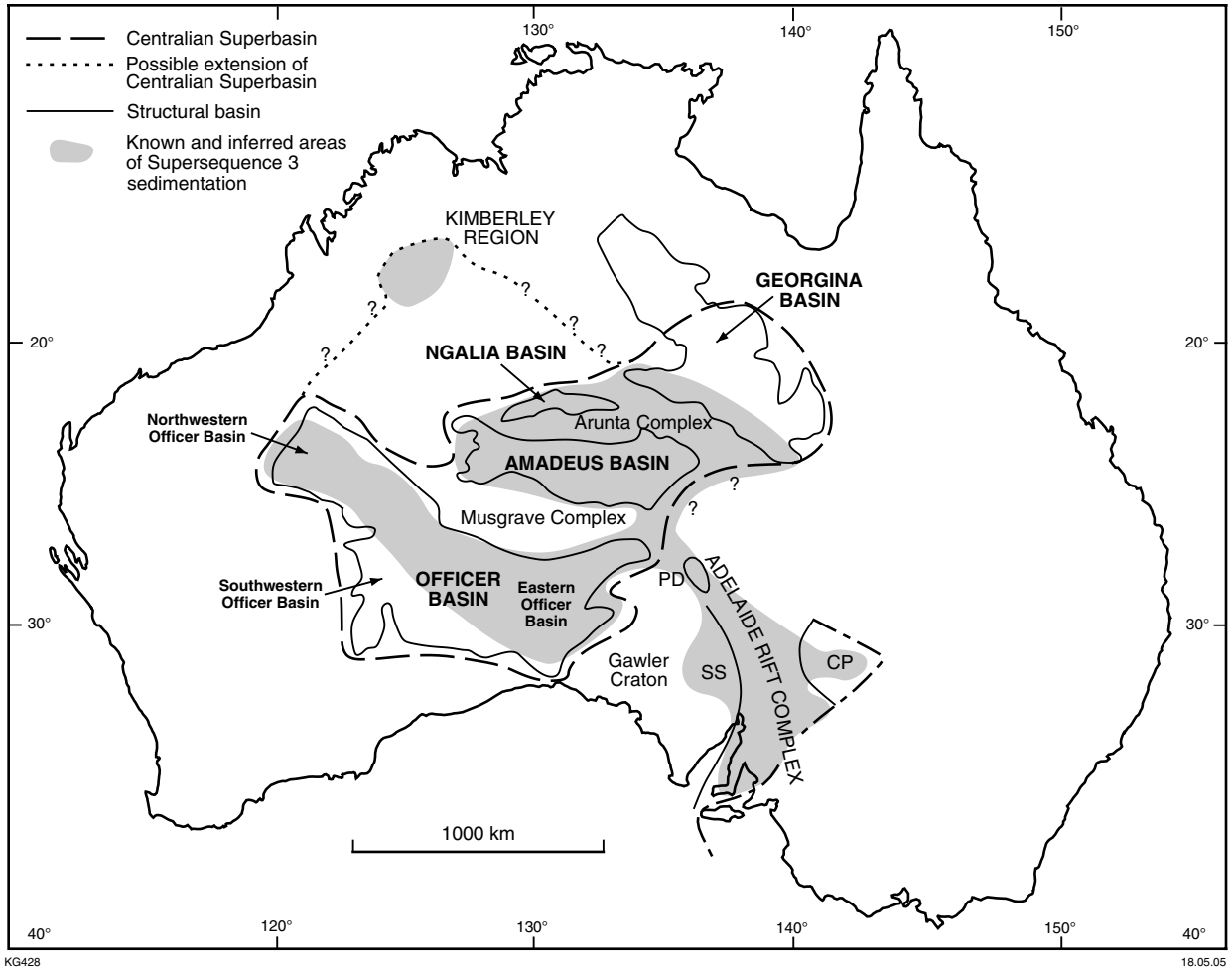

Figure 1. Centralian Superbasin and Adelaide Rift Complex (dot and dash outline) and constituent structural basins (stippled). Modified from Walter et al. (1995) and Walter and Veevers (1997). PD, Peak and Denison Ranges; CP, Curnarmona Province; SS, Stuart Shelf

the Browne Formation contains the *Acaciella australica* Stromatolite Assemblage. Also of significance is the presence of an unnamed form of *Tungussia* in a greenish silty dolostone in the middle Hussar Formation. The same form is present at about the same level in Empress 1A. Identified specimens will be left in situ in the core trays.

Black, carbonaceous discs were observed at several points in the core. Studies are underway to determine whether these are specimens of the megascopic alga *Chuaria circularis* Walcott 1899; emend. Vidal and Ford 1985.

Palynological observations

466.5 – 707.5 m (core depth), Kanpa Formation

Samples from the Kanpa Formation contain a similar suite of palynomorphs throughout, although the numbers of certain taxa vary depending on preservation. The assemblage is similar to that recorded in Empress 1A (Grey, 1999a). The most noticeable species in the assemblage is the large wrinkled acritarch, *Cerebrosphaera buickii*. *Leiosphaeridia crassa* (Naumova 1949) Jankauskas 1989, *Leiosphaeridia jacutica* (Timofeev 1966) emend. Mikhailova and Jankauskas in Jankauskas et al. 1989, *Leiosphaeridia minutissima* (Naumova 1949) emend. Jankauskas in Jankauskas et al. 1989, and *Leiosphaeridia tenuissima* Eisenack 1958 are present in most samples, with rare colonial clusters of *Synsphaeridium* sp. Some samples contain a variety of filaments, including several species of *Siphonophycus.*

707.5 – 1201.9 m (core depth), Hussar Formation

Lithologies in the upper Hussar Formation are generally unsuitable for palynological sampling above about 920 m. Below this depth, samples contain *Leiosphaeridia* sp., which are commonly poorly preserved. Several samples are barren of identifiable palynomorphs, and contain only severely degraded organic debris.

1201.9 – 1478.9 m (core depth), Browne Formation

Much of the Browne Formation is lithologically unsuitable for palynology and only three samples were processed. One is barren, and from preliminary inspection the other two contain only poorly preserved leiospheres.

1478.9 – 1501.2 m (core depth), ?Cornelia Sandstone

A single sample from the ?Cornelia Sandstone is barren.

Discussion

Palynomorphs present in the Kanpa Formation are consistent with those found at the same level elsewhere in the basin (Grey and Cotter, 1996; Grey and Stevens, 1997; Cotter, 1997, 1999; Grey, 1999a; Hill et al., 2000). They are characterized by the presence of *Cerebrosphaera buickii*, which appears to be a significant middle Cryogenian (Supersequence 1 of Walter et al., 1995) marker species across Australia (Hill et al., 2000). Samples from the lower Hussar and Browne Formations are poorly preserved, but apparently lack *Cerebrosphaera buickii*. From comparison with Empress 1A and other drillholes in the Officer Basin (Fig. 2), the first appearance of this species probably lies within the predominantly sandstone part of the Hussar Formation, and future studies will involve trying to find any suitable mudstone partings in this interval that might help to define the boundary more precisely.

Cerebrosphaera buickii was previously recorded from the poorly time-constrained Svanbergfjellet Formation of Spitsbergen (Butterfield et al., 1994), which is probably about the same age as the upper Buldya Group in the Officer Basin (Hill et al., 2000). This acritarch is also known from the Burra Group in the Adelaide Rift Complex (Hill et al., 2000), and was recently discovered near the top of the Bitter Springs Formation in the Amadeus Basin (Grey, K., unpublished data; Fig. 3).

Maturity

Maturity was determined using a thermal alteration index (TAI; Traverse, 1988, p. 431–435, Pl. 1). The index was devised for Phanerozoic spores and pollen, and needs to be applied with caution to Proterozoic samples, inasmuch as the colour variation exhibited by Proterozoic acritarchs and other biogenic material may be slightly different, and is not well calibrated. In spite of these constraints, the colour of Proterozoic biogenic matter is still a useful guide to maturity, and is generally consistent with results obtained from organic geochemistry. Most samples from the Kanpa and Hussar Formations show a TAI of 3 to 3+, but at about 965 m, in the lower Hussar Formation, maturity increases to 4. Most samples lie within the oil-generation window, although samples from the lower Hussar Formation downward are within the dry-gas window.

Stromatolite biostratigraphy

Detailed logging and identification of the many stromatolites present in the core is still in progress, but preliminary observations indicate a similar succession to that in Empress 1A (Grey, 1999b), and to outcrops and drillholes elsewhere in the western Officer Basin (Fig. 2). The two assemblages present allow correlation with other Cryogenian successions across Australia (Fig. 3).

477 m – ?1143 m, *Baicalia burra* Assemblage

The stromatolites present indicate that this interval belongs to the *Baicalia burra* Stromatolite Assemblage (Stevens and Grey, 1997; Hill et al., 2000). As in Empress 1A (Grey, 1999b), the Kanpa Formation consists of cyclic units in which stromatolitic carbonate horizons are dominated by *Baicalia burra* Preiss 1972; other stromatolites are less common. The cycles are not as well defined as in Empress 1A (Grey, 1999b), and the identification of forms other than *B. burra* requires additional work. Stromatolites are common in the upper part of the Hussar Formation, but are absent in the sandier interval in the middle of the formation. They are sparser and more poorly preserved in the lower part of the Hussar Formation. The earliest *Baicalia burra* appears to be at 1142.83 m.

B. burra is known from outcrops along the Eagle Highway near the western margin of the Officer Basin, in the Neale Formation near Neale Junction, at Constance Headland, and in Kanpa 1A (Fig. 2; Stevens and Grey, 1997; Grey et al., in prep.). It is widespread in the Burra Group and lateral equivalents in South Australia (Preiss, 1972, 1974, 1987), and it has been recorded as an erratic in diamictite (Griffin and Preiss, 1976) in what is now the Julius River Member of the Black River Dolomite in northwestern Tasmania.

934–953 m, *Tungussia* form indet., Hussar Formation

A specimen here referred to as *Tungussia* form indet. is present in greenish-grey, silty dolomite in the Hussar Formation at two intervals: 934 to 943.2 m and 951 to 953.2 m. It is identical to a form observed in the Hussar Formation in Empress 1A at 1077.4 m. This stromatolite has only been observed in drillcore so far, and insufficient material is available for it to be identified to Form level. It has semi-horizontal columns with irregular margins and highly irregular, wispy laminae, and a growth habit similar to that of the Group *Tungussia*.

1323.5 – 1355.25 m, *Acaciella australica* Assemblage, Browne Formation

As in Empress 1A, the pinkish dolomite of the Woolnough Member contains stromatolite forms characteristic of

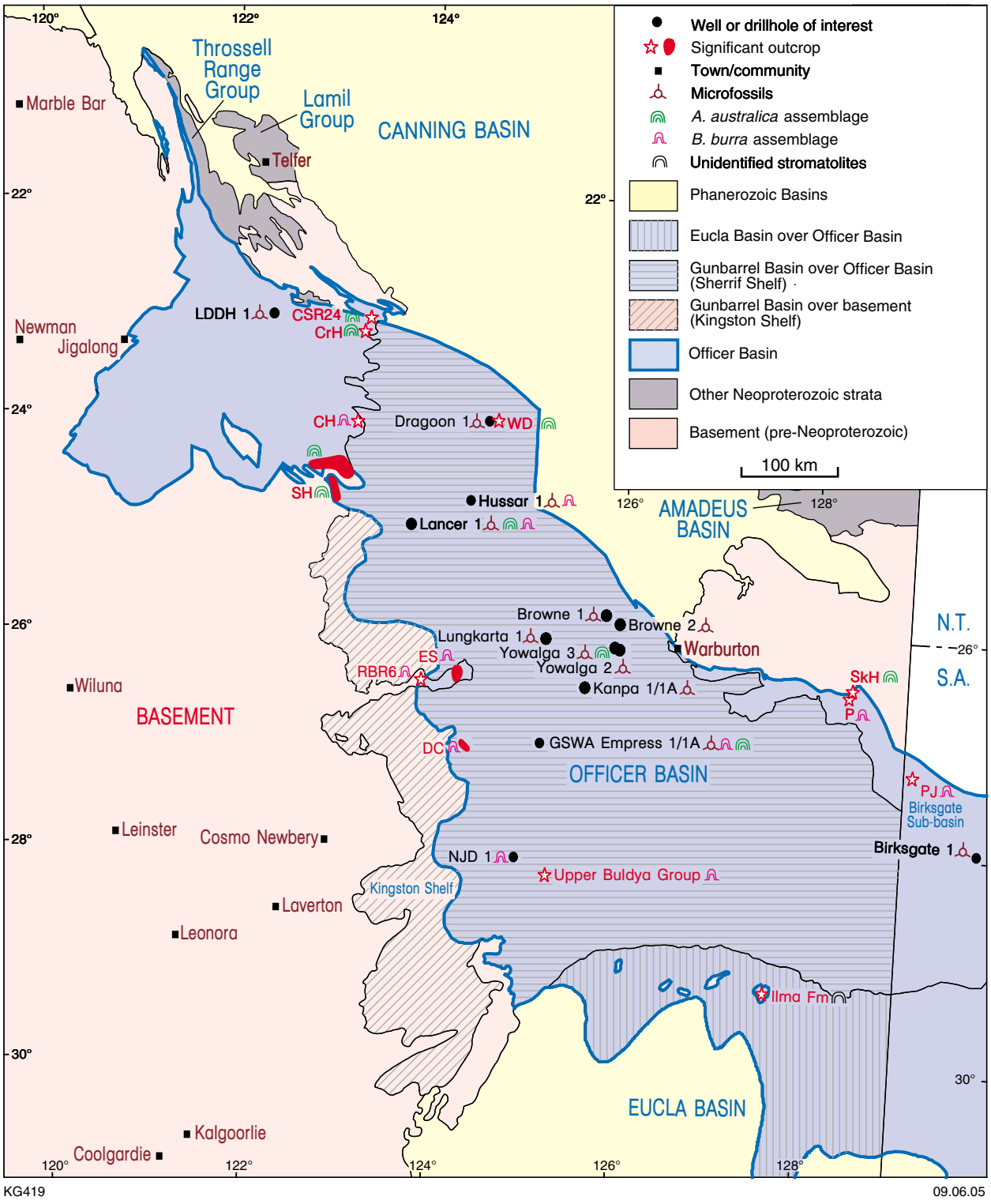

Figure 2. **Western Officer Basin, Western Australia showing location of drillholes with Cryogenian palynomorph assemblages or containing stromatolites and outcrops sampled. LDDH 1, Lake Disappointment Drillhole 1; NJD 1, Neale Junction Drillhole 1; Outcrops: CH, Constance Headland; ES, Empress Spring; CSR24, Canning Stock Route Well 24; CrH, Cronin Hills; RBR6, Robert 1:250 000 localities; DC, David Carnegie Road localities; SkH, Skirmish Hill; P, Pirrilyungka; PJ, Patricia Johnson Hills; SH, Skates Hills localities; WD, Woolnough Hills Diapir. Base map modified after Stevens and Grey (1997), Apak and Moors (2000); basin boundaries modified after Grey et al. (2005)**

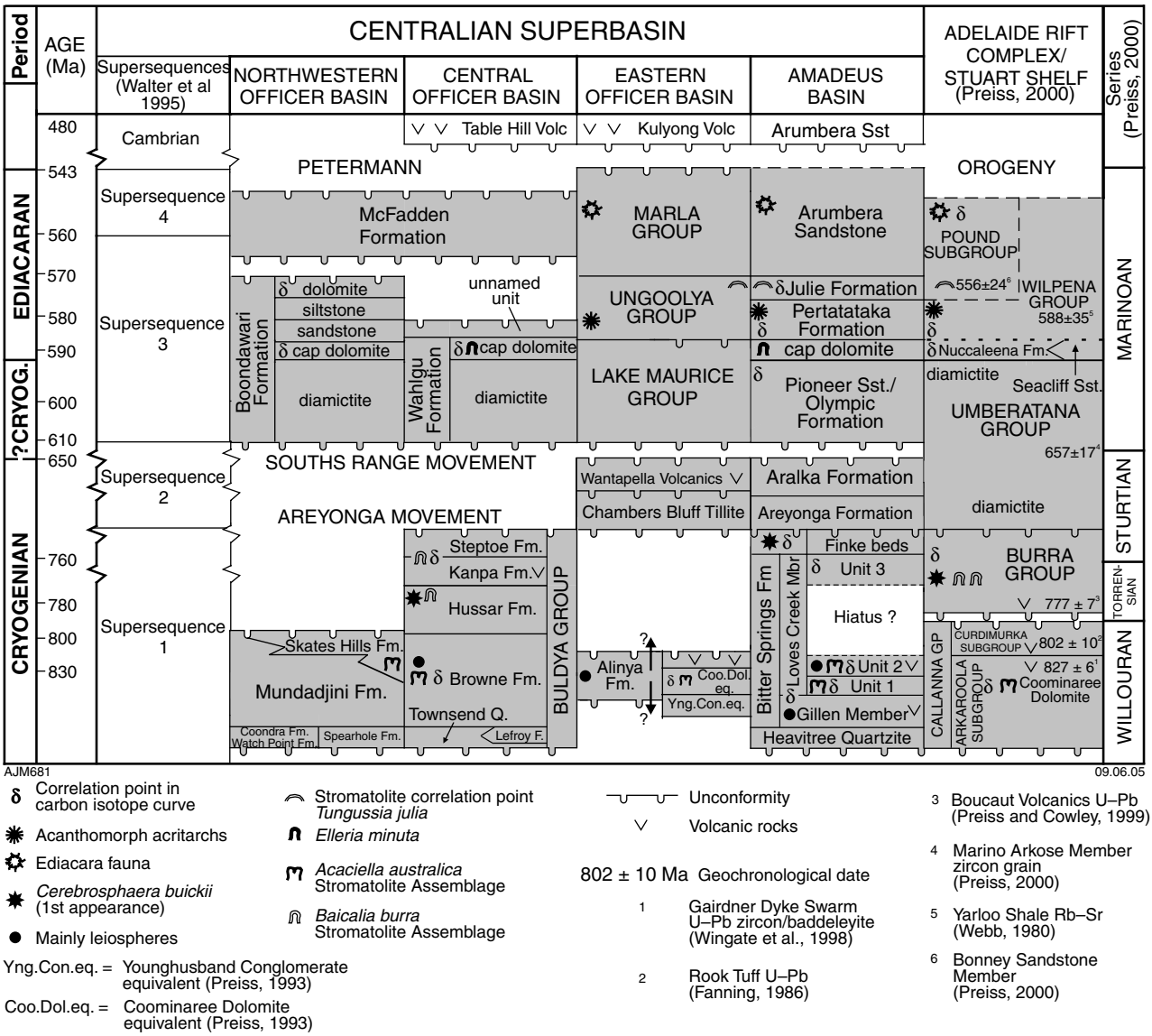

Figure 3. Lithostratigraphic correlation of the Centralian Superbasin and Adelaide Rift Complex, with ages calibrated in Ma (modified from Walter et al., 1995; Walter and Veevers, 1997; Grey and Corkeron, 1998; and Walter et al., 2000 and references therein), and showing position of key tie points based on biostratigraphy and isotope chemostratigraphy

the *Acaciella australica* Stromatolite Assemblage. The dominant form in the interval is *Acaciella australica* (Howchin 1914) Walter 1972, but *Basisphaera irregularis* Walter 1972 is also present. Other forms await identification. *A. australica* was previously recorded from a series of outcrops in the Skates Hills Formation of the Savory Sub-basin and in Yowalga 3 at 2390 m (Grey, 1995), and was subsequently identified in outcrop at Woolnough Hills (Stevens and Grey, 1997). Its distribution in other areas of Australian Neoproterozoic sedimentation was discussed in Grey (1995) and Hill et al. (2000). The assemblage forms a significant Australia-wide marker assemblage (see below).

Discussion

Australia-wide correlations for some sections of the Neoproterozoic are now feasible using stromatolite biostratigraphy, and results are consistent with correlations based on palynology and isotope chemostratigraphy (Hill and Walter, 2000; Hill et al., 2000). Lancer 1 confirms stratigraphic distributions of stromatolites that were observed previously both in the field and in the core from Empress 1A (Grey, 1999b), where the relative vertical positions of the principal taxonomic associations were demonstrated for the first time in a continuous section. Distribution patterns match those documented for the

Adelaide Rift Complex (Preiss, 1972, 1973a,b, 1974, 1987) and the Centralian Superbasin (Walter, 1972; Walter et al., 1979), and are consistent with correlations based on isotope chemostratigraphy (Hill and Walter, 2000) and palynology as discussed above.

Two main assemblages are present in the Cryogenian in Western Australia: the *Acaciella australica* Stromatolite Assemblage and the *Baicalia burra* Stromatolite Assemblage (Stevens and Grey, 1997; Hill et al., 2000). Currently recorded ranges are mainly restricted to carbonate horizons, and are constrained to some extent by major lithological changes. For example, the Woolnough Member is overlain by sandstone, which is not a suitable environment for stromatolite growth, so although the observed top of the *A. australica* Stromatolite Assemblage coincides with the top of the Woolnough Member, the inferred top of the assemblage may be higher than this. However, none of the *A. australica* Assemblage components are present in carbonates younger than the Woolnough Member. None of the stromatolite taxa are found within carbonate horizons of similar facies beyond the relatively short intervals in which they have been documented, and individual taxa are found in a range of carbonate lithologies within their vertical range. This contradicts claims that stromatolite distributions are facies controlled, because if that were the case, taxa would show random distributions throughout the geological column whenever their preferred facies type was present, and each taxon would be restricted to a particular facies type. Observations are completely contrary to expectations if palaeoenvironment was the principal controlling factor. Consequently, stromatolites can be demonstrated to show biostratigraphic distribution patterns, and the range of each taxon can be inferred to be age dependent.

The older *A. australica* Stromatolite Assemblage is widespread in the western Officer Basin. It is present in the Woolnough Member of the Browne Formation at Woolnough Diapir, in Yowalga 3 and Empress 1A, and at fifteen localities in the Skates Hills Formation (Grey, 1995, 1999b, and unpublished data; Stevens and Grey, 1997). More recently, it has been recognized in the Waltha Woora Formation and Tarcunyah Group, along the northeastern margin of the Officer Basin (Grey, unpublished data). It is common in the Loves Creek Member of the Bitter Springs Formation of central Australia (Walter, 1972; Walter et al., 1979), and present in the Yackah beds of the Georgina Basin (Walter et al., 1979) and Coominaree Dolomite of the Callanna Group in the Adelaide Rift Complex (Preiss, 1973b, 1987). The Coominaree Dolomite underlies the Rook Tuff, which has been dated at 802 ± 10 Ma (Fanning et al., 1986), and the Boucaut Volcanics, which is a basal unit of the Burra Group dated at 777 ± 7 Ma (Preiss, 2000). The *A. australica* Stromatolite Assemblage therefore most probably has an age of about 825 to 800 Ma.

The younger *Baicalia burra* Stromatolite Assemblage is also widespread in the western Officer Basin. It outcrops at several localities in undifferentiated upper Buldya Group near the Eagle Highway and Neale Junction, and in drillhole WMC NJD 1 (Preiss, 1976; Stevens and Grey, 1997, Hill et al., 2000; Hocking, 2003). It is recorded from the Kanpa Formation in Hussar 1 and in more than 60 horizons in the middle Hussar, Kanpa, and Steptoe Formations in Empress 1A (Grey, 1999b), and is present at the top of the succession at Constance Headland. The assemblage is common in the Burra Group in the Adelaide Rift Complex (Preiss, 1972, 1974, 1987), but has not yet been recorded in central Australia, either because of non-deposition, or, more likely, as a result of erosion during the subsequent Areyonga and Souths Range Movements. *B. burra* is present as a glacial erratic in diamictite at or near the top of the Black River Dolomite in Tasmania, which is of probable Sturtian-glaciation age (Griffin and Preiss, 1976; Calver, 1998).

In South Australia, the assemblage overlies the 777 ± 7 Ma Boucaut Volcanics near the base of the Burra Group (Preiss, 2000). A U–Pb zircon date of 758 ± 3.5 Ma was obtained on an ash bed in unit 1C from the Ombombo Subgroup of Namibia (Hoffman et al., 1996), and this unit is equivalent to the middle Kanpa Formation based on a tie line linking the heaviest-known values of $\delta^{13}C_{carb}$ present in the Cryogenian (Hill et al., 2000). These dates are consistent with a detrital zircon U–Pb SHRIMP age of 725 ± 11 Ma from the Kanpa Formation in Empress 1A (Geological Survey of Western Australia, in prep.; GSWA 154667, 692.4 – 694.3 m) is no reliable dating on the age of the Sturtian glaciation, which is presumably equivalent to the lacuna between the Kanpa and Wahlgu Formations in Lancer 1, and Steptoe and Wahlgu Formations in Empress 1A. It is usually estimated to have an age of about 700 Ma, which is younger than some ages obtained on diamictites elsewhere in the world that are thought to be equivalent to this glaciation. However, some of these dates are older than the age of the detrital zircon from the Kanpa Formation referred to above. The Wahlgu Formation, a diamictite that oversteps upper Buldya Group formations in the western Officer Basin, and which is present in both Lancer 1 and Empress 1 and 1A, has been correlated with a younger glaciation (typified by the Elatina Formation and part of sequence set Marinoan 2 of Preiss, 2000). Volcanic rocks associated with lateral equivalents of this glaciation in King Island and Tasmania were recently dated at c. 580 Ma (Calver et al., 2004). The age of the *Baicalia burra* Stromatolite Assemblage is therefore younger than 777 Ma and probably older than 700 Ma.

Other fossils

Dark carbonaceous discs, about 1 mm in diameter, have been observed at several levels (at 651 to 659 m and 659.35 m) in mudstones in the Kanpa Formation, and possibly at 961.2 and 965.8 m in the Hussar Formation. Further study is required to establish the nature of these carbonaceous structures. They may belong to the carbonaceous megafossil *Chuaria circularis.*

Conclusions

Palynomorphs in Lancer 1 are well preserved in parts, especially in the Kanpa Formation, and can be correlated with other Cryogenian assemblages at the same level

in drillholes throughout the Officer Basin, and in particular in Empress 1A. Organic material is moderately abundant and consists of a mixture of acritarchs and filamentous and coccoid mat fragments that were most probably derived from benthic mats developed in the photic zone.

Stromatolites are abundant in Lancer 1, although they are not quite as common as in Empress 1A. Taxa present belong to either the *Acaciella australica* Stromatolite Assemblage or the younger *Baicalia burra* Stromatolite Assemblage. These assemblages allow correlation with outcrop and other drillholes in the western Officer Basin, with successions in other parts of the Centralian Superbasin (the Amadeus and Georgina Basins), with the Adelaide Rift Complex, and indirectly with Neoproterozoic successions in Tasmania.

References

APAK, S. N., and MOORS, H. T., 2000, Basin development and petroleum exploration potential of the Yowalga area, Officer Basin, Western Australia: Western Australia Geological Survey, Report 76, 61p.

BUTTERFIELD, N. J., KNOLL, A. H., and SWETT, K., 1994, Paleobiology of the Neoproterozoic Svanbergfjellet Formation, Spitsbergen: Oslo, Fossils and Strata, no. 34, 84p.

CALVER, C. R., 1998, Isotope stratigraphy of the Neoproterozoic Togari Group, Tasmania: Australian Journal of Earth Sciences, v. 45, p. 865–874.

CALVER, C. R., BLACK, L. P., EVERARD, J. L., and SEYMOUR, D. B., 2004, U–Pb zircon age constraints on late Neoproterozoic glaciation in Tasmania: Geology, v. 32, p. 893–896.

COTTER, K. L., 1997, Neoproterozoic microfossils from the Officer Basin, Western Australia: Alcheringa, v. 21, p. 247–270.

COTTER, K. L, 1999, Microfossils from Neoproterozoic Supersequence 1 of the Officer Basin: Western Australia: Alcheringa, v. 23, p. 63–86.

FANNING, C. M., LUDWIG, K. R., FORBES, B. G., and PREISS, W. V., 1986, Single and multiple grain U–Pb zircon analyses for the early Adelaidean Rook Tuff, Willouran Ranges, South Australia: Geological Society of Australia, Abstracts, No. 15, p. 255–304.

GEOLOGICAL SURVEY OF WESTERN AUSTRALIA, in prep., Compilation of geochronology data 2003: Western Australia Geological Survey, Record

GREY, K., 1995, Neoproterozoic stromatolites from the Skates Hills Formation, Savory Basin, Western Australia, and a review of the distribution of *Acaciella australica*: Australian Journal of Earth Sciences, v. 42, p. 123–132.

GREY, K., 1999a, Appendix 7: Proterozoic palynology of samples from Empress 1A, *in* GSWA Empress 1 and 1A well completion report, Yowalga Sub-basin, Officer Basin, Western Australia *compiled by* M. K. STEVENS and S. N. APAK: Western Australia Geological Survey, Record 1999/4, p. 68–69.

GREY, K., 1999b, Appendix 8: Proterozoic stromatolite biostratigraphy of Empress 1A, *in* GSWA Empress 1 and 1A well completion report, Yowalga Sub-basin, Officer Basin, Western Australia *compiled by* M. K. STEVENS and S. N. APAK: Western Australia Geological Survey, Record 1999/4, p. 70–72.

GREY, K., 1999c, A modified palynological preparation technique for the extraction of large Neoproterozoic acanthomorph acritarchs and other acid insoluble microfossils: Western Australia Geological Survey, Record 1999/10, 23p.

GREY, K., and CORKERON, M., 1998, Late Neoproterozoic stromatolites in glacigenic successions of the Kimberley region, Western Australia: evidence for a younger Marinoan glaciation: Precambrian Research, v. 92, p. 65–87.

GREY, K., and COTTER, K. L., 1996, Palynology in the search for Proterozoic hydrocarbons: Western Australia Geological Survey, Annual Review 1995–96, p. 70–80.

GREY, K., HOCKING, R. M., STEVENS, M. K., BAGAS, L, CARLSEN, G. M, IRIMIES, F., PIRAJNO, F., HAINES, P. W., and APAK, S. N., 2005, Lithostratigraphic nomenclature of the Officer Basin and correlative parts of the Paterson Orogen, Western Australia: Western Australia Geological Survey, Report 93, 89p.

GREY, K., and STEVENS, M. K., 1997, Neoproterozoic palynomorphs of the Savory Sub–basin, Western Australia, and their relevance to petroleum exploration: Western Australia Geological Survey, Annual Review 1996–97, p. 49–54.

GRIFFIN, B. J., and PREISS, W. V., 1976, The significance and provenance of stromatolitic clasts in a probable late Precambrian diamictite in north-western Tasmania: Papers and Proceedings of the Royal Society of Tasmania, v. 110, p. 111–127.

HAINES, P. W., MORY, A. J., STEVENS, M. K., and GHORI, K. A. R., 2004, GSWA Lancer 1 well completion report (basic data), Officer and Gunbarrel Basins, Western Australia: Western Australia Geological Survey, Record 2004/10, 39p.

HILL, A. C., 2005, Stable isotope stratigraphy, GSWA Lancer 1, Officer Basin, Western Australia: Western Australia Geological Survey, Record 2005/4, p. 1–12.

HILL, A. C., COTTER, K. L., and GREY, K., 2000, Mid-Neoproterozoic biostratigraphy and isotope stratigraphy in Australia: Precambrian Research, v. 100, p. 281–298.

HILL, A. C., and WALTER, M. R., 2000, Mid-Neoproterozoic (~830–750 Ma) isotope stratigraphy of Australia and global correlation: Precambrian Research, v. 100, p. 181–211.

HOCKING, R. M., (compiler), 2003, Drillhole WMC NJD 1, Western Officer Basin, Western Australia: Stratigraphy and petroleum geology: Western Australia Geological Survey, Record 2002/18, 26p.

HOFFMAN, P. F., HAWKINS, D. P., ISACHSEN, C. E., and BOWRING, S. A., 1996, Precise U–Pb zircon ages for early Damaran magmatism in the Summas Mountains and Welwitschia inlier, northern Damara belt, Namibia: Communications of the Geological Survey of Namibia, no. 11, 82p.

NELSON, D., 1994, GSWA sample 154667: Kanpa Formation in Empress 1A, *in* Compilation of geochronology data, October 2004 update: Western Australia Geological Survey.

PREISS, W. V., 1972, The Systematics of South Australian Precambrian and Cambrian stromatolites, Part I: Transactions of the Royal Society of South Australia, v. 96, p. 67–100.

PREISS, W. V., 1973a, Early Willouran stromatolites from the Peake and Denison Ranges and their stratigraphic significance: South Australia Department of Mines, Report Book, 73/208.

PREISS, W. V., 1973b, The Systematics of South Australian Precambrian and Cambrian stromatolites, Part II: Transactions of the Royal Society of South Australia, v. 97, p. 91–125.

PREISS, W. V., 1974, The Systematics of South Australian Precambrian and Cambrian stromatolites, Part III: Transactions of the Royal Society of South Australia, v. 98, p. 185–208.

PREISS, W. V., 1976, Proterozoic stromatolites from the Nabberu and Officer Basins, Western Australia, and their biostratigraphic significance: South Australia Geological Survey, Report of Investigations, no. 47.

PREISS, W. V., (compiler), 1987, The Adelaide Geosyncline: late Proterozoic stratigraphy, sedimentation, palaeontology and tectonics: Geological Survey of South Australia, Bulletin 53, 438p.

PREISS, W. V., 2000, The Adelaide Geosyncline of South Australia and its significance in Neoproterozoic continental reconstruction: Precambrian Research, v. 100, p. 21–63.

STEVENS, M. K. and GREY, K., 1997, Skates Hills Formation and Tarcunyah Group, Officer Basin — carbonate cycles, stratigraphic position, and hydrocarbon prospectivity: Western Australia Geological Survey, Annual Review 1996–97, p. 55–60.

TRAVERSE, A., 1988, Palaeopalynology: Boston, Unwin Hyman, 600p.

WALTER, M. R., 1972, Stromatolites and the biostratigraphy of the Australian Precambrian and Cambrian: London, Palaeontological Association, Special Papers in Palaeontology, v. 11, 190p.

WALTER, M. R., KRYLOV, I. N., and PREISS, W. V., 1979, Stromatolites from Adelaidean (Late Proterozoic) sequences in central and South Australia: Alcheringa, v. 3, p. 287–305.

WALTER, M. R., and VEEVERS, J. J., 1997, Australian Neoproterozoic palaeogeography, tectonics, and supercontinental connections: AGSO Journal of Australian Geology and Geophysics, v. 17, p. 73–92.

WALTER, M. R., VEEVERS, J. J., CALVER, C. R., GORJAN, P., and HILL, A. C., 2000, Dating the 840–544 Ma Neoproterozoic interval by isotopes of strontium, carbon, and sulfur in seawater, and some interpretative models: Precambrian Research, v. 100, p. 371–433.

WALTER, M. R., VEEVERS, J. J., CALVER, C. R., and GREY, K., 1995, Neoproterozoic stratigraphy of the Centralian Superbasin, Australia: Precambrian Research, v. 73, p. 173–195.

ZANG, W., 1995, Early Neoproterozoic sequence stratigraphy and acritarch biostratigraphy, eastern Officer Basin, South Australia: Precambrian Research, v. 74, p. 119–175.

Palynology of samples from GSWA Lancer 1, Gunbarrel Basin, Western Australia

by

J. Backhouse
Backhouse Biostrat Pty Ltd

Abstract

Of six samples processed from between 50 and 166 m in GSWA Lancer 1, cuttings from 86–88 m yielded extremely low numbers of probable Stage 1 palynomorphs, implying a Westphalian to Stephanian (Late Carboniferous) age for that interval. The other samples were either barren or contained too few palynomorphs to identify.

Introduction

Two cuttings and four core samples from Lancer 1 in the Officer Basin were processed for palynology. Only two samples yielded palynomorphs (Table 1).

Palynostratigraphy

Sample 181761, 50–52 m (cuttings)

The sample gave an extremely low yield including some organic fragments and one possible Permian spore. Therefore, the sample age is regarded as indeterminate.

Sample 181764, 86–88 m (cuttings)

The sample contains extremely low numbers of *Potonieisporites* sp. cf. *P. novicus*, *Verrucosisporites* cf. sp. M of Jones and Truswell (1992), *Jayantisporites* sp. cf. J. *variabilis*, a possible specimen of *Spelaeotriletes ybertii*, and several specimens of *Punctatisporites* sp. This assemblage can be assigned somewhere between the *Spelaeotriletes ybertii* Assemblage and the Stage 1 used in Powis (1994), implying a Namurian to Stephanian age, but is more likely to be Stage 1 (late Westphalian to Stephanian, in the Late Carboniferous).

Samples 121.7 – 165.65 m (four core samples)

All four samples yielded unstructured opaque fragments. In the highest two samples the fragments are small (<20 microns) to medium (40+ microns) in size, angular and with a mineralized appearance. Material of unequivocally organic origin is absent, except for minor fragments (probably from dust) and rare modern pollen. The 161.1 m samples yielded angular fragments

Table 1. Summary of results, Lancer 1

Depth (m)	*GSWA number*	*Sample type*	*Palynomorph yield*	*Zone*	*Age*	*Environment*	*TAI*
50–52	181761	cuttings	virtually barren	indeterminate	indeterminate	indeterminate	–
86–88	181764	cuttings	extremely low	*Spelaeotriletes ybertii* Assemblage to Stage 1	Namurian to Stephanian	no evidence for marine	~2 –
121.7	193614	core	barren	indeterminate	indeterminate	indeterminate	–
134.95	193615	core	barren	indeterminate	indeterminate	indeterminate	–
161.1	193613	core	barren	indeterminate	indeterminate	indeterminate	–
165.65	193612	core	barren	indeterminate	indeterminate	indeterminate	–

NOTE: TAI: thermal alteration index (measure of maturity)

of consistently medium size, and the 165.65 m sample yielded small- to medium-sized fragments that are slightly rounded. The complete absence of organic material of obvious plant origin (except for probable contaminants) suggests that all four samples may be extremely overmature, or not of sedimentary origin. Alternatively, the samples may be from totally oxidized intervals.

References

JONES, M. J., and TRUSWELL, E. M., 1992, Late Carboniferous and Early Permian palynostratigraphy of the Joe Joe Group, southern Galilee Basin, Queensland, and implications for Gondwanan stratigraphy: BMR Journal of Australian Geology and Geophysics, v. 13, p. 143–185.

POWIS, G. D., 1984, Palynostratigraphy of the Late Carboniferous Sequence, Canning Basin, W.A., *in* The Canning Basin, W.A. *edited by* P. G. PURCELL: Proceedings of the Geological Society of Australia/PESA Symposium, Perth, 1984, p. 429–438.

Petrography and geochemistry of the Keene Basalt (527 to 576 m), GSWA Lancer 1, Officer Basin, Western Australia

by

F. Pirajno
Geological Survey of Western Australia

Abstract

The Keene Basalt in Lancer 1 consists of olivine thoeliites, but is too weathered to date with conventional methods. A geochemical comparison with other (flood-type) basaltic rocks in Australia indicates it is an intraplate subalkaline tholeiitic basalt of almost identical composition to the Mingary mafic dykes in South Australia, although more enriched in light rare earth elements.

Introduction

The section of drillcore examined is a 49 m interval between the depths of 527 and 576 m. This interval comprises a succession of thoeliitic basalt lava flows, named the Keene Basalt (Haines et al., 2004). A concentration of amygdales marks the top and base of each flow unit, thereby indicating a contact between two flows. Using this criterion, a total of at least five flow units were logged. Figure 1 shows a schematic log of the flow units in Lancer 1. The top flow (no. 5) shows lithic fragments towards the top, but at the contact with overlying sedimentary rocks the lava is holocrystalline and medium grained, suggesting that its flow top was truncated before sedimentation resumed. The first flow (no. 1) at the base is vesicular and fragmented, suggesting interaction with shallow water.

A total of 30 core samples were collected and thin sectioned; three samples were analysed for major and trace elements (see **Geochemistry** section) and two samples analysed using X-ray powder diffraction and scanning electron microscope to determine the nature of clay minerals.

Petrographic descriptions

The following are brief descriptions of individual samples, from top to base.

Sedimentary hangingwall

Sample No: 193501
Depth: 526.9 m
Petrography: sedimentary rock unit above basalt section; a packed aggregate of spheroids (0.1 mm or less), with little interstitial material, interbedded with siltstone laminae, between 1 and 2 mm thick. The spheroids are probably oolitic carbonate; the silt material consists of quartz grains and minor feldspar. Chalcedonic chert is present and forms convoluted laminae cut by black filaments (possibly organic material). Some pyrite blebs, possibly framboids, are associated with the silt laminae.

Flow 5

Sample No: 193502
Depth: 527.3 m
Petrography: plagioclase crystals, all pervasively altered to clay–illite, chaotically disposed and/or fragmented and interspersed with patches or zones of clay minerals, probably interlayered kaolinite–illite; also present are green smectite clays, and bright-green celadonite. Some clay minerals have outlines suggestive of pyroxenes. Disseminated pyrite and hematite are present as blebs and veinlets that locally form networks due to brecciation of the host matrix. The relatively coarse texture suggests that this sample is from the mid-section of the weathered lava flow.

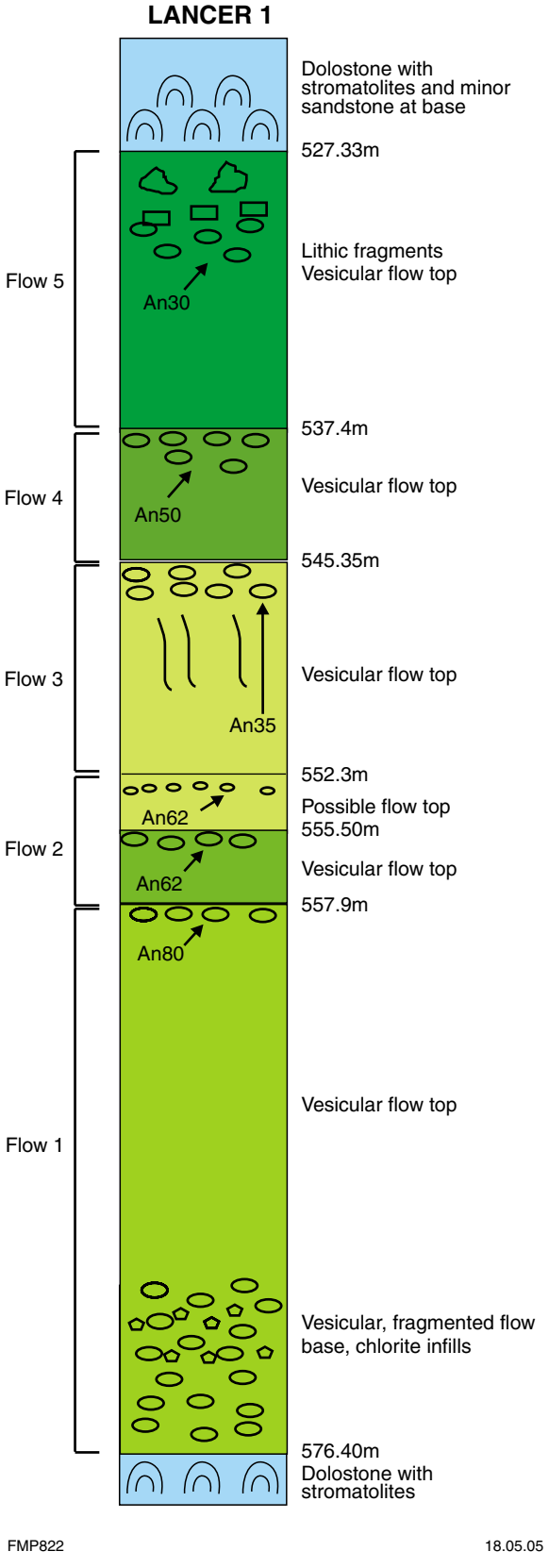

Figure 1. **Schematic log of the Keene Basalt succession cored in Lancer 1. Optically determined plagioclase composition are shown in terms of anorthite content (An)**

Sample No: 193503
Depth: 527.6 m
Petrography: plagioclase laths about 4 to 5 mm long, altered to clay. Illitic and nontronitic or celadonite clays replacing possible pyroxene crystals; serpentinized olivines also present; disseminated skeletal ilmenite.

Sample No: 193504
Depth: 528.1 m
Petrography: 4–5-mm long plagioclase laths, set in a finer grained, plagioclase-rich matrix, all pervasively replaced by clay minerals. Illite and celadonite are the main alteration minerals. Jasper lithic fragments containing spherules possibly represent silica replacement of oolitic carbonate. Chalcedony veinlet.

Sample No: 193505
Depth: 529.25 m
Petrography: section contains fragments of jasper and chert material; aggregate of clays, mostly kaolinite, illite, celadonite and perhaps halloysite. Relic crystal shapes suggest that the clays replace plagioclase laths, olivines, and pyroxenes, forming a microgabbroic texture. Celadonite also forms bright-green irregular patches. Disseminated FeTi oxides and some sulfides.

Sample No: 193506
Depth: 529.7 m
Petrography: fine-grained texture; fresh plagioclase of oligoclase–andesine (An_{30}) composition (optically determined); zoned plagioclase phenocrysts; possible weathered olivine crystals, now replaced by saponite clays; orthopyroxene also present. Interstitial clays. Disseminated FeTi oxides. Minor carbonate alteration.

Sample No: 193507 (Fig. 2a)
Depth: 530.65 m
Petrography: equant plagioclase and pyroxene crystals partially altered to celadonite, with interstitial clays and celadonite; well-zoned kaolinite–celadonite spots probably filling former cavities. Disseminated FeTi oxides. Veinlets of brecciated material.

Sample No: 193508 (Figs 2b and c)
Depth: 532.2 m
Petrography: typical basaltic texture; interlocking plagioclase laths and pyroxene grains with phenocrysts of fresh plagioclase, locally forming glomeroporphyritic bunches. The pyroxene is probably an augite; possible olivine (completely replaced by goethite and saponitic clay and rimmed by FeTi oxides). Interstitial material is mostly kaolinite and celadonite with some goethite (replacing glass). Magnetite blebs and disseminated FeTi oxides.

Sample No: 193509 (Fig. 2d)
Depth: 534.7 m
Petrography: glomeroporphyritic texture; bunches of phenocrysts up to 5 mm across; mineralogy same as 193508. This sample was selected for geochemical analysis.

Sample No: 193510
Depth: 535.45 m
Petrography: plagioclase laths and clinopyroxene with weathered interstitial glass; cut by chalcedonic and calcite veinlets, and some celadonite.

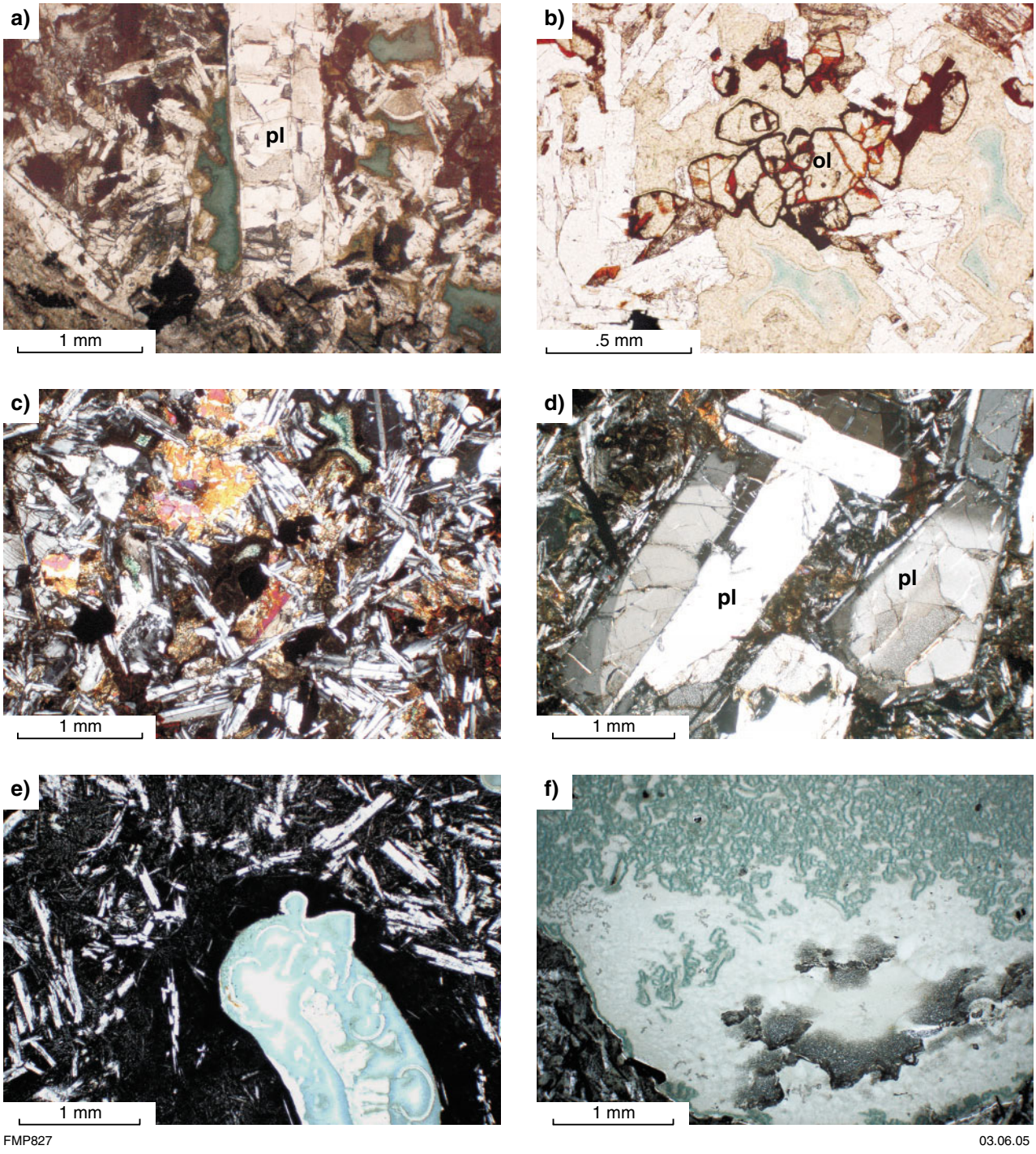

Figure 2. **Photomicrographs: a) sample 193507 — celadonite (green mineral) replacing a plagioclase lath (pl); plane-polarized light; b) sample 193508 — weathered olivine (ol) rimmed by Fe oxides and associated with kaolinite and celadonite patches (brown and green respectively); plane-polarized light; c) sample 193508 — a typically basaltic texture with plagioclase laths and weathered ferromagnesian silicates; crossed polars; d) sample 193509 — a bunch of plagioclase laths (pl) forming a glomeroporphyritic texture; crossed polars; e) sample 193512 — colloform celadonite (green) and chalcedonic quartz, possibly after a fragment of ancient soil (paleosol), surrounded by a chilled margin (black), incorporated in fine-grained glassy basaltic lava; plane-polarized light; f) sample 193513 — zoned amygdale containing chalcedonic quartz and chlorite at top; this can be considered as a geopetal structure indicating stratigraphic top (chlorite, lighter mineral); plane-polarized light**

Sample No: 193511
Depth: 536.15 m
Petrography: lower part of flow 5; large plagioclase laths forming a glomeroporphyritic texture; dark glassy matrix. Abundant disseminated magnetite needles.

Flow 4

Sample No: 193512 (Fig. 2e)
Depth: 537.65 m
Petrography: reddish brown, vesicular and fragmented top of flow 4; intersertal texture; swallow-tail plagioclase (due to rapid quenching) in a devitrified glassy groundmass; large and abundant vesicles (up to 2 cm long) and veins of celadonite, kaolinite, microcrystalline quartz, and chalcedonic quartz. Skeletal magnetite needles and rare sulfide specks (?pyrite). Large blebs of chlorite and celadonite, with ?chilled margins, possibly representing fragments of ?paleosol incorporated into the flowing lava. Fe oxides. XRD analysis of this material identified colloform celadonite, chlorite and chalcedony.

Sample No: 193513 (Fig. 2f)
Depth: 538.8 m
Petrography: middle of flow 4; intergranular texture; plagioclase laths and pyroxene grains (cannot determine whether clinopyroxene or orthopyroxene because of alteration); chlorite and bright-green celadonite as alteration products. Large amygdales contain chalcedonic quartz, celadonite, calcite and microcrystalline quartz; spheroidal composite amygdales show chalcedonic quartz overlain by chlorite; this zoning denotes trapping of fluids and volatiles during solidification of the lava and is a geopetal structure (quartz at base and chlorite at top).

Sample No: 193514
Depth: 539.65 m
Petrography: a vesicular lava in flow 4, possible lower contact with another flow; intersertal texture; plagioclase microlites and microphenocrysts in an altered glassy groundmass; skeletal magnetite crystals; minor green clay alteration (?nontronite); possible pyroxene grains weathered to clays and ?celadonite. Amygdales about 0.5 – 1 cm across, from core to periphery composed of calcite, chalcedony, microcrystalline quartz, or polygonal quartz, and fibrous quartz.

Sample No: 193515
Depth: 541.3 m
Petrography: spotted, greenish coloured basaltic lava; flow 4. Plagioclase laths; optically determined composition is andesine–labradorite (An_{50}); plagioclase microphenocrysts also present; clay altered pyroxene grains and possible olivine; these clay-altered FeMg silicates have networks of FeTi oxides. Magnetite is present as acicular and octahedral crystals.

Sample No: 193516
Depth: 543.15 m
Petrography: bottom-central part of flow 4; basaltic texture; plagioclase laths and clinopyroxene; abundant ilmenite crystals with well-developed exsolution lamellae; unusual zoned clays with yellow-brown rims (kaolinite or ?saponite) to bright-green celadonite.

Sample No: 193517
Depth: 544.8 m
Petrography: towards base of flow 4; glomeroporphyritic texture defined by bunches of plagioclase laths, set in a groundmass of plagioclase microlites and olivine (weathered to iddingsite) with interstitial glass, weathered to a brown clay. Possible pyroxenes (also weathered); disseminated FeTi oxides as acicular crystals and octahedra; networks of these oxides penetrate the weathered glass material.

Flow 3

Sample No: 193518
Depth: 545.8 m
Petrography: near top of flow 3; vesicular basalt; plagioclase rich, optical determinations indicate andesine compositions ($An_{30–35}$); weathered pyroxene and olivine; interstitial Fe oxides and clays after glass material. FeTi oxides as acicular and octahedral crystals; white spots in hand specimen are plagioclase laths.

Sample No: 193519
Depth: 548.2 m
Petrography: middle part of flow 3; intergranular texture; plagioclase laths, clinopyroxene and olivine crystals; little interstitial glass; olivine partly altered to ?saponite. Clays, plagioclase compositions (optically determined) range from andesine to labradorite ($An_{44–54}$). Disseminated skeletal magnetite (altered to hematite) and rare sulfide specks (?pyrrhotite).

Sample No.193520
Depth: 551.45 m
Petrography: middle part of flow 3; plagioclase-phyric; plagioclase laths with optically determined compositions at about An_{72} (bytownite); olivine present, but mostly weathered (?saponite); interstitial brown clays (?illite–kaolinite) probably after glass; abundant FeTi oxides (skeletal magnetite), weathered to goethite. Possible pyroxene, weathered to green clays. Sample selected for geochemical analysis.

Sample No: 193521
Depth: 551.9 m
Petrography: middle part of flow 3; plagioclase laths with bytownite composition (An_{72}) and clinopyroxene in a subophitic texture; olivine weathered to iddingsite; abundant interstitial and irregularly shaped zone of bright-green celadonite; calcite patches. Disseminated acicular and octahedral magnetite crystals.

Sample No: 193522
Depth: 553.8 m
Petrography: mid-bottom part of flow 3; subophitic texture, with plagioclase laths, clinopyroxene and olivine; plagioclase has a composition of about An_{62} (labradorite; optically determined). Olivine is altered to iddingsite. Clays, calcite, zeolite and quartz as alteration/weathering products. Bright-green fibrous clay (?nontronite or ?celadonite). FeTi oxides.

Flow 2

Sample No: 193523
Depth: 556.1 m
Petrography: top-middle part of flow 2; subophitic texture; clinopyroxene, plagioclase, olivine; clinopyroxene subophitically encloses the plagioclase, which has a composition (optically determined) of An_{62} (labradorite). Olivine is altered to clays and reddish brown iddingsite; olivine also present as microphenocrysts. Irregular patches of colloform, clay-like minerals and smaller amounts of calcite, possibly due to weathering of interstitial glass. Disseminated skeletal magnetite.

Flow 1

Sample No: 193524
Depth: 560.7 m
Petrography: near middle-top of flow 1; almost all altered to a mixture of brown clay and chalcedonic quartz; round structures containing opaline silica and chalcedonic quartz are probably former vesicles. Skeletal magnetite and secondary Fe oxides.

Sample No: 193525
Depth: 564.15 m
Petrography: upper-middle part of flow 1; subophitic and glomeroporphyritic texture; clinopyroxene (and possibly orthopyroxene) enclosing plagioclase laths. Plagioclase has a bytownite composition (An_{80}, optically measured and the highest recorded in the section). About 5–7% by volume of olivine, partly altered to iddingsite. Interstitial greenish clays, probably from glass, cut by late celadonite veins. Magnetite and secondary Fe oxides associated with altered olivine.

Sample No: 193526
Depth: 565.9 m
Petrography: middle part of flow 1; glomeroporphyritic textures; plagioclase bunches 2–3 mm across; clinopyroxene and plagioclase laths in a subophitic texture; minor olivine, altered to iddingsite; round structure as in 193525, probably vesicles. Skeletal magnetite crystals up to 5–7% by volume.

Sample No: 193527
Depth: 572.2 m
Petrography: near base of flow 1; subophitic texture, fresh plagioclase, clay-weathered olivine and pyroxene; veinlets of zeolite–quartz and prehnite. Interstitial green clays (?nontronite), probably after glass. Rare sulfides (identified as chalcopyrite and bornite).

Sample No: 193528
Depth: 572.8 m
Petrography: base of flow 1; brecciated, very fine grained, quench texture (skeletal crystals); fresh plagioclase laths and irregular zones of nontronitic clays, associated with low-birefringence zeolite minerals. Skeletal FeTi oxides and small chalcopyrite specks. Lithic fragments (chalcedonic quartz–illite) have a rim of dark glassy material (?quench), suggesting rapid cooling.

Sample No: 193529
Depth: 575.2 m
Petrography: base of flow 1; very fine grained, glomeroporphyritic texture; plagioclase, olivine and pyroxene granules, all pervasively altered; interstitial glass. Plagioclase is altered to chlorite, quartz, and zeolite. Abundant irregular zones or patches of chlorite and zeolite (probably natrolite as sheafs and clusters of fibrous aggregates). No FeTi oxides, but only some small chalcopyrite specks. Lithic fragment on one side of the thin section. Sample selected for geochemical analysis.

Sedimentary footwall

Sample No: 193530
Depth: 576.2 m
Petrography: sedimentary rock at the base of the basaltic succession; microbial laminite; microcrystalline and cryptocrystalline quartz; cross-cutting calcite veinlets; black filaments (?organic); possibly a silicified micritic carbonate.

Discussion

The petrography of these samples indicates that the Keene Basalt in Lancer 1 is a weathered olivine thoeliite. Two minerals are especially common: celadonite and iddingsite. Celadonite is a dioctahedral mica (together with muscovite and phengite), with an ideal composition of $K(Mg,Fe)^{2+}(Fe,Al)^{3+}(OH)^{-2}[Si_4O_{10}]$ and a structure similar to glauconite and of low-temperature paragenesis (Fleet, 2003). Celadonite is commonly found in cavities and veins in basaltic rocks. The presence of celadonite suggests interaction with seawater around volcanic islands, not far from a continental shelf, where glauconitic minerals are being deposited (Einsele, 2000). As such, the presence of celadonite (green marine-clays facies) is indicative of slightly reducing conditions in comparatively shallow seas (Einsele, 2000). Iddingsite, a common alteration product of olivine, is a strongly yellow to reddish brown coloured mineraloid, generally amorphous and containing goethite.

Flows 1 and 2 have calcic plagioclase (labradorite–bytownite), whereas the plagioclase of flows 3, 4, and 5 have oligoclase–andesine compositions. This is suggestive of a differentiation trend to more evolved lavas (less calcic plagioclase; Fig. 1).

The submarine weathered and altered nature of these tholeiitic lavas precludes the use of conventional dating methods (K–Ar, Ar–Ar, or SHRIMP U–Pb). The K–Ar and Ar–Ar systems would be unreliable, whereas no suitable mineral phases (zircons or baddelyite) have been detected for the U–Pb method. Instead, two sandstone samples from the sedimentary units above and below the basaltic succession have been selected for extraction of detrital zircons to be dated by the U–Pb method.

Geochemistry

Three samples (GSWA 193509, 193520, and 193529) were analysed for major and trace elements. Results and analytical methods are given in Table 1. Two samples

Table 1. Major- and trace-element analyses of Keene Basalt samples performed by Geoscience Australia

	Analytical method	*Detection level*	*Sample no. 193509*	*193520*	*193529*
Depth (m)			534.7	551.45	575.7
Flow unit			5	3	1
			Weight percent		
SiO_2	XRF	0.01	48.133	46.719	34.812
Al_2O_3	XRF	0.005	13.659	13.251	12.507
Fe_2O_3T	XRF	0.005	13.825	17.353	20.553
FeO	TITR	0.01	4.164	3.283	12.637
K_2O	XRF	0.005	1.274	1.068	1.076
MgO	XRF	0.01	5.874	5.592	16.33
CaO	XRF	0.005	7.485	5.575	0.496
MLOI	CALC	0.008	4.663	5.237	10.951
MnO	XRF	0.005	0.114	0.093	0.058
Na_2O	XRF	0.01	2.324	2.3	0.689
P_2O_5	XRF	0.005	0.236	0.265	0.201
Fe_2O_3	CALC	0.005	9.198	13.705	6.510
TiO_2	XRF	0.005	2.215	2.357	2.135
SO_3	XRF	0.005	0.05	0.051	0.083
LOI	GRAV	0.010	5.156	5.633	12.407
			Part per million (unless otherwise indicated)		
Ag	ICP-MS	0.01	0.03	0.04	0.01
As	ICP-MS	0.5	2	2.7	2.6
As	XRF	0.5	-0.5	0.7	-0.5
Ba	ICP-MS	2	210	217	48
Be	ICP-MS	0.1	1.1	1.1	0.9
Bi	ICP-MS	0.1	-0.1	0.1	0.1
Cd	ICP-MS	0.1	0.15	0.22	-0.1
Ce	ICP-MS	0.1	43.3	46.55	39.28
Cr	XRF	2	56	138	133
Cs	ICP-MS	0.01	0.41	0.37	0.31
Cu	XRF	1	111	130	112
Dy	ICP-MS	0.01	5.46	5.96	5.53
Er	ICP-MS	0.01	3.06	3.37	2.99
Eu (ppb)	ICP-MS	1	1766	1896	1539
F	XRF	50	778	616	1083
Ga	ICP-MS	0.2	21.3	21.2	18.9
Gd	ICP-MS	0.01	5.97	6.32	5.75
Ge	ICP-MS	0.1	1.8	1.6	1.5
Hf	ICP-MS	0.1	4.5	4.9	4.5
Ho	ICP-MS	0.01	1.13	1.22	1.06
La	ICP-MS	0.02	18.95	20.86	17.93
Lu	ICP-MS	0.01	0.36	0.42	0.34
Mo	ICP-MS	0.005	1	1.3	1.4
Nb	ICP-MS	0.1	14.6	15.8	14.2
Nd	ICP-MS	0.01	25.62	27.74	23.3
Ni	XRF	2	60	88	84
Pb	ICP-MS	0.5	5.9	7.4	3.8
Pr	ICP-MS	0.01	6.2	6.79	5.68
Rb	ICP-MS	1	27.6	27.5	6.8
Sb	ICP-MS	0.1	6.2	1.4	0.4
Sc	XRF	2	33	30	28
Sm	ICP-MS	0.01	5.73	6.38	5.21
Sn	ICP-MS	0.5	2.1	2.3	2.5
Sr	ICP-MS	1	251.8	251	38.2
Ta	ICP-MS	0.1	0.8	0.9	0.8
Tb	ICP-MS	0.01	0.97	1.05	0.98
Th	ICP-MS	0.1	4.5	4.9	3.8
U	ICP-MS	0.1	0.77	0.88	1.1
V	XRF	5	315	293	369
Y	ICP-MS	0.5	28.3	32	25.6
Yb	ICP-MS	0.01	2.59	2.85	2.48
Zn	XRF	1	76	104	134
Zr	XRF	1	160	174.3	154.6

NOTES: XRF: X-ray fluorescence; ICP-MS: Inductively coupled plasma mass spectrometry; CALC: Calculated; GRAV: Measured gravimetrically

MLOI: Measured loss on ignition. %MLOI is calculated by subtracting from 100 the XRF major-element-oxide determinations for SiO_2, TiO_2, Al_2O_3, Fe_2O_3, MnO, MgO, CaO, Na_2O, K_2O, P_2O_5, and SO_3 plus the determinations for trace-element oxides BaO, Cr_2O_3, NiO, CuO, ZnO, Rb_2O, SrO, and ZrO_2 obtained on the same fused disc

LOI: Loss on ignition. %LOI is an indication of the level of volatile components, normally comprising C, CO_2, and H_2O, present in a sample. It is measured gravimetrically by weighing an aliquot of the sample, igniting it, and then reweighing it, noting the weight difference, which is attributed to volatile species. It is calculated by correcting %MLOI for the uptake of oxygen by ferrous iron and sulfur during the sample/flux fusion. During this process FeO is converted to Fe_2O_3 and S is converted to SO_3. The factors used are derived as follows: 2FeO has a molecular weight of 143.7, Fe_2O_3 has a molecular weight of 159.7. This gives a conversion factor of 1.1113 for FeO oxidizing to Fe_2O_3. In other words FeO requires an amount of oxygen the equivalent of 11.13% of its own weight percent to oxidize to Fe_2O_3. SO_3 has a molecular weight of 80 (32 plus 16 × 3, i.e. it is 40% S and 60% O). Since S is most commonly present in a silicate as sulfide, 60% of the SO_3 determination is presumed to be atmospheric oxygen taken up during oxidization. Knowing this, LOI is calculated by the equation: $\%LOI=\%MLOI+(0.1113\times\%FeO) + (0.6\times\%SO_3)$

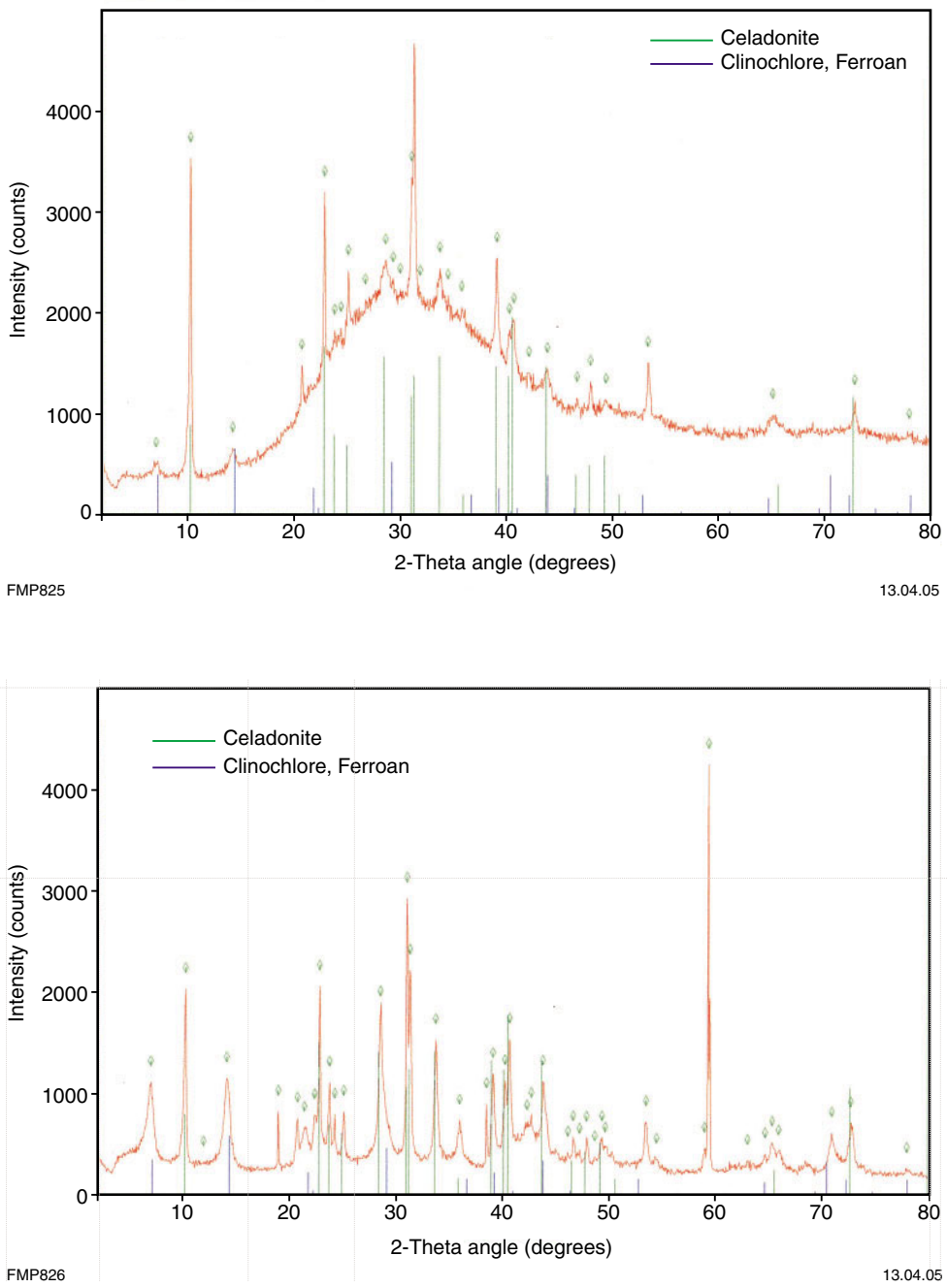

Figure 3. Diffractograms for: a) sample GSWA 193512; and b) GSWA 193513 from flow 4. The main minerals detected are celadonite and ferroan clinochlore

(GSWA 193512 and 193513) were analysed by X-ray powder diffraction (XRPD) and energy dispersive X-ray analysis (EDXRA) on a scanning electron microscope at the Chemistry Centre, Perth. The diffractograms, shown in Figure 3 indicate the presence of celadonite and ferroan clinochlore.

An attempt was made to compare the geochemistry of the Keene Basalt with other intraplate (flood-type) basaltic rocks in Australia. The datasets used are from the mafic sill complexes of the Bangemall Supergroup, including the Glenayle Dolerite, (Morris and Pirajno, 2005) in Western Australia, the Alcurra Dolerite dykes (Glikson et al., 1996) in central Australia, Neoproterozoic mafic dykes from the Mingary 1:100 000 map sheet (South Australia), and the metabasalt of the Wooltana Volcanics in South Australia (Crooks, 2002; Crawford and Hilyard, 1990). The latter two datasets were chosen on the assumption that the dykes and metabasalts of the Adelaide Geosyncline in South Australia (Crawford and Hilyard, 1990) are of the same age as the Gairdner Dyke Swarm (c. 827 Ma; Crawford and Hilyard, 1990; Wingate et al., 1998) and may be correlated stratigraphically with the Keene Basalt. The present geochemical data indicate that the Keene Basalt is an intraplate subalkaline tholeiitic basalt with almost identical composition as the Mingary mafic dykes

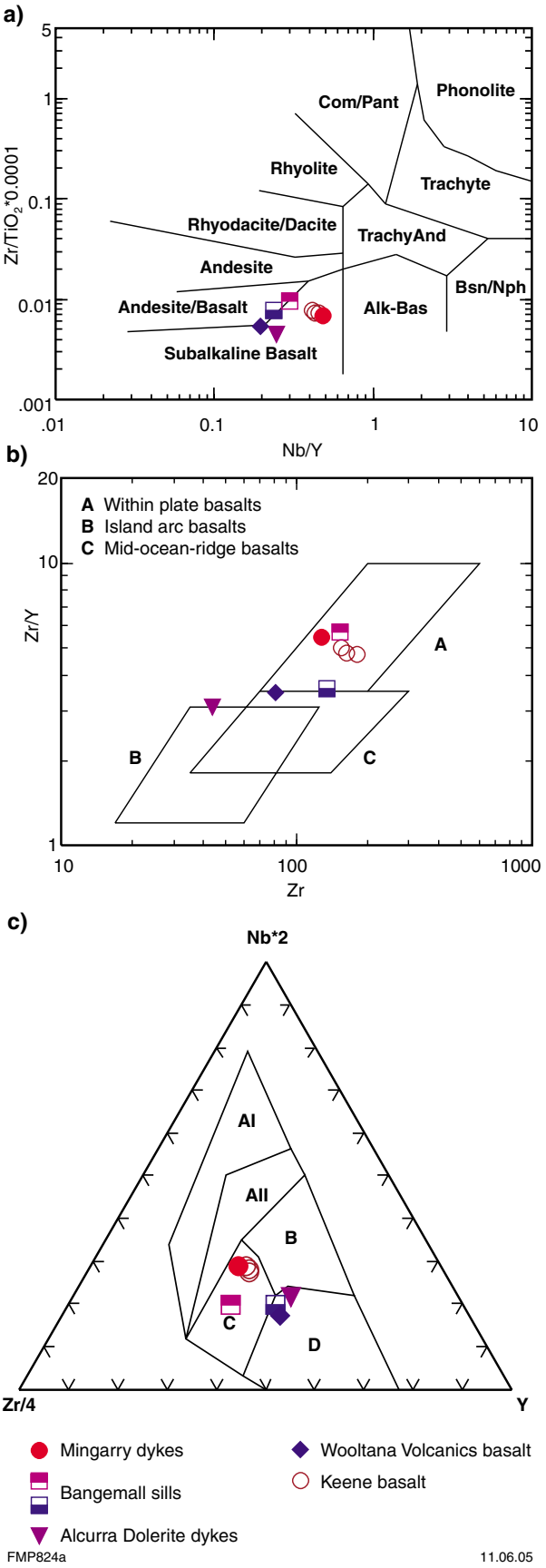

Figure 4. **Diagrams for the discrimination of volcanic rocks after a) Winchester and Floyd (1977); b) Pearce and Norry (1979); and c) Meschede (1986). In all the Keene Basalt plots in the field of within plate subalkaline basalt**

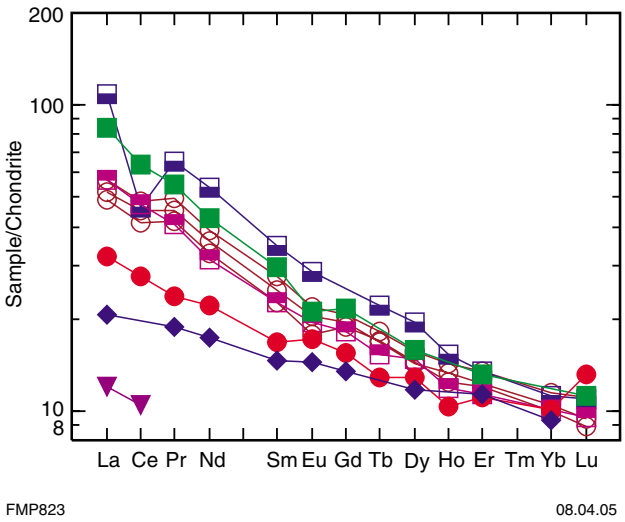

Figure 5. **Rare-earth elements (REE), normalized to chondritic values (after Sun and McDonough, 1989). See Figure 4 for an explanation of symbols, green squares represent the Glenayle Dolerite (Bangemall sills)**

(Figs 4a,b,c). A chondrite-normalized rare earth elements (REE; Fig. 5) plot shows that the Keene Basalt is light rare earth elements (LREE) enriched, with a pattern similar to those of the Bangemall Supergroup sill complexes, but more enriched in LREE than the Mingary dykes and the Wooltana Volcanics metabasalt. This enrichment may be an effect of crustal contamination of primary melts.

The paucity of the available geochemical data does not permit a more rigorous assessment of the geochemical character of the Keene Basalt or a comparative analysis with mafic rocks, assumed to be of the same age. However, the preliminary appraisal presented here confirms that the Keene Basalt is of continental origin and may correlate with the Mingary dykes.

References

CRAWFORD, A. J., and HILYARD, D., 1990, Geochemistry of Late Proterozoic tholeiitic flood basalts, Adelaide Geosyncline, South Australia: The Geological Society of London, Special Publication 16, p. 49–67.

CROOKS, A. F., 2002, Mafic rocks of the Mingarry 1:100 000 map area — a review: Primary Industry and Resources South Australia, Report Book 2002/027.

EINSELE, G., 2000, Sedimentary basins — Evolution, facies and sediment budget: Berlin, Springer, 792p.

FLEET, M. E., 2003, Rock Forming Minerals, Volume 3A, Sheet silicates: micas (2nd Edition): The Geological Society of London, 758p.

GLIKSON, A. Y., STEWART, A. J., BALLHAUS, C. G., CLARKE, G. L., FEEKEN, E. H. J., LEVIN, J. H., SHERATON, J. W., and SUN, S-S., 1996, Geology of the western Musgrave Block, central Australia, with particular reference to the mafic–ultramafic Giles Complex: Australian Geological Survey Organisation, Bulletin 239, p. 41–68.

HAINES, P. W., MORY, A. J., STEVENS, M. K., and GHORI, K. A. R., 2004, GSWA Lancer 1 well completion report (basic data),

Officer and Gunbarrel Basins, Western Australia: Western Australia Geological Survey Record 2004/10, 45p.

MESCHEDE, M., 1986, A method of discriminating between different types of mid-ocean ridge basalts and continental thoeliites with the Nb–Zr–Y diagram: Chemical Geology, v. 56, p. 207–218.

MORRIS, P. A., and PIRAJNO, F., 2005, Mesoproterozoic sill complexes in the Bangemall Supergroup, Western Australia: geology, geochemistry, and mineralization potential: Western Australia Geological Survey Report 99.

PEARCE, J. A., and NORRY, M. J., 1979, Petrogenetic implications of Ti, Zr, Y and Nb variations in volcanic rocks: Contributions to Mineralogy and Petrology, v. 69, p. 33–47.

SUN, S-S., and McDONOUGH, W. F., 1989, Chemical and isotopic systematics of oceanic basalts: implications for mantle compositions and processes: The Geological Society of London, Special Publication 42, p. 313–345.

WINCHESTER, J. A., and FLOYD, P. A., 1977, Geochemical discrimination of different magma series and their differentiation products using immobile elements: Chemical Geology, v. 20, p. 325–343.

WINGATE, M. T. D., CAMPBELL, I. H., COMPSTON, W., and GIBSON, G. M., 1998, Ion microprobe U–Pb ages for Neoproterozoic basaltic volcanism in south-central Australia and implications for the breakup of Rodinia: Precambrian Research, v. 87, p. 135–159.

A preliminary assessment of porosity, permeability, diagenetic history, and possible bitumen in Lancer 1

by

P. J. Hamilton
Department of Applied Geology, Curtin University of Technology[1]

Abstract

Eight core samples from GSWA Lancer 1 were analysed by SEM/EDX or ultraviolet light microscopy, or both, to investigate the origin of the large permeability variations in the sandstones, and whether liquid hydrocarbons had ever been present in the section.

The sandstone porosity is mainly intergranular and well connected, resulting in generally excellent permeabilities. The presence or absence of pore-bridging fibrous illite has a major influence on reduction of permeability with a much lesser influence on porosity reduction, as the pore-bridging habit produces a highly tortuous path for fluid flow. Volumes of other diagenetic cements (quartz, adularia, dolomite, kaolin, halite, sylvite, chlorite–illite mixed-layer clay or illitized chlorite, and anhydrite) are generally low. They are responsible for some reduction in porosity, but could not have been major contributors to the large variations in permeability.

Porosity and permeability measurements may have been compromised by mud-filtrate invasion in some samples. Observed occurrences of halite or sylvite may have originated in this way. Mud-filtrate invasion may also have caused some dissolution of pre-existing diagenetic cements, thus artificially increasing porosity and permeability. Fluid flow in the sandstone units channelled by interbedded low-permeability dolostone barriers is another possible explanation for dissolution of pre-existing diagenetic cements, thereby naturally increasing porosity and permeability.

Some of the observations made on samples indicated the potential presence of hydrocarbons in the core. Generally dull white to yellow-cream fluorescence observed in polished thick sections is ascribed to dolomite-cement. The intensity of the fluorescence appears to correlate with the abundance of the carbonate cement. Brown-coloured smears on sawn surfaces of core at some depths have the appearance of oil stains. However these proved under SEM examination to be the result of contamination with the saw and are comprised mainly of calcite and an iron-oxide mineral. There is no fluid-inclusion or petrographic evidence in the samples analysed to suggest that there had ever been liquid hydrocarbons present in Lancer 1.

Introduction

GSWA Lancer 1 was cored between 104 and 1501.3 m. Eight core samples between 131.9 and 1488.1 m were analysed by scanning electron microscope (SEM) micrographs with energy dispersive X-ray (EDX) spectra and/or ultraviolet light microscopy in order to understand:

1. the very high porosity and permeability in sandstone facies over an interval approximately 1356 m thick;
2. the variation of about two to four orders of magnitude in permeability between samples that differ by only about 5% or less in porosity;
3. the thin fluorescing zones between 861 and 892 m interpreted as hydrocarbons when the core was first examined, brown-coloured smears on sawn surfaces of core at 861 and 869 m thought to be bitumen, and the ubiquitous occurrence in some samples of dark amorphous globules that could be bitumen; and
4. whether liquid hydrocarbons had ever been present in the section.

[1] Present address: Department of Chemical Engineering, University of the West Indies, Saint Augustine, Trinidad and Tobago

Sampling and methods

SEM/EDX analyses of seven samples (Table 1) were undertaken at the Curtin University Electron Microscope Centre using the Phillips XL-30 instrument. Six of the samples were analysed as chips of about 0.5 cm^3 mounted on aluminium stubs and carbon coated. While the carbon coat returns a small carbon signal during the energy dispersive X-ray analysis, this is much less intense than would be recovered from bitumen. In addition, one fluid-inclusion wafer (707.57 m) was gold coated and subjected to SEM/EDAX to ascertain the origin of dark, amorphous globular particles observed in some sections. Thick (80 μm) polished sections of four samples were examined under a petrographic microscope using ultraviolet light for fluorescence and oil-bearing fluid inclusions.

Sandstone porosity and permeability

Figure 1 illustrates the considerable ranges in both porosity and permeability values in the sandstones, and in particular the very large ranges in permeabilities that can exist over relatively small changes in porosity. There is no correlation of these properties with depth. The samples analysed in this study cover much of the cored depth interval and much of the total ranges in porosity and permeability (Table 1). The sandstones are generally quartzose, range from fine- to medium- to coarse-grained, and have little or only minor 'muddy' matrix. Low-magnification SEM images of four of the sandstone samples show that the finest-grained and most poorly sorted sample (193587, 863.4 m) has the lowest permeability (Fig. 2). This indicates that at least some of the variations in porosity and permeability are due to lithological differences. There must be other causes, however, as significant variation in porosity and permeability is evident even in samples that are lithologically very similar.

Some compaction is evident from concavo–convex quartz grain contacts. Compaction would have been more effective in finer grained and more poorly sorted sandstones, such as sample 193587 (863.4 m, Fig. 2c). However, the lack of grain suturing and stylolitization, and the friable nature of a high proportion of the sandstones, suggest that mechanical compaction has never played a major role in control of porosity and permeability development in this section.

Diagenetic history

As neither lithological contrast nor compaction appear to be major causes of the marked contrasts in porosity and permeability, it remains to examine differences in diagenetic history as a possible cause. The diagenetic history inferred from petrographic analysis is discussed below with respect to measured porosity and permeability values for the samples selected. It is clear that some halite and sylvite within pores is due to drilling-fluid invasion, especially as large amounts of KCl (15.5 t) and NaCl (18.95 t) were added to the drilling mud below 217 m and 974 m respectively (Haines et al., 2004, table 1.3).

Sample 193605 (core depth 358.0 m; Wahlgu Formation; red-brown, medium- to coarse-grained sandstone). This sample has the second highest porosity (24%) and second highest permeability (1624 mD) of the four samples selected. SEM images (Figs 2a and 3) and EDX analyses indicate that the major cause for porosity loss was pore-occluding dolomite. Subsequent partial dissolution of some dolomite rhombs is discernible, but could have only slightly enhanced porosity. Some minor, secondary porosity is evident as micro-scale pores within partially dissolved detrital K-feldspar grains (Fig. 3a). Highly corroded grains of potassium chloride (sylvite) represent the last mineral to have formed (Fig. 3b). Some sylvite grains appear to have been moulded on pre-existing cubic or rhombic crystals. Given the observation of partial dissolution of diagenetic dolomite, some sylvite could

Table 1. Sample details

GSWA No.	*Other ID*	*Depth (m)*	*Formation*	*Heϕ %*	*K_{air} mD*	*Method*
193605 (plug offcut)	SEM stub 4	358.0	Wahlgu	24	1 624	SEM-EDX
193594 (plug offcut)	SEM stub 3	708.5	Hussar	13.8	1 380	SEM-EDX
193587 (plug offcut)	SEM stub 2	863.4	Hussar	21.2	252	SEM-EDX
193576 (plug offcut)	SEM stub 1	1202.6	Browne	26.2	9 980	SEM-EDX
181784	Thin section	707.57	Hussar	–	–	UV petrography, SEM-EDX
181785	Thin section	707.76	Hussar	–	–	UV petrography
181774	Thin section and piece of core	861.44 (2 pieces)	Hussar	–	–	UV petrography SEM-EDX
181775	Thin section and piece of core	869.38 (2 pieces)	Hussar	–	–	UV petrography, SEM-EDX

NOTES: SEM: Scanning-electron microscope
EDX: Energy dispersive X-ray
K_{air}: Permeability to air
Heϕ: Porosity measured by helium injection

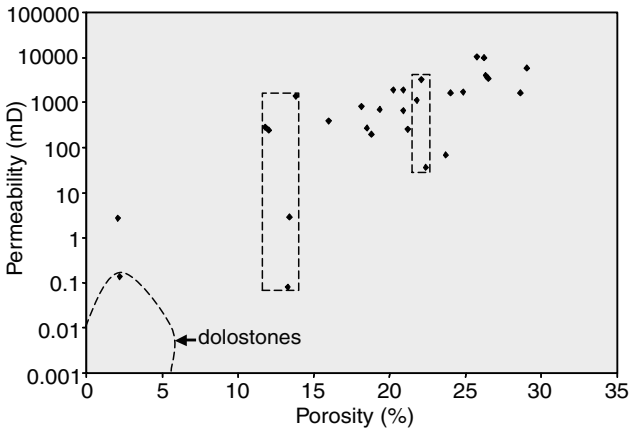

Figure 1. Core plug porosity and permeability values for sandstones. Regions of large permeability variation over small porosity change in sandstones are illustrated by the rectangles. The marked contrast in range of porosity and permeability of interbedded dolostone is also illustrated (most permeability values for dolostones are below 0.1 mD, and cannot be accurately located on the plot). Data from Haines et al. (2004; table 3)

have entirely replaced dolomite grains. It is noted that the inferred dissolution of dolomite prior to the formation of sylvite requires a major change in pore water pH from alkaline to acidic.

Many detrital grains have a thin clay coating (Fig. 3b). High-magnification SEM observations coupled with EDAX analyses that yielded Si>Al>K=Mg>Fe indicate the grain coatings comprise hematite with diagenetic mixed layer chlorite–illite or illitized chlorite (Fig. 3d). Associated with the grain-coating clays are occasional small tabular crystals (Fig. 3d) that yield EDAX spectra dominated by calcium and sulfur, indicating that they are anhydrite.

Sample 193594 (core depth 708.5 m; Hussar Formation; grey, medium- to coarse-grained sandstone). This sample has the lowest porosity (14%), but of the four samples examined, its permeability is not the lowest (1380 mD).

Diagenetic porosity reduction is evident from quartz overgrowths and the filling of some intergranular pore space with diagenetic kaolin booklets (Fig. 4). Some of the kaolin is partly enclosed by quartz cement, indicating that it formed contemporaneously with, and/or subsequent to,

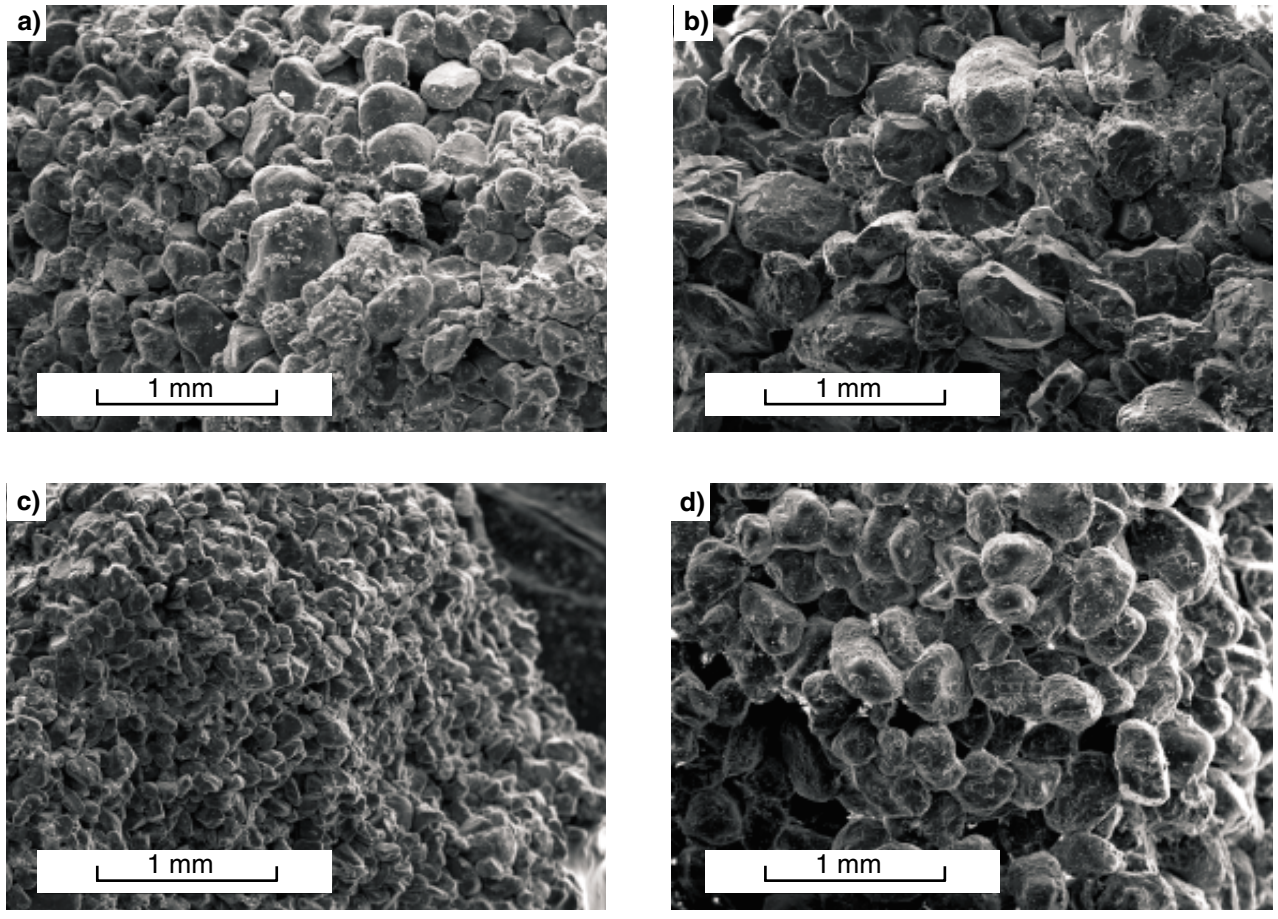

Figure 2. SEM photomicrographs of four sandstone samples showing differences in grain size and sorting, and distribution of interconnected porosity: a) 358.0 m (ϕ = 24%, K = 1624 mD); b) 708.5 m (ϕ = 13.8%, K = 1380 mD); c) 863.4 m (ϕ = 21.2%, K = 252 mD); d) 1202.6 m (ϕ = 26.2%, K = 9980 mD)

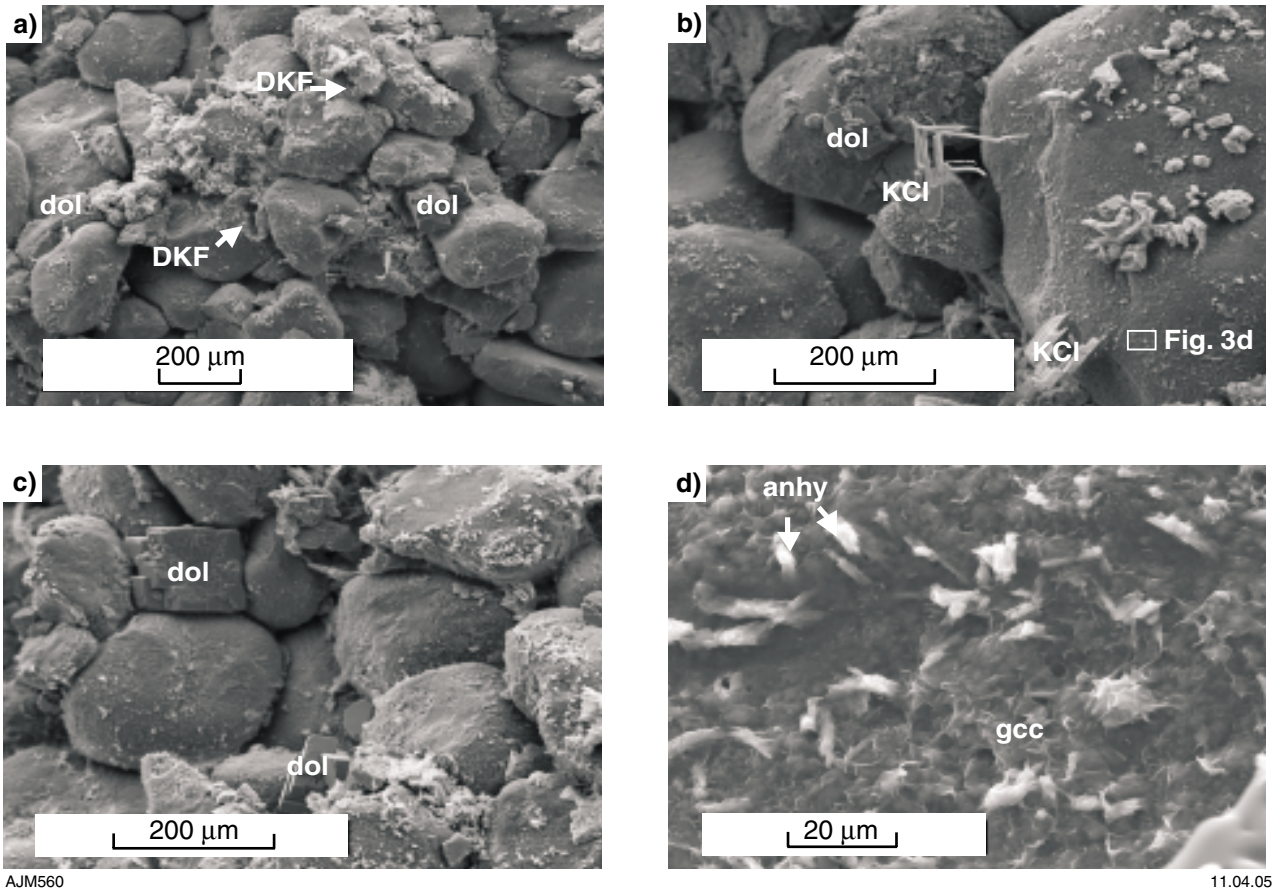

Figure 3. SEM photomicrographs of sample 193605 (358.0 m) illustrating: a)–c) pore-occluding diagenetic dolomite (dol) rhombs; a) partially dissolved detrital K-feldspar (DKF) grains; b) sylvite (KCl); and d) small anhydrite (anhy) crystals overlying grain-coating diagenetic hematite and diagenetic chlorite–illite or chloritized illite (gcc) mixed-layer clay. Note that d) is a high-magnification view of the area indicated in b)

kaolin precipitation (Fig. 4b). The high proportion of pore space that has only been reduced by quartz overgrowths has allowed permeability to remain fairly high through the preservation of interconnected pore space (Fig. 2b).

Sample 193587 (core depth 863.4 m; Hussar Formation; light grey, medium-grained sandstone). Although this sample has a reasonable porosity (21%), it has the lowest permeability (252 mD) of the samples examined. Porosity has been reduced by the formation of quartz and adularia overgrowths (Figs 5c,d) and pore-bridging illite fibres, which are particularly well illustrated in Figure 5e. Volumetrically, neither the quartz nor adularia would be sufficient to explain the marked reduction in permeability compared with other sandstone samples of comparable porosity. The tendency for fibrous illite to extend into and bridge pore space considerably increases the tortuosity for fluid pathways, and thereby considerably reduces permeability with only a relatively minor impact on porosity. Some secondary porosity is evident in occasional detrital K-feldspar grains, which have been altered to fibrous illite and adularia (Figs 5a,b).

Sample 193576 (core depth 1202.6 m; Browne Formation; light brown, medium-grained sandstone). This is the deepest of the four samples examined, yet has the highest porosity (26%) and highest permeability (9980 mD). Crystalline masses of halite (Fig. 6) are ubiquitous throughout this sample and partially coat nearly every grain observed. It appears to be the latest phase formed as it overlies the minor amounts of quartz and adularia that comprise the only other diagenetic phases observed (Figs 6b,c,d). Before the Browne Formation was intersected, the drilling mud was changed from KCl to NaCl in anticipation of encountering and stabilizing salt beds. Consequently, the halite observed may have been precipitated as a result of drilling-fluid invasion of the formation. Measured porosity and permeability values in this and any other similarly affected sample may have been compromised.

Samples 181774 and 181775 (core depths 861.44 m and 869.38 m respectively; Hussar Formation). A significant diagenetic feature observed in these samples is the sporadic distribution of high abundances of dolomite cement (Fig. 7a). This appears to have been the first cement phase to have formed and is possibly contemporaneous with, and related to, the early stages of diagenesis in the dolostones. Where most abundant it precludes all intergranular porosity. Dolomite, where seen in SEM samples, consistently shows dissolution features. It

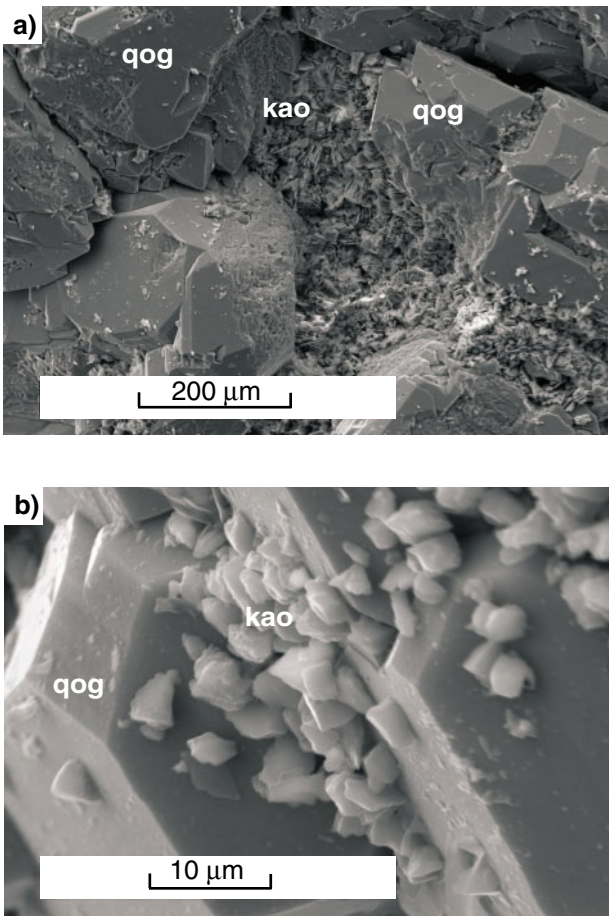

Figure 4. SEM photomicrographs of sample 193594 (708.5 m) illustrating: a) pore-filling kaolin booklets (kao) and quartz overgrowths (qog); and b) the partial enclosure of kaolin plates by quartz overgrowths

is likely that patches of highly abundant dolomite cement as observed in Figure 7a were once much more pervasive and laterally more continuous.

A tentative diagenetic history based on the observations made from this relatively small number of samples is illustrated in Figure 8.

Summary of sandstone porosity and permeability

The reasons for the extreme variability in sandstone porosity and permeability are not completely resolved, although some important controlling diagenetic processes have been identified. The major features of the relationships between porosity, permeability, and diagenesis are:

- The major porosity type is intergranular, which is largely interconnected giving rise to excellent permeabilities. Minor porosity at the microscale is associated with limited grain-coating diagenetic clay between fibres of diagenetic illite and in sparse secondary pores associated with diagenetic alteration of detrital K-feldspar grains.
- The presence or absence of diagenetic fibrous illite with a pore-bridging habit seems the most important factor in generating the marked contrasts in permeability, although it had a much lesser influence on porosity reduction.
- Other diagenetic cements include quartz and adularia (both forming outgrowths and overgrowths), dolomite, kaolin, halite, sylvite, chlorite–illite mixed-layer clay (or illitized chlorite), and trace anhydrite.
- In some samples, mud-filtrate invasion may have precipitated halite or sylvite, thereby possibly compromising the porosity and permeability measurements. Alternatively, the mud filtrate may have dissolved pre-existing diagenetic cements, thus artificially increasing porosity and permeability.
- The lowest permeability zones measured are dominated by dolostone, which could define the upper and lower boundaries of fluid-flow units by acting as barriers to vertical fluid movement between the intervening sandstones. Fluid flow channelled in this manner may have led to dissolution of pre-existing diagenetic cements, thus naturally increasing porosity and permeability. There is an absence of evidence for major amounts of pre-existing diagenetic cements that have been dissolved. It is noted that dolomite is the dominant and abundant cement in the dolostones, and could have been more abundant in the interbedded sandstones where it now is the only diagenetic cement to show dissolution features.

Hydrocarbon migration and entrapment

Distribution and origin of fluorescence

Strong fluorescence under ultraviolet illumination was observed from slabbed core at some depths as illustrated for samples 181774 and 181775 at 861.44 m and 869.38 m respectively (Fig. 9). Generally dull white to yellow-cream fluorescence was also observed in each of the polished thick sections from these samples. The intensity and distribution of the fluorescence correlates with the abundance and distribution of dolomite cement and is therefore ascribed in both core and thick sections to mineral fluorescence.

All four of the thick sections from the Hussar Formation contain abundant opaque particles of dark, amorphous globular appearance (Fig. 7), although A. Cook (*in* Haines et al., 2004) found no evidence of such particles. Further analyses were undertaken as part of this study to determine if these particles are bitumen, and therefore indicate the prior existence of oil in the drilled formations. Four polished thick sections (Table 1) were examined under a petrographic microscope under

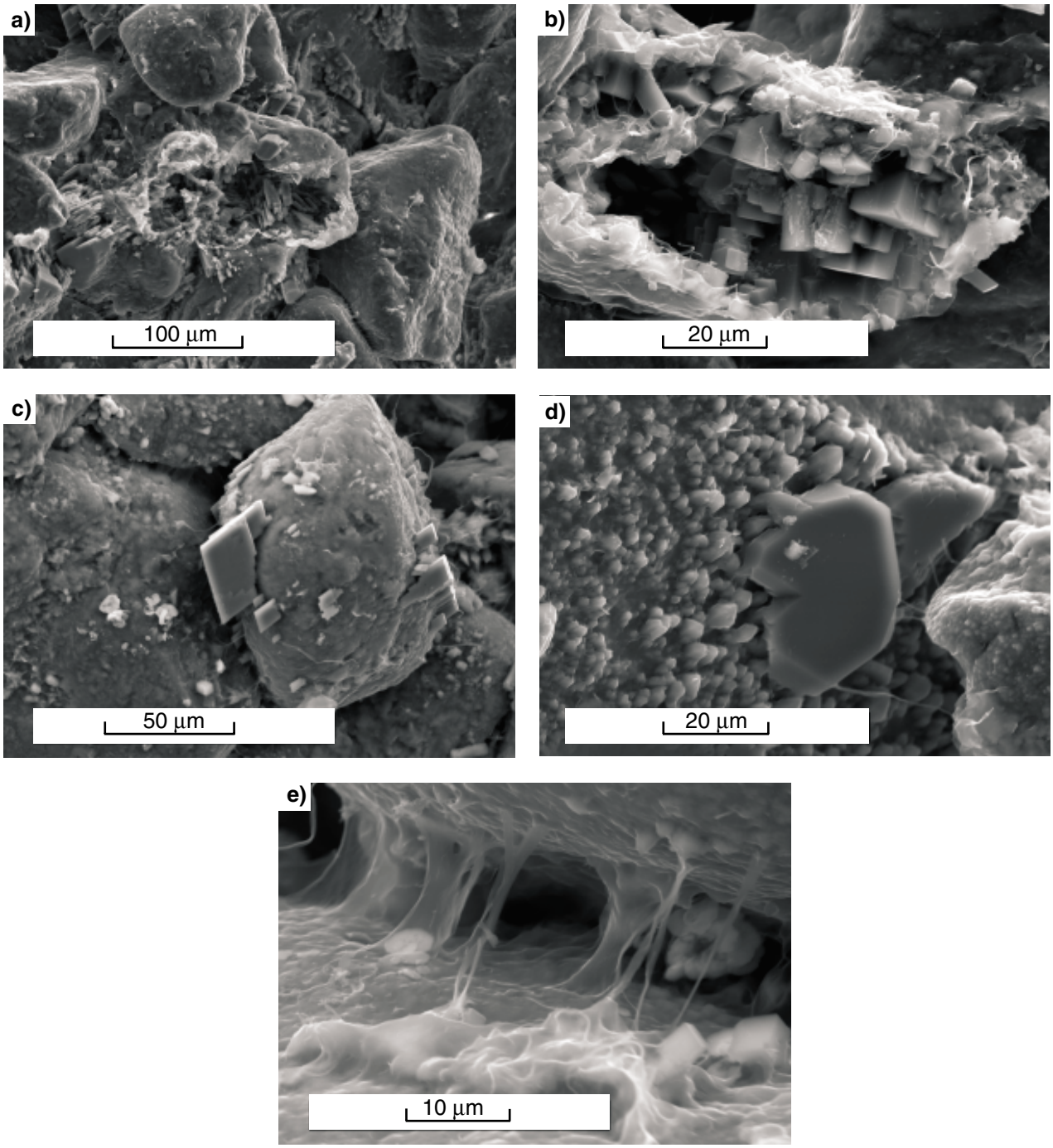

Figure 5. SEM photomicrographs of sample 193587 (863.4 m) illustrating: a) and b) dissolution of detrital grains of K-feldspar with the original grain volumes now occupied by diagenetic adularia rhombs, diagenetic fibrous illite, and secondary porosity; c) small outgrowths and overgrowths of adularia; d) small outgrowths and overgrowths of quartz; and e) fibres of diagenetic illite bridging pore space between two adjacent grains that have thin coatings of small quartz outgrowths and diagenetic chloritic clay

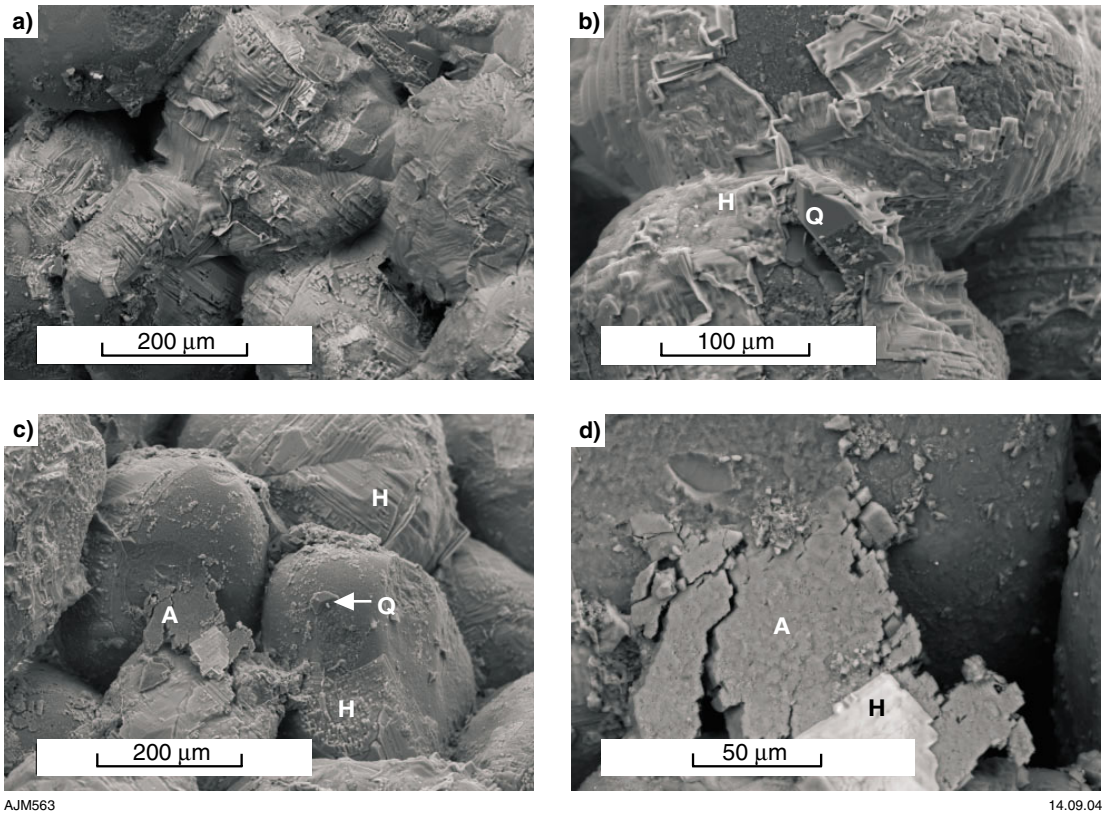

Figure 6. **SEM photomicrographs of sample 193576 (1202.6 m) showing: a)–d) grain-coating halite (H); b) halite overlying quartz cement (Q) and c); adularia (A); d) magnified view of part of c**

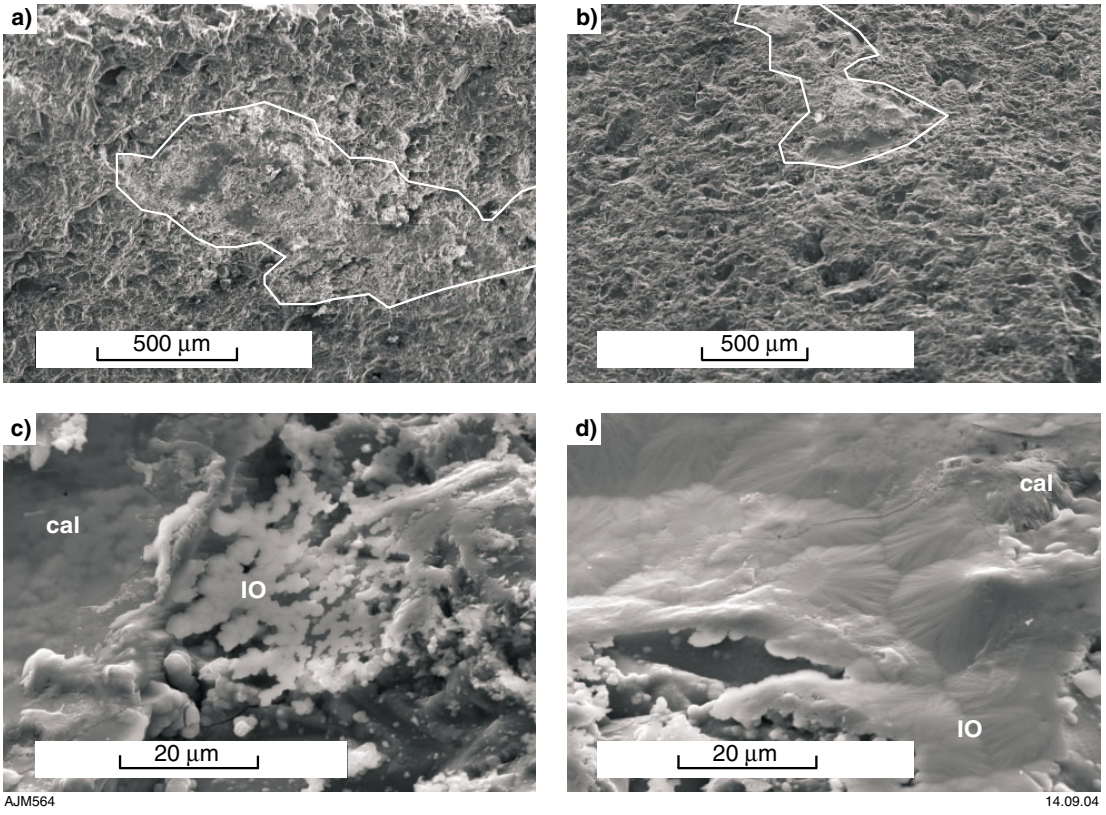

Figure 7. **Magnified binocular microscope views of polished surfaces of thick sections with globular, dark, amorphous matter (outlined in yellow): a) sample 181775 (869.38 m) also showing porosity occlusion by abundant dolomite cement (outlined in white showing the lack of blue dyed intergranular porosity); b) sample 181775 (869.38 m); and c) sample 181774 (861.44 m)**

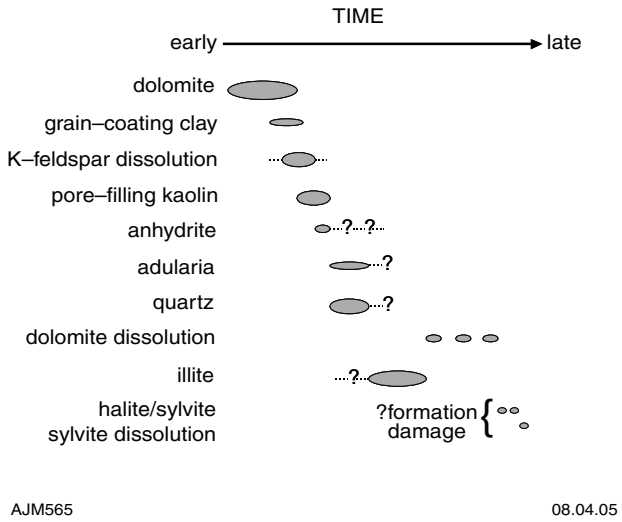

Figure 8. Relative sequence of diagenetic events, Lancer 1

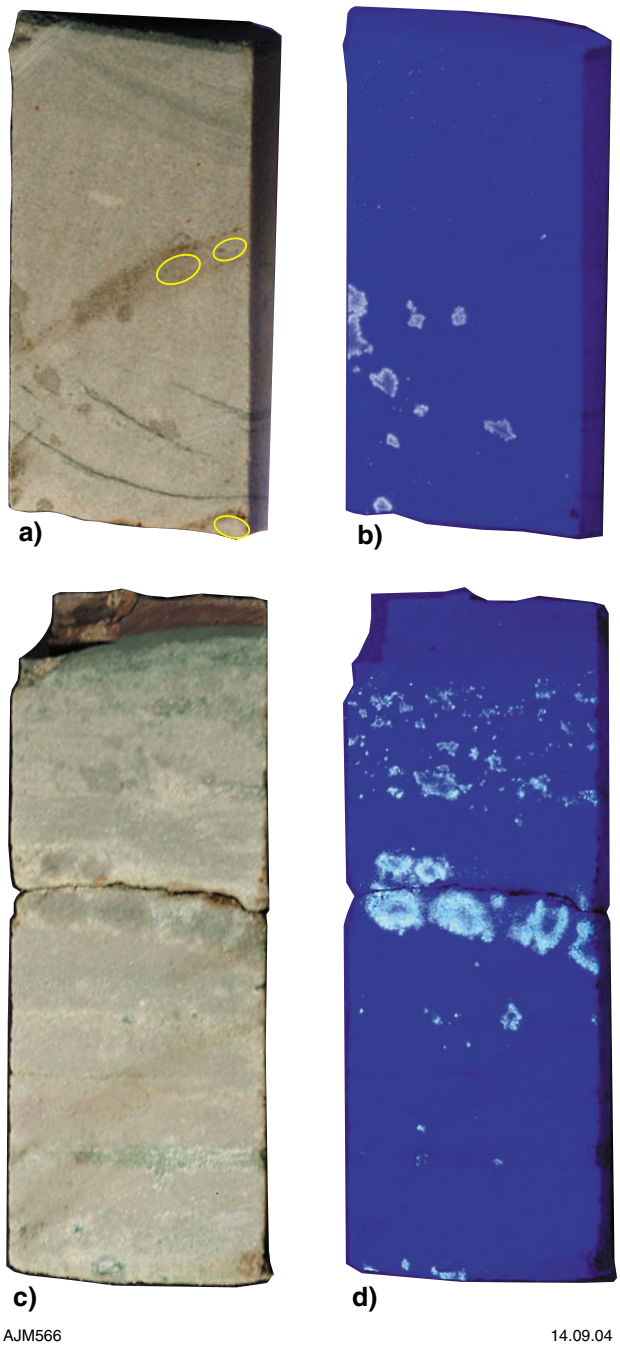

Figure 9. Distribution and intensity of fluorescence on slabbed core surfaces under ultraviolet light compared to the distribution and abundance of dolomite cement. Examples of the brown staining, possibly indicative of oil staining (as discussed in the text), are outlined in yellow

ultraviolet light. Liquid hydrocarbon fluoresces under ultraviolet light, and is readily detected if present in fluid inclusions or absorbed onto mineral surfaces. No such evidence for the present or past existence of oil in the Hussar Formation was revealed.

Fluorescence of the extremely low amounts of extractable organic matter from Lancer 1 sandstone samples have been compared to that of the rod grease used during drilling, which is a potential contamination source (Grice and Dawson, 2005). The grease has a distinctive blue fluorescence under ultraviolet light. This does not match to any of the fluorescence characteristics of the samples examined in this study and is therefore not the origin of these dark globular particles.

The particles were also evident in one of the polished-section samples when examined under the SEM (Fig. 10), but none of the sample chips used for the SEM analyses (described in the previous section) revealed the existence of these particles. The SEM photomicrographs of the polished section (sample 181784, 707.57 m) from near the top of the Hussar Formation clearly illustrate these particles in pore spaces (Fig. 10). They appear to be the last material to have formed in the pore spaces. EDX spectra of these particles are dominated by carbon, as are adjacent areas of the epoxy resin. The particles do not have the appearance of bitumen, and their abundance in sections, but absence from the SEM chips sampled from similar levels, suggests that they may be related to the section-making process. Therefore, it is unlikely that they are bitumen, and are probably an oil or grease contaminant introduced during thick-section manufacture, smeared and concentrated into pore spaces by sawing, grinding, and polishing.

Origin of staining in samples

On the sawn surface of the core between 869 and 892 m (Fig. 9), areas of brown staining were noted. The origin of these were investigated further, particularly in regard to the possibility of these zones containing bitumen. Closer visual inspection revealed these zones to be confined to the sawn surface. SEM observations (Fig. 11) and EDX analyses revealed the stained areas to be comprised of extremely fine grained coatings of calcite and iron oxide. It is suggested that these are a contaminant in some manner introduced from the sawing procedure, and furthermore do not contain any bitumen.

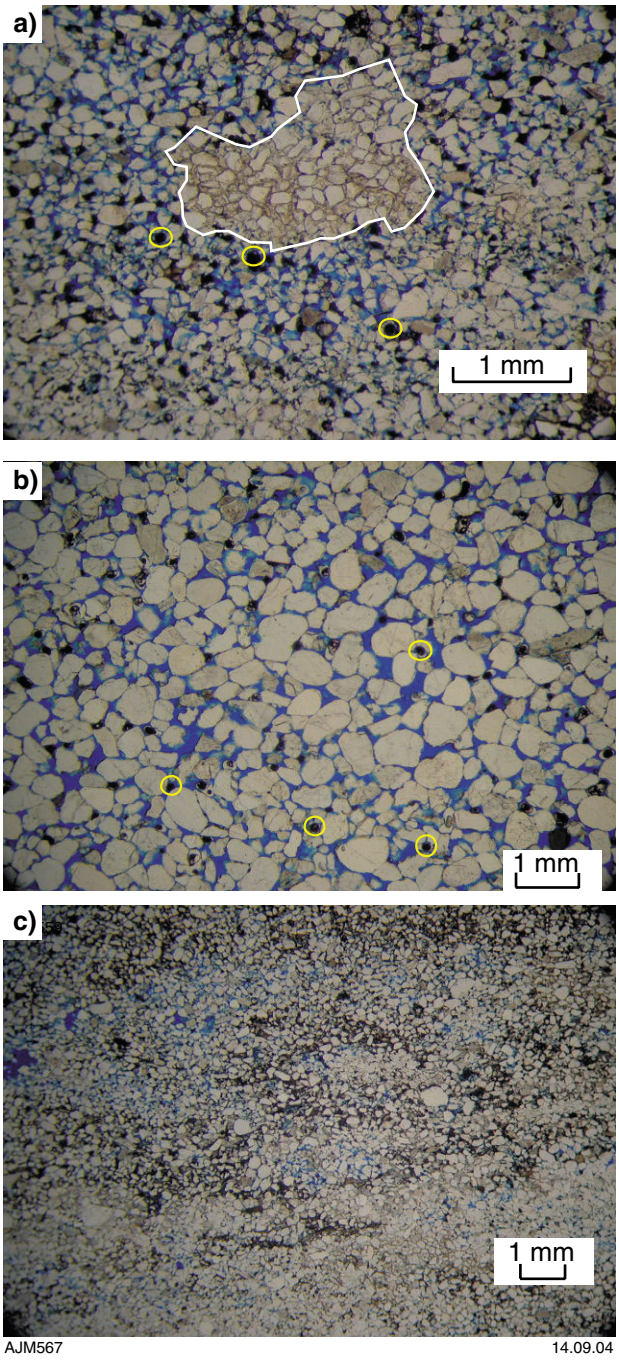

Figure 10. a) and b) SEM photomicrographs of gold-coated polished thick section 181784 (707.57 m) showing abundant dark, rounded particles in pore space. The fine-grained mineral matter in some pore spaces comprises diagenetic kaolin booklets

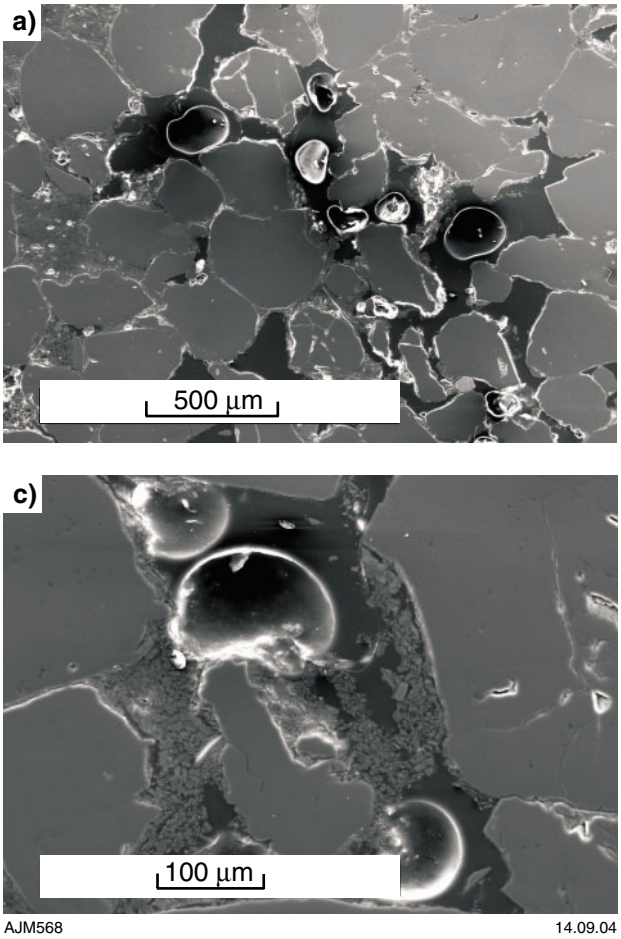

Figure 11. SEM photomicrographs of sawn surfaces of core samples a) 181775, and b) 181774 showing that the areas of brown staining are comprised of extremely fine grained material; c) and d) higher magnification observations of sample 181774 coupled with EDX analysis illustrating that such areas consist of finely crystalline calcite (cal) and iron oxide (IO)

Summary of evidence for hydrocarbon migration and entrapment

A number of possible indicators of the presence of indigenous liquid hydrocarbons in Lancer 1 have proven to be false. White to yellow-cream fluorescence under ultraviolet illumination observed in polished thick sections and in core is ascribed to dolomite-cement fluorescence. Brown-coloured smears on sawn surfaces of core at some depths have the appearance of oil stains. However these proved under SEM examination to be the result of contamination with the saw and are comprised mainly of calcite and an iron oxide mineral. Dark, globular, amorphous particles are of common occurrence in polished sections of more-porous samples and are ascribed to a contaminant introduced during the section-making process. In conclusion it is noted that there is no fluid-inclusion or petrographic evidence in the samples analysed to suggest that there had ever been liquid hydrocarbons present in Lancer 1.

References

GRICE, K., and DAWSON, D., 2005, Biomarkers in drilling fluids, Lancer 1: Western Australia Geological Survey, Record 2005/4, p. 48–53.

HAINES, P. W., MORY, A. J., STEVENS, M. K., and GHORI, K. A. R., 2004, GSWA Lancer 1 well completion report (basic data), Officer and Gunbarrel Basins, Western Australia: Western Australia Geological Survey, Record 2004/10, 39p.

Biomarkers in drilling fluids, GSWA Lancer 1, Officer Basin, Western Australia

by

K. Grice[1] and D. Dawson[1]
[1]ARC/Stable Isotope and Biogeochemistry Group,
Centre for Applied Organic Geochemistry,
Curtin University of Technology, Perth

Abstract

No hydrocarbon products were used in the drilling mud for Lancer 1, but characteristics of two greases used during drilling suggest they are a likely source for the trace hydrocarbons recovered from five core samples.

Introduction

Preliminary molecular characterization (using molecular fossils or biomarkers) by gas chromatography-mass spectrometry (GC-MS) was made to evaluate hydrocarbons reported from core samples of Neoproterozoic age from GSWA Lancer 1. The samples from conglomerate of the Wahlgu Formation and four deeper sandstone samples from the Hussar Formation contained fluorescent zones, which at the well site were associated with a faint smell of hydrocarbons.

Samples and methods

Surface extractions of sandstones and conglomerates

Five sandstone and conglomerate samples (Table 1) provided by GSWA were surface-extracted (before grinding) with a 9:1 mixture of dichloromethane and methanol in an ultrasonic bath for 1.5 hours. Extracts were dried using a heated sand bath. Due to low relative amounts of extract it was not possible to weigh the extracts below a milligram. Whole extracts were analysed by GC-MS (see below for conditions). The whole extracts were then further fractionated into saturate- and aromatic-hydrocarbon fractions by silica-column chromatography involving elution with *n*-pentane (2 mL) and *n*-pentane/dichloromethane (30:70, 2 mL), respectively. The solvent from each fraction was removed on a heated sand bath. The saturate and aromatic fractions obtained for each sample were analysed by GC-MS (see below for details). A blank-surface-extraction procedure was performed and analysed to account for any possible contamination from the work-up procedure (e.g. from solvents, glassware etc.).

Soxhlet extractions

Soxhlet extractions were performed on the four sandstone samples from the Hussar Formation (Table 1). A large proportion of the samples were ground to a fine powder,

Table 1. Lancer 1 sample details

Sample #	*Depth (m)*	*Weight of sample extracted (g)*	*Formation*	*Lithology*
181774	861.44 – 861.57	23.5	Hussar	sandstone
181775	869.38 – 869.50	20.2	Hussar	sandstone
181776	890.17 – 890.32	21.2	Hussar	sandstone
181777	891.83 – 891.98	26.8	Hussar	sandstone
181767	428.6 – 428.7	na	Wahlgu	conglomerate

NOTE: na: not available

and a known quantity (between 20 and 27 g, Table 1) of each sample was extracted by Soxhlet extraction using a 9:1 mixture of dichloromethane and methanol. Extracts were dried using a heated sand bath. Again, due to low relative amounts of extract, it was not possible to obtain a weight. Whole extracts were analysed by GC-MS (see below for conditions). The whole extracts were then further fractionated into saturate- and aromatic-hydrocarbons fractions and by silica-column chromatography involving elution with *n*-pentane (2 mL) and *n*-pentane/dichloromethane (30:70, 2 mL), respectively. The solvent from each fraction was removed on a heated sand bath. The saturate and aromatic fractions obtained for each sample were analysed by GC-MS (see below for details).

ZN50 is a thread grease used on the connections of the 3 m-long drilling rods each time they were connected to the drill string during drilling and while tripping back into the hole after the rods were recovered to the surface (e.g. after a bit change). It is a medium grey colour, and has no fluorescence in long-wavelength ultraviolet light. APXT is a bearing grease used in small quantities at the back end of the core inner tube. It is dark blue, and has dull grey fluorescence with possible very dull white fluorescence in long-wavelength ultraviolet light. Ultrasonic extractions of both grease samples followed the same procedures as for the surface-extracted core samples.

Gas chromatography-mass spectrometry (GC-MS)

The saturate and aromatic hydrocarbon fractions were analysed by GC-MS in both full scan and single ion modes. GC-MS analysis was performed using a HP 5973 MSD interfaced to HP 6890 gas chromatograph, which was fitted with a 60 m × 0.25 mm i.d. column containing a ZB-5 phase (Phenomenex, 0.25 µm phase thickness). The GC oven was programmed from 40 to 325°C at 3°C/min with initial and final hold times of 1 and 40 minutes respectively. Samples were dissolved in hexane and injected using a vapourizing injector (pulsed-splitless mode) using a HP 6890 auto-sampler. Helium was used as the carrier gas at a linear velocity of 28 cm/sec with the injector operating at constant flow. Typically the MS was operating at an ionization energy of 70 eV, a source temperature of 230°C, an electron multiplier voltage of 1800 V, and a mass range of 50 to 550 amu.

Results

GC-MS analyses of saturate hydrocarbon fractions

Typical GC-MS chromatograms of saturate hydrocarbon fractions for the Soxhlet extracts from the core samples are shown in Figure 1 and for the grease samples in Figure 2. All samples are characterized by an unresolved complex mixture (UCM), indicating that the hydrocarbons

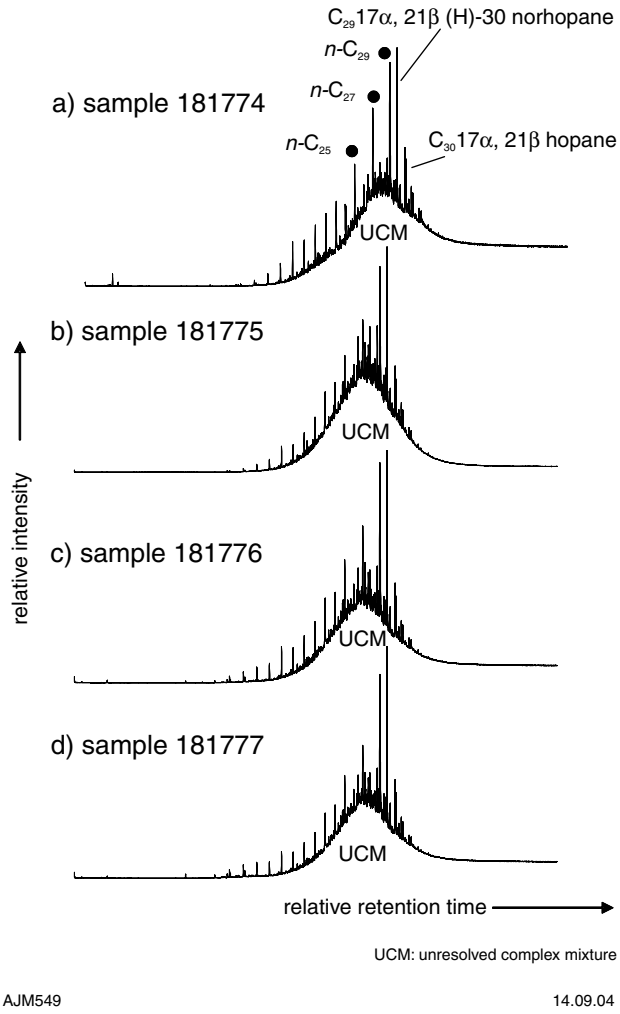

Figure 1. GC-MS chromatograms of saturate hydrocarbons from Soxhlet extracted samples

have been affected by processes such as biodegradation, extensive microbial reworking of the original organic matter, and/or waterwashing (see Trolio et al., 1999 and references therein). There is a low relative abundance of the lower-carbon numbered *n*-alkanes in the chromatograms, but a strong odd/even predominance between *n*-C_{25} and *n*-C_{30} dominated by *n*-$C_{29,}$ and is similar for both core and grease samples. This was not evident from the total-ion chromatogram shown, due to the high unresolved complex mixture in the grease samples, but was evident from mass chromatograms *m/z* 85 and *m/z* 71 (results not shown). This distribution can be attributed to a dominant higher plant source (unlikely for these samples); alternatively, for Neoproterozoic samples, this distribution could be due to anoxygenic photosynthetic bacteria, such as *Chloroflexus* species (Arouri et al., 2000 and references therein).

GC-MS chromatograms of saturate hydrocarbon fractions for the surface extracts (Fig. 3) show similar features to the Soxhlet extracts. However, three of the five core samples contain higher relative amounts of the low-molecular weight *n*-alkanes (except sample 181775).

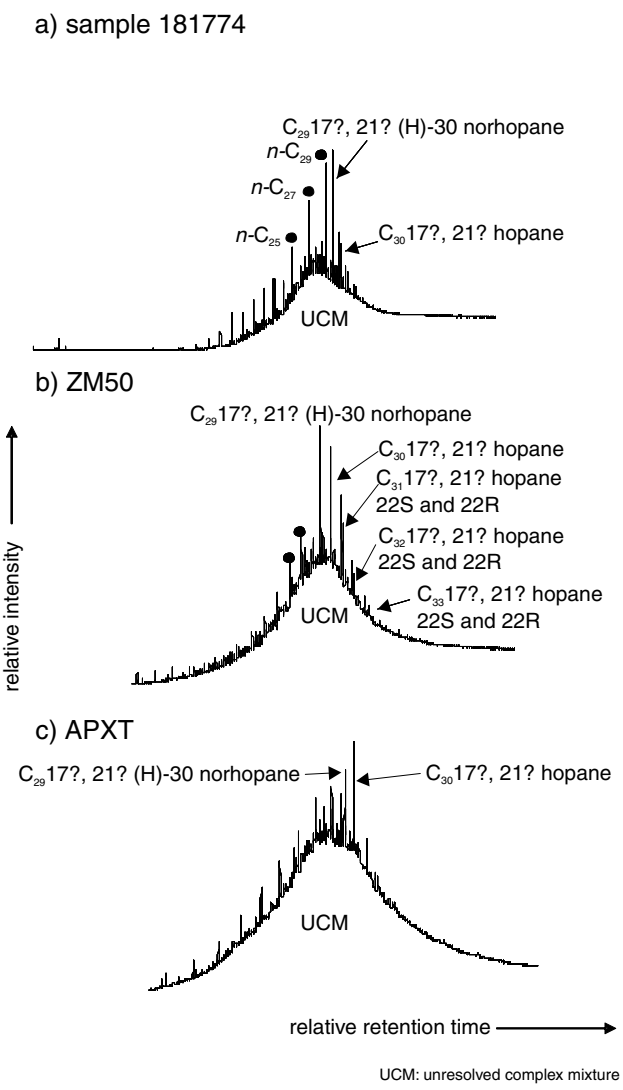

Figure 2. GC-MS chromatograms of saturate hydrocarbons from samples a) Lancer Sandstone (181774), b) ZM50, and c) APXT

Isoprenoid distributions

All samples contain low relative abundances of the acyclic isoprenoids pristane (Pr) and phytane (Ph). These are ubiquitous biomarkers in sediments, coals, and crude oils.

Hopane distributions

The hopane distributions do not vary significantly between the samples. The hopanes are dominated by the C_{30} α,β hopane in the Soxhlet extracts (Fig. 4). Interestingly, the C_{29} 17α,21β(H)-30-norhopane is relatively higher than the C_{30} α,β hopane in the surface extracts, which is quite different to that observed in the Soxhlet extracts (Figs 4 and 5) and the ZN50 (Fig. 6b). This variation might be explained by ZN50 grease dominating the surface extract (Figs 5 and 6b), and APXT grease perhaps dominating the Soxhlet extract (Figs 4 and 6c). The C_{29} 17α,21β(H)-30-norhopane is relatively higher in the sandstone, which is slightly different to that observed in APXT. All samples contain abundant extended hopanes (>C_{31+}), indicating a high cyanobacterial input. Relative abundances of steranes to hopanes are low in the samples and do not appear to significantly differ in their distributions.

Sterane distributions

The steranes are minor components in these samples and consist of C_{27}, $C_{28,}$ and C_{29} demethylsteranes generally dominated by C_{29} homologues, with the exception of the surface and APXT extracts (Fig. 7).

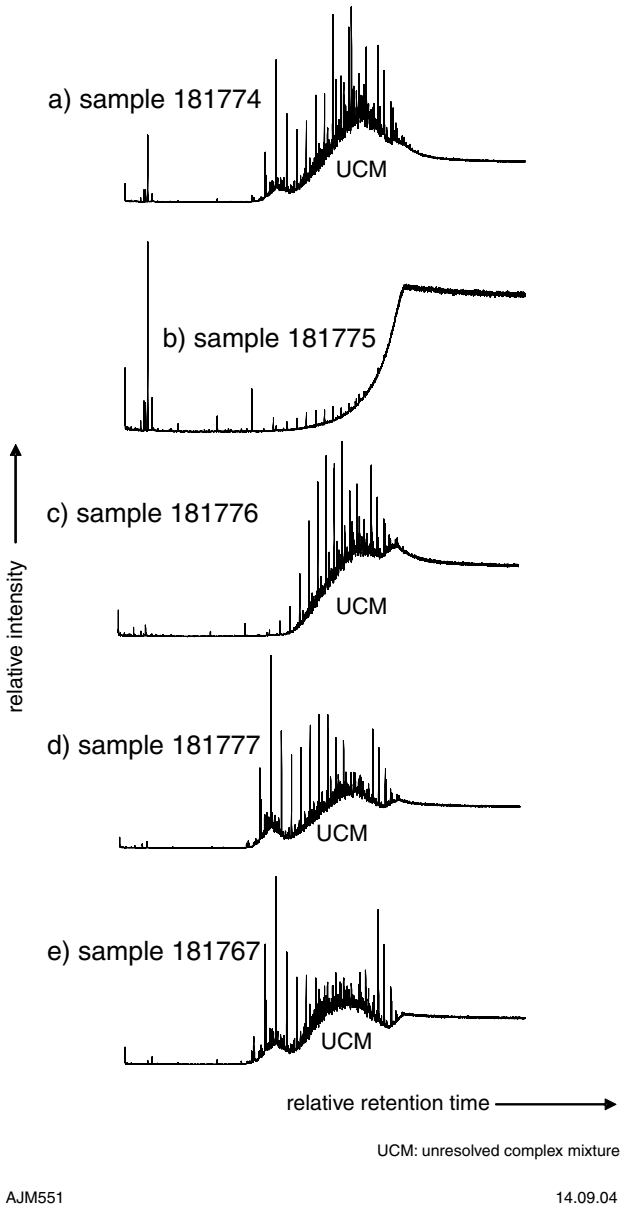

Figure 3. GC-MS chromatograms of surface-extracted saturate hydrocarbons from Lancer 1

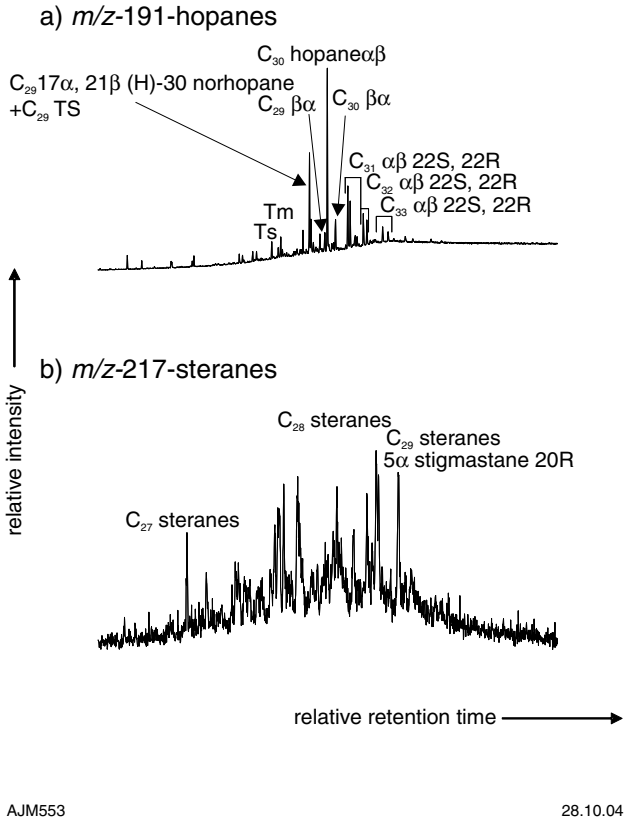

Figure 4. GC-MS chromatograms of saturate hydrocarbon from Soxhlet extract of sample 181774

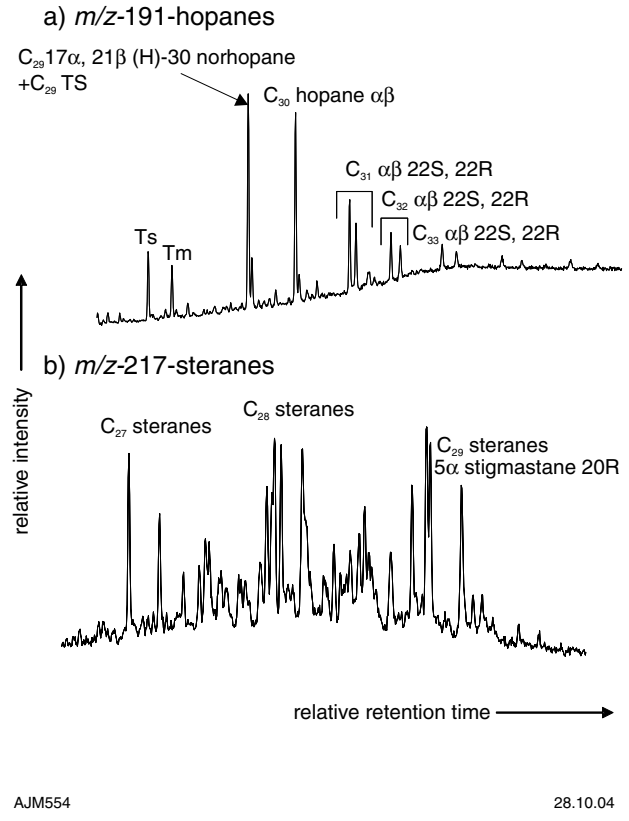

Figure 5. GC-MS chromatograms of saturate hydrocarbon from a surface extract of sample 181774

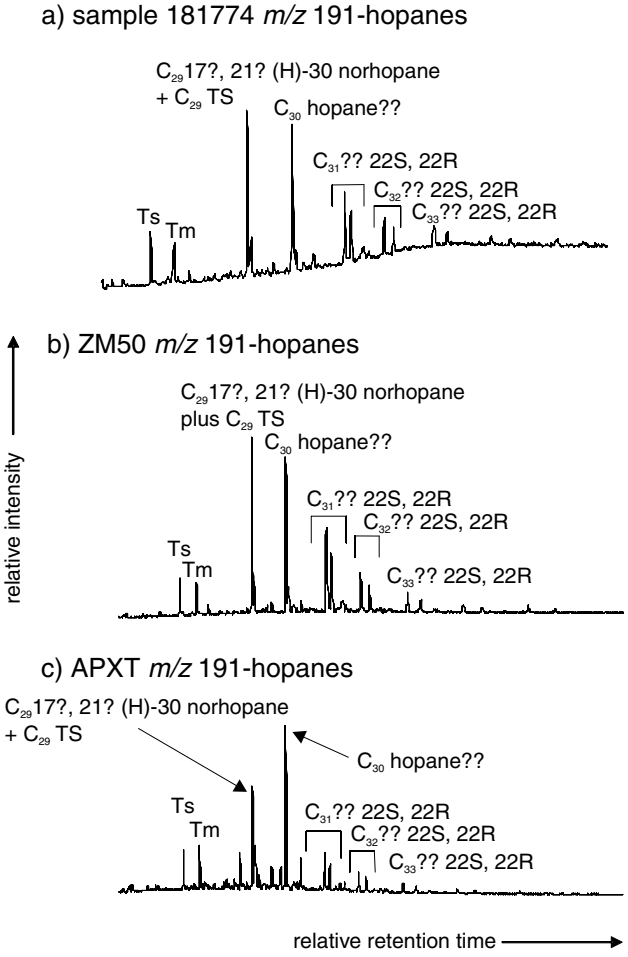

Figure 6. GC-MS chromatographs of saturate hydrocarbons (hopanes) from a) sample 181774, b) ZM50, and c) APXT

C_{29} sterane/C_{30} hopane ratios

The low C_{29} sterane/C_{30} hopane ratios (Table 2) are typical of high microbial inputs (i.e. cyanobacteria). Higher ratios have been reported in Neoproterozoic strata (McKirdy and Imbus, 1992); however, they are not common in pre-Phanerozoic rocks. In general, the C_{29} sterane/C_{30} hopane ratio is slightly higher in the surface extracts.

C_{31} (22S)/(C_{31}22S+22R) hopane ratios

The $C_{31}(22S)/(C_{31}\ 22S+22R)$ hopane ratios (Table 3) indicate the samples have reached a high level of thermal maturity. Samples showing ratios in the range 0.57 to 0.62 indicate that the main phase of oil generation has been reached or surpassed (Peters and Moldowan, 1993).

Branched alkanes

Extracts from the Lancer 1 sandstones were scrutinized for the presence of unusual branched alkanes, which have

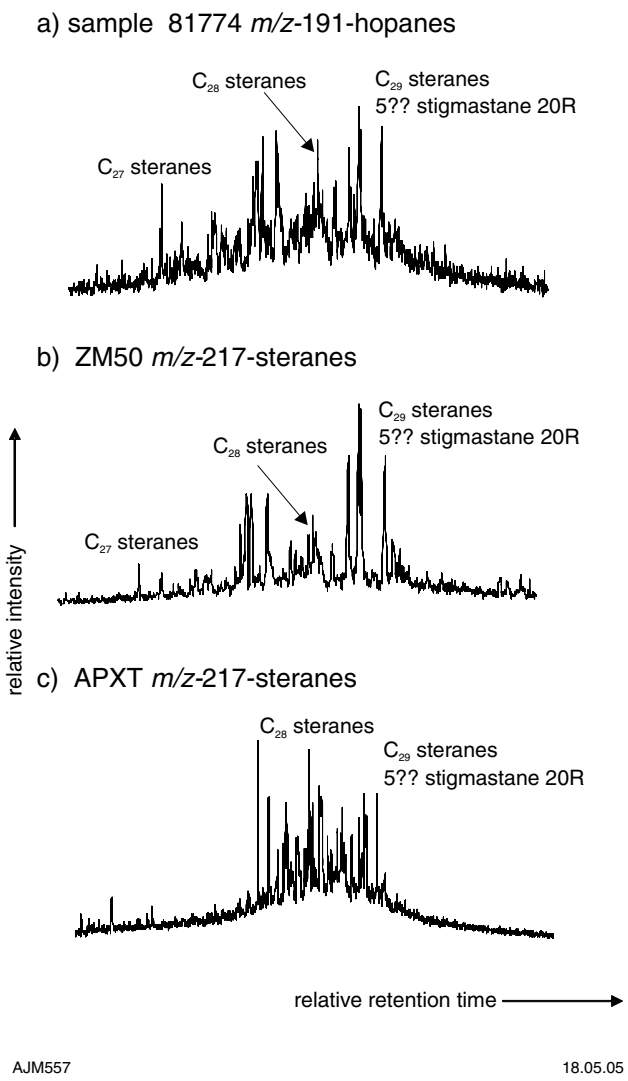

Figure 7. GC-MS chromatographs of saturate hydrocarbons (steranes) from a) sample 181774, b) ZM50, and c) APXT

been found previously in Neoproterozoic sedimentary rocks of the Officer Basin (see Arouri et al., 2000; Greenwood et al., 2003), but these compounds were not present in any of the samples.

GC-MS analyses of aromatic hydrocarbon fractions

Typical GC-MS chromatograms of aromatic hydrocarbon fractions for the Soxhlet extracts and for the surface extracts are shown in Figures 8 and 9, respectively. None of the samples (including greases) appear to contain significant quantities of resolved aromatic hydrocarbon components. Aromatic hydrocarbons from surface extracts show some saturate-hydrocarbon components, probably due to the low levels of aromatics in the samples and relatively higher levels of saturate hydrocarbons. Fluorescence of the samples might be attributed to an aromatic unresolved complex mixture.

Table 2. C_{29} sterane/C_{30} hopane ratios for Lancer 1 samples

Sample	*Soxhlet C_{29} sterane/C_{30} hopane*	*Surface extract C_{29} sterane/C_{30} hopane*
181774	0.08	0.11
181775	0.07	na
181776	0.08	0.15
181777	0.05	0.13
181767	na	0.10

NOTE: na: not available

Table 3. (C_{31} 22*S*)/(C_{31} 22*S*+22*R*) hopane ratios for Lancer 1 samples

Sample	*Soxhlet*	*Surface extract*
181774	0.57	0.59
181775	0.57	na
181776	0.57	0.57
181777	0.57	0.58
181767	na	0.59

NOTE: na: not available

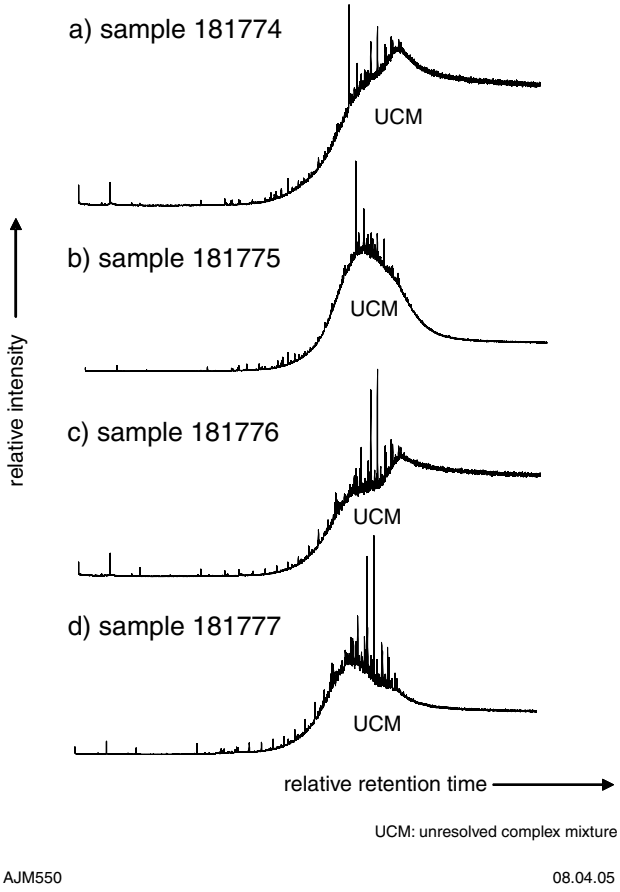

Figure 8. GC-MS chromatograms of aromatic hydrocarbons from Soxhlet extracted samples

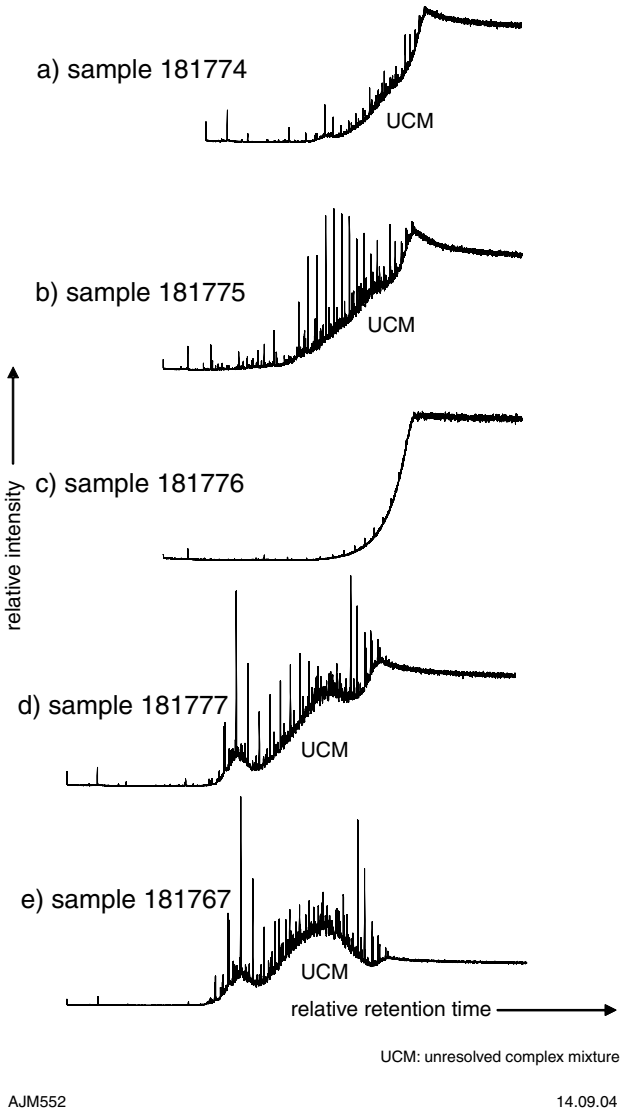

Figure 9. GC-MS chromatograms of aromatic hydrocarbons from surface extracted samples

Discussion

The level of hydrocarbons in these clastic samples was extremely low (less than a microgram), and was insufficient for stable carbon-isotope analysis of individual hydrocarbons using gas chromatography – isotope ratio mass spectrometry. Contamination during drilling was evaluated by comparing the molecular characterization of two greases (ZN50 and APXT) — the only hydrocarbon products used during drilling of Lancer 1. The GC-MS results for ZN50 and APXT materials show a similar distribution of hydrocarbons to those reported in the core samples. The grease samples contain a low relative abundance of the lower-carbon numbered *n*-alkanes, an odd/even predominance between *n*-C_{25} and *n*-$C_{30,}$ an unresolved complex mixture, and similar distributions of hopane and sterane biomarkers. The trace hydrocarbons recovered from the clastic samples were most similar to those from the ZN50 thread grease and, to a lesser extent, the APXT bearing grease. Therefore conclusions about the characteristics of the hydrocarbons extracted from the clastic samples should be viewed with caution, as some or all of the hydrocarbons are likely to be contamination.

Biomarker ratios suggest that the samples have reached a high level of thermal maturity, whereas analyses by A. Cook (Table 2 in Haines et al., 2004) indicate the section is still within the oil window. The extracts are all characterized by an unresolved complex mixture that is expected from processes such as biodegradation, extensive microbial reworking of the original organic matter, and/or water washing. The low relative abundance of the lower-carbon numbered *n*-alkanes and the strong odd/even predominance between *n*-C_{25} and *n*-C_{30} dominated by *n*-C_{29} could be attributed to a dominant higher plant source or anoxygenic photosynthetic bacteria such as *Chloroflexus*. Given the thermal maturity of these samples, the odd/even predominance is unusual, but this feature has been observed previously in Neoproterozoic samples with large unresolved complex mixtures. There is also an unusual lack of GC resolved aromatic hydrocarbons in the samples; GC resolved aromatic hydrocarbons are usually present in crude oils and sediments. The samples are characterized by biomarkers indicative of a high microbial input (i.e. cyanobacteria). Unusual branched alkanes, which have been found previously in Neoproterozoic sedimentary rocks of the Officer Basin, were not detected in any of the samples.

References

AROURI, K., CONAGHAN, P. J., WALTER, M. R., BISCHOFF, G. C. O, and GREY, K., 2000, Reconnaissance sedimentology and hydrocarbon biomarkers of Ediacaran microbial mats and acritarchs, lower Ungoolya Group, Officer Basin: Precambrian Research, v. 100, p. 235–280.

GREENWOOD, P. F., AROURI, K. R., LOGAN, G. A., and SUMMONS, R. E., 2004, Abundance and geochemical significance of C_{2n} dialkylalkanes and highly branched C_{3n} alkanes in diverse Meso- and Neoproterozoic sediments: Organic Geochemistry, v. 35, p. 1211–1222.

HAINES, P. W., MORY, A. J., STEVENS, M. K., and GHORI, K. A. R., 2004, GSWA Lancer 1 well completion report (basic data), Officer and Gunbarrel Basins, Western Australia: Western Australia Geological Survey, Record 2004/10, 39p.

McKIRDY, D. M., and IMBUS, S. W., 1992, Precambrian petroleum: a decade of changing perceptions, *in* Luminescence Microscopy: quantitative and qualitative aspects *edited by* M. SCHIDLOWSKI, S. GOLUBIC, M. M. KIMBERLEY, D. M. McKIRDY, and P. A. TRUDINGER: SEPM Short Course 25, p. 37–57.

PETERS, K. E., and MOLDOWAN, J. M., 1993, The Biomarker Guide. Interpreting molecular fossils in petroleum and ancient sediments: New Jersey, Prentice Hall, 363p.

TROLIO, R., GRICE, K., FISHER, S. J., ALEXANDER, R., and KAGI, R. I., 1999, Biphenyls and diphenylmethanes as indicators of petroleum biodegradation: Organic Geochemistry, v. 10, p. 1241–1254.

Composition of mudrocks from GSWA Lancer 1, Officer and Gunbarrel Basins, Western Australia

by

M. D. Raven[1] and D. N. Dewhurst[2]
[1]CSIRO Land and Water
[2]CSIRO Petroleum

Abstract

X-ray diffraction and fluorescence spectrometry of Neoproterozoic and Carboniferous mudrocks from the Lancer 1 stratigraphic drillhole show that the major mineral phase present in almost all samples is illite, although orthoclase is common from the Kanpa Formation downwards. The Wahlgu Formation and some Hussar Formation mudrocks contain significant quantities of dolomite. Apart from the Paterson Formation, these mudrocks are relatively coarse grained (generally <30% clay fraction) and their clay contents are moderate (generally >40%). Cation-exchange capacities are consistent with other illite-rich mudrocks apart from one sample, which contains smectite. Potassium (K_2O) and iron (Fe_2O_3) contents are high as would be expected for a suite of mainly red illitic mudrocks.

Introduction

Thirteen mudrock samples from Lancer 1 (Fig. 1, Table 1) were preserved in oil for future geomechanical testing by CSIRO. This paper deals with the mineralogy and chemical composition of these samples, as this is an important starting point for understanding mudrock geomechanics. Future documents will cover geomechanical and acoustic testing of these samples in order to characterize sealing properties and seismic response, and the change in these properties with varying stress and pore pressure. All depths reported are core depths unless otherwise specified.

Methodology

The mineralogy of the mudrock samples was determined on both whole rock and the <2-µm fraction by X-ray diffraction (XRD). Bulk samples were pre-ground for 15 seconds in a tungsten-carbide mechanical mill to pass through a 0.5-mm sieve. A 0.5 g subsample was further ground for 8 minutes in a McCrone micronizing mill under ethanol. The resulting slurry was oven dried at 60°C then thoroughly mixed in an agate mortar and pestle before being lightly pressed into aluminium sample holders for X-ray diffraction analysis.

The remaining bulk samples were shaken for 10 minutes with 10 ml of a 10% solution of sodium hexametaphosphate and deionized water. The slurries were then repeatedly dispersed and centrifuged to recover all of the <2-µm fractions. The suspensions were treated with acetic acid to remove carbonate minerals, twice calcium saturated (using 1M $CaCl_2$), washed with water then alcohol, and oven dried at 60°C. These powders were then lightly pressed into aluminium sample holders to maintain a random orientation of the mineral particles for XRD analysis.

Subsamples (each 120 mg) of the <2-µm powders were redispersed in deionized water and the suspensions placed under vacuum onto two cellulose nitrate filter discs to maximize the random orientation of the platy clay-mineral particles. One of these oriented samples was saturated with glycerol to aid identification of the clay-mineral components by XRD. The other, saturated with barium (using 1M $BaCl_2$), was analysed by X-ray fluorescence spectrometry (XRF) to determine the cation-exchange capacity and major-element chemistry of the clay fractions.

X-ray diffraction patterns were recorded with a Philips PW1800 microprocessor-controlled diffractometer using Co-K_α radiation, variable divergence slit, and graphite monochromator. The diffraction patterns were recorded in steps of 0.05° 2θ every 1.0 second, and logged to data files for quantitative analysis with SIROQUANT from Sietronics Pty Ltd. The data were first background subtracted and calibrated for the automatic divergence slit. The results were normalized to 100%, and hence do not include unidentified or amorphous materials. Note that the numbering and names in the key at the top left of the diffractograms in Appendix 1 are from the International

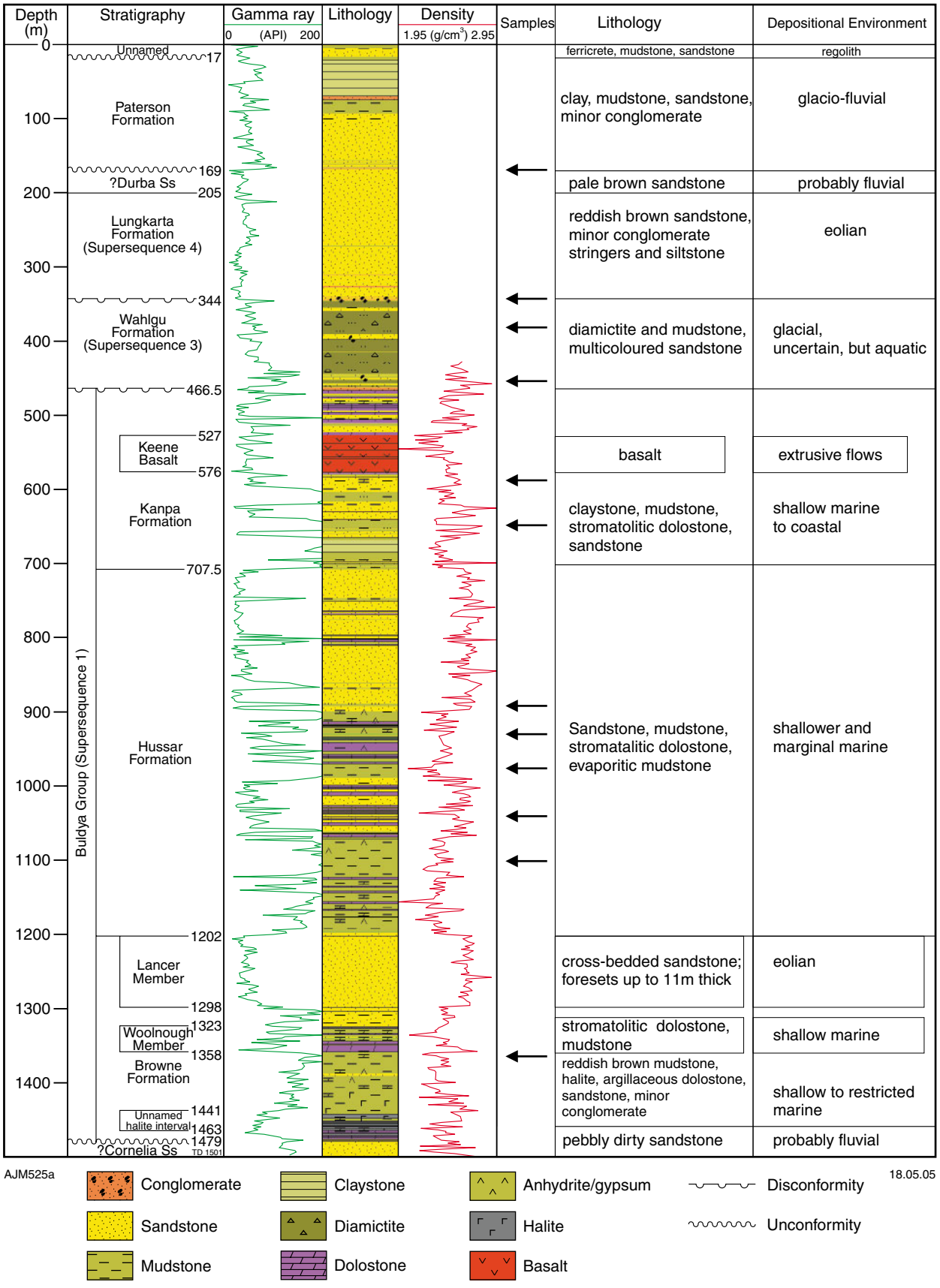

Figure 1. Stratigraphy in Lancer 1 (modified from Haines et al., 2004). Arrows indicate the mudrock samples analysed for this study

Table 1. Mudrock samples from Lancer 1

GSWA sample no.	*Depth (m)*	*Formation*	*Basin*	*Core type and size (mm)*
181722	166.40 – 166.60	Paterson	Gunbarrel	PQ, 85–
181723	347.25 – 347.50	Wahlgu	Officer	PQ, 85
181724	389.00 – 389.20	Wahlgu	Officer	PQ, 85
181768	456.46 – 456.83	Wahlgu	Officer	HQ, 63.5
181769	500.88 – 501.05	Kanpa	Officer	HQ, 63.5
181770	603.56 – 603.79	Kanpa	Officer	HQ, 63.5
181771	665.47 – 665.76	Kanpa	Officer	HQ, 63.5
181778	900.85 – 901.10	Hussar	Officer	HQ, 63.5
181779	930.73 – 931.01	Hussar	Officer	HQ, 63.5
181780	970.02 – 970.22	Hussar	Officer	HQ, 63.5
181781	1 027.73 – 1 027.95	Hussar	Officer	HQ, 63.5
181782	1 114.56 – 1 114.86	Hussar	Officer	HQ, 63.5
181783	1 358.69 – 1 358.89	Browne	Officer	HQ, 63.5

Centre for Diffraction Data (ICDD) database of standard XRD patterns. The 'syn' refers to the pattern in the database being from a synthetic mineral. Most, if not all, mineral phases have other elements in them, so synthetic pure patterns are usually preferred over natural specimens for identification purposes.

Results and discussion

In terms of bulk mineralogy, the sample from the Paterson Formation is dominantly illite (48%), together with 2M1 muscovite and quartz (Table 2). It has a clay fraction (i.e. <2-μm fraction) of 52% and a high clay content (i.e. amount of clay minerals) of 59%. It also has a high proportion of hematite (7%), as do many of the clays analysed in these tests, which explains the red coloration. The clay fraction contains mainly illite and muscovite, together with much of the hematite (Table 3). This sample has the lowest cation-exchange capacity of all the mudrocks tested due to its low illite content and high mica content, as compared to the other clays. In terms of chemistry of the clay fraction, this sample is the most silica poor and the most iron rich, with much of the iron incorporated into hematite and chlorite (Table 4).

The bulk mineralogy of the three Wahlgu Formation mudrock samples (Table 2) is dominated by illite (40–49%) and quartz (18–30%), but this formation is also highly dolomitic (13–25%). Total clay content has a range of 43–51%, but the clay size fraction makes up only 22–28% of the bulk rock. Smaller amounts of orthoclase, hematite, and chlorite are also present. The clay fraction (Table 3) comprises dominantly illite (~80%), with minor quartz and hematite. The cation-exchange capacity of the <2-μm fraction has a range of 26–30 cmol/kg and is representative of the large amount of illite present in this size fraction (Table 4).

The two mudrock samples from the Kanpa Formation are dominantly illitic (35–45%) in terms of bulk composition (Table 2), with significantly more orthoclase (19–29%) and quartz (22–25%) than samples from overlying formations. Small amounts of chlorite are also present, and these two samples are the only ones from Lancer 1 that contain kaolinite. Clay contents vary from 41% in the upper sample to 58% in the lower one, although the clay fraction is again very small, between 17 and 23%. The <2-μm fraction comprises mainly clays (illite dominantly, plus kaolinite and chlorite) with some orthoclase and quartz (Table 3). The cation-exchange capacity is lower than that of the Wahlgu Formation (21–23 cmol/kg), reflecting the lower illite content in the clay fraction (Table 4).

The five mudrock samples from the Hussar Formation show some variation in composition, although all comprise codominant illite and orthoclase in terms of bulk mineralogy (Table 2). Quartz is also present in significant quantities. The uppermost two samples (181778 and 181779) and the basal sample (181782) are dolomitic (10–15%). All samples contain small amounts of hematite, and all but one (181781) contain minor chlorite. Sample 181779 is the only one containing smectite, and analysis of the diffractogram of the glycolated <2-μm fraction (Fig. 2) suggests a mixed-layer smectite–illite containing about 90% smectite interlayers, based on the method outlined in Moore and Reynolds (1997). The clay content for these Hussar Formation samples ranges between 32 and 44%, while the clay fraction varies from 13 to 26%. The clay fraction is dominantly illite (Table 3), although most samples have significant amounts of orthoclase feldspar. The one exception (181779) has a large proportion of smectite, commensurate with this mineral's extremely fine grain size. The cation-exchange capacity for this sample is the highest of all those measured (36 cmol/kg) as smectitic clays generally account for the largest proportion of exchangeable cations amongst the clay minerals (Greene et al., 2002). While most of the chemically analysed Hussar Formation clay fractions are relatively similar in composition (Table 4), the smectite-rich sample has more MgO and P_2O_5 but less Al_2O_3 and K_2O than the other samples.

The bulk mineralogy of the single Browne Formation mudrock sample (Table 2) is dominated by orthoclase

Table 2. Bulk mineralogy by X-ray diffraction for twelve mudrock samples from Lancer

GSWA sample no.	*Depth (m)*	*Formation*	*Quartz*	*Albite*	*Orthoclase*	*Kaolin*	*Illite*	*Chlorite*	*Smectite*	*Hematite*	*Dolomite*	*Halite*	*Mica*	*Clay content*
			%											
181722	166.4 – 166.6	Paterson	15	<1	2	0	48	11	0	7	0	0	16	59
181723	347.25 – 347.5	Wahlgu	30	0	7	0	44	1	0	3	14	0	0	45
181724	390.00 – 390.2	Wahlgu	20	0	11	0	49	2	0	5	13	0	0	51
181768	456.46 – 456.83	Wahlgu	18	0	9	0	40	3	0	4	25	0	0	43
181770	603.56 – 603.79	Kanpa	25	4	29	2	35	4	0	2	0	0	0	41
181771	665.47 – 665.76	Kanpa	22	<1	19	7	45	6	0	0	0	0	0	58
181778	900.85 – 901.10	Hussar	20	0	33	0	29	3	0	3	11	0	0	32
181779	930.73 – 931.01	Hussar	21	0	21	0	27	4	11	1	15	0	0	42
181780	970.02 – 970.22	Hussar	15	0	47	0	32	5	0	<1	0	0	0	37
181781	1 027.73 – 1 027.95	Hussar	18	0	36	0	42	0	0	4	0	0	0	42
181782	1 114.56 – 1 114.86	Hussar	14	4	26	0	42	2	0	2	10	0	0	44
181783	1 358.69 – 1 358.89	Browne	21	0	31	0	24	<1	0	3	21	<1	0	25

NOTE: Sample 181722 (166.4 – 166.6 m) contains both illite and 2M1 muscovite, whereas the remaining samples contain only illite

Table 3. Mineralogy of the <2-µm fraction of twelve mudrock samples from Lancer 1

GSWA sample no.	*Depth (m)*	*Formation*	*Quartz*	*Orthoclase*	*Kaolin*	*Illite*	*Chlorite*	*Hematite*	*Dolomite*	*Smectite*	*Mica*	*CEC*
181722	166.4 – 166.6	Paterson	6	1	–	46	9	11	–	–	27	17
181723	347.25 – 347.5	Wahlgu	10	4	–	79	<1	5	1	–	–	28
181724	390.00 – 390.2	Wahlgu	7	5	–	80	1	6	1	–	–	30
181768	456.46 – 456.83	Wahlgu	8	4	–	78	4	6	1	–	–	26
181770	603.56 – 603.79	Kanpa	5	18	4	60	10	2	–	–	–	21
181771	665.47 – 665.76	Kanpa	7	9	9	73	1	–	–	–	–	23
181778	900.85 – 901.10	Hussar	2	24	–	65	2	7	–	–	–	19
181779	930.73 – 931.01	Hussar	12	8	–	46	3	2	–	29	–	36
181780	970.02 – 970.22	Hussar	8	29	–	57	6	–	–	–	–	16
181781	1 027.73 – 1 027.95	Hussar	9	23	–	62	-	6	–	–	–	19
181782	1 114.56 – 1 114.86	Hussar<1	19	–	74	2	5	–	<5	–	24	
181783	1 358.69 – 1 358.89	Browne	3	27	–	58	2	7	2	–	–	18

NOTE: Sample 181722 (166.4 – 166.6 m) contains both illite and 2M1 muscovite, whereas the remaining samples contain only illite
CEC: Cation-exchange capacity

Table 4. Major-element chemistry and cation-exchange capacity of the <2-µm fraction of twelve mudrock samples from the Lancer 1

GSWA sample no.	Depth (m)	Formation	SiO_2	Al_2O_3	MgO	P_2O_5	K_2O	TiO_2	MnO	Fe_2O_3	BaO	Sum	CEC cmol/kg
			%										
181722	166.4 – 166.6	Paterson	45.1	20.8	5.2	0.1	5.2	0.6	0.1	15.6	1.2	94.0	17
181723	347.25 – 347.5	Wahlgu	52.8	18.8	4.7	0.2	6.2	0.8	0.1	9.4	2.0	94.9	28
181724	390.00 – 390.2	Wahlgu	50.7	18.2	5.4	0.2	6.0	0.9	0.0	10.8	2.2	94.4	30
181768	456.46 – 456.83	Wahlgu	51.0	17.9	5.8	0.2	5.7	0.9	0.0	11.7	1.9	95.1	26
181770	603.56 – 603.79	Kanpa	51.0	21.0	5.0	0.1	6.9	0.8	0.0	8.9	1.6	95.3	21
181771	665.47 – 665.76	Kanpa	53.4	22.2	3.4	0.1	6.1	0.9	0.0	7.5	1.7	95.3	23
181778	900.85 – 901.10	Hussar	49.9	18.2	4.9	0.2	7.9	0.8	0.1	11.9	1.4	95.3	19
181779	930.73 – 931.01	Hussar	53.3	11.2	15.9	0.5	4.0	0.6	0.0	7.1	2.7	95.4	36
181780	970.02 – 970.22	Hussar	58.0	18.3	4.9	0.1	8.5	0.8	0.0	7.1	1.1	98.8	16
181781	1 027.73 – 1 027.95	Hussar	54.6	18.1	3.2	0.1	7.8	0.7	0.0	12.8	1.4	98.7	19
181782	1 114.56 – 1 114.86	Hussar	49.7	17.9	6.9	0.2	7.2	0.8	0.2	10.2	1.7	94.9	24
181783	1 358.69 – 1 358.89	Browne	49.3	17.7	5.4	0.2	8.0	0.8	0.1	11.2	1.3	93.9	18

NOTES: CEC: Cation-exchange capacity

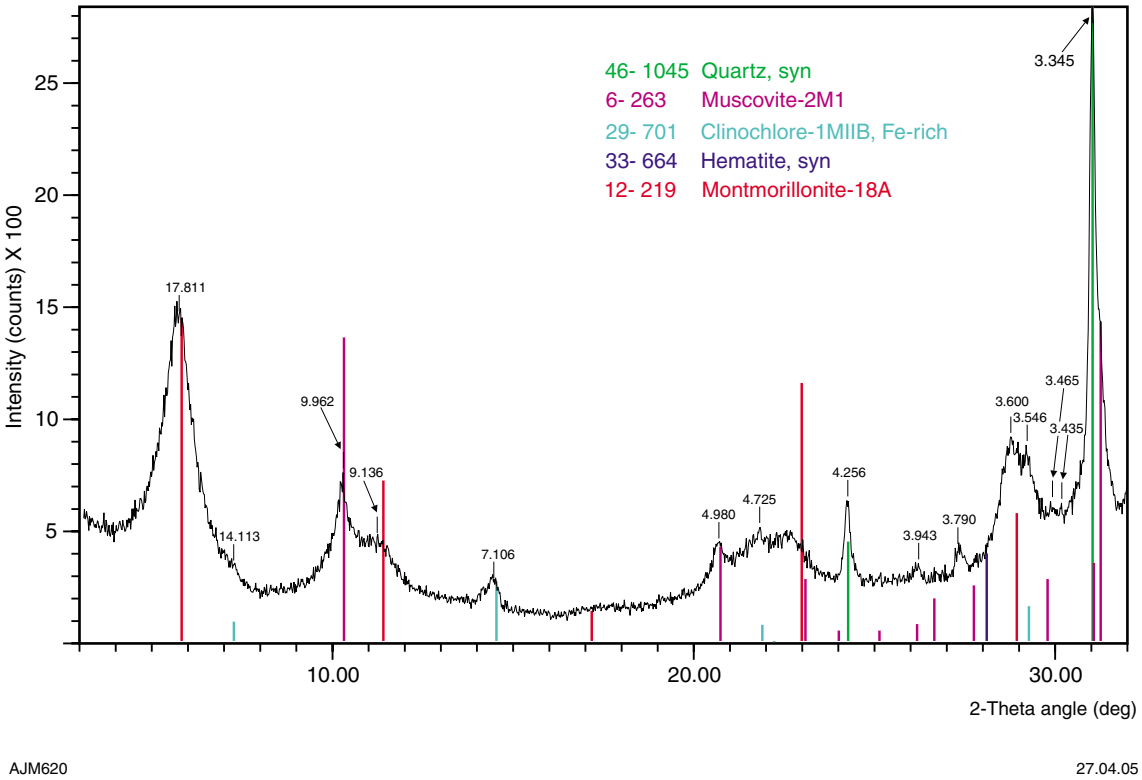

Figure 2. Diffractogram for the <2-µm fraction of sample 181779 (930.73 – 931.01 m), showing the mixed-layer illite–smectite peak on the far left-hand side at around 5.8° 2θ

(31%), but also contains significant proportions of illite (24%), quartz, and dolomite (both 21%). Clay content in this sample is only 25% (illite plus trace chlorite) and the clay fraction is just 11%. The cation-exchange capacity of 18 cmol/kg is among the lowest measured in these mudrocks and is representative of the low percentage of illite (58%) and total clays (60%) contained in this fraction compared to the other samples.

Conclusions

The mudrock samples taken from the Lancer 1 stratigraphic drillhole are relatively coarse grained with clay fractions in the range 11–28%, apart from the shallowest sample from the Paterson Formation, which has a clay fraction of 52%. Clay content ranges from 25 to 59%. In terms of clay mineralogy, the samples are generally dominated by illite, with significant amounts of orthoclase present from the Kanpa Formation downwards. The Wahlgu Formation and some of the Hussar Formation mudrocks are also highly dolomitic. Quartz, and smaller amounts of chlorite and hematite, are found in all samples. The clay fractions are dominated by illite and show cation-exchange capacities in a range expected for this mineral (17–30 cmol/kg), although one sample containing significant smectite has a cation-exchange capacity higher than this range. In terms of chemistry of the clay fraction, slight variations are noted amongst the mudrocks sampled, but potassium and iron contents are high as might be expected in a suite comprising mainly red, illitic mudrock.

References

GREENE, R. S. B., EGGLETON, R. A., and RENGASAMY, P., 2002, Relationships between clay mineralogy and the hard setting properties of soils in the Carnarvon horticultural district of Western Australia: Applied Clay Science, v. 20, p. 211–23.

HAINES, P. W., MORY, A. J., STEVENS, M. K., and GHORI, K. A. R., 2004, GSWA Lancer 1 well completion report (basic data), Officer and Gunbarrel Basins, Western Australia: Western Australia Geological Survey, Record 2004/10, 39p.

MOORE, D. M., and REYNOLDS, R. C., 1997, X-Ray Diffraction and the Identification of Clay Minerals: New York, Oxford University Press, 378p.

Appendix 1

Diffractograms

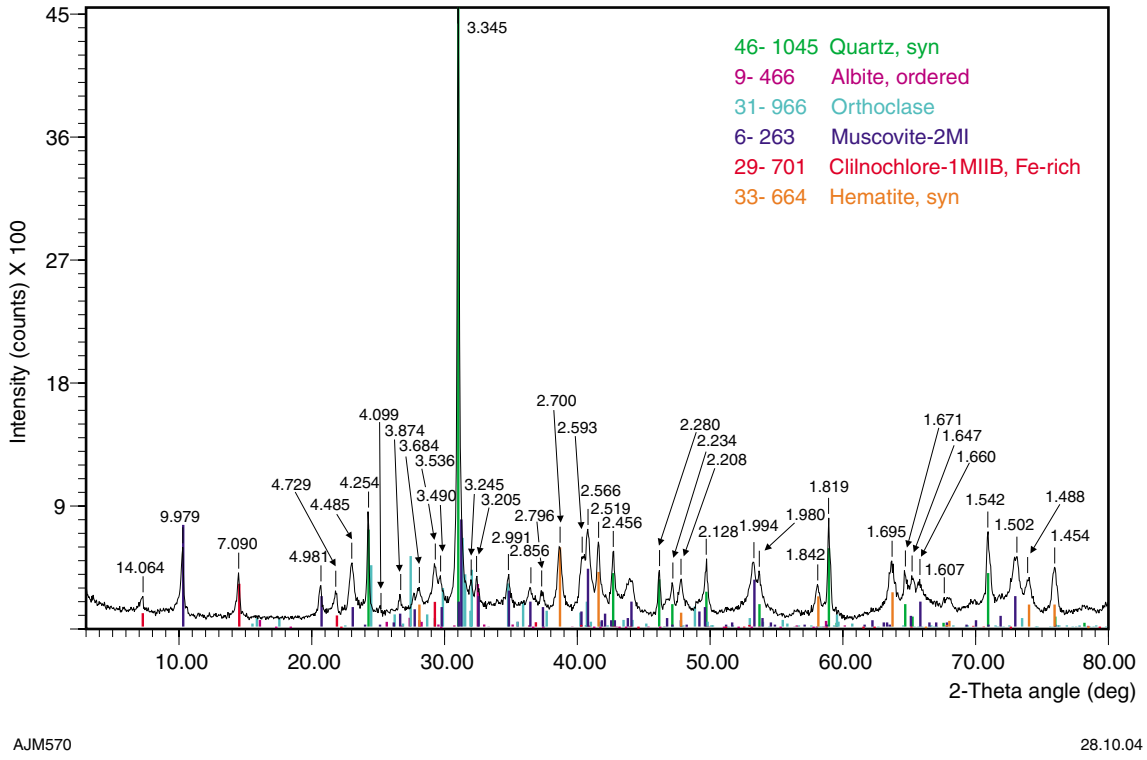

Figure 1.1. Diffractogram for the bulk rock of sample 181722 (166.4 – 166.6 m)

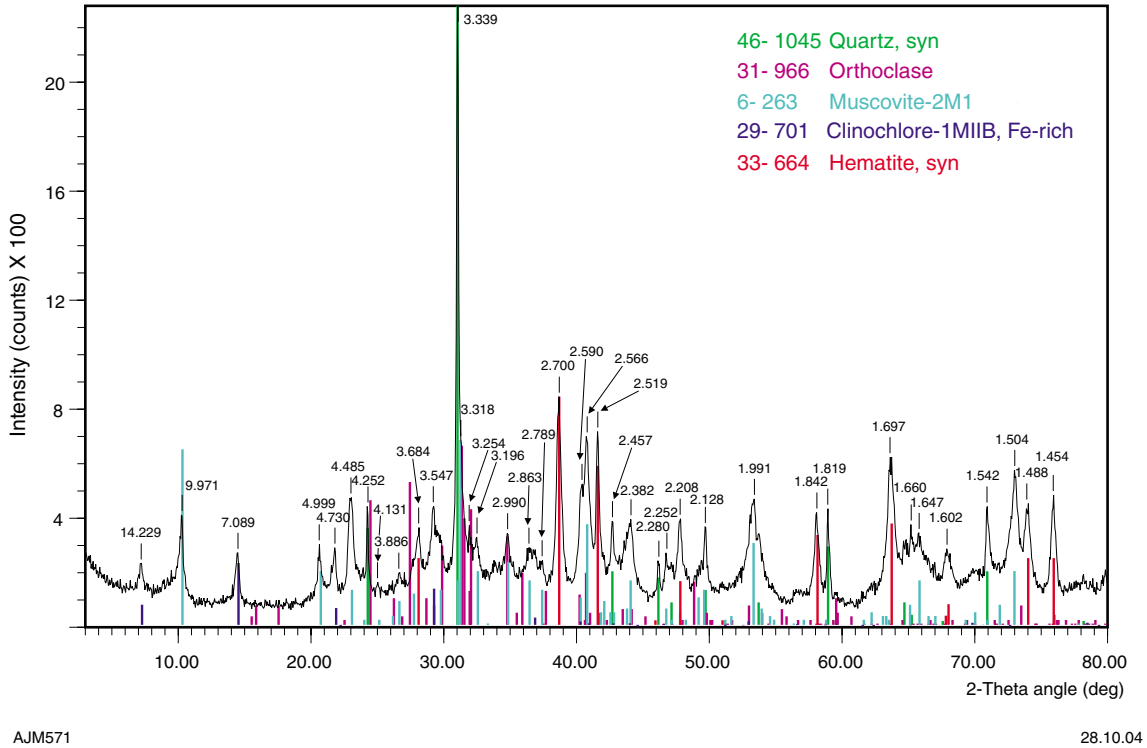

Figure 1.2. Diffractogram for Ca-saturated <2-µm fraction of sample 181722 (166.4 – 166.6 m)

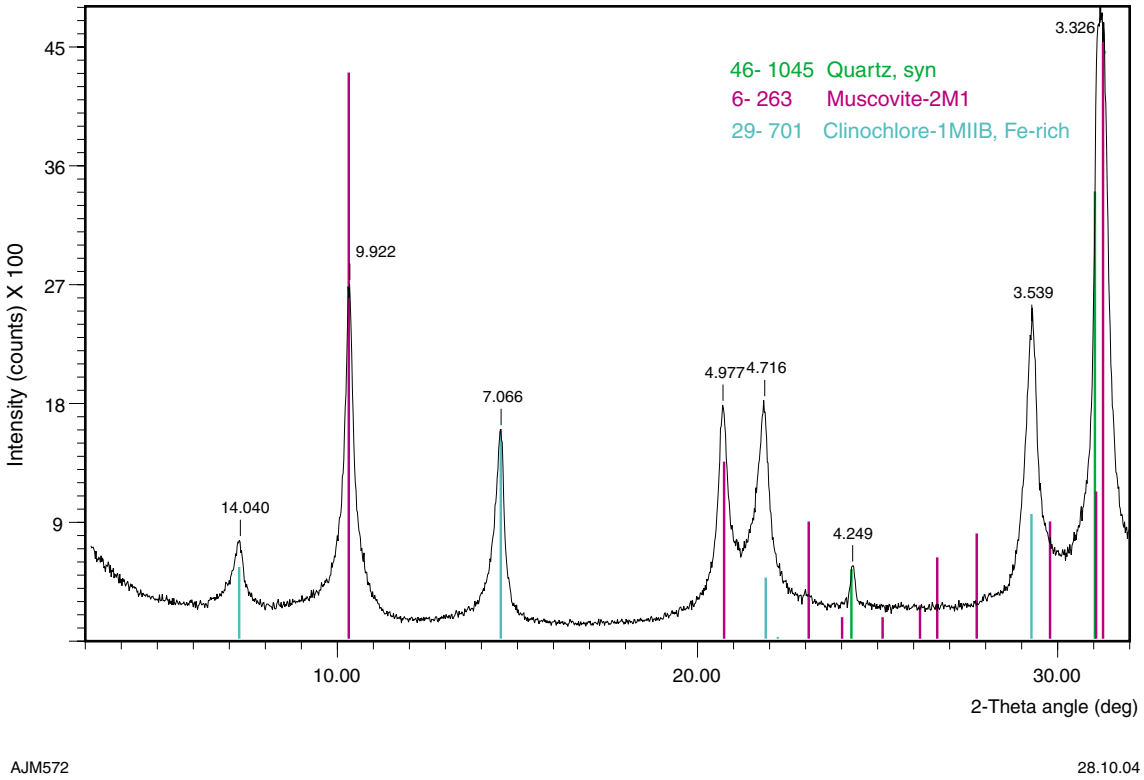

Figure 1.3. Diffractogram for Ca-saturated <2-µm fraction with glycerol of sample 181722 (166.4 – 166.6 m)

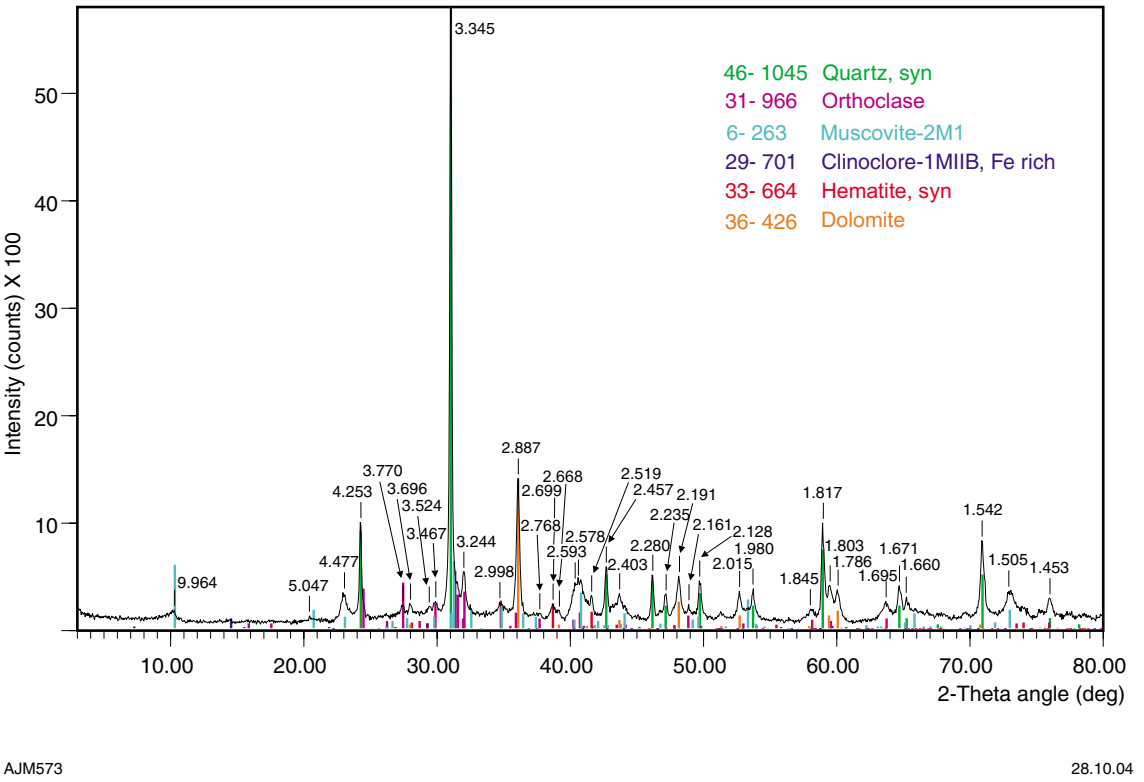

Figure 1.4. Diffractogram for the bulk rock of sample 181723 (347.25 – 347.5 m)

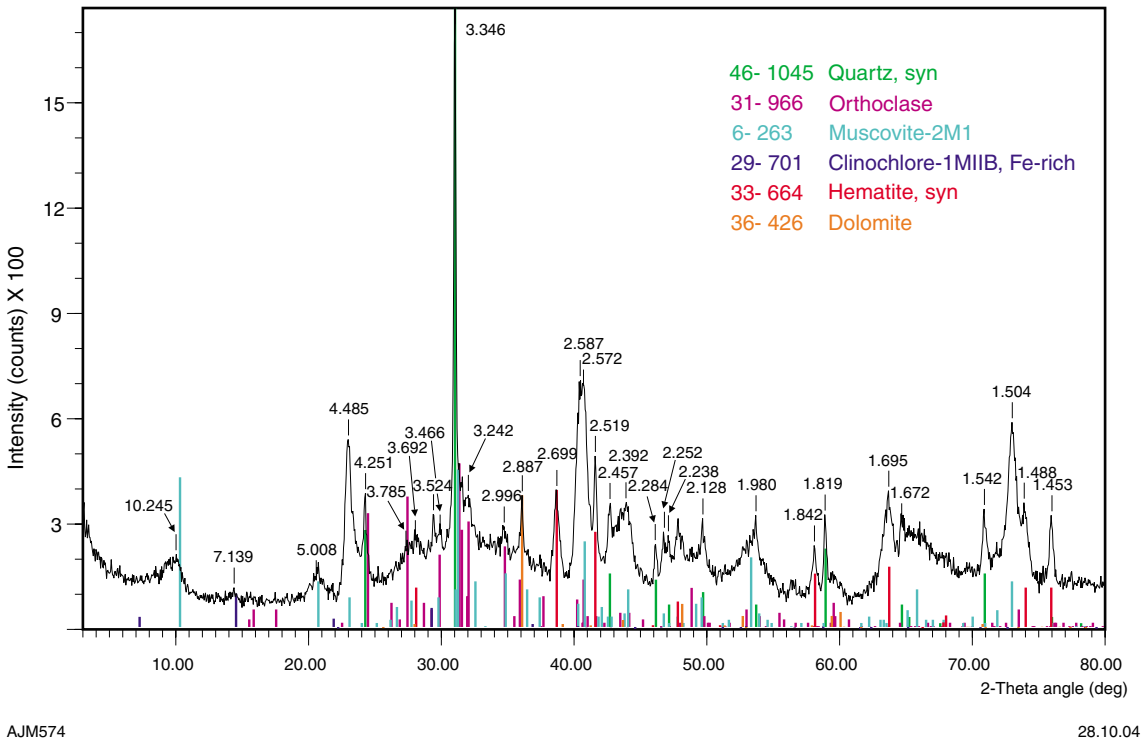

Figure 1.5. Diffractogram for Ca-saturated <2-µm fraction of sample 181723 (347.25 – 347.5 m)

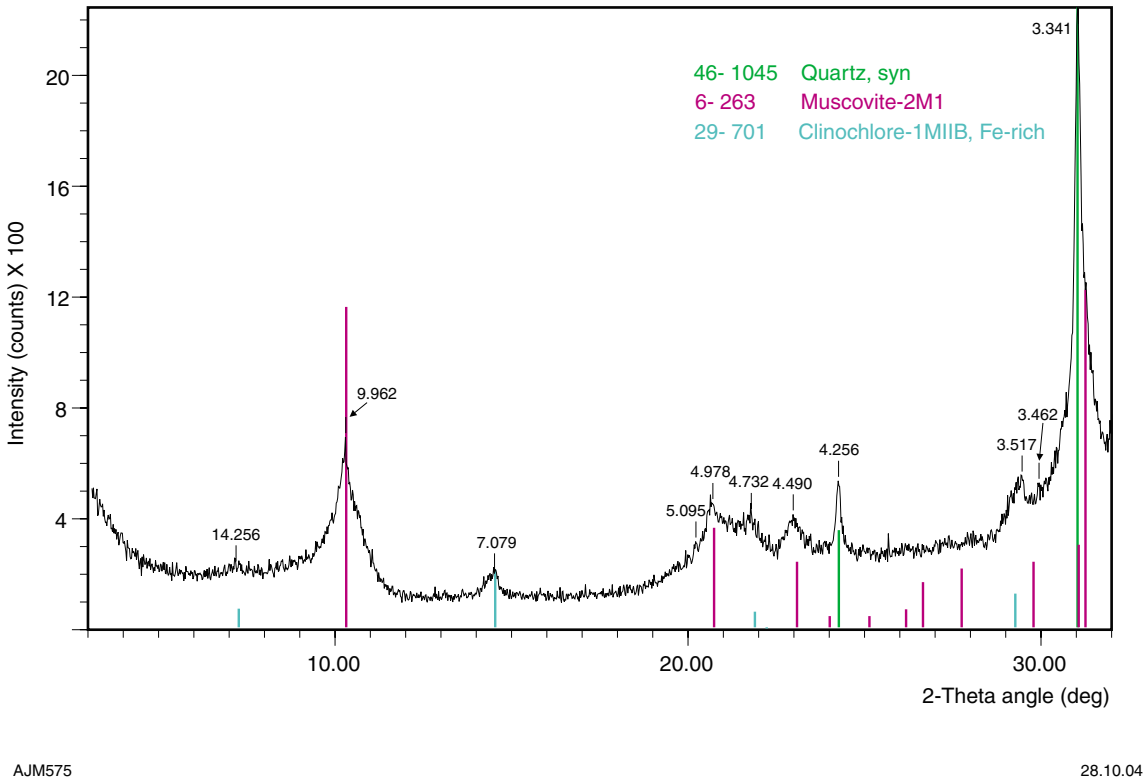

Figure 1.6. Diffractogram for Ca-saturated <2-µm fraction with glycerol of sample 181723 (347.25 – 347.5 m)

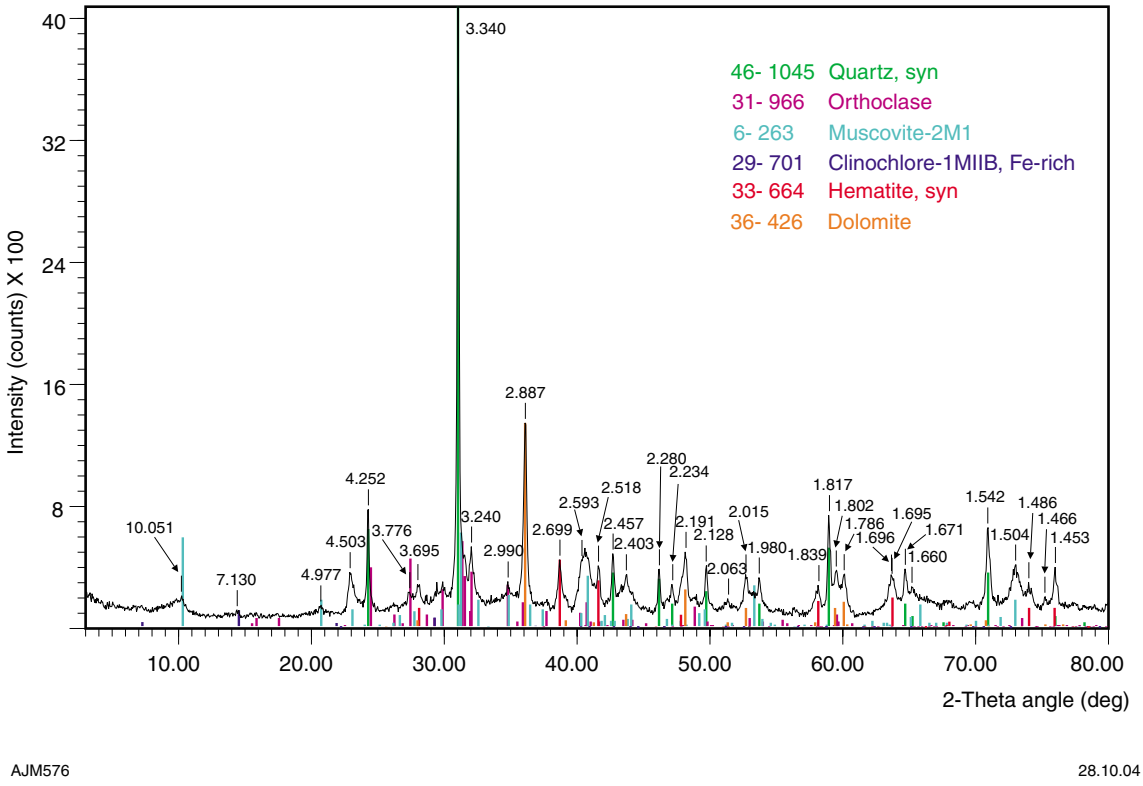

Figure 1.7. Diffractogram for the bulk rock of sample 181724 (389.0 – 389.2 m)

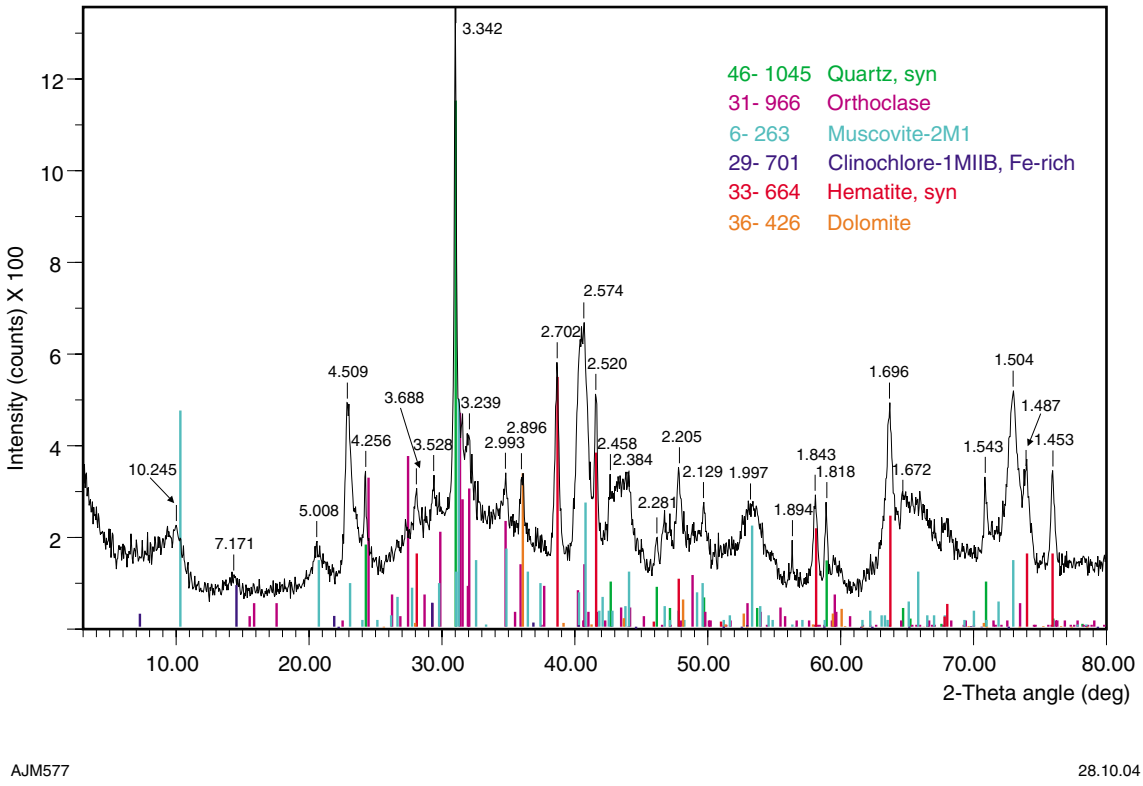

Figure 1.8. Diffractogram for Ca-saturated <2-µm fraction of sample 181724 (389.0 – 389.2 m)

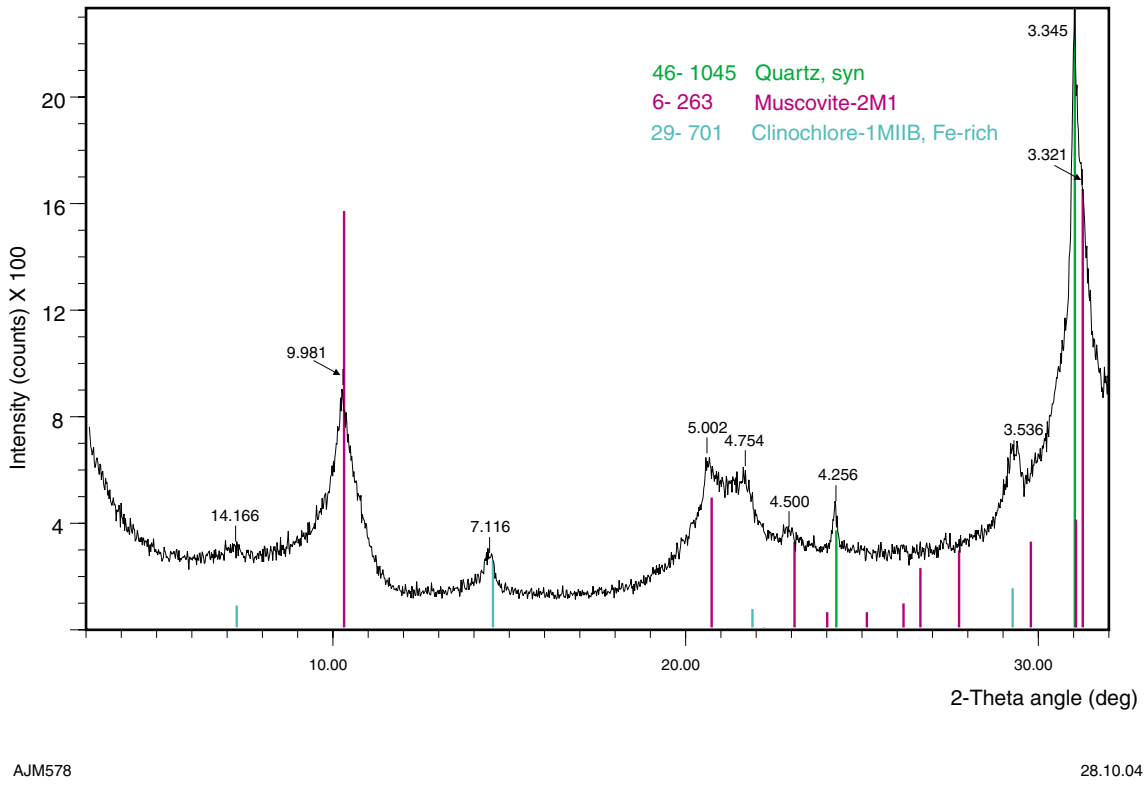

Figure 1.9. Diffractogram for Ca-saturated <2-µm fraction with glycerol of sample 181724 (389.0 – 389.2 m)

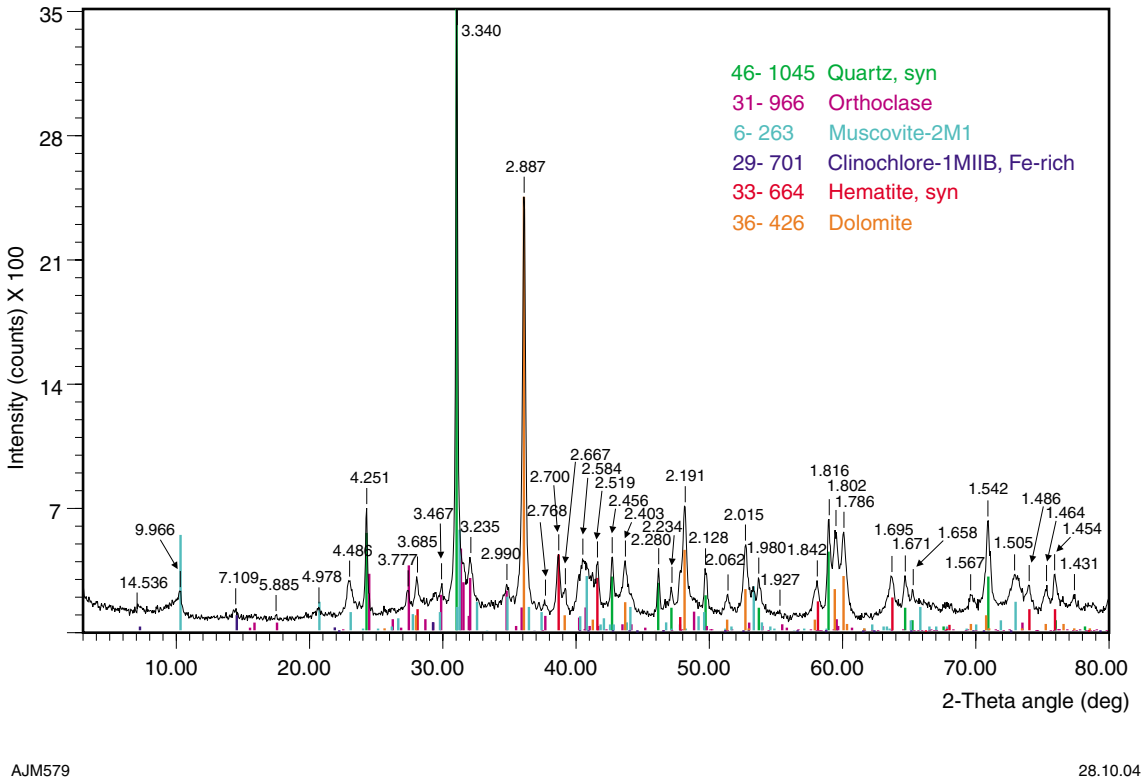

Figure 1.10. Diffractogram for the bulk rock of sample 181768 (456.46 – 456.83m).

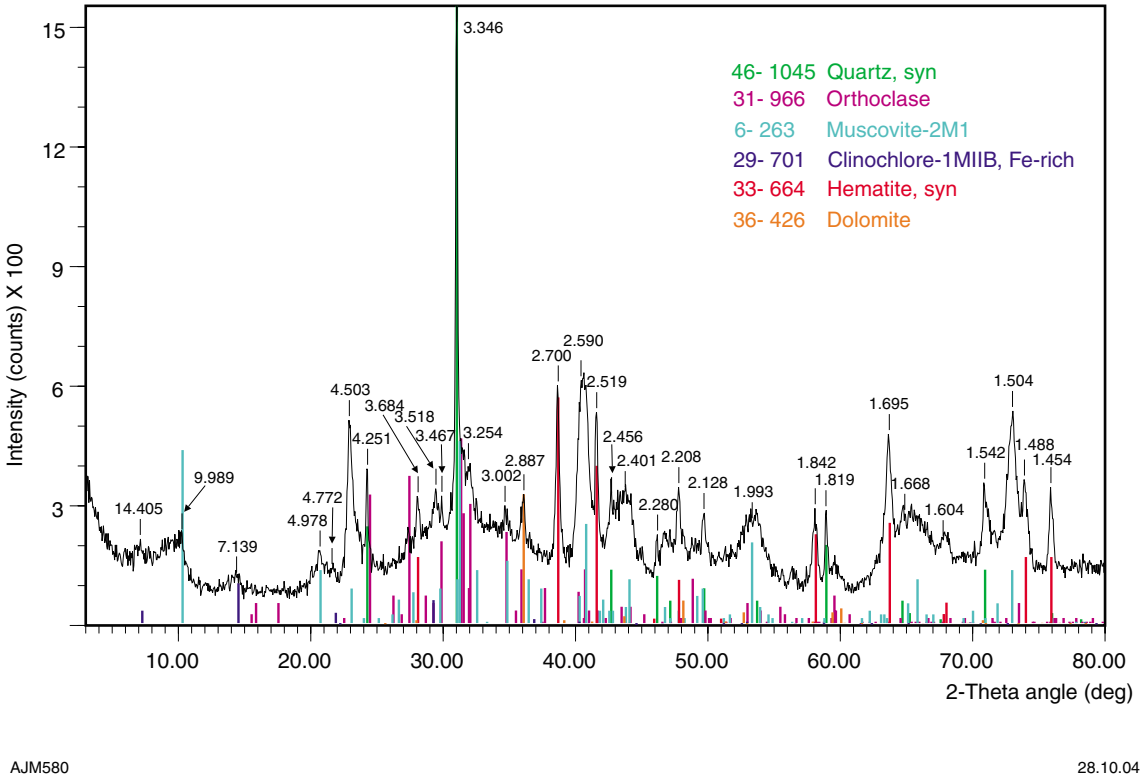

Figure 1.11. Diffractogram for Ca-saturated <2-µm fraction of sample 181768 (456.46 – 456.83m).

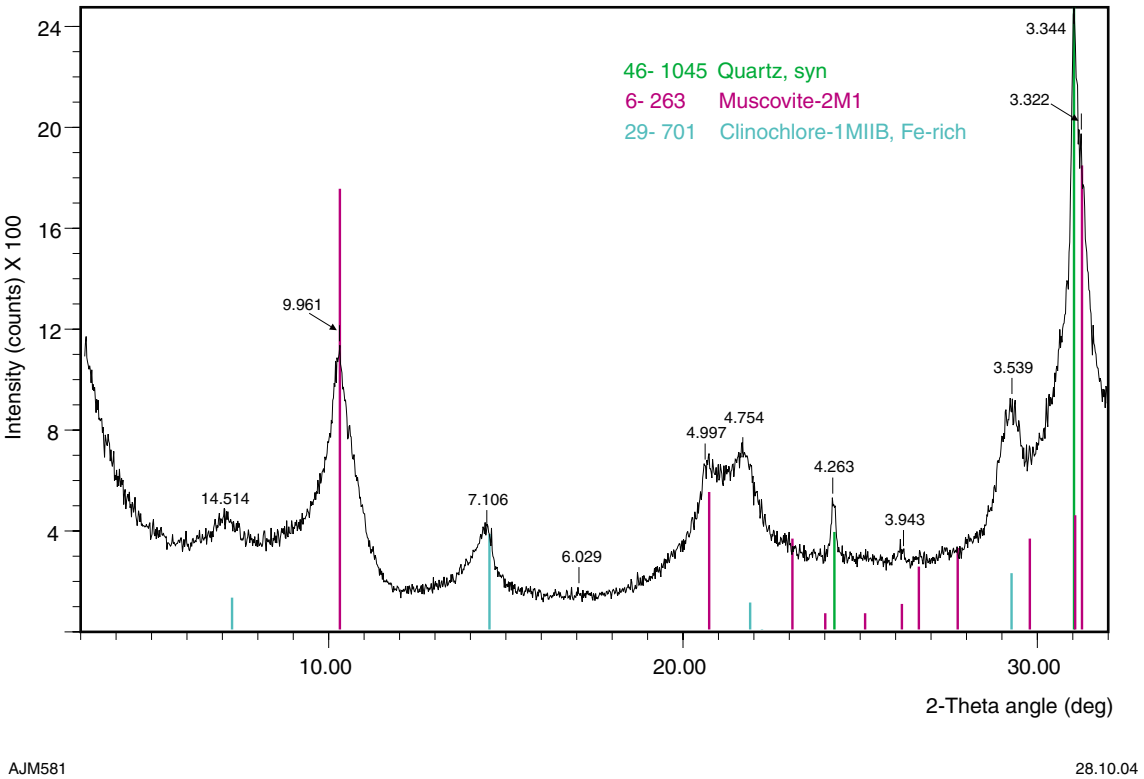

Figure 1.12. Diffractogram for Ca-saturated <2-µm fraction with glycerol of sample 181768 (456.46 – 456.83 m)

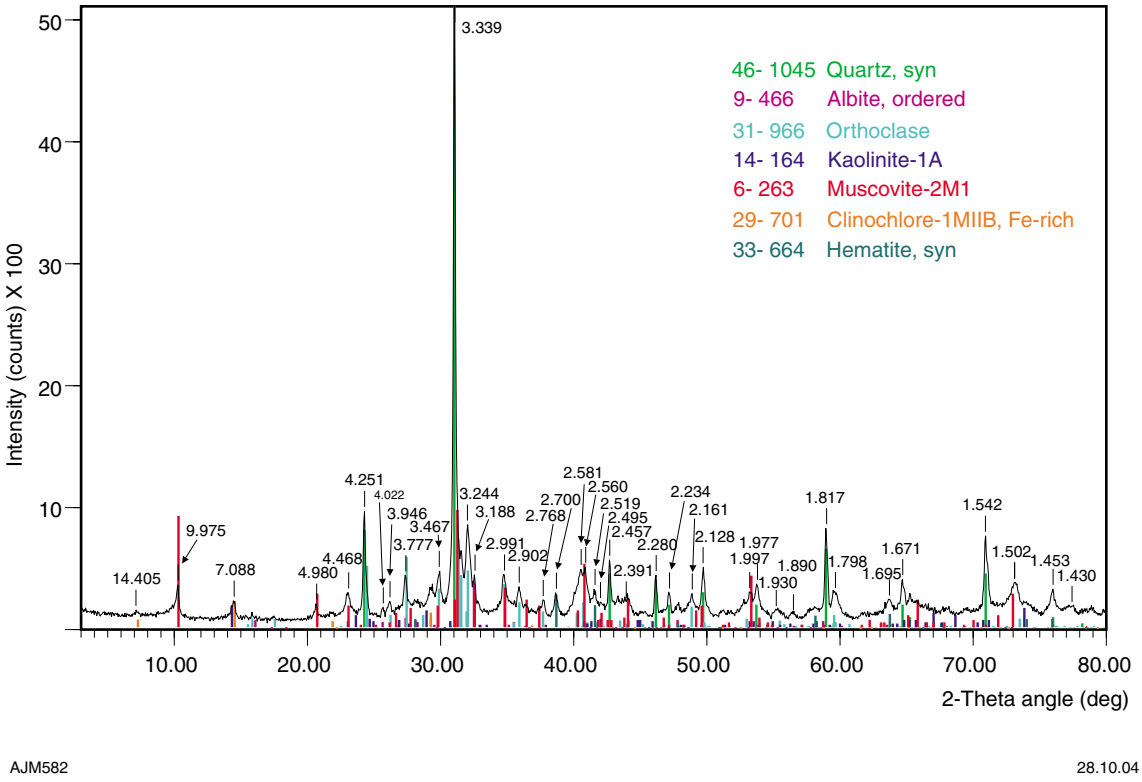

Figure 1.13. Diffractogram for the bulk rock of sample 181770 (603.56 – 603.79 m)

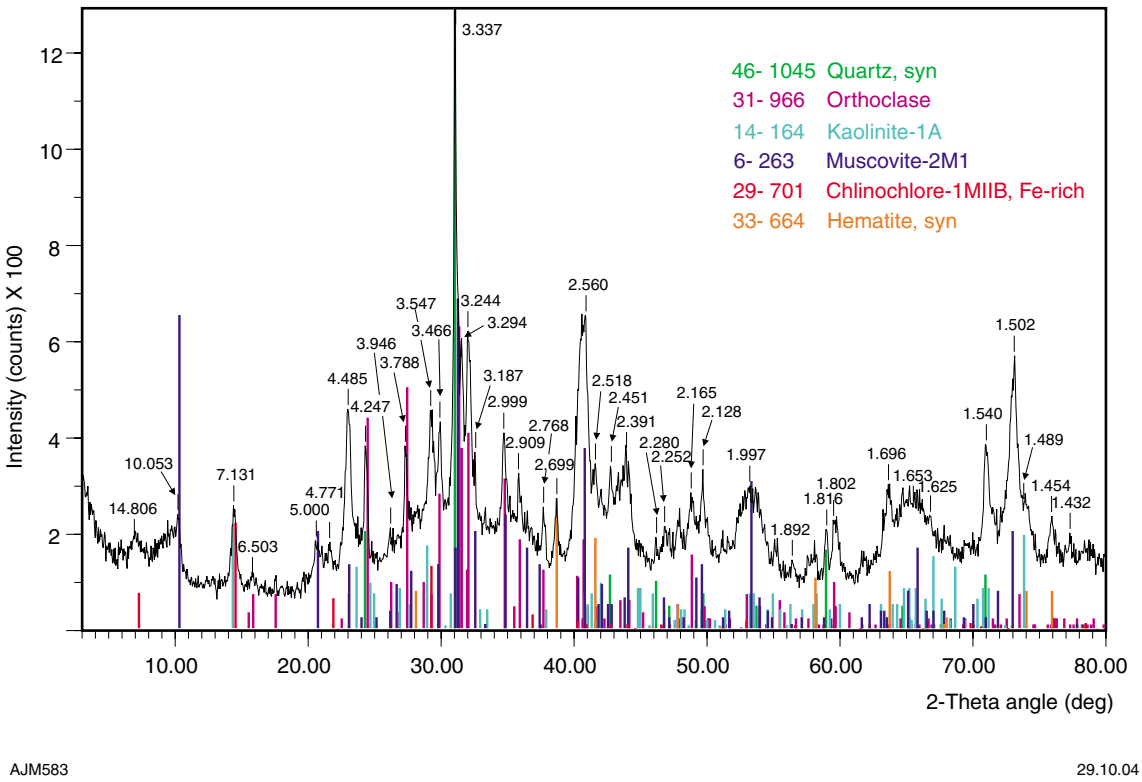

Figure 1.14. Diffractogram for Ca-saturated <2-µm fraction of sample 181770 (603.56 – 603.79 m)

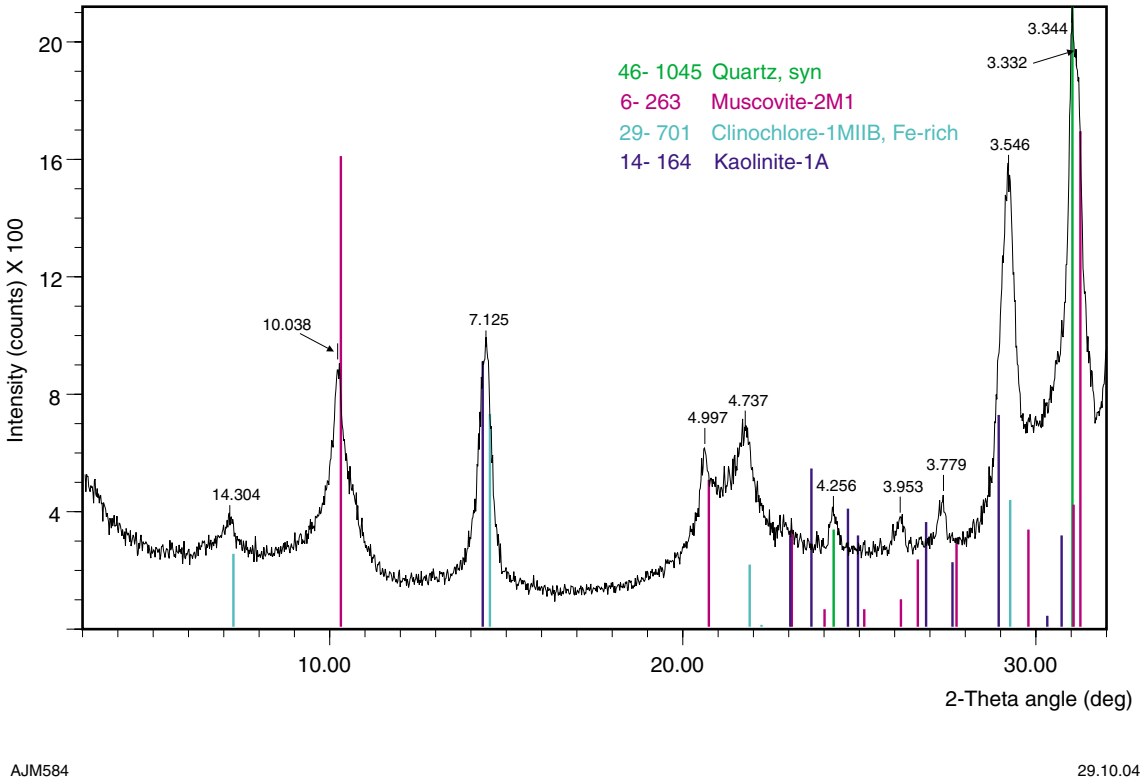

Figure 1.15. Diffractogram for Ca-saturated <2-µm fraction with glycerol of sample 181770 (603.56 – 603.79 m)

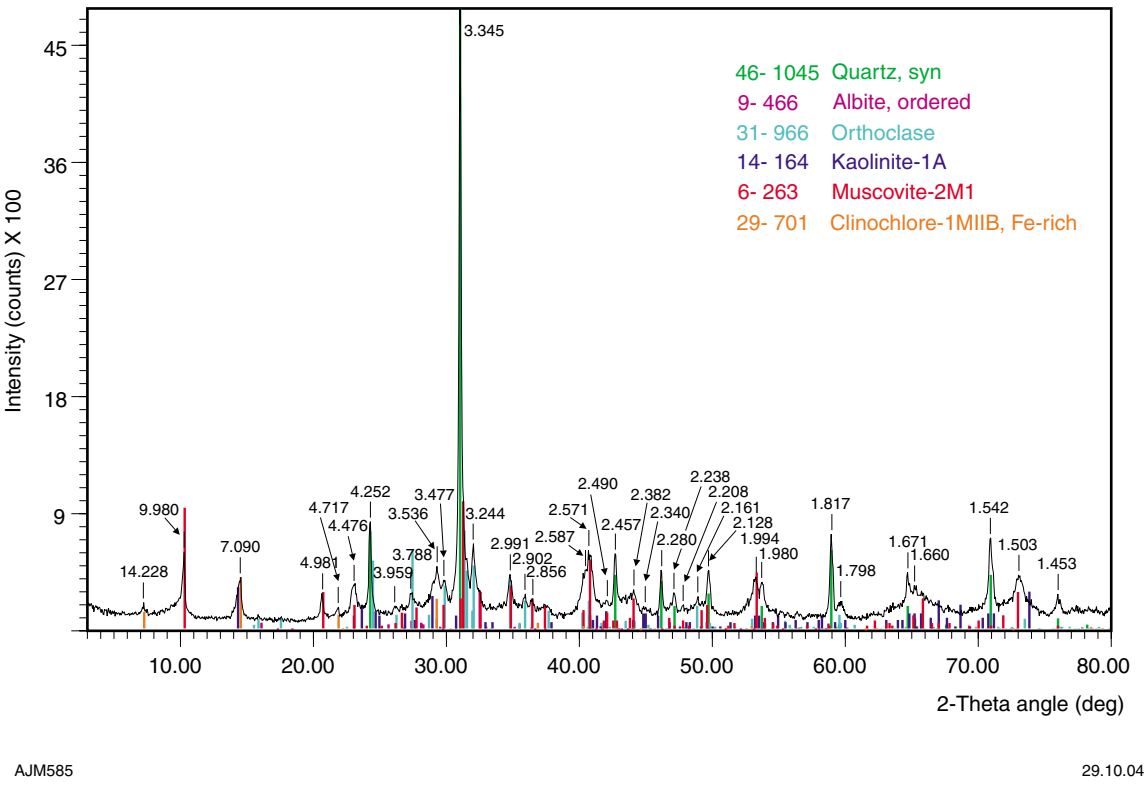

Figure 1.16. Diffractogram for the bulk rock of sample 181771 (665.47 – 665.76 m)

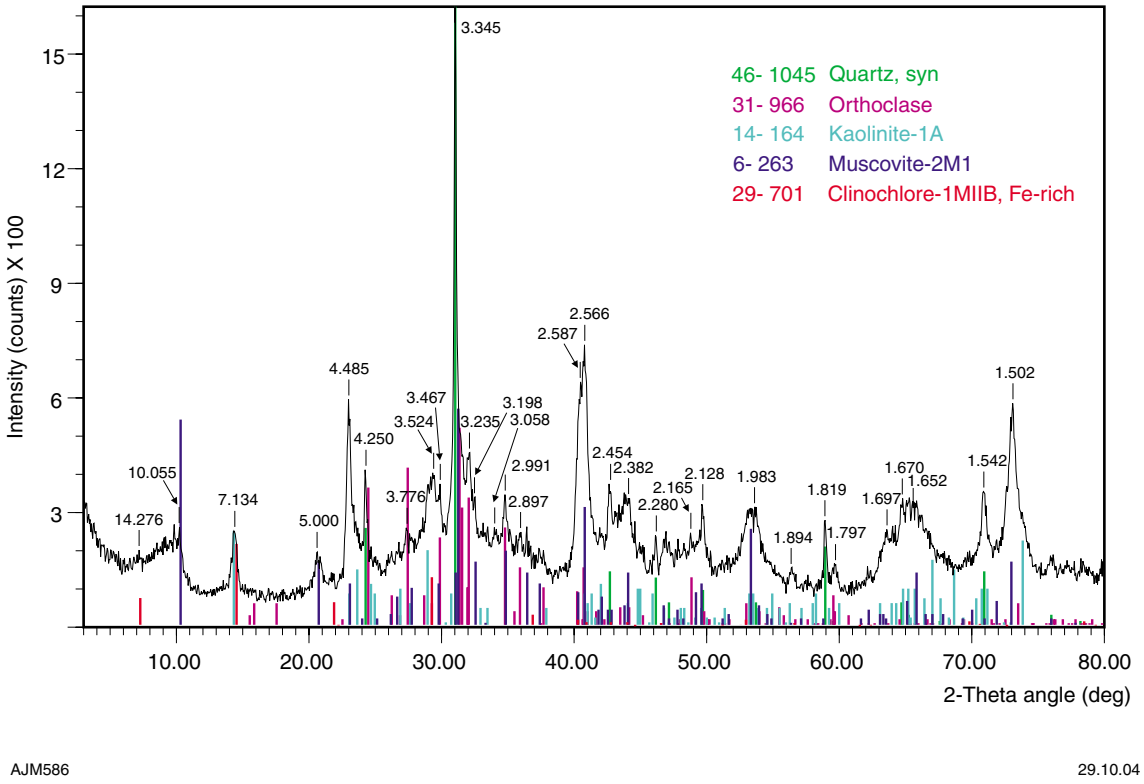

Figure 1.17. Diffractogram for Ca-saturated <2-µm fraction of sample 181771 (665.47 – 665.76 m)

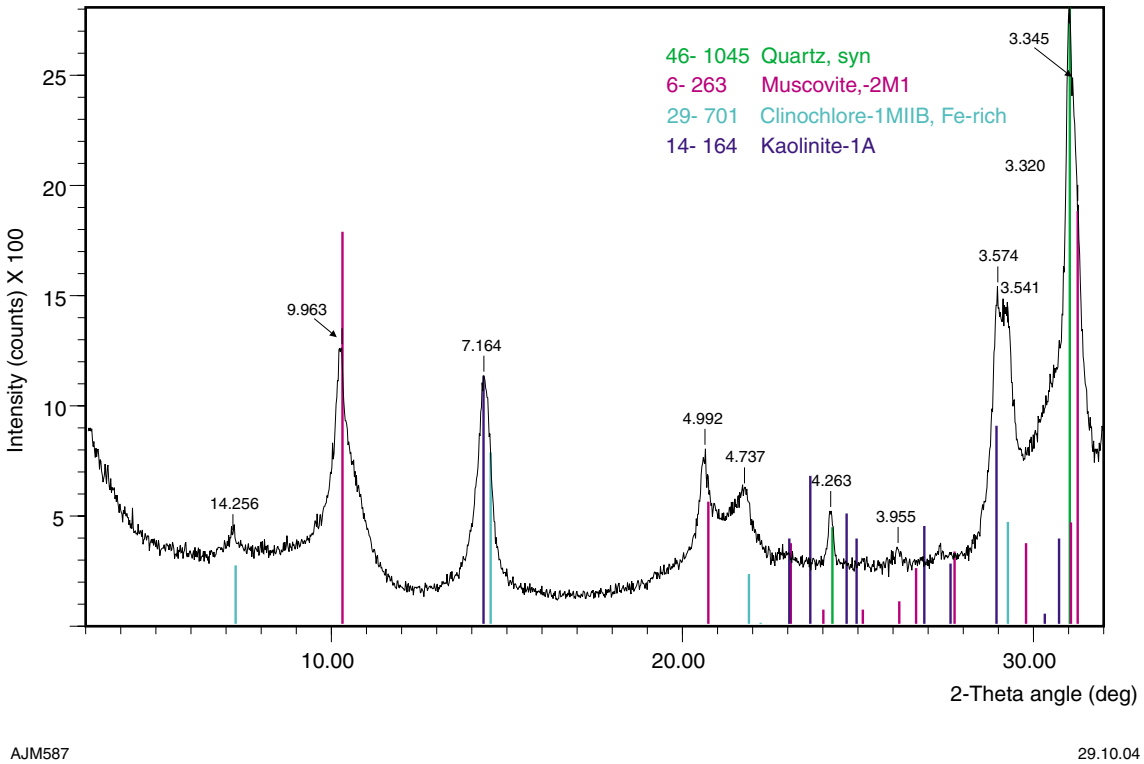

Figure 1.18. Diffractogram for Ca-saturated <2-µm fraction with glycerol of sample 181771 (665.47 – 665.76 m)

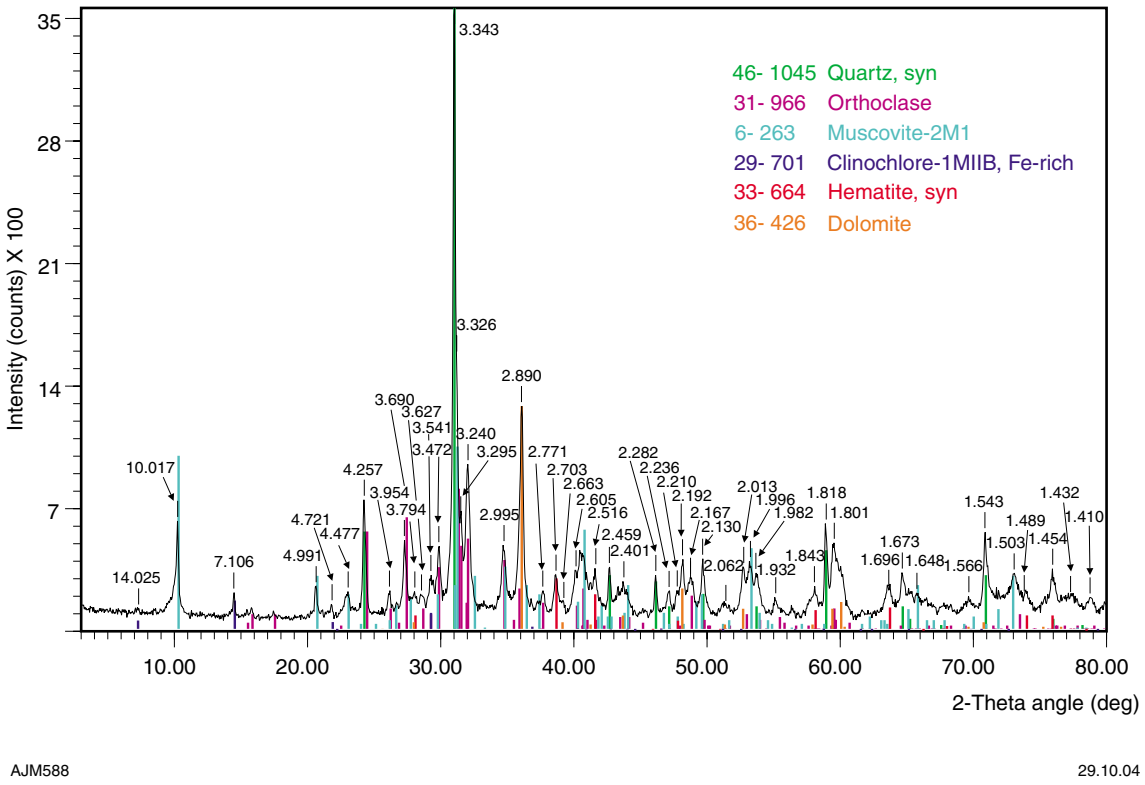

Figure 1.19. Diffractogram for the bulk rock of sample 181778 (900.85 – 901.10 m)

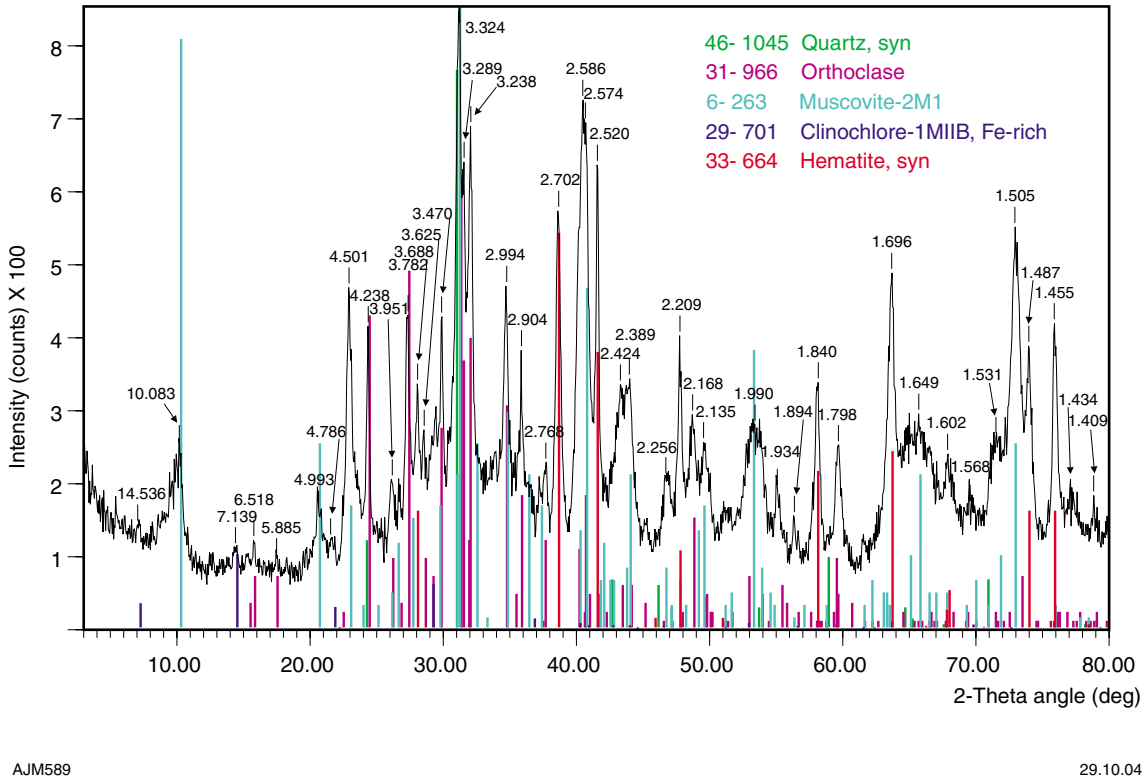

Figure 1.20. Diffractogram for Ca-saturated <2-µm fraction of sample 181778 (900.85 – 901.10 m)

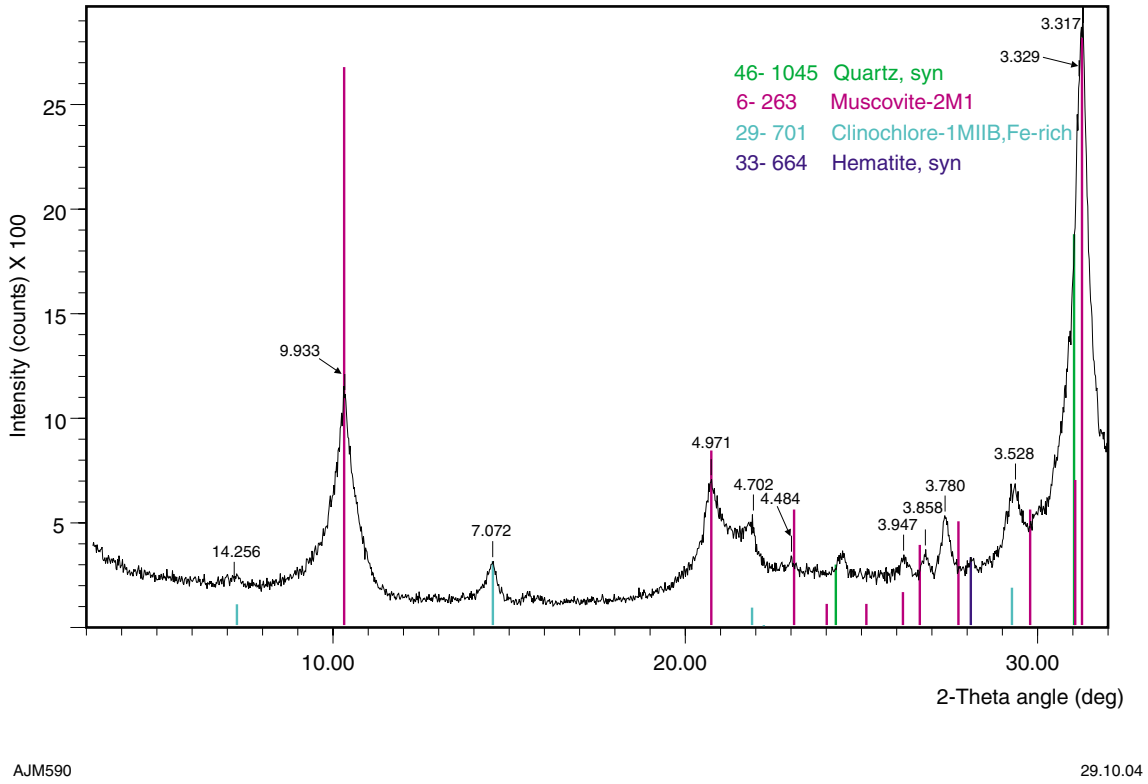

Figure 1.21. Diffractogram for Ca-saturated <2-µm fraction with glycerol of sample 181778 (900.85 – 901.10 m)

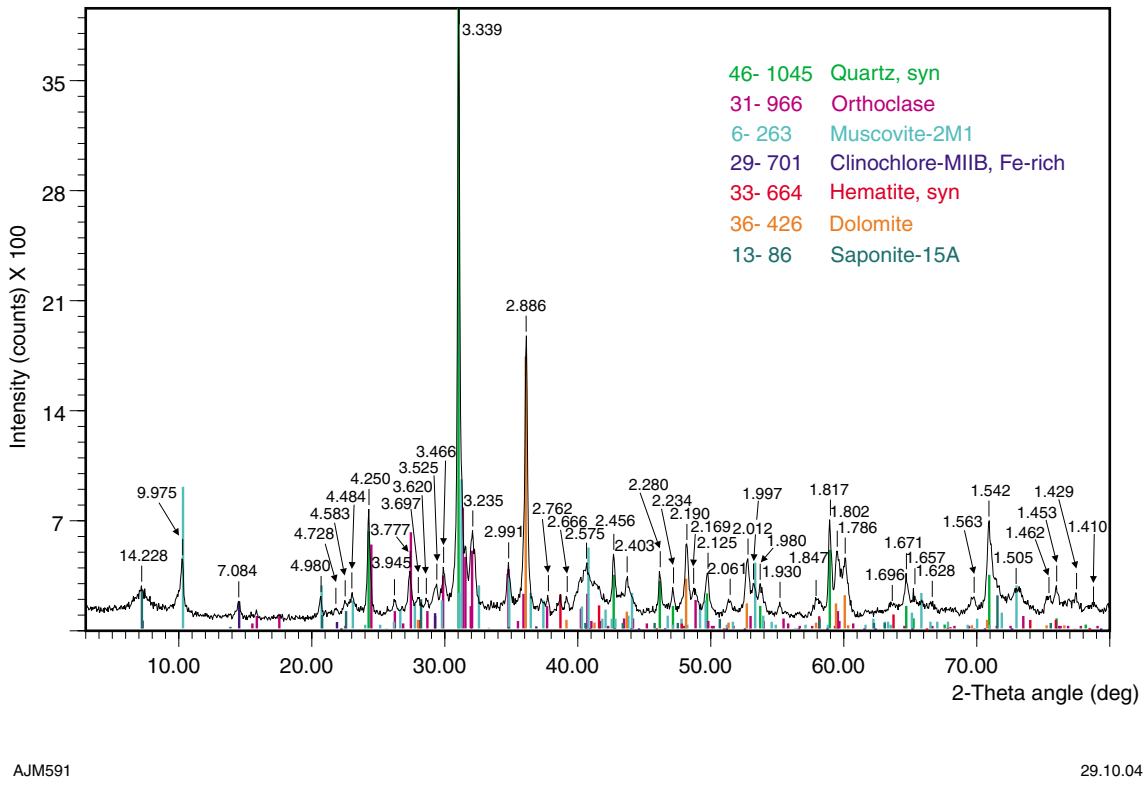

Figure 1.22. Diffractogram for the bulk rock of sample 181779 (930.73 – 931.10 m)

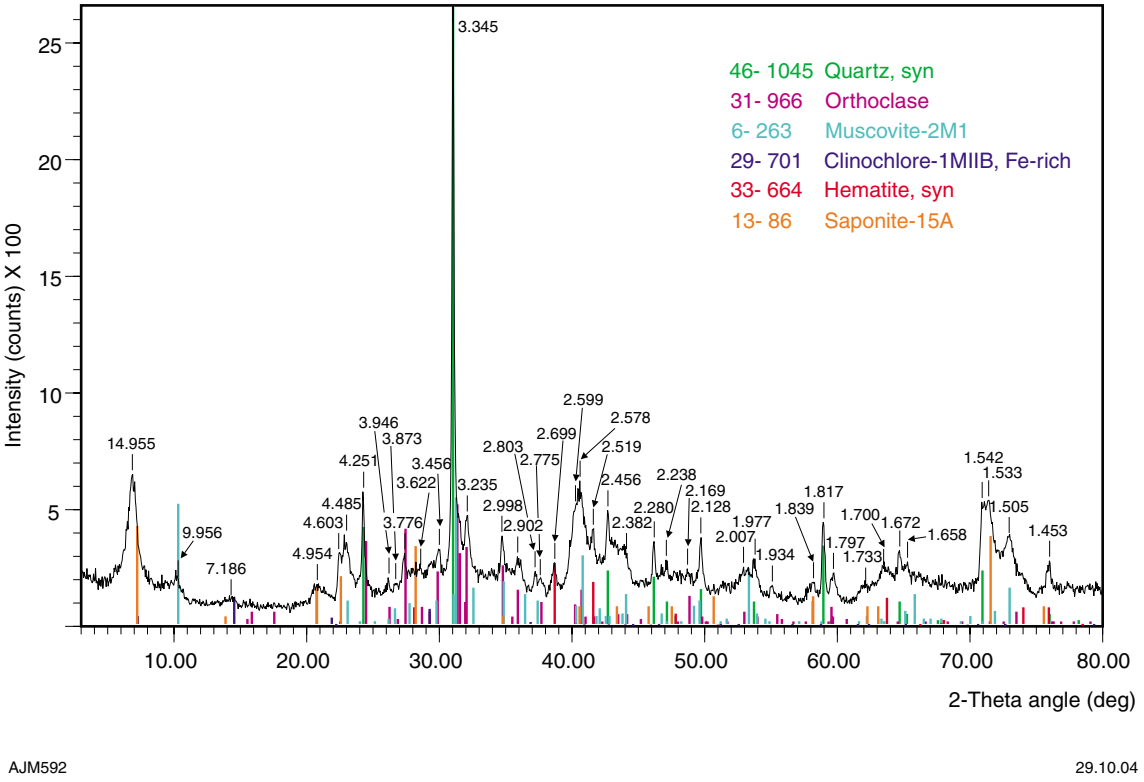

Figure 1.23. Diffractogram for Ca-saturated <2-µm fraction of sample 181779 (930.73 – 931.10 m)

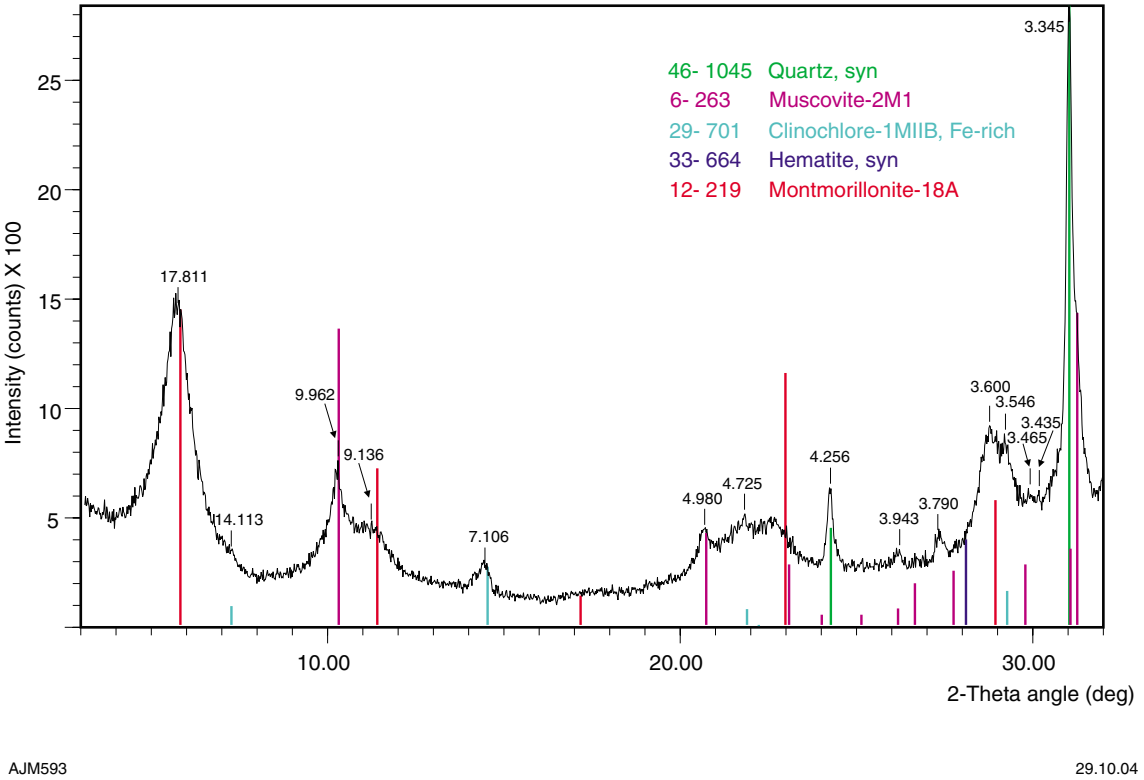

Figure 1.24. Diffractogram for Ca-saturated <2-µm fraction with glycerol of sample 181779 (930.73 – 931.10 m)

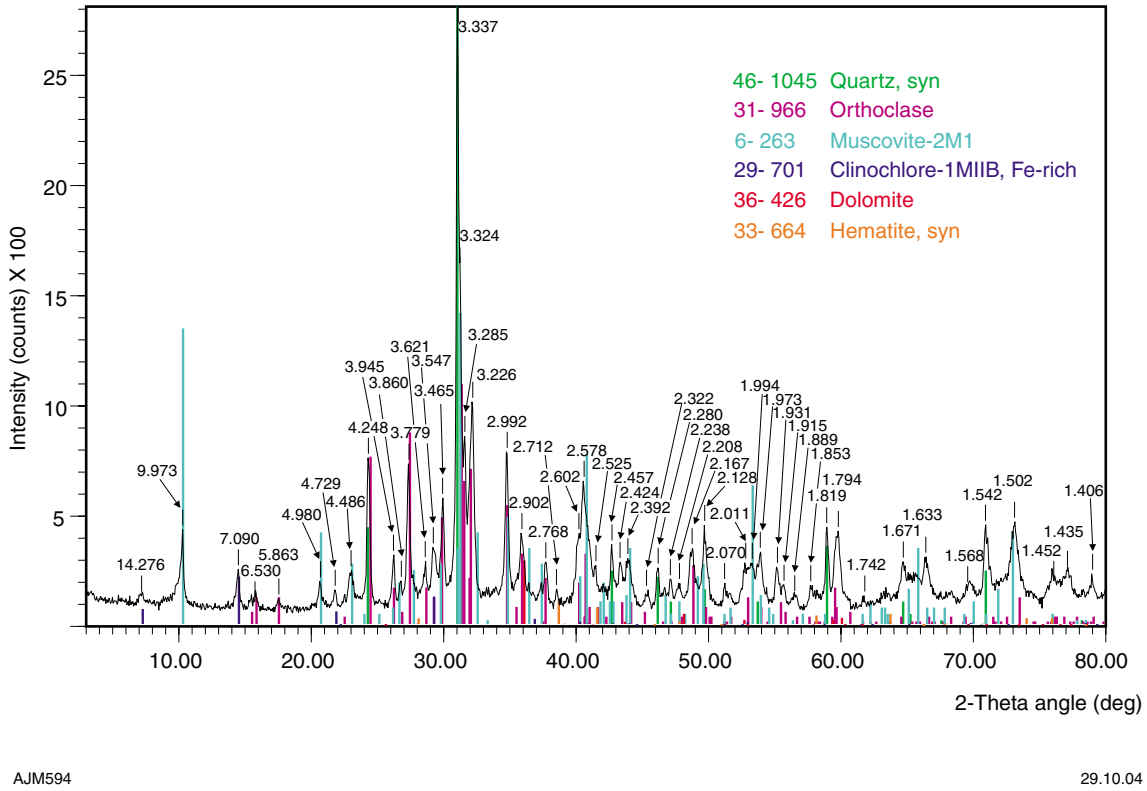

Figure 1.25. Diffractogram for the bulk rock of sample 181780 (970.02 – 970.22 m)

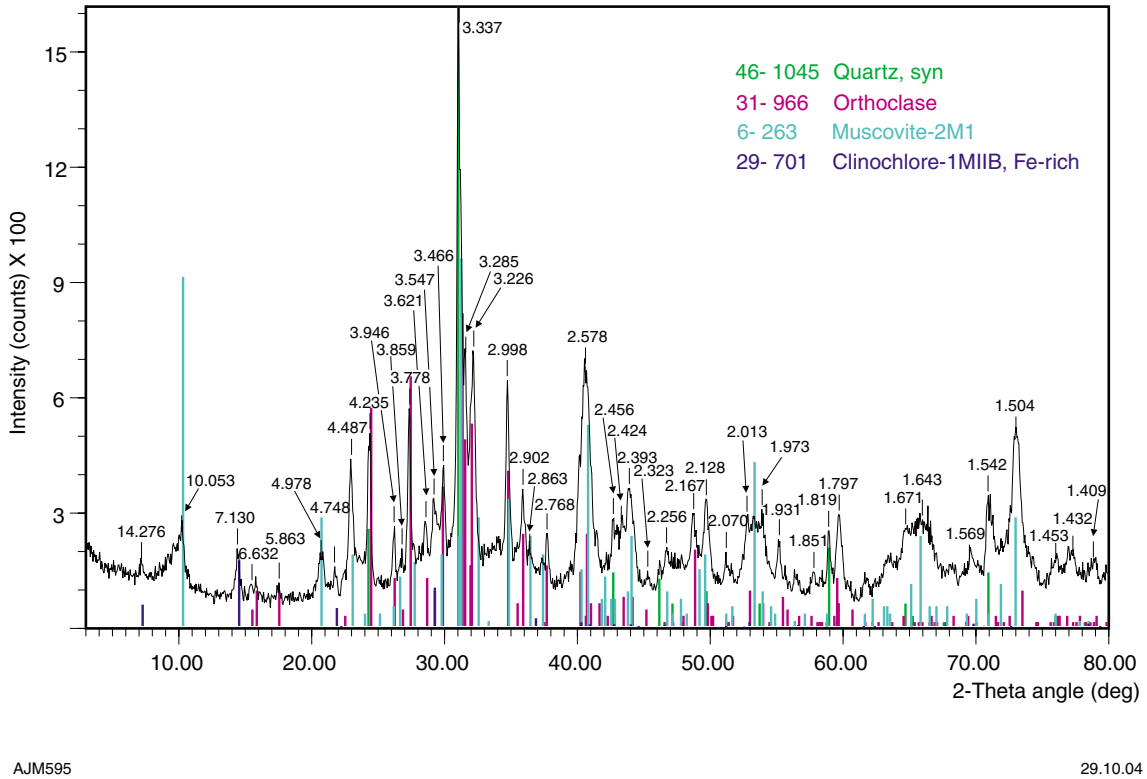

Figure 1.26. Diffractogram for Ca-saturated <2-µm fraction of sample 181780 (970.02 – 970.22 m)

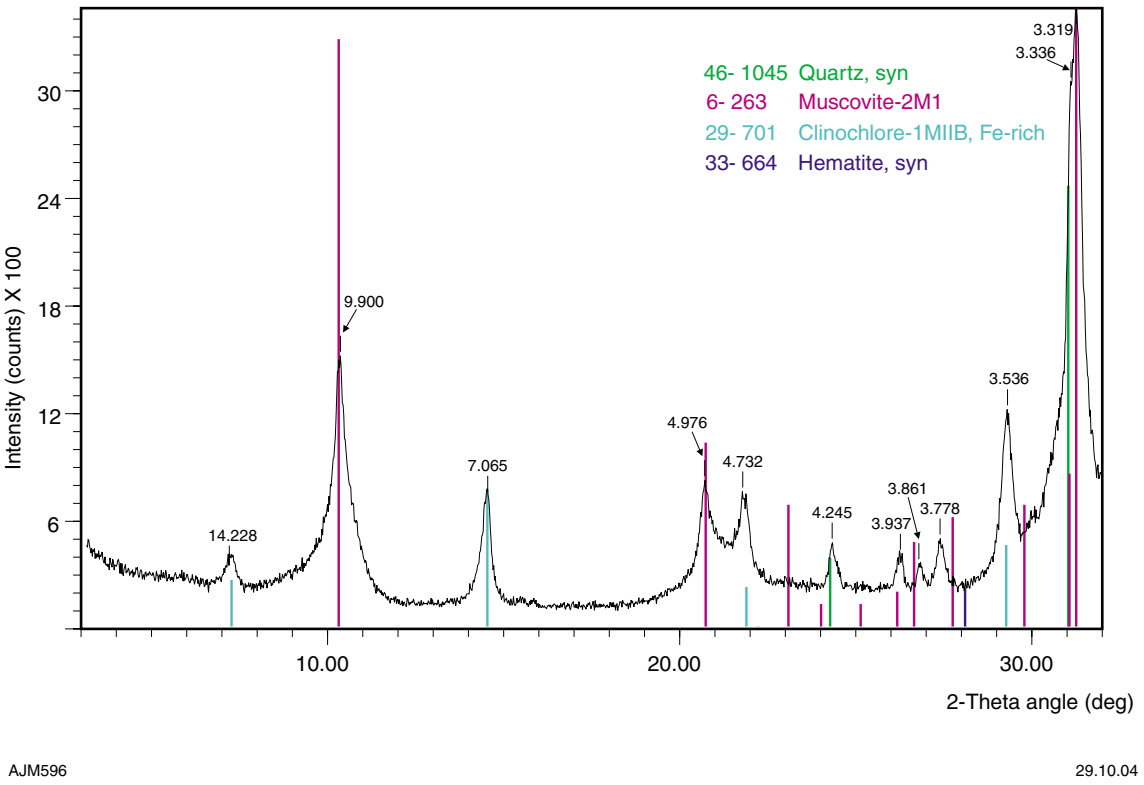

Figure 1.27. Diffractogram for Ca-saturated <2-µm fraction with glycerol of sample 181780 (970.02 – 970.22 m)

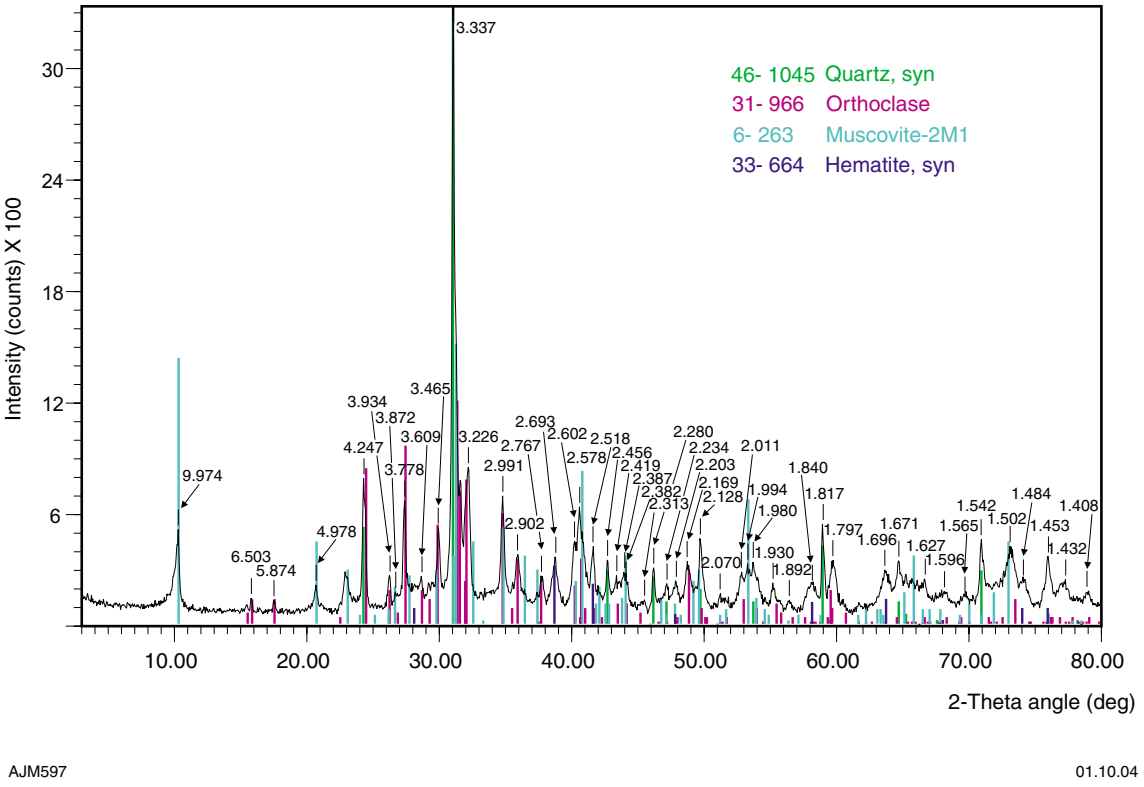

Figure 1.28. Diffractogram for the bulk rock of sample 181781 (1027.73 – 1027.95 m)

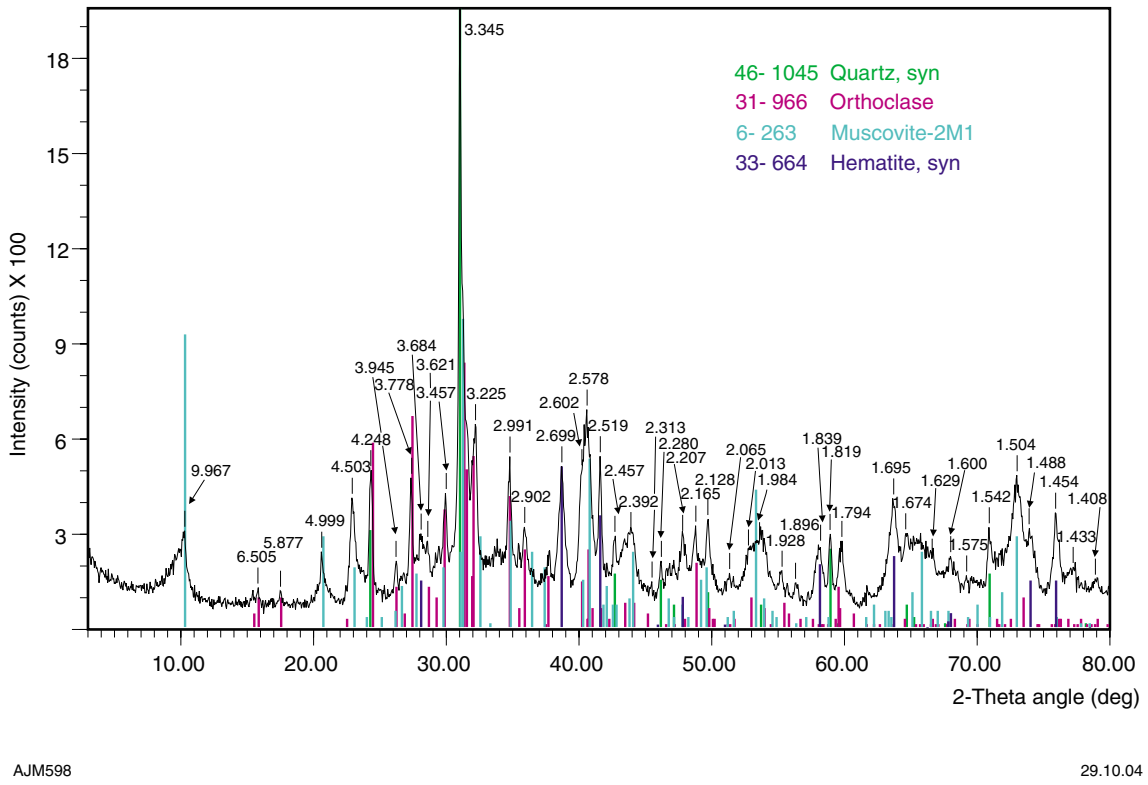

Figure 1.29. Diffractogram for Ca-saturated <2-µm fraction of sample 181781 (1027.73 – 1027.95 m)

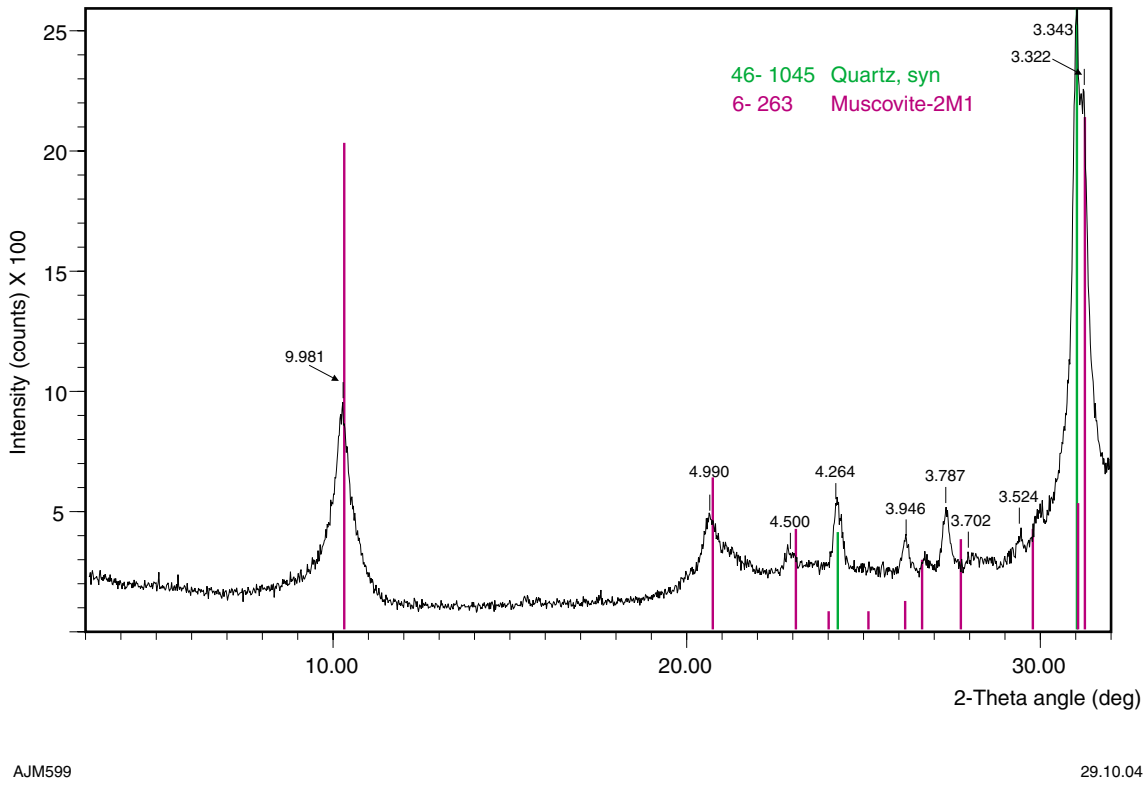

Figure 1.30. Diffractogram for Ca-saturated <2-µm fraction with glycerol of sample 181781 (1027.73 – 1027.95 m)

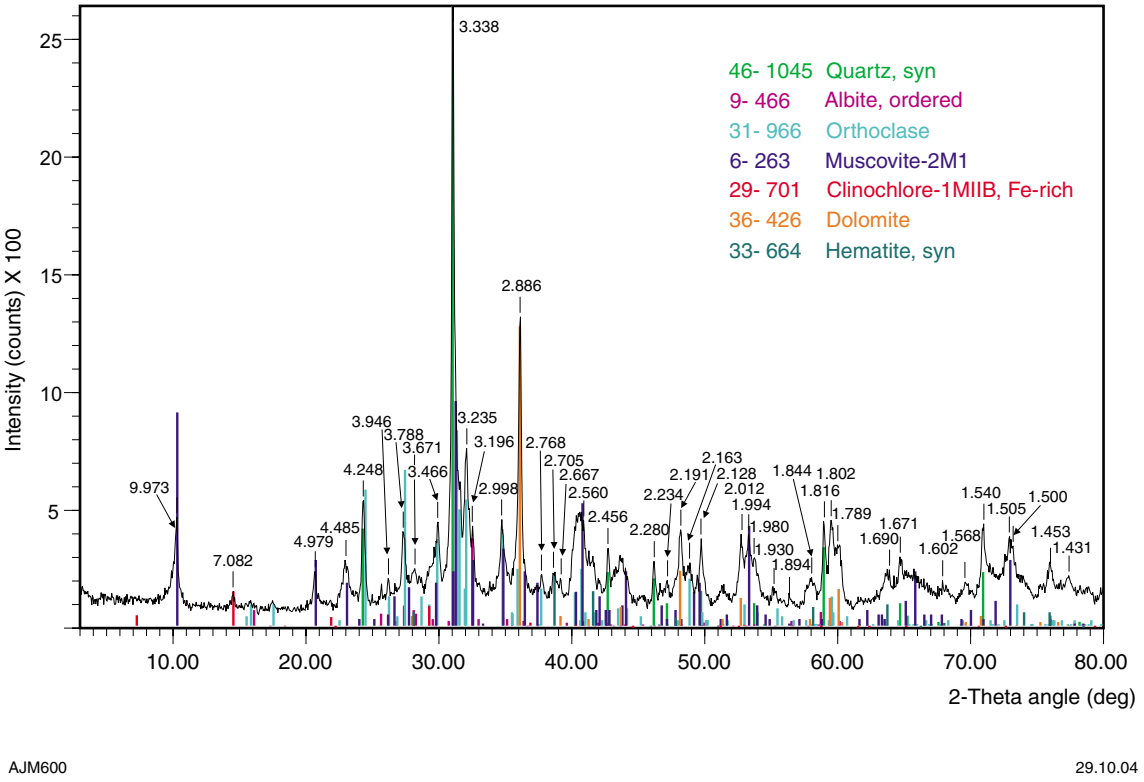

Figure 1.31. Diffractogram for the bulk rock of sample 181782 (1114.56 – 1114.86 m)

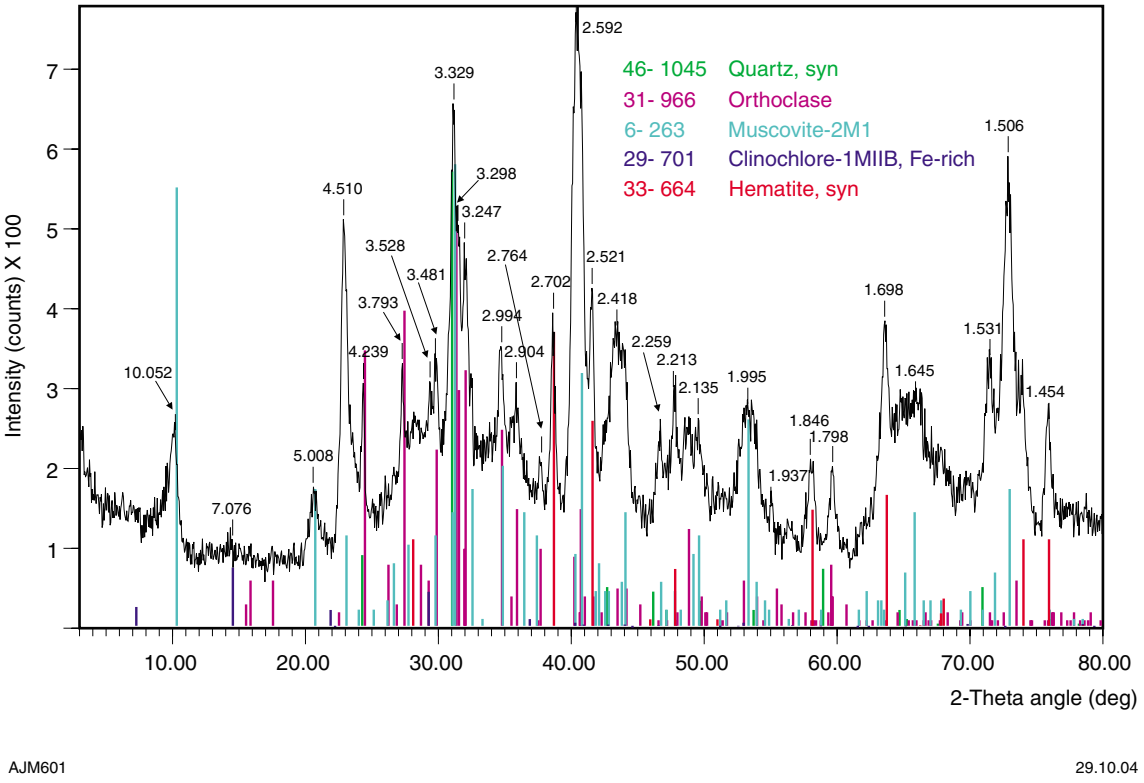

Figure 1.32. Diffractogram for Ca-saturated <2-µm fraction of sample 181782 (1114.56 – 1114.86 m)

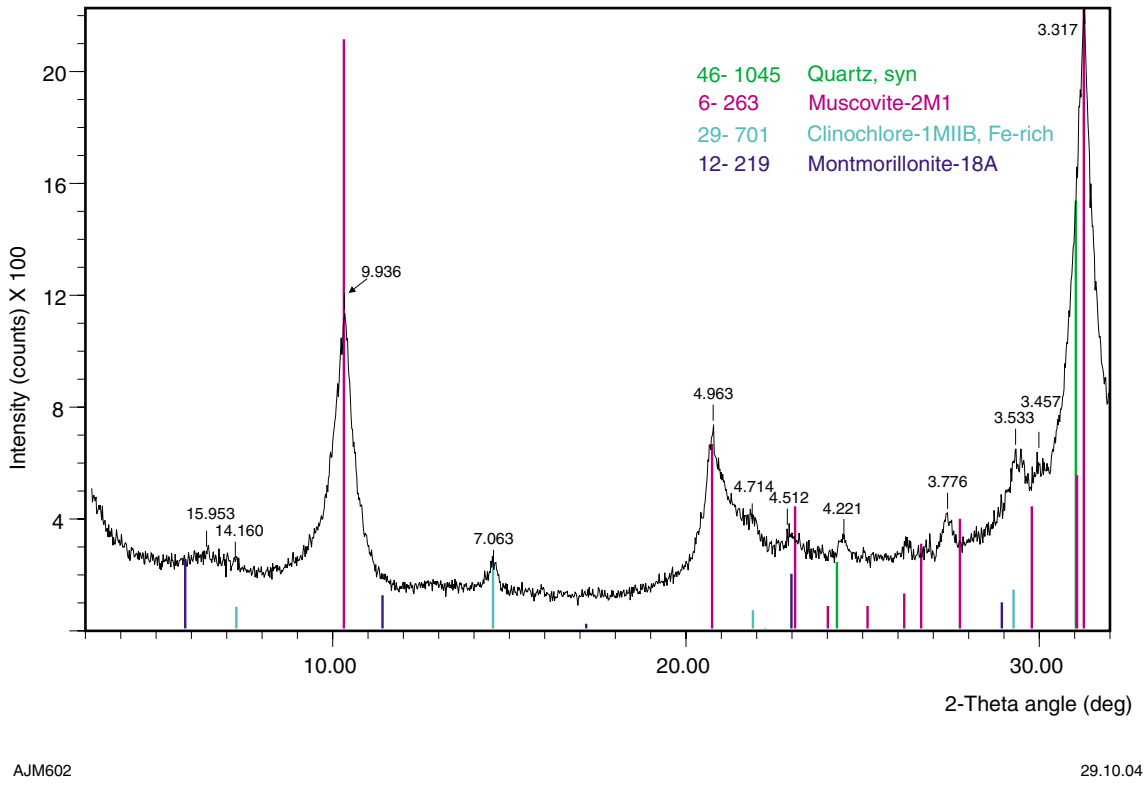

Figure 1.33. Diffractogram for Ca-saturated <2-µm fraction with glycerol of sample 181782 (1114.56 – 1114.86 m)

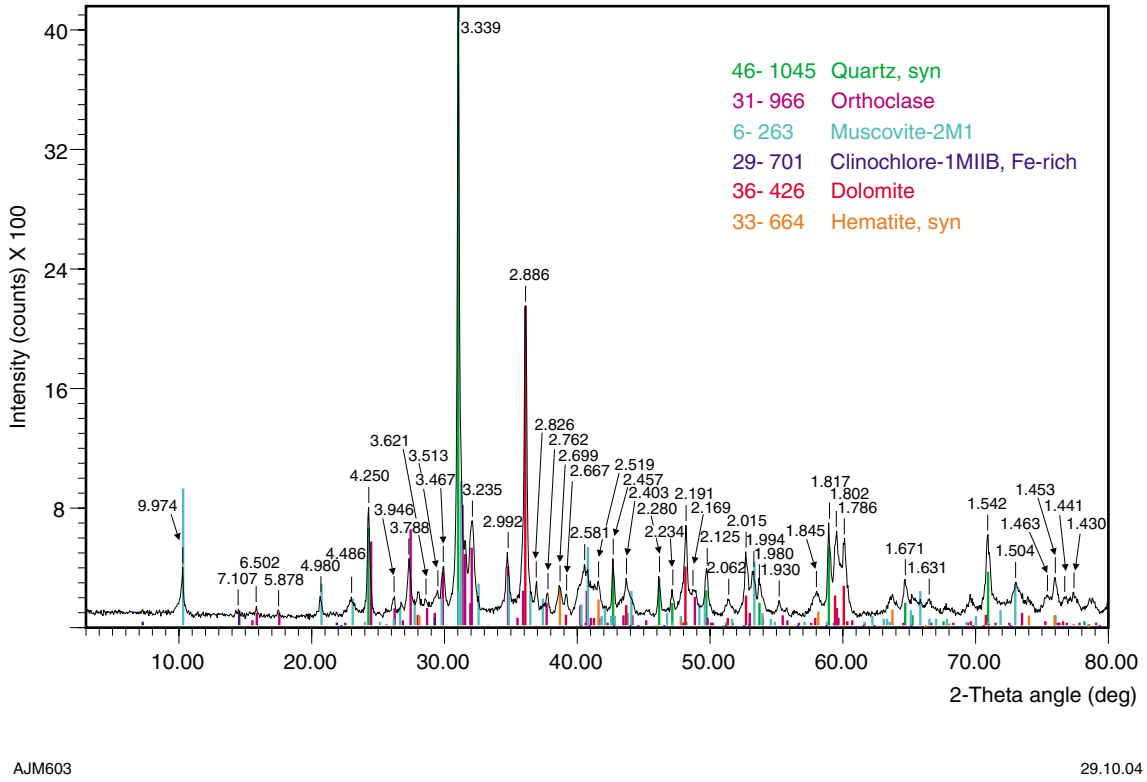

Figure 1.34. Diffractogram for the bulk rock of sample 181783 (1358.69 – 1358.89 m)

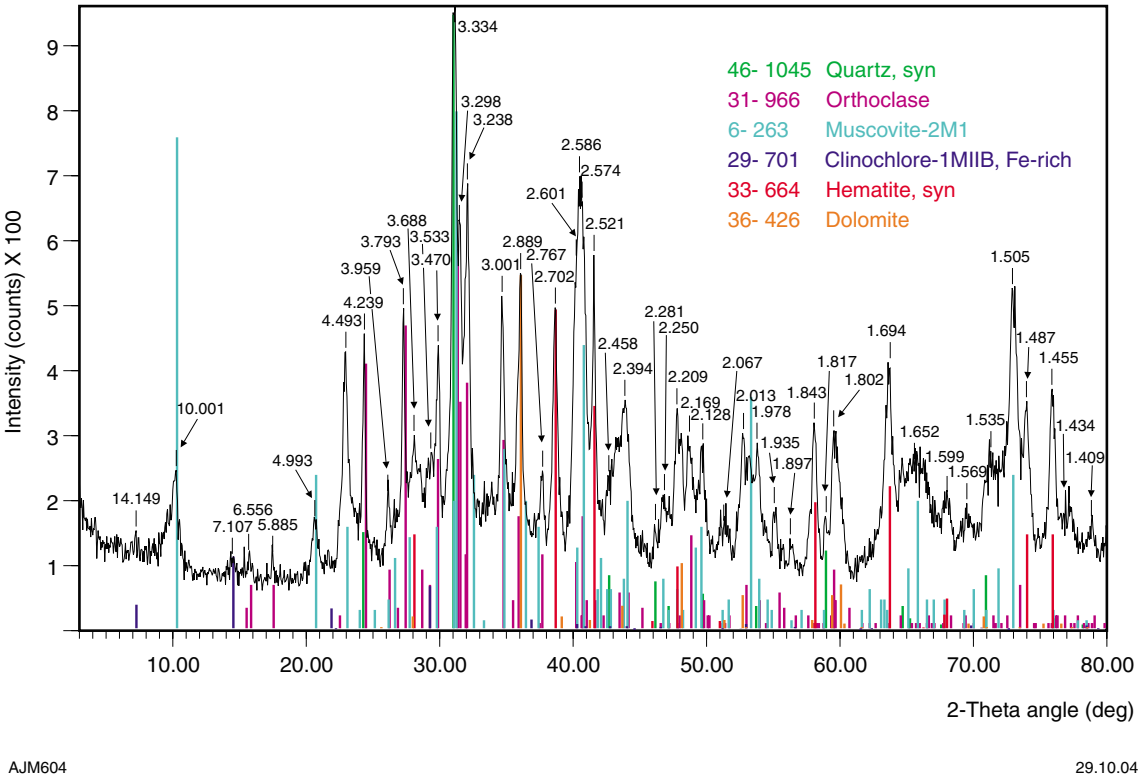

Figure 1.35. Diffractogram for Ca-saturated <2-µm fraction of sample 181783 (1358.69 – 1358.89 m)

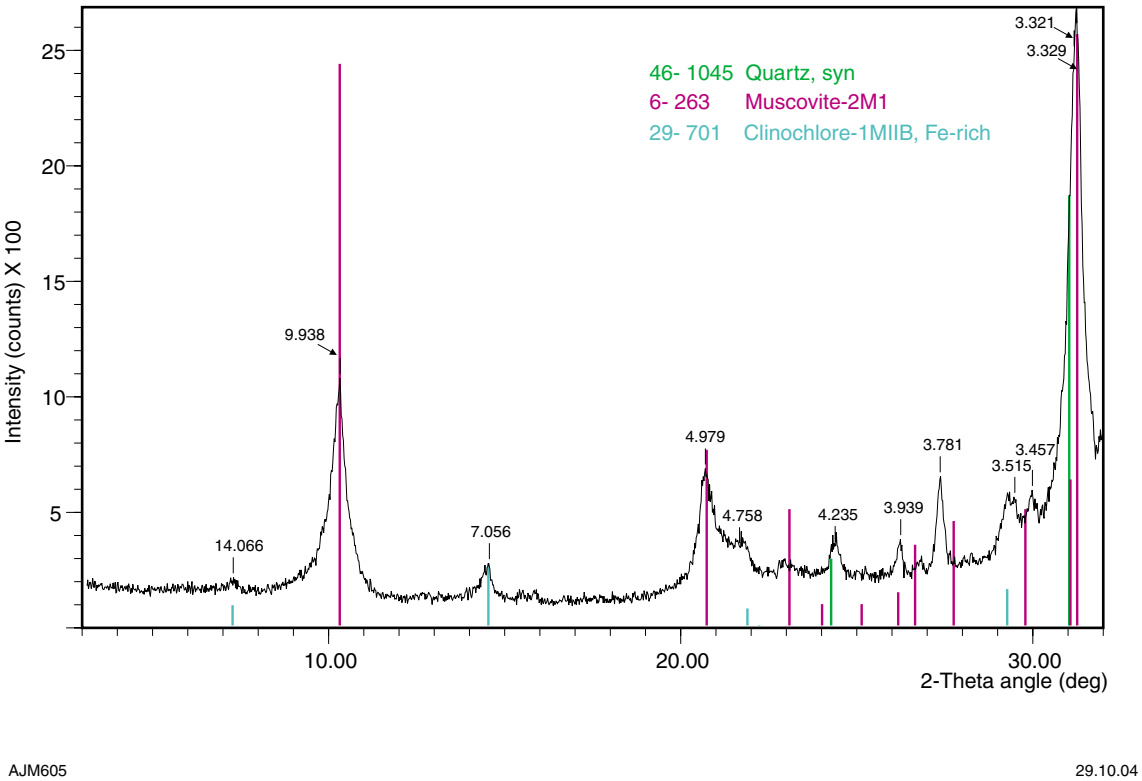

Figure 1.36. Diffractogram for Ca-saturated <2-µm fraction with glycerol of sample 181783 (1358.69 – 1358.89 m)

Amendments to the long-spaced density calibration coefficient in GSWA Lancer 1, Officer Basin, Western Australia

by

M. K. Stevens[1] and G. Koch[2]
[1]Geological Survey of Western Australia
[2] Geoscience Associates Australia, Adelaide

Abstract

The raw data long-spaced density (LSD) log from Lancer 1 gives anomalously high values when compared to bulk densities calculated from core plugs and specific gravity measurements of mudstone cores. The cause of these high LSD values was traced to an extra calibration point (of 1.35 g/cm^3) that was introduced to the long-spaced density calibration coefficient from a core-density analysis of coal for a previous client. Reprocessing of the LSD from the raw data without this extra calibration point has produced a good-quality log suitable for calculation of mechanical properties from the fullwave sonic log.

Introduction

The Lancer 1 stratigraphic drillhole was drilled by the Geological Survey of Western Australia (GSWA) and wireline logged by Geoscience Associates Australia in November 2003. At the time, the majority of these logs were considered to be of good quality. However, the long-spaced density log values were not considered reliable because they were greater than the short-spaced density values where the caliper indicated no reason for such a difference (Haines et al., 2004, p. 4). This report details the process by which a more reliable long-spaced density log was obtained by reprocessing the raw data.

It was considered important to get an accurate density log as D. Dewhurst (CSIRO Petroleum) requested preserved mudstone samples from Lancer 1 to investigate their mechanical properties. The acquisition of a Fullwave sonic log enabled the calculation of mechanical properties in the hole that can be compared with those measured in the core, but many of these properties include the density value in their calculation.

Recognition of the problem with the density log

The original processing of the formation-density tool displayed the following curves: gamma ray (GR in API units), caliper (CALI in mm), long-spaced density (LSD in g/cm^3), short-spaced density (SSD in g/cm^3), bed-resolution density (BRD in cps), and density correction (DRHO in g/cm^3). The tool was in open hole from total depth of 1501 m up to 426 m, where it entered HWT casing.

The GR and CALI logs acquired with the formation-density tool are considered to be of good quality and will not be further discussed. The formation-density tool is a single source, three-receiver tool. The BRD log has the shortest receiver spacing, and hence the best vertical resolution for detecting changes in density, but is not calibrated in g/cm^3. Logs calibrated in g/cm^3 include the SSD log, which has an intermediate receiver spacing and the LSD, which has the greatest receiver spacing and hence the greatest depth of investigation. The DRHO log records the density compensation applied to the LSD to correct for mud cake and hole rugosity.

The values in the LSD log were initially viewed with suspicion because in large sections of the hole the DRHO log was reading about +0.3 g/cm^3. This is a large density correction and was considered to be excessive given that the drillhole was generally in excellent gauge with a non-rugose, 'smooth' well bore as shown by the CALI log. A 'smooth' well bore was confirmed over large segments of the drillhole by the acoustic scanner log.

A composite well log for Lancer 1 was published as Plate 1 in Haines et al. (2004). The LSD and neutron

logs are plotted on a so-called 'limestone scale'; in other words, the LSD is plotted from 1.95 to 2.95 g/cm^3 and the neutron from 45 to –15% limestone porosity. In this display the LSD log should plot a few percent neutron porosity units to the left of the neutron curve in clean quartzose sandstone. However, the LSD curve plots to the right of the neutron curve through the vast majority of the drillhole, even where the core description indicates clean quartzose sandstone.

Points used for LSD log calibration

Forty porosity, grain density, and permeability measurements were made at ambient temperature and pressure on sandstone and dolostone from Lancer 1 (Haines et al., 2004, table 3). Core plugs at selected depths were used to calculate bulk densities using the equation:

$$RhoB = Por \times RhoF + (1 - Por) \times RhoMa$$

Where RhoB = bulk density, Por = porosity, RhoF = fluid density, and RhoMa = matrix density. The results of these calculated densities are presented in Table 1.

It was interpreted from this data that the SSD values were close to the calculated values but that the LSD values were significantly larger than expected. In low-porosity carbonates the grain density measured in core plugs should be only slightly greater than their bulk density and hence are also useful for investigating the logged density response. A comparison of five carbonates from Lancer 1 is compared with logged densities in Table 2.

The asterisks in the LSD and SSD columns denote that the log was not constant at the relevant depth, and hence is not necessarily useful for comparison with the measured grain density. It was interpreted that the SSD values were close to the measured values but that the LSD values were larger than expected in the majority of the cases. The core at 967.0 m depth is logged as a dolostone, but the grain density of 2.7 g/cm^3 suggests it is more likely to be a limestone.

It was decided that some density readings from mudstone cores would also be useful to validate the reprocessing of the LSD log. Specific-gravity measurements for diamictite and mudstone were taken for nine samples from four zones at GSWA's Carlisle laboratories, and these are compared with the original SSD log values in Table 3. The favourable comparison between the SSD and SG values suggests that the formation-density tool is probably functioning correctly.

Reprocessing of the LSD log

Geoscience Associates Australia undertook a rigorous statistical analysis of all three density receivers including gamma and caliper raw count channels, and this indicated that problems with tool functionality was highly unlikely. The density tool used for logging Lancer 1 was calibrated

Table 1. Lancer 1 calculated and November 2003 logged bulk densities

Core depth (m)	*Log depth (m)*	*Lithology*	*Porosit\y helium %*	*Grain density (g/cm^3)*	*Calculated density (g/cm^3) (RhoF = 1)*	*Calculated density (g/cm^3) (RhoF = 1. 1)*	*LSD (g/cm^3)*	*SSD (g/cm^3)*
450.8	450.8	sandstone	13.4	2.68	2.483	2.496	2.70	2.50
597.1	597.1	sandstone	23.7	2.64	2.251	2.275	2.50	2.32
863.4	863.9	sandstone	21.2	2.64	2.292	2.313	2.62	2.39
872.9	873.4	sandstone	11.8	2.64	2.446	2.458	2.64	2.44
896.2	896.7	sandstone	20.9	2.64	2.297	2.318	2.56	2.33
1 055.0	1 055.5	sandstone	18.5	2.65	2.34	2.36	2.57	2.40
1 202.6	1 203.5	sandstone	26.2	2.63	2.20	2.23	2.47	2.29
1 292.1	1 293.1	sandstone	20.2	2.65	2.33	2.34	2.57	2.38
1 488.1	1 489.5	sandstone	0.5	2.61	2.602	2.603	2.76	2.64

Table 2. Lancer 1 grain density and November 2003 logged bulk densities

Core depth (m)	*Log depth (m)*	*Lithology*	*Porosity helium %*	*Grain density (g/cm^3)*	*LSD (g/cm^3)*	*SSD (g/cm^3)*
804.1	804.6	dolostone	0.5	2.84	3.02	2.87
914.4	914.9	dolostone	0.0	2.82	2.92	2.77*
967.0	967.6	dolostone ?limestone	0.1	2.7	2.92*	2.8
1 030.1	1 030.7	dolostone	0.3	2.84	3.00	2.84*
1 122.9	1 123.6	cherty dolostone	0.1	2.77	3.00	2.80*
1 142.6	1 143.5	dolostone	1.1	2.98	3.02	2.92

Table 3. Lancer 1 Specific Gravity measurements and November 2003 SSD logged bulk densities

Top core depth (*m*)	*Base core depth* (*m*)	*Lithology*	*WIA* (*g*)	*WIW* (*g*)	*SG*	*Comments*	*Log depth* (*m*)	*SSD* (g/cm^3)	*SSD – SG* (g/cm^3)
433.77	433.81	Diamictite	1 006.09	596.62	2.47	WIW unstable, air escaping from sample	433.8	2.60	0.13
433.89	434.02	Diamictite	958.55	573.00	2.49	WIW very slowly increasing	433.9	2.57	0.08
986.87	986.94	Mudstone	464.71	286.32	2.61	fragile sample	986.4	2.70	0.10
987.83	987.89	Mudstone	451.04	277.70	2.60	fragile sample	987.3	2.70	0.10
1 093.95	1 094.14	Mudstone	1 543.43	940.44	2.56	WIW very slowly increasing	1 093.4	2.69	0.13
1 094.15	1 094.34	Mudstone	1 469.36	897.90	2.57		1 093.6	2.66	0.09
1 360.93	1 361.03	Mudstone	834.28	513.52	2.60		1 359.6	2.74	0.14
1 361.03	1 361.23	Mudstone	1 672.28	1 030.26	2.61		1 359.7	2.70	0.10
1 361.23	1 361.32	Mudstone	687.80	423.28	2.60		1 359.9	2.75	0.15

NOTES: WIA: weight in air
WIW: weight in water

with respect to the Amdel calibration facility in South Australia. It was found that an extra calibration point (of 1.35 g/cm^3) was introduced to the long-spaced density calibration coefficient from a core density analysis of coal for a client in Central Queensland. Although the addition of this calibration point provided a more accurate g/cm^3 reduction for coal, it caused problems with rock densities above 2.5 g/cm^3. GSWA provided a series of core density results that were used in the calibration process. These results provided the basis for the revised long-spaced density log that has now been delivered by Geoscience Associates Australia to GSWA. The revised DRHO log calculated from these results indicates a good relationship between long- and short-spaced density curves.

Additional work to be undertaken relating to wireline logs

Geoscience Associates Australia will recalculate the mechanical properties logs derived from the Fullwave sonic log with the revised density values.

GSWA will revise the Lancer 1 composite log with the new LSD log.

A zone of anomalously low Poisson's ratio (<0.2) has been identified in a relatively homogeneous sandstone from 871.5 to 874.5 m log depth. D. Dewhurst will measure the dynamic Poisson's ratio from core plugs over this zone to help determine if this low ratio is due to a mineralogical affect, or whether it is possibly due to a compressible fluid in the porosity.

Geoscience Associates Australia has agreed to investigate whether the Keene Basalt may have affected the readings of the magnetic compass in the acoustic-scanner tool, and if this is considered likely to have occurred, whether any correction can be made to help correctly orient this tool. If these investigations indicate that the Keene Basalt is likely to have affected the acoustic scanner's compass, then the preliminary palaeomagnetic results obtained by Pisarevsky and Wingate (2005) over this formation will need to be reviewed.

Conclusions

Concerns over the reliability of the LSD log expressed in Haines et al. (2004) were confirmed by comparing this log with calculated bulk densities from core plugs and by taking SG measurements in mudstones. The SSD log values were reasonably close to the calculated bulk densities from core plugs and SG measurements in mudstones, suggesting that the formation-density tool was probably functioning correctly. The reason for the high LSD values was traced to an extra calibration point that had been introduced to the long-spaced density calibration coefficient from a core density analysis of coal for a previous client.

The LSD log has been recalculated from the raw data and is now considered to be reliable.

References

HAINES, P. W., MORY, A. J., STEVENS, M. K., and GHORI, K. A. R., 2004, GSWA Lancer 1 well completion report (basic data), Officer and Gunbarrel Basins, Western Australia: Western Australia Geological Survey, Record 2004/10, 39p.

PISAREVSKY, S. A., and WINGATE, M. T. D., 2005, Preliminary palaeomagnetic results from GSWA Lancer 1, Officer Basin, Western Australia: Western Australia Geological Survey, Record 2005/4, p. 13–19.

Revised well index sheet

ORGANIZATION: Geological Survey of Western Australia **Statutory Petroleum Exploration Report No.: S20880**
WELL: GSWA Lancer 1 **BASINS:** Gunbarrel Basin over Officer Basin **TYPE:** Stratigraphic
SPUDDED: 10 Oct 2003 **SUB-BASINS:** Sherriff Shelf over Westwood Shelf
COMPLETED: 20 Nov 2003 **ELEVATION GL:** 450 m AHD; RT: 449.3 m AHD
TD: 1501.3 m [(a)] BHT: 63.5°C **LATITUDE:** 25°02'44.5"S; **LONGITUDE:** 123°45'20.1"E (GDA 94)
STATUS: Plugged and abandoned **EASTING:** 576220; **NORTHING:** 7229780 (MGA Zone 51J)

FORMATION	TOPS (m)		LITHOLOGICAL SUMMARY
	DRILL	SUBSEA	
GUNBARREL BASIN:			
Cainozoic	0	+450.0	Reddish brown fine-grained sand, brown mudstone and ferricrete overlying multi-coloured sandstone
Paterson Formation	?17	+433	Clay, grey mudstone, grey to brown sandstone, minor conglomerate
OFFICER BASIN:			
Durba Sandstone	169.1	+280.9	Pale brown quartz-rich cross-bedded sandstone
Lungkarta Formation	205.0	+245.0	Reddish brown sandstone and minor basal polymict conglomerate
Wahlgu Formation	344.3	+105.7	Red diamictite and mudstone, multicoloured sandstone
Kanpa Formation	466.5	16.5	Brown to grey claystone and mudstone, grey stromatolitic dolostone, grey to brown sandstone
Keene Basalt	527.4 – 576.2	77.4 – 126.2	Dark, fine- to coarse-grained basalt, locally amygdaloidal, erosional upper surface
Hussar Formation	707.5	257.5	Brown sandstone, mudstone and stromatolitic dolostone
Browne Formation	1201.9	751.9	Reddish brown sandstone and mudstone, red–grey dolostone, halite
Lancer Member	1201.9 – 1297.7	751.9 – 847.7	Reddish brown crossbedded sandstone in foresets up to 11 m thick
Woolnough Member	1323.4 – 1357.7	873.4 – 907.7	Red–grey stromatolitic dolostone, mudstone
lower Browne Formation	1357.7 – 1478.9	907.7 – 1028.9	Reddish-brown mudstone with halite crystals becoming abundant towards halite interval; grey, argillaceous dolostone, halite, fine-grained sandstone, minor conglomerate and mudstone below halite interval
unnamed halite interval	1440.8 – 1472.4	990.8 – 1022.4	Halite, reddish brown mudstone, grey argillaceous dolostone
?MESOPROTEROZOIC BASIN			
?Cornelia Sandstone	1478.9 – 1501.3	1028.9 – 1051.3	Bluish-grey, pebbly, clayey, medium-grained, cross-bedded sandstone, well cemented

CORES	Continuously cored:	PQ: 104–429.5 m (driller, 100% recovery);	HQ: 429.5–1501.3 m (driller, 100% recovery)
LOGS	Run 1:	16" normal resistivity	420–1501 m
	Run 2:	64" normal resistivity	420–1501 m
	Run 3 (Gam/G-N):	SPR	420–1501 m
		SP	420–1501 m
		N	0–1501 m
	Run 4 (GAA/DDC):	GR	0–1501 m
		LD	0–1501 m
		SD	0–1501 m
		Caliper	0–1501 m
	Run 5:	Sonic (full-waveform)	420–1501 m
	Run 6:	BHTV (acoustic scanner)	1450–1500 m; 1200–1365 m; and 420–900 m
CASING	7" (OD 178 mm, ID 172 mm):		0–6 m
	PW (OD 140 mm, ID 127 mm):		104–428 m
	HWT (OD 114 mm, ID 102 mm):		428–1501.3 m

NOTES: (a) Depth from driller
The resistivity, SP, and SPR logs are adversely affected by the highly saline mud in the hole

GSWA

GSWA Lancer 1 well completion report (interpretive papers)
Officer and Gunbarrel Basins, Western Australia

RECORD 2005/4

This Record is published in digital format (PDF) as part of a digital dataset on CD. It is also available online at: www.doir.wa.gov.au/gswa/onlinepublications. Laser-printed copies can be ordered from the Information Centre for the cost of printing and binding.

Further details of geological publications and maps produced by the Geological Survey of Western Australia can be obtained by contacting:

Information Centre
Department of Industry and Resources
100 Plain Street
East Perth WA 6004
Phone: (08) 9222 3459 Fax: (08) 9222 3444

www.doir.wa.gov.au/gswa/onlinepublications

Department of Industry and Resources
HON. ALAN CARPENTER, M.L.A.
MINISTER FOR STATE DEVELOPMENT
JIM LIMERICK
DIRECTOR GENERAL

Geological Survey of Western Australia
TIM GRIFFIN
DIRECTOR

GSWA Lancer 1
Revised composite well log

Company	Geological Survey of WA
Well Name	Lancer 1
Well type	Stratigraphic, vertical corehole
Status	Plugged and abandoned
Basins	Gunbarrel over Officer Basin
Sub-Basins	Sherrif Shelf over Westwood Shelf
Latitude	25°02'44.5" S
Longitude	123°45'20.1" E
Easting	576220 (MGA Zone 51J)
Northing	7229780
Elevation GL	450 m AHD
Elevation RT	449.3 m AHD
Height datum	Mean sea level
Total depth	1501.3 m (driller)
Bottom hole temperature	63.5°C
Date spudded	10 October 2003
Date completed	20 November 2003
Rig	UDR 1500
Drilling company	Drillcorp Western Deephole
Logging company	Geoscience Associates
Logging geologists	Peter Haines (core), Mark Stevens (cuttings)

CORES

PQ	104–429.5 m
HQ	429.5–1501.2 m

LOGS

Run 1	16" normal resistivity†	420–1501 m
Run 2	64" normal resistivity†	420–1501 m
Run 3	SPR†	420–1501 m
	SP†	420–1501 m
	Neutron*	0–1501 m
Run 4	GR*	0–1501 m
	LS density	0–1501 m
	SS density	0–1501 m
	Caliper	0–1501 m
Run 5	Sonic (full waveform)	420–1501 m
Run 6	BHTV (acoustic scanner)	1450–1500 m; 1200–1365 m; 420–900 m

CASING

7"	0–6 m
PW	0–104 m
HWT	104–428 m

† 16" normal resistivity, 64" normal resistivity, SP, and single point resistance logs are considered unreliable due to the highly saline mud in the hole.

* GR and Neutron are logged through casing above 428 m.

LITHOLOGIES

Conglomerate; Sandstone; Mudstone; Claystone; Diamictite; Dolostone; Anhydrite/gypsum; Halite; Basalt

LITHOLOGY MODIFIERS

Pebbly; Pebbly (angular clasts); Sandy; Argillaceous/silty; Dolomitic or dolostone interbeds; Oolitic; Cherty or chert beds/nodules; Anhydritic/gypsiferous; Halite-bearing

SYMBOLS

Flat bedding or lamination; Current ripple lamination; Cross-bedding; Large foresets; Irregular or wavy bedding; Unconformity; Flutes; Soft-sediment deformation, slump; Soft-sediment fault; Sandstone dyke along soft-sediment faults; Dessication cracks; Synaeresis cracks; Vein/fracture; Stylolites; Vugs; Stromatolites; Microbial lamination; Vesicles/amygdales; Pyrite; Glauconite; Intraclasts (colour indicates lithology)

Scale 1:500

Lithological descriptions
Cuttings: 0–104 m
Core: 104–1501 m

0.0 – ?17.0 m CAINOZOIC (?17.0 m thick)

0.0 – 0.2 m. Sand: reddish-brown, fine grained, unconsolidated
0.2 – 2.0 m. Mudstone and ferricrete: moderate brown to moderate yellowish-brown, ferruginous, minor quartz granules, well consolidated (rotary cuttings only)
2.0 – 5.0 m. Mudstone: moderate yellowish-brown, minor fine-grained sandstone (rotary cuttings only)
5.0 – 8.0 m. Mudstone: as for 2–5 m; Sandstone: grey, fine to medium grained, coarsening downhole (rotary cuttings only)
8.0 – 14.0 m. Sandstone: light yellow to light pink, medium grained (rotary cuttings only)
14.0 – 17.0 m. Sandstone: light grey to light yellow, fine to coarse grained, porous, 10–30% grey mudstone (rotary cuttings only)

?17.0 – ?169.1 m PATERSON FORMATION (?152.1 m thick)

17.0 – 21.0 m. Mudstone: light green, grey and yellow, minor fine to medium grained sandstone (rotary cuttings only)
21.0 – 33.0 m. Clay: brown to yellow, minor quartz granules above 25 m, unconsolidated (rotary cuttings only)
33.0 – 70.0 m. Clay: yellow, green, and grey (mostly grey below 58 m), unconsolidated, rare granule fragments at 39.0 – 41.0 m and 49.0 – 70.0 m, rare consolidated mudstone to very fine sandstone chips below 64 m (rotary cuttings only)
70.0 – 74.5 m. Mudstone and conglomerate: multicoloured, sedimentary clasts 1–10 mm, clasts sub-angular to sub-rounded (rotary cuttings only)
74.5 – 77.0 m. Mudstone: light grey, moderate consolidation, 80–90%; Conglomerate: as for 70.0 – 74.5 m, 10–20%, increases upward, probably contamination (rotary cuttings only)
77.0 – 93.0 m. Mudstone: moderate grey to moderate grey-green, poorly consolidated, fissile in parts, trace of carbonaceous material at 81.0 – 82.0 m, 86.0 – 88.0 m, 91.0 – 93.0 m (rotary cuttings only)
93.0 – 95.0 m. Mudstone: as for 77.0 – 93.0 m, 90%; Sandstone: light brown, very fine to fine grained, quartzose, poor to fair porosity, moderate consolidation (rotary cuttings only)
95.0 – 104.0 m. Mudstone and sandstone: as for 93.0 – 95.0 m, but sandstone increases downward to 40% (rotary cuttings only)

104.0 m. Start of PQ coring

104.0 – 125.0 m. Sandstone: light to moderate grey-green (locally reddish), medium grained, moderately to well sorted, rounded, subfriable, porous, quartz dominant but significant lithic, feldspar, and mica content, cross-bedded, claystone intraclasts
125.0 – 133.0 m. Sandstone: as for 104.0 – 125.0 m, but alternating light grey to mottled reddish-brown.
133.0 – 155.5 m. Sandstone: light reddish-brown, medium to coarse grained, moderately to poorly sorted, cross-bedded, increased clay matrix and lithic-feldspathic content compared to 104.0 – 133.0 m, red mud-clast horizons, slightly pyritic in parts
155.5 – 156.0 m. Mudstone: red with greenish bands and mottles, minor sandy bands weakly fissile
156.0 – 159.1 m. Sandstone: as for 133.0 – 155.5 m, patchy calcareous cementation
159.1 – 159.8 m. Mudstone: as for 155.5 – 156.0 m
159.8 – 161.1 m. Sandstone: as for 156.0 – 159.1 m
161.1 – 162.7 m. Mudstone: as for 155.5 – 156.0 m
162.7 – 165.6 m. Sandstone: as for 156.0 – 159.1 m, green mudstone intraclasts at top
165.6 – 167.0 m. Mudstone: as for 155.5 – 156.0 m, poorly sorted coarse sandy to granule interbeds, possible desiccation cracks
167.0 – 168.2 m. Conglomerate: reddish-brown, polymict pebbles to 1 cm, rounded, very poorly sorted, alternates with red mudstone; in part a diamictite
168.2 – 169.0 m. Sandstone: reddish-brown, fine to medium grained, moderate to well sorted, current ripple cross-laminations
169.0 – 169.1 m. Erosional surface at 169.1 m overlain by 5 cm conglomerate with metamorphic clasts to 8 cm

169.1 – 205 m DURBA SANDSTONE (35.9 m thick)

169.1 – 205.0 m. Sandstone: pale brown, medium grained, moderate sorted, generally rounded, quartz rich, minor clay matrix, rare red mudstone interbeds and intraclasts, cross-bedded, concretions common in lower half, sparse pyrite mainly near base

205 – 344.3 m LUNGKARTA FORMATION (139.3 m thick)

205.0 – 214.0 m. Sandstone: reddish-brown, fine to coarse grained, fining upward, lithic granule conglomerate horizons in lower half, poorly sorted, mostly flat-bedded
214.0 – 270.9 m. Sandstone: reddish-brown, medium grained, well sorted, well rounded, porous, very large foresets with dips up to 30°, sparse pyrite in upper 22 m
270.9 – 271.6 m. Diamictite: reddish-brown and minor grey, sandy mudstone with angular lithic clasts to 2 cm
271.6 – 310.2 m. Sandstone: as for 214.0 – 270.9 m, soft-sediment deformation at top of interval
310.2 – 311.0 m. Sandstone: reddish-brown, massive, pebbly, polymict angular granules and pebbles up to 8 mm
311.0 – 325.7 m. Sandstone: as for 214.0 – 270.9 m
325.7 – 326.5 m. Conglomerate: reddish-brown sandy matrix, polymict rounded to angular clasts up to 6 cm
326.5 – 339.9 m. Sandstone: as for 214.0 – 270.9 m
339.9 – 341.3 m. Conglomerate and sandstone: reddish-brown, sharp-based fining-upward succession from polymict granule conglomerate with coarse sandy matrix to cross-bedded, medium to coarse grained pebbly sandstone, poorly sorted, angular to rounded clasts
341.3 – 344.3 m. Conglomerate and sandstone: reddish-brown, sharp-based fining-upward succession from polymict granule conglomerate with coarse sandy matrix to flat-laminated medium-grained sandstone

344.3 – 466.5 m WAHLGU FORMATION (122.2 m thick)

344.3 – 345.7 m. Sandstone: white to green (reddened at top), medium grained, well sorted, rounded, porous, green claystone intraclasts, flat bedded
345.7 – 349.1 m. Diamictite: red, fine sandy matrix; Mudstone: red, sparse pebbles
349.1 – 350.0 m. Sandstone: green with red mottles, medium grained, poorly sorted with muddy matrix, sparse pebbles, weak lamination and soft-sediment deformation
350.0 – 354.5 m. Diamictite: red with green bands and mottles, matrix of very poorly sorted muddy sandstone, large striated igneous clast at 352.4 m
354.5 – 358.3 m. Sandstone: red, fine to coarse grained, moderately to well sorted, flat-bedding, foreset bedding, climbing current ripple lamination
358.3 – 359.0 m. Sandstone: white to pale green, medium to coarse grained, well sorted, rounded, foreset bedding, possible glauconite
359.0 – 388.0 m. Diamictite: red, local green reduction spots, matrix very poorly sorted muddy sandstone, pebble-, cobble- and boulder-size clasts, angular to rounded, some clasts striated, mostly massive, local soft-sediment deformation. Mudstone: red
388.0 – 390.2 m. Mudstone: red, scattered sand grains, rare pebbles
390.2 – 391.0 m. Sandstone: green grading to red at top, coarse grained, rounded, pebbly, abundant mud clasts, possible glauconite
391.0 – 397.0 m. Sandstone: red, coarse-grained, pebbly, moderately sorted, grains rounded, weak foreset bedding; 30 cm basal sandstone bed pale green to white, medium to coarse grained, well sorted, cross-bedded, possible glauconite
397.0 – 405.0 m. Diamictite: as for 359.0 – 388.0 m
405.0 – 413.5 m. Diamictite: as for 359.0 – 388.0 m, but mostly with mudstone matrix, clasts reach 0.5 m near base, largest clasts are mafic igneous
413.5 – 414.4 m. Sandstone: green with red centre, medium grained, green mudstone bands, irregular bedding
414.4 – 424.5 m. Diamictite: as for 359.0 – 388.0 m
424.5 – 427.9 m. Diamictite: moderate grey, mudstone matrix, massive
427.9 – 428.6 m. Sandstone: red, medium to coarse grained, graded, interbedded with red mudstone, possible glauconite
428.6 – 428.7 m. Conglomerate: red, polymict, clast supported, coarse-grained sandy matrix
428.7 – 443.7 m. Diamictite: brown (grey and red near top), mudstone matrix with significant fine sandy content below 439.0 m, massive; Sandstone dyke at 442.2 – 443.7 m filled with white medium-grained well-silicified sandstone
443.7 – 449.5 m. Mudstone: brown, fractured, slickensides, massive to locally flat laminated, soft-sediment deformation, minor fine-grained green sandstone
449.5 – 452.0 m. Sandstone: brown, medium grained, poorly sorted, abundant sandstone and mudstone intraclasts in lower part, flat bedding and current ripple laminations, graded and reverse-graded beds
452.0 – 456.5 m. Diamictite: grey, varying to green and brown near base, soft-sediment deformation near base
456.5 – 457.0 m. Mudstone: reddish-brown, fractured
457.0 – 459.0 m. Sandstone: reddish-brown, poorly sorted, pebble clasts and mudstone intraclasts in lower part, flat-bedded, soft-sediment deformation and faulting
459.0 – 459.5 m. Mudstone: reddish-brown
459.5 – 462.5 m. Diamictite: reddish-brown, muddy sandstone matrix, grading down into poorly sorted sandstone, soft-sediment deformation and faulting
462.5 – 466.5 m. Dolostone and sandstone: interpreted as dolostone-clast conglomerate with sandy matrix and sandstone interbeds, grey to green. Sandstone: medium to coarse grained, poorly sorted

466.5 – 707.5 m KANPA FORMATION (122.2 m thick)

466.5 – 470.9 m. Dolostone: grey, argillaceous and locally sandy, fractured at top, 10 cm ooid packstone
470.9 – 474.8 m. Mudstone: dark grey to greenish-grey, sandy interbeds, strongly sheared (minor fault?), argillaceous dolostone at base
474.8 – 477.0 m. Dolostone: grey, argillaceous, stylolitic, stromatolitic and microbially laminated (at 476.2 – 477.0 m), vuggy dolostone intraclast conglomerate with medium to coarse sandy matrix at 475.0 – 475.4 m, dolomitic sandstone
477.0 – 481.0 m. Sandstone: grey to locally green and brown, fine to coarse grained, moderately sorted, locally porous and friable, dolomitic at top and base, mudstone interbeds
481.0 – 483.6 m. Mudstone: grey, flat laminated, dolomitic, dolostone interbeds
483.6 – 493.8 m. Dolostone: grey, argillaceous, stylolitic, stromatolitic at 486.1 – 486.4 m, 487.0 – 488.3 m, 490.2 – 490.6 m, 492.8 – 493.1 m, flat laminated, minor intraclasts and grainstone, dolomitic sandstone and mudstone interbeds, minor pyrite at top
493.8 – 495.4 m. Sandstone: light grey to green, medium to coarse grained, well sorted, in part porous and friable, dolomitic at top, thin mudstone at base
495.4 – 499.4 m. Dolostone: grey, stromatolitic, stylolitic, intraclast conglomerate at top, chert nodules at 498.8 m
499.4 – 501.5 m. Sandstone: grey, medium to coarse grained, mostly well rounded, well sorted, in part porous and friable, flat laminations, mudstone interbeds, dolomitic at top
501.5 – 505.5 m. Mudstone: dark grey to black in lower part, grey to green and brown above, coarsening upward, thin sandstone interbeds in upper part, flat laminated, dolomitic, intraclastic sandstone at base
505.5 – 510.5 m. Dolostone: grey, stromatolitic at 505.5 – 505.8 m, 506.6 – 506.9 m, 508.0 – 508.5 m, oiod grainstone at 506.9 – 507.7 m, intraclastic horizons, sandy horizons, stylolitic
510.5 – 514.0 m. Mudstone: grey in upper half, brown to green and black in lower, dolomitic, fine sandstone interbeds, flat laminations and current ripple laminations. Dolostone: stylolitic, possibly stromatolitic
514.0 – 522.0 m. Sandstone: grey, brown near top, coarsening upward from fine grained near base to medium and coarse at top, well sorted, rounded, porous, subfriable, weakly flat laminated, ripple cross-laminations, mudstone interbeds at base
522.0 – 527.0 m. Dolostone: grey, stromatolitic at 522.8 – 523.6 m, 524.7 – 525.5 m, 526.2 – 527.0 m, dolomitic sandstone and mudstone interbeds, locally oolitic, stylolitic, flat laminated where not stromatolitic
527.0 – 527.4 m. Sandstone: grey, muddy, coarse to fine grained, poorly sorted, pyritic, flat bedded, overlies erosional surface on top of basalt

527.4 – 576.2 m KEENE BASALT (48.8 m thick)

527.4 – 576.2 m. Basalt: dark greenish-grey to black, locally reddened, fine to coarse grained, locally amygdaloidal, common fractures filled with chlorite, calcite, and red chert, pyritic near top and base. Lava flows: 4 or 5 separate flows; flow tops at 537.4 m, ?545.5 m, 555.5 m and 558 m; flow tops typically fine grained, amygdaloidal and in some cases reddened; top of unit eroded

KANPA FORMATION (continued)

576.2 – 579.4 m. Dolostone: grey to locally red, variably recrystallized by contact metamorphism, top 15 cm mostly silicified, local vuggy porosity, stromatolitic at 576.5 – 577.1 m and possibly near base, grades down to dolomitic mudstone
579.4 – 582.0 m. Interbedded dolomitic and calcareous mudstone, sandstone and dolostone: grey to green, black mudstone near base, sandstone fine to medium grained, fining-upward sequence, flat to wavy laminations, synaeresis cracks
582.5 – 583.0 m. Dolostone: red and green, intraclastic, sandy
583.0 – 595.1 m. Sandstone: multicoloured, fine to medium grained, minor coarse grained near base, moderately sorted, dolomitic and calcareous in part, interbedded mudstone, flat laminations, synaeresis cracks
595.1 – 598.3 m. Sandstone: white to light brown, fine to medium grained, well sorted, rounded, weak flat bedding to low-angle cross-bedding
598.3 – 618.4 m. Mudstone: light to dark grey, locally green, brown near base, interbeds of fine- to medium-grained sandstone, flat laminations, pot and gutter casts, synaeresis cracks, soft-sediment deformation
618.4 – 629.2 m. Sandstone: white to light brown, locally greenish, mostly medium grained, well sorted, rounded, porous, weak flat bedding and low-angle cross-bedding, local mudstone interbeds, erosive base with mudstone intraclasts, locally ferruginous
629.2 – 639.6 m. Sandstone: light brown, reddened near top and base, medium grained, well sorted, rounded, porous, weak flat bedding and cross-bedding, erosional base with abundant green mudstone intraclasts
639.6 – 656.0 m. Mudstone: grey, flat laminated, thin graded fine- to medium-grained sandstone interbeds with flat to current ripple laminations, micaceous, locally pyritic, soft-sediment deformation and microfaulting
656.0 – 663.8 m. Sandstone: grey in upper half grading to reddish-brown in lower, medium grained, well sorted, rounded, flat bedded to cross-bedded, grey to black mudstone interbeds in upper half, ferruginous concretions near base
663.8 – 669.0 m. Mudstone: grey, thin very fine-grained sandstone interbeds, massive to flat laminated
669.0 – 680.0 m. Claystone: grey, minor siltstone interbeds, massive to flat laminated
680.0 – 689.5 m. Claystone coarsening to mudstone downhole: brown and grey in upper half, brown below, flat laminated, thin sandstone interbed near base
689.5 – 695.6 m. Mudstone: grey, fine- to medium-grained sandstone interbeds, flat to current ripple laminations, synaeresis cracks near base, local soft-sediment deformation
695.6 – 696.9 m. Sandstone: light grey, medium grained, well sorted, subfriable, porous, erosional fluted base, cross-bedding near top, vertical fractures
696.9 – 699.7 m. Sandstone: white to reddish-brown and green, fine to medium grained, common mudstone laminae, fining-upward sequence to greenish-brown mudstone at top
699.7 – 707.5 m. Mudstone: brown, fine- to medium-grained sandstone interbeds between 702.5 and 703.7 m, minor very fine-grained sandstone interbeds elsewhere, flat laminated, synaeresis cracks

707.5 – 1201.9 m HUSSAR FORMATION (494.4 m thick)

707.5 – 731.0 m. Sandstone: light brown to white, medium to coarse grained, well sorted, rounded, subfriable (unconsolidated at 413.3 – 413.6 m), porous, flat bedded and cross-bedded with massive intervals, local vertical fractures
731.0 – 746.5 m. Sandstone: as for 707.5 – 731.0 m, but colour changes to reddish-brown with some green horizons, becomes white near base, rare thin mudstone interbeds, minor pyrite at base
746.5 – 750.6 m. Mudstone: mostly greenish-grey, fine-grained sandstone interbeds, flat and current ripple laminations
750.6 – 762.7 m. Sandstone: reddish-brown in upper half to mainly white in lower, medium to coarse grained, well sorted, rounded, subfriable, porous, flat bedded to cross-bedded, 10 cm nodular magnesite or anhydrite at top, top 1 m dolomitic and vuggy
762.7 – 765.9 m. Dolostone: brown, possible stromatolites at 762.7 – 763.2 m, stylolitic. Sandstone: brown, medium grained, flat bedded, dolomitic, magnesite or anhydrite beds and intraclasts, vuggy, porous
765.9 – 768.2 m. Dolostone: grey-brown, stromatolitic at 766.7 – 768.0 m, 10 cm sandy ooid grainstone at base, stylolitic
768.2 – 774.3 m. Sandstone: light brown (top reddish-brown), upper half medium to coarse grained, well sorted, porous, subfriable, lower half fine to medium grained and less friable, flat laminations and cross-bedding
774.3 – 774.9 m. Mudstone: brown, flat laminated, fine sandy interbeds near base
774.9 – 794.5 m. Sandstone: white to very light brown, mostly medium grained (fine at top), mostly well sorted, rounded, subfriable and porous, quartzose, flat bedded to cross-bedded
794.5 – 797.5 m. Dolostone and sandstone: brown, interbedded lithologies, stromatolitic dolostone at 796.6 – 796.9 m, sandstone is medium to coarse grained, well sorted, rounded, porous, flat bedded and cross-bedded, anhydrite nodules
797.5 – 800.3 m. Sandstone: light brown, fine to medium, and locally, coarse grained, poorly to well sorted, porous near base, flat bedding and ripple cross laminations
800.3 – 800.7 m. Dolostone: brownish-grey, stromatolitic, stylolitic, anhydrite nodules
800.7 – 802.2 m. Mudstone: brown to minor green, flat laminated
802.2 – 805.1 m. Dolostone: brown, stromatolitic at 802.8 – 803.3 m, 803.9 – 804.1 m, stylolitic, intraclast horizon, oolitic horizons, anhydrite nodules partly silicified
805.1 – 807.9 m. Sandstone and mudstone: brown, red, and green, interbedded lithologies
807.5 – 809.5 m. Dolostone: brown, stromatolitic at 808.8 – 809.1 m, stylolitic, chert and anhydrite nodules, sandy
809.5 – 833.1 m. Sandstone: light reddish-brown, medium to coarse grained, minor fine grained, mostly well sorted and rounded, subfriable, porous, flat bedded to cross-bedded, current ripple laminations, minor muddy intervals, local pyrite
833.1 – 838.0 m. Sandstone and dolomitic sandy mudstone: light brown to minor green, lithologies interbedded, sandstone medium to coarse grained, well sorted, porous, flat bedded to cross-bedded
838.0 – 859.6 m. Sandstone: pale brown, medium to coarse grained, mostly well sorted, rounded, subfriable to friable in parts, porous, flat bedded and cross-bedded, local soft-sediment deformation, local pyrite
859.6 – 861.4 m. Mudstone: brown, minor yellow and green, flat laminations, fine-grained sandstone interbeds, minor anhydrite
861.4 – 866.0 m. Sandstone: pale green, fine to medium grained, well sorted, rounded, slightly porous, flat laminations and current ripple cross-laminations, thin brown mudstone interbeds, minor anhydrite, possible glauconite
866.0 – 868.5 m. Mudstone: brown, flat laminations, fine-grained sandstone interbeds near top
868.5 – 888.8 m. Sandstone: upper half pale brown grading to white below, medium grained, well sorted, rounded, subfriable in parts, porous, massive to flat bedded and cross-bedded, anhydrite and mudstone interbeds in upper part
888.8 – 891.8 m. Mudstone: brown and green, common medium-grained sandstone interbeds; Sandstone: moderately to well sorted, rounded, slightly porous, flat laminations and current ripple laminations, possible glauconite
891.8 – 898.5 m. Sandstone: pale green, medium to coarse grained, mostly well sorted, rounded, subfriable, porous, flat bedded, cross-bedded near base
898.5 – 912.3 m. Mudstone: red, green reduction spots in lower part, locally dolomitic, massive to flat laminated, current ripple laminations, desiccation cracks, graded siltstone and very fine sandstone interbeds, anhydrite in nodules and veins
912.3 – 921.0 m. Dolostone: pale brown, stromatolitic at 913.5 – 913.9 m, 917.0 – 917.6 m, 919.0 – 919.3 m, stylolitic, interbeds of brown and reddish-brown mudstone and dolomitic mudstone, anhydrite and chert nodules, intraclasts common, local desiccation cracks
921.0 – 929.0 m. Mudstone: reddish-brown and green, dolomitic, dolostone interbeds, flat and current ripple laminations, common anhydrite nodules and veins, rip-up intraclasts, desiccation cracks
929.0 – 933.1 m. Mudstone: grey and reddish-brown, dolomitic, dolostone interbeds, flat and current ripple laminations, common anhydrite nodules and veins, 20 cm massive anhydrite bed below 929.3 m
933.1 – 936.1 m. Anhydrite: white, fine- to coarse-grained, massive, interbedded with and capped by argillaceous dolostone
936.1 – 952.3 m. Dolostone: grey, stromatolitic at 939.4 – 939.5 m, 940.1 – 941.9 m, 943.0 – 943.2 m, 944.9 – 945.15 m, 945.7 – 945.8 m, 948.1 – 948.3 m, 948.8 – 952.3 m, stylolitic, interbedded grey dolomitic mudstone, anhydrite nodules, sparse pyrite, soft-sediment deformation
952.3 – 956.5 m. Mudstone: dark grey to black, in part dolomitic, interbedded pale-grey dolostone, flat laminated, minor soft-sediment deformation, sparse fine pyrite
956.5 – 961.2 m. Dolostone: grey, stromatolitic at 956.5 – 957.2 m, 960.3 – 960.7 m, 961.0 – 961.2 m, stylolitic, dark-grey to black dolomitic mudstone interbeds, cauliflower anhydrite nodules, sparse fine pyrite
961.2 – 965.8 m. Mudstone: grey, minor brown and black horizons, dolomitic, massive to flat-laminated, dolostone intraclast horizons, anhydrite nodules
965.8 – 966.2 m. Anhydrite: chicken-wire texture grading to nodules in mudstone matrix
966.2 – 969.0 m. Dolostone: grey, argillaceous, flat laminated, anhydrite nodules and interbeds, minor chicken-wire texture
969.0 – 988.5 m. Mudstone: grey and green near top, grading to brown with green reduction spots below 973 m, dolomitic near top, siltstone to very fine-grained sandstone interbeds, flat laminated, current ripple laminations near top
988.5 – 997.8 m. Sandstone: light brown to green, mostly medium to coarse grained, moderately to well sorted, rounded, variable porosity, flat bedded to cross-bedded, current ripple laminations, possible glauconite, mudstone interbeds
997.8 – 1003.5 m. Dolostone: reddish-brown, ferruginous, stromatolitic at 997.8 – 1000.5 m, stylolitic, locally vuggy, oolitic grainstone in lower half, porous, medium to coarse grained sandstone interbed in centre
1003.5 – 1005.9 m. Sandstone: light green, medium to coarse grained, well sorted, rounded, subfriable in parts, slightly porous, flat bedding
1005.9 – 1007.0 m. Mudstone: red, flat laminated, fine-grained sandstone interbeds
1007.0 – 1012.0 m. Dolostone: reddish-brown, stromatolitic at 1008.3 – 1010.0 m, stylolitic, recrystallized grainstone at top and base, common intraclasts near top, anhydrite nodules
1012.0 – 1025.1 m. Sandstone: light reddish-brown to white, medium to coarse grained, moderately to well sorted, rounded, subfriable in part, porous in part, flat bedded to cross-bedded, thin mudstone interbeds in central part
1025.1 – 1027.1 m. Dolostone: reddish-brown, stromatolitic at 1025.3 – 1025.7 m, 1026.5 – 1027 m, stylolitic, sandy in part
1027.1 – 1029.0 m. Sandstone: brown, coarse grained, dolomitic and intraclastic near base
1029.0 – 1031.1 m. Dolostone: reddish-brown, wavy laminations, ooids near base, minor silicification, stylolitic
1031.1 – 1037.5 m. Dolostone, sandstone, and mudstone: mostly reddish-brown, lithologies interbedded, possibly stromatolitic dolostone 1033.2 – 1033.5 m, 1035.0 – 1035.4 m, stylolitic, local chert nodules, local ooids
1037.5 – 1040.0 m. Sandstone: light green, medium grained, moderately to well sorted, rounded, subfriable, slightly porous, flat bedded
1040.0 – 1041.0 m. Dolostone: brown, argillaceous, flat laminated
1041.0 – 1043.0 m. Sandstone: brown, medium to coarse grained, moderately to poorly sorted, dolomitic, mudstone, interbeds in lower part, flat bedded, desiccation cracks near base
1043.0 – 1045.3 m. Dolostone: brown, argillaceous, chicken-wire anhydrite near top, locally sandy, stylolitic, flat laminations
1045.3 – 1047.8 m. Sandstone: light brown to green, medium to coarse grained, moderately sorted, sub-angular grains, slightly porous horizons, flat to ripple cross-laminations, mudstone interbeds
1047.8 – 1051.8 m. Dolostone: brown, flat laminated, anhydrite and chert breccia near top, possible stromatolites in lower part, stylolitic, partly silicified ooid grainstone near base
1051.8 – 1059.5 m. Sandstone: mostly grey, medium to coarse grained in lower part, poor to well sorted, sub-angular to rounded grains, cross-bedded
1059.5 – 1062.2 m. Mudstone: red and brown, flat to ripple cross-lamnated, desiccation cracks, sandstone interbeds in upper part
1062.2 – 1068.0 m. Dolostone: brown, mostly flat laminated, local microbial laminations, stylolitic, abundant intraclastic breccia near base, anhydrite and chert nodules, dolomitic sandstone interbed near top
1068.0 – 1069.7 m. Mudstone: brown, dolomitic, sandstone interbeds, flat to ripple cross-laminations, desiccation cracks, intraclastic horizon at base
1069.7 – 1070.3 m. Dolostone: brown, flat laminated, anhydrite, halite pseudomorphs, erosive top
1070.3 – 1121.6 m. Mudstone: reddish-brown and lesser green, calcareous in upper half, graded siltstone to very fine sandstone interbeds, flat and current ripple laminations, desiccation cracks, anhydrite nodules
1121.6 – 1124.5 m. Dolostone: grey, partly replaced by chert, fractured, some fractures filled with anhydrite or gypsum, intraclast horizons in upper part, ooids present in lower part, stylolitic
1124.5 – 1134.1 m. Mudstone: mostly reddish-brown, minor green layers and reduction spots, dolomitic in part, mostly massive, sparse anhydrite
1134.1 – 1135.4 m. Dolostone: grey, partly replaced by chert, fractured in lower part, interbeds of anhydrite or gypsum
1135.4 – 1140.8 m. Mudstone: as for 1124.5 – 1134.1 m
1140.8 – 1143.1 m. Dolostone: grey, partly replaced by chert, strongly fractured, stromatolitic between 1141.2 – 1142.0 m, interbeds of anhydrite or gypsum near base, stylolitic
1143.1 – 1154.5 m. Mudstone: as for 1124.5 – 1134.1 m
1154.5 – 1157.0 m. Dolostone: grey, partly replaced by chert, fine-grained ooid grainstone between 1155.8 – 1156.2 m, anhydrite nodules near top, stylolitic
1157.0 – 1165.9 m. Mudstone: as for 1124.5 – 1134.1 m, anhydrite more abundant as thin stringers and vertical veins up to 3 m, thin dolostone interbed near base
1165.9 – 1167.1 m. Dolostone: grey, interbeds of anhydrite or gypsum, intraclast horizons, partly brecciated
1167.1 – 1175.2 m. Mudstone: as for 1124.5 – 1134.1 m
1175.2 – 1175.7 m. Dolostone: pink to brown, flat-laminated, argillaceous, recrystallized, small chert nodules possibly replacing anhydrite
1175.7 – 1195.1 m. Mudstone: as for 1124.5 – 1134.1 m, irregular and disrupted laminations, anhydrite more abundant, minor fine-grained sandy horizons
1195.1 – 1195.3 m. Anhydrite: bands of small nodules, partly replaced by chert and chalcedony, hosted by brown mudstone
1195.3 – 1197.0 m. Mudstone: as for 1124.5 – 1134.1 m
1197.0 – 1201.9 m. Mudstone: as for 1124.5 – 1134.1 m, scattered sand grains and medium- to coarse-grained sandstone interbeds, mudstone intraclasts in basal sandstone bed

1201.9 – 1478.9 m BROWNE FORMATION (277 m thick)

1201.9 – 1297.7 m Lancer Member (95.8 m thick)

1201.9 – 1242.0 m. Sandstone: reddish-brown, medium grained, mostly well sorted, well rounded, subfriable, porous, quartzose, large foresets to 11 m with dips to 25°, minor irregularly flat-bedded horizons, sandstone dykes along small-scale faults
1242.0 – 1261.0 m. Sandstone: as for 1201.9 – 1242.0 m, but average grain size increases to borderline coarse sand, increased proportion of finer moderately sorted irregularly flat bedded horizons, foresets to 3 m
1261.0 – 1279.0 m. Sandstone: as for 1201.9 – 1242.0 m, foresets to 3 m with dips to 27°
1279.0 – 1297.7 m. Sandstone: as for 1201.9 – 1279.0 m, but irregularly flat bedded horizons become dominant over 1 m-scale foreset horizons, fine to coarse grained, moderately to well sorted, inclined open fractures common, 60 cm green sandstone at base
1297.7 – 1301.9 m. Sandstone: basal 80 cm green grading to reddish-brown above, medium grained and moderately sorted at base grading upward to fine-grained and poorly-sorted muddy sandstone above, irregular laminations
1301.9 – 1322.0 m. Sandstone: mostly reddish-brown with local green interbeds, fine to very fine grained (rarely medium) with high mud content, poorly sorted, irregular laminations
1322.0 – 1323.4 m. Sandstone: reddish-brown, medium grained with coarse interbeds, moderately sorted, subangular grains, cross-bedded

1323.4 – 1357.7 m Woolnough Member (34.3 m thick)

1323.4 – 1325.6 m. Dolostone: light reddish-brown, stromatolitic at 1323.5 – 1324.1 m, 1324.6 – 1325.6 m, interbedded with mudstone
1325.6 – 1331.9 m. Mudstone and dolostone: multicoloured, interbedded lithologies, flat laminations and ripple cross laminations, possible desiccation cracks, vertical anhydrite veins
1331.9 – 1333.8 m. Dolostone: reddish-grey, argillaceous, stromatolitic, stylolitic, vertical anhydrite vein
1333.8 – 1345.9 m. Mudstone and dolostone: reddish-brown and grey, interbedded lithologies, flat to current ripple laminations, desiccation cracks, intraclast horizons, minor medium to coarse grained sandstone, anhydrite layers and veins
1345.9 – 1347.3 m. Dolostone: brownish-grey, microbially laminated and stromatolitic
1347.3 – 1357.7 m. Dolostone: brownish-grey, stromatolitic at 1348.8 – 1350.9 m, 1351.3 – 1351.7 m, 1353.7 – 1355.3 m, sandy at top, locally argillaceous, grainstone and intraclastic horizons, vertical anhydrite vein, minor mudstone interbeds

1357.7 – 1478.9 m lower Browne Formation (123.6m thick)

1357.7 – 1378.0 m. Mudstone: red with common green reduction spots and mottles, weakly dolomitic, massive to irregularly laminated
1378.0 – 1382.2 m. Mudstone: as for 1357.7 – 1378.0 m, but with thin horizons containing scattered fine to medium sand grains, massive
1382.2 – 1386.5 m. Mudstone: as for 1357.7 – 1378.0 m, but with anhydrite or gypsum in veins and filling pseudomorphs after probable halite, massive
1386.5 – 1390.0 m. Mudstone: as for 1357.7 – 1378.0 m, but with poorly sorted and lithic medium to coarse grained sandstone horizons, irregularly laminated, minor anhydrite or gypsum
1390.0 – 1408.5 m. Mudstone: reddish-brown, green reduction spots, dolomitic, dolostone interbeds, sparse medium to coarse sandy horizons, flat to irregular and current ripple laminations, desiccation cracks, anhydrite or gypsum, halite pseudomorphs
1408.5 – 1414.9 m. Mudstone: reddish-brown, green reduction spots, dolomitic, dolostone interbeds, mostly massive, halite rimmed by anhydrite or gypsum, nodular anhydrite layers between 1414.4 – 1414.9 m
1414.9 – 1440.8 m. Mudstone: reddish-brown, green reduction spots, dolomitic, massive to weakly laminated, rare sandy interbeds, common clear halite as isolated crystals, crystal clusters and veins
1440.8 – 1447.0 m. Halite: orange, interbeds and lenses of flat-laminated dolomitic mudstone
1447.0 – 1450.0 m. Mudstone: reddish-brown, flat laminated. Halite: orange, thin beds and isolated crystals
1450.0 – 1451.0 m. Halite: as for 1440.8 – 1447.0 m
1451.0 – 1451.6 m. Mudstone: reddish-brown, dolomitic, flat laminated, isolated halite
1451.6 – 1456.5 m. Halite: as for 1440.8 – 1447.0 m
1456.5 – 1457.4 m. Mudstone: brown, flat laminated, dolomitic, isolated halite, grey argillaceous dolostone at top
1457.4 – 1463.4 m. Halite: as for 1440.8 – 1447.0 m, grey dolostone interbeds in lower half
1463.4 – 1465.1 m. Dolostone: grey, argillaceous, halite beds and isolated crystals
1465.1 – 1466.2 m. Halite: as for 1440.8 – 1447.0 m
1466.2 – 1467.0 m. Dolostone: as for 1463.4 – 1465.1 m
1467.0 – 1469.6 m. Halite: as for 1440.8 – 1447.0 m
1469.6 – 1471.4 m. Dolostone: as for 1463.4 – 1465.1 m, minor black intervals, minor fine-grained sandstone interbeds
1471.4 – 1472.4 m. Halite: as for 1440.8 – 1447.0 m
1472.4 – 1475.2 m. Dolostone: as for 1463.4 – 1465.1 m, minor black horizons, sandy interbeds
1475.2 – 1478.9 m. Sandstone interbedded with conglomerate, dolostone, and mudstone: brown, grey, and black, 10 cm basal sandy conglomerate over erosional surface, minor halite and anhydrite, bedding dips 2°

1478.9 – 1501.2 m ?CORNELIA SANDSTONE (>22.3 m thick)

1478.9 – 1501.2 m. Sandstone: bluish-grey, medium grained, minor coarse interbeds, sparse small pebbles, moderately sorted, subrounded, minor clay matrix, feldspathic, micaceous, well cemented, cross-bedded; 1 cm mudstone interbed dips 4°

PWH23 01.06.05